COMPUTER SIMULATION OF ELECTROMIGRATION INDUCED VOID-GRAIN BOUNDARY INTERACTIONS AND THE PREDICTION OF CATHODE FAILURE TIMES IN BAMBOO STRUCTURES

ERSIN EMRE ÖREN

JANUARY 2003

1956
Middle East Technical University

COMPUTER SIMULATION OF ELECTROMIGRATION INDUCED VOID-GRAIN BOUNDARY INTERACTIONS AND THE PREDICTION OF CATHODE FAILURE TIMES IN BAMBOO STRUCTURES

A THESIS SUBMITTED TO
THE GRADUATE SCHOOL OF NATURAL AND APPLIED SCIENCES
OF
THE MIDDLE EAST TECHNICAL UNIVERSITY

BY

ERSIN EMRE ÖREN

IN PARTIAL FULFILLMENT OF THE REQUIREMENTS FOR THE DEGREE
OF
DOCTOR OF PHILOSOPHY
IN
THE DEPARTMENT OF METALLURGICAL & MATERIALS ENGINEERING

JANUARY 2003

Approval of the Graduate School of Natural and Applied Sciences

Prof. Dr. Tayfur ÖZTÜRK
Director

I certify that this thesis satisfies all the requirements as a thesis for the degree of Doctor of Philosophy.

Prof. Dr. Naci SEVINÇ
Head of Department

This is to certify that we have read this thesis and that in our opinion it is fully adequate, in scope and quality, as a thesis for the degree of Doctor of Philosophy.

Prof. Dr. Tarik Ö. OGURTANI
Supervisor

Examining Committee Members

Prof. Dr. Tarik Ö. OGURTANI

Prof. Dr. Macit ÖZENBAS

Prof. Dr. Erman TEKKAYA

Prof. Dr. Lütfi ÖVEÇOGLU

Assoc. Prof. Dr. Kadri AYDINOL

ABSTRACT

COMPUTER SIMULATION OF ELECTROMIGRATION INDUCED VOID - GRAIN BOUNDARY INTERACTIONS AND THE PREDICTION OF CATHODE FAILURE TIMES IN BAMBOO STRUCTURES

ÖREN, Ersin Emre
Doctor of Philosophy, Department of Metallurgical and Materials Engineering
Supervisor: Prof. Dr. Tarik Ö. OGURTANI

January 2003, 242 pages

The purpose of this work is to provide such a comprehensive picture of void dynamics, shape changes and void grain boundary interactions that one should eventually be able to predict main reasons and conditions under which premature failure of metallic thin film interconnects occurs.

By introducing the concept of assembly of discrete microelements a rigorous reformulation of the internal entropy production and the rate of entropy flow terms is developed for the multi-component systems composed of surfaces and/or interfaces. The generalized forces and conjugate fluxes associated with the virtual displacement of a triple junction and the ordinary points are determined. This formalism also takes into account in a natural way the mass transport process between the bulk phase and the void region, in terms of the normalized local values of Gibbs free energy of transformation in addition to the contribution due to local curvature of the advancing reaction front.

A well posed moving boundary value problem describing the dynamics of curved interfaces and surfaces associated with voids that are interacting with grain boundaries is obtained. Utilizing indirect boundary element method, the Laplace equation is solved. The resulted nonlinear partial differential equation is solved numerically by Euler's method of finite difference.

As a special application of the theory extensive computer simulations are performed on the void configurational evolution during the inter- and intra-granular motion, under the actions of capillary and electromigration forces in thin film interconnects.

In this thesis, very rich computer simulation results have been obtained in regard to void motion and shape changes under various experimental conditions such as applied electric field, the wetting parameter, interconnect width, the initial void morphology and finally the grain textures.

A set of formulas representing not only the upper and lower bonds for the cathode failure times but also the median time to failure is deduced for the bamboo and/or near-bamboo structures which is in excellent agreement with the published experimental data.

Key words: Electromigration, surface diffusion, metallization, void morphology, bamboo-lines, grain boundary, texture, median time to failure.

ÖZ

ELEKTROGÖÇ’E BAGLI BOSLUK-TANECIK SINIRI ETKILESIMLERININ BILGISAYAR MODELLEMESI VE BAMBU YAPILARDAKI KATOT BOZULMA ZAMANLARININ TAHMINI

ÖREN, Ersin Emre
Doktora, Metalurji ve Malzeme Mühendisligi Bölümü
Tez Yöneticisi : Prof. Dr. Tarik Ö. OGURTANI

Ocak 2003, 242 sayfa

Bu çalismanin amaci; mikro-elektronik devrelerdeki metalik ince filmlerin bozulma nedenlerinin ve yasam sürelerinin tahminini saglamak için gerekli olan bosluk dinamigi, bosluklarin sekil degisiklikleri ve bosluk ile tane sinirlari arasindaki etkilesimlerin ayrintili bir sekilde incelenmesidir.

Yüzeyler ve/veya arayüzeyler içeren çok bilesenli sistemler için, içsel entropi üretimi ve entropi akma hizi terimleri, sinirli mikroelemanlar toplulugu kavrami kullanilarak gelistirilmistir. Üçlü kavsaklar ve siradan noktalarin hareketleri ile baglantili olarak genellestirilmis kuvvetler ve bunlara bagli akilar elde edilmistir. Bu yaklasim, boyutsuzlastirilmis yerel egrilige ek olarak yerel Gibbs dönüsüm serbest enerjisini de göz önüne alarak esas faz ile bosluk arasindaki madde transferini de dogal bir sekilde açiklamaktadir.

Tane sinirlari ile etkilesim halindeki bosluklar ile ilgili olarak egimli yüzey ve arayüzeylerin dinamigini tarif eden, iyi tavirli hareketli sinir deger problemi elde edilmistir. Laplace denklemi dolayli sinir elemani yöntemi kullanilarak çözülmüstür. Elde edilen dogrusal olmayan kismi diferansiyel denklem sayisal olarak Euler'in belirli fark yöntemi kullanilarak çözülmüstür.

Bu teorinin özel bir uygulamasi olarak, uygulanan elektrik alan, islatma parametresi, metalik ara-baglantilarin kalinligi, baslangiç bosluk morfolojisi ve tane yapisi gibi farkli deney degiskenleri kullanilarak, boslugun tane içi ve taneler arasi hareketi ve sekil degisiklikleri ile ilgili çok zengin bilgisayar simülasyon sonuçlari elde edilmistir.

Ayrica, katot bozulma süreleri için sadece alt ve üst sinirlari degil ayni zamanda ortalama süreyi de veren bir dizi formül elde edilmis ve bunlarin yayimlanmis deneysel veriler ile mükemmel bir sekilde uyusmakta oldugu gözlenmistir.

Anahtar Sözcükler: Elektrogöç, yüzey difüzyonu, metallestirme, bosluk morfolojisi, bambu hatlari, tane sinirlari, tane yapisi, ortalama bozulma zamani.

To My Wife & Daughter

Çigdem Özbag & Ayse Doga

ÖREN

ACKNOWLEDGEMENTS

I thank to Prof. Dr. Tarik Ö. Ogurtani for his invaluable guidance and support during the study of this thesis. It has been a great pleasure for me to work under his supervision.

I would like to thank Profs. M. Özenbas, G. Gündüz and K. Aydinol of Middle East Technical University (METU), and Prof. E. Arzt and Dr. C. Volkert of Max-Planck-Institute (MPI) for Metals Research, for their very valuable suggestions.

I also thank to The Directorate of Human Resources Development (BAYG) of The Scientific and Technical Research Council of Turkey (TUBITAK) for the NATO A-2 scholarship for my visit to MPI for Metals Research at Stuttgart Germany.

I also wish to acknowledge the help, provided me in various aspects, by the Metallurgical and Materials Engineering Department of METU.

Special thanks to Mr. Tevfik Tolga Ören, my brother, for his invaluable helps during the preparation of this thesis.

Finally, I am grateful to Çigdem Özbag Ören, my wife, for the encouragement and constant support she gave me during this study.

TABLE OF CONTENTS

CHAPTER

APPENDICES

NOMENCLATURE

i. Latin Letters

A : area

A_s^j : affinity of the j^{th} chemical reaction taking place in $_s$ phase

BEM : boundary element method

c : atomic volumetric concentration

CPFT : cathode-pad failure time

d_a : inter-atomic distance

$\tilde{D}_s$: self diffusivity

D_s^0 : minimum surface diffusivity corresponding to a specific surface orientation

DF : density function

DT : detachment time

e : unit electronic charge

E_0 : remote applied electric field

F : Helmholtz free energy

F_i : generalized force

FS : fundamental solution

FT : flight time

g : specific Gibbs free energy density

$\breve{g}$: volumetric Gibbs free energy density

g_{vb} : specific Gibbs free energy of formation

G : activation energy

GFET : Gibbs free energy of transformation

h : thickness

H : activation enthalpy

IBEM : indirect boundary element method

IEP : internal entropy production

J_i : generalized conjugated flux

k : Boltzmann constant

ℓ : curvilinear coordinate along the void surface (arc length)

ℓ_g : mean distance between bamboo grain boundaries or the grain size

L : interconnect length

LBCFT : lower bond cathode failure time

LGMCFT : logarithmic mean cathode failure time

m : dimensionless parameter that determine the grain symmetry through the number of crystallographic directions corresponding to fast diffusion paths (half fold number)

m_d : number of division for the numerical integration

MTTF : mean time to failure

n : number of chemical species

n_b : mean number of bamboo grain boundaries

$\hat{n}$: surface normal vector at the centroids

N : fold number or rotational degree of symmetry

P : source point

$\overline{P}$: mean isotropic pressure in the layer

q : heat received by the system

Q_d : deviatoric part of the stress tensor

Q : field or observation point

$\vec{r}$: node position vectors

$\vec{r}_c$: centroid position vector,

r_o : mean initial void radius

r_{crt} : critical initial void radius

REF : rate of entropy flow

s_i : segment length

$s_{\max}$: maximum segment length

$s_{\min}$: minimum segment length

S : entropy

t : time

t_d : detachment time

t_f : failure time

t_{flight} : flight time

$\hat{t}$: surface tangent

T : temperature

$T(P,Q)$: directional derivative of the fundamental solution

TJ : triple junction

U : internal energy

$U(P,Q)$: fundamental solution of Laplace equation and represents the field generated by a concentrated unit charge at P acting at a point Q

UBCFT : upper bond cathode failure time

x_i : atomic fractions

V : volume

w : width

Z : effective electromigration charge

ii. Greek Letters

g : surface tension

d : variational operator

e : boundary of the singularity

q_i : segment turning angle

q : angle formed by the local surface tangent and the direction of the applied electric field

k : curvature

l : wetting parameter

m : chemical potential

$m(P)$: density function that are continuously distributed over the boundary

r : radius of curvature

t_o : normalized time

f : the misorientation of the symmetry direction with respect to the direction of the applied electric field

c : electron wind intensity

y : angle that denotes the amount of rotation of the microelements adjoint to the triple junction in the anti-clockwise direction

w : reversible work done on the system

A : surface diffusion anisotropy strength

Γ : specific mean atomic density

Δ : space-scaling operator

$\Delta\vec{r}$: vector that connects the successive nodes

M : generalized phenomenological mobility

P : power dissipation

Φ : energy received by the system

W : amount of energy transported to the individual phase from the other phases through mass transfer

Ω : mean atomic specific volumes

iii. Symbols

dx_s^j : extent of the j^{th} chemical reaction taking place in s phase

$\Re$: phenomenological mobility coefficient

J : electrostatic potential

j : dihedral angle

u : grain boundary tilt angle

∇ : del operator

∇^2 : Laplace operator

iv. Subscripts

b : bulk

em : electromigration

ex : external

in : internal

g : grain boundary

ord : ordinary point

s : surroundings

v : void

a : bulk phase

b : bulk phase

s : interfacial layer

v. Superscripts

$-$: left hand side of the system

$+$: right hand side of the system

long : longitudinal

trans : transverse

vi. Signs over symbols

$\breve{}$: denotes volumetric quantities

$\hat{}$: denotes surface densities

$\hat{}$: denotes normal vectors

$\vec{}$: denotes vector quantities

$\bar{}$: denotes normalized quantities

LIST OF TABLES

LIST OF FIGURES

PREFACE

Electromigration is the mass transport of a metal due to the momentum transfer between the conduction electrons and the diffusing metal atoms when an electrical current passes through a metal thin film.

Gerardin first reported electromigration in 1861. This and all the subsequent early studies were concerned with liquid alloys and it was until the 1930's that the much slower process of electromigration in the solid state was demonstrated and investigated. For at least a hundred years, electromigration was an interesting problem in solid-state physics, fascinating research at the universities, but of no interest whatsoever commercially.

When the integrated circuits made its commercial appearance in 1966, all of this changed; electromigration was rediscovered and has been the subject of intense study. This discovery, coming as a surprise to the industry, threatened to stop integrated circuit development in its tracks until solutions to problem become available. This was possible only through intense research and development efforts. The reason electromigration was a problem in integrated circuit technology lies in the peculiar combination of material properties inherent in integrated circuit conductors and in the relatively severe use conditions (Lloyd, 1997).

Commercial interest in the subject of electromigration led to extensive research efforts in the 1970's. After 1975, most of the important concepts associated with electromigration failure had been identified, but many of the finer details of these concepts, and their interaction to produce reliability problems were not completely appreciated. In the two decades following, these concepts have been refined to the point where a reasonable understanding of what makes a circuit reliable and unreliable has been achieved.

Among a variety of approaches developed to study electromigration phenomenon, computer simulation is a powerful and efficient one. Through a computer simulation, it is easier to consider multiple mechanisms involved in electromigration to enhance the accuracy of the model. Also it enables one to observe the macroscopic effects of the microscopic variables to reveal the insights of this phenomenon that may not be experimentally possible.

The electromigration induced failure of metallic interconnects is a complicated process, which involves flux divergence, vacancy and/or atom accumulation with or without compositional variations, void and hillock nucleation, growth and shape changes (Arzt and Nix, 1991; Nix and Arzt, 1992). A near-bamboo grain structure is produced as the width of these interconnects is reduced to microscopic dimensions. This near-bamboo structure contains both interconnected networks of grain boundaries as well as grains, which span the width of the line. In this case, electromigration-induced failure processes become more complicated due to the existence of grain boundary diffusion in addition to the surface and bulk diffusion mechanisms (Sanches *et al.*, 1992).

In Chapter 1 of this thesis, a detailed literature review for the electromigration phenomenon and the void grain boundary interactions in terms of triple junctions is summarized.

A summary of the rigorous irreversible thermodynamic treatment of morphological evolution of curved void surface layer, interacting with the grain boundaries, at the presence of electromigration-induced forces is presented in Chapter 2. A completely normalized and scaled partial differential equation obtained through this phenomenological treatment is useful not only for the computer simulation studies of alloy systems, but also gives some clues how certain material parameters of a specific system may or may not be important in the determination of durability of interconnects.

In Chapter 3, the numerical methods and procedures used in the solution of the completely normalized and scaled partial differential equation obtained in Chapter 2, are outlined comprehensively.

The extensive simulation experiments on the configurational changes associated with voids during the inter- and intra-granular motions in two dimensional space, which is utilizing various initial void morphology, interconnect texture, with or without anisotropic surface diffusion and vacancy diffusion from the bulk (void growth) are summarized in Chapter 4.

The computer program, which is developed in *C Code* for the computer simulation studies, is listed in Appendix B.

CHAPTER 1

LITERATURE SURVEY

1.1. Overview

Modern semiconducting chips include a dense array of narrow, thin-film metallic conductors that serve to transport current between the various devices on the chip. These metallic conductors are called interconnects.

As integrated circuits become progressively more complex, the individual components must become increasingly more reliable if the reliability of the whole is to be acceptable. With the complexity of today's microelectronics; an extraordinary level of reliability must be maintained. For instance, if the probability of failure for a transistor is one in a million, and the integrated circuit (IC) contains a million transistors, failure is very near certainty. And today's modern integrated circuits can have more than ten million circuit elements. Consequently, for any acceptable reliability on the chip level, today's circuit elements must be among the most reliable things ever built in the world.

However, due to continuing miniaturization of very large scale integrated (VLSI) circuits, thin-film metallic conductors or interconnects are subject to increasingly high current densities. Under these conditions, electromigration can lead to the electrical failure of interconnects in very short times by reducing the circuit lifetime to an unacceptable level (Mahadevan *et al*, 1996).

It is therefore of great technological importance to understand and control electromigration failure in thin film interconnects.

In conventional metal wires like those used in house wiring, joule heating limits the allowable current to about $10^4 A/cm^2$. At current densities higher than this the wire will heat up and fuse. Because they are deposited onto large efficient single crystal silicon heat sinks, thin film interconnects in integrated circuits can sustain current densities up to $10^7 A/cm^2$ (Wang *et al*., 1996) without immediate damage.

Electromigration causes several different kinds of failure in narrow interconnect. The most familiar are void failures along the length of the line (called internal failures) and diffusive displacements at the terminals of the line that destroy electrical contact. Recent research has shown that both of these failure modes are strongly affected by the microstructure of the line and can, therefore be delayed or overcome by metallurgical changes that alter the microstructure.

1.2. Interconnects and Processing

Interconnect metals and alloys must meet most of the requirements listed below

- Low resistivity
- Make ohmic contacts to p and n type silicon (Si)
- Low level of stress
- Coefficient of thermal expansion (CTE) close to Si
- Good adhesion to Si and silicon oxide (SiO_2)
- Reaction to Si and SiO_2 should be minimum during fabrication
- Resist the transport of matter (called electromigration) due to high current densities in integrated circuits
- Remain morphologically stable under high temperatures
- Be able to be deposited into thin films by simple deposition techniques such as sputtering.

By 1965, aluminum (Al) met most of the requirements above. The main obstacle in 1965 was the requirements between Si and Al. The solution was to add 1-2% Si to Al film.

By 1968, integrated circuits decreased in size. This caused an increase in electromigration failure of Al interconnects. As integrated circuit dimensions decrease, the current density and the contact resistance increase. This results in the increase in electromigration failure, which in turn result in a short lifetime of the integrated circuit. In 1968, the solution was to add 1-2% copper (Cu) to Al.

But as the years went by, integrated circuits interconnect dimensions have decreased ever since and the dangers of electromigration failure have increased. Additional restrictions, rather than requirements, were needed for interconnection and circuit design. These are called scaling laws which were used to maximize integrated circuit performance.

- Electrical signals must be above a noise level
- Technological requirements that fix operating voltages

Today, the major challenges of interconnects are stress and electromigration. Both of these challenges lead to hillock and hole/void formation, which ultimately lead to device failure.

One of the requirements of acceptable metal interconnect in integrated circuits is its ability to be deposited into a thin film form. The metal must also be able to be deposited by simple deposition techniques. These techniques include:

- Vacuum evaporation
- Sputtering
- Chemical vapor deposition

In figure 1.2.1 a cross-sectional view of the interconnect structure can be seen.

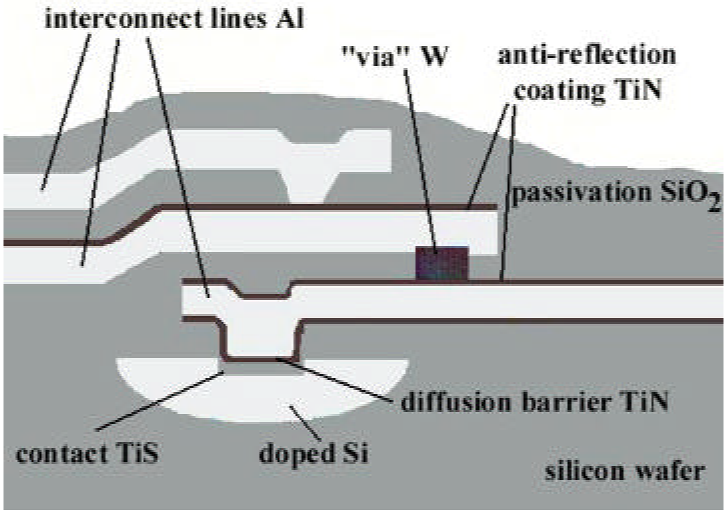

Figure 1.2.1: Cross-sectional view of the interconnect structure.

The deposited metal is often highly polycrystalline. The resistivity of the deposited metal is usually greater than the bulk values. Table 1.2.1 below shows example metal comparing bulk and thin film resistivity.

Table 1.2.1: Resistivity of some metals used in thin films.

Metal	*Thin film* *(W m x 10^8)*	*Bulk* *(W m x 10^8)*	**Deposition Technique**
Al	2.8-3.3	2.67	Vacuum evaporation
Au	2.4	2.2	Vacuum evaporation or sputtering
Ni	12	2.9	Vacuum evaporation or sputtering
Mo	10	5.7	Sputtered and annealed

The increased resistivity is due to the structure of the thin film, which is more disordered with smaller grains than its bulk counterpart. These smaller grains carry a higher defect and dislocation density. This causes the electrons to scatter more frequently at the grain boundary region due to the smaller grains and its highly crystalline structure. This increases the residual resistivity, which in turn ads to the overall resistivity via Matthiessens's rule.

After the deposition process, the unwanted portion of the thin film is etched away by using lithographic or similar techniques. This leaves the wanted interconnects.

Many devices today require interconnect dimensions of about $1m$ or less. At these small dimensions, along with steep topography, a uniform film deposition is needed to ensure uniform contact.

1.3. The Physical Basis of Electromigration

Electromigration in generally considered to be the result of momentum transfer from the electrons, which move in the applied electric field, to the ions which make up the lattice of the interconnect material (Arzt, and Nix, 1991).

When electrons are conducted through a metal, they interact with imperfections in the lattice and scatter. Scattering occurs whenever an atom is out of place for any reason. Thermal energy produces scattering by causing atoms to vibrate. This is the source of resistance of metals. The higher the temperature, the more out of place the atom is, the greater the scattering and the greater the resistivity.

For electromigration one needs a lot of electrons, and also one needs electron scattering. Electromigration does not occur in semiconductors, but may in some semiconductor materials if they are so heavily doped that they exhibit metallic conduction.

To describe the electromigration process let us use an electrostatic analogue. The driving force for electromigration expressed in this way is

$$F = Z^{*}eE \tag{1.3.1}$$

Here, Z^{*} is the effective valance or effective charge, e is the unit electrostatic charge and E is the electrostatic field. The Value of Z^{*} has been expressed by Huntington 1961, as

$$Z^{*} = \frac{1}{2}\left(\frac{r_d N}{r N_d}\right)\frac{m^{*}}{\left|m^{*}\right|} \tag{1.3.2}$$

Here N is the density of conduction electrons, r_d is the specific defect resistivity, N_d the defect density, r is the metal resistivity, and m^{*} is the effective mass of the electrons near the Fermi surface taking part in the momentum exchange.

The effective charge Z^{*} characterizes the momentum transfer, its value which is not well understood, can be inferred from experimental data.

In analyzing electromigration, it is useful to separate the net driving force on an impurity into two parts. One part is called the '*electron wind force*' that refers to the effect of momentum transfer from the incident electrons to the ionic atoms when an electrical current is applied to a conductor. The other part is called the '*direct force*'; while the ions tend to move in the direction of the impulse during the momentum exchange, which is in the direction opposite to the electrical field, they also tend to move in the direction of the applied field since they are positively charged. The balance of these two forces determines the movement of the ions.

$$F_{total} = F_{direct} + F_{wind} \tag{1.3.3}$$

For simplicity, the term "electron wind force" often refers to the net effect of these two electrical forces. This simplification will also be used throughout the following discussion. The schematic picture of these forces can be seen in figure 1.3.1.

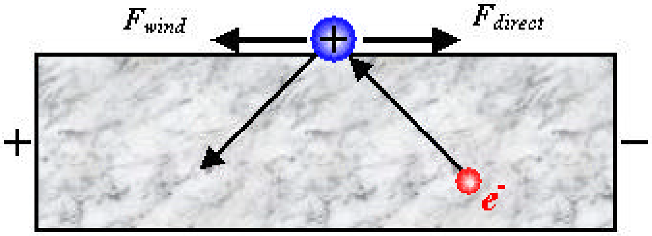

Figure 1.3.1: The driving force for electromigration.

Using the Einstein - Nerst relation for diffusion in a potential field, the drift velocity is obtained as,

$$v_{drift} = BF = \frac{D}{kT}F = \frac{DZ^{*}eE}{kT} = \frac{DZ^{*}erj}{kT} \qquad (1.3.4)$$

Here, B is the mobility, D is diffusivity, k is Boltzman's constant, T is absolute temperature and j is the current density.

From Eq. (1.3.4) electromigration induced mass flow is seen to be directly proportional to the current density and the diffusion constant D.

The drift velocity, v_{drift}, will be a function of the diffusion pathway and the temperature dependence of v_{drift} will be characterized by the activation energy of the predominant diffusion mechanism, Q, as shown in the following equation (D_o is the temperature independent pre-exponential);

$$D = D_o \exp(-\frac{Q}{kT}) \qquad (1.3.5)$$

In general, one can separate electromigration-driven diffusion into three: Surface electromigration, bulk electromigration and grain boundary electromigration. The schematic picture of these diffusion paths can be seen in figure 1.3.2.

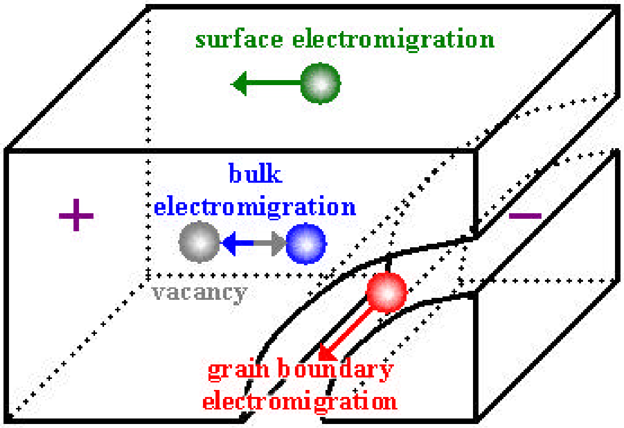

Figure 1.3.2: The diffusion paths of electromigration.

The surface diffusion is the fastest one and in generally grain boundary transport is more rapid than interfacial or bulk diffusion. According to Lloyd (1997), the activation energies, *E*, for the pathways are in general,

$$E_{surface} = \frac{3}{2} E_{grain\ boundary} = 3E_{bulk} \qquad (1.3.6)$$

Figure 1.3.3 shows the differences between wide and narrow interconnects. In a wide line, grain boundaries form a continuous network, and as discussed above diffusion on grain boundaries is faster than diffusion in lattice so the latter is negligible (Wang and Suo, 1996). By contrast, a narrow line has a bamboo-like grain structure, where grain boundaries are far apart and nearly perpendicular to the interconnect line direction.

In addition to rounded voids, slits have been observed both in bamboo-like grain and single crystalline interconnects (Sanches *et al.*, 1992; and Rose, 1992).

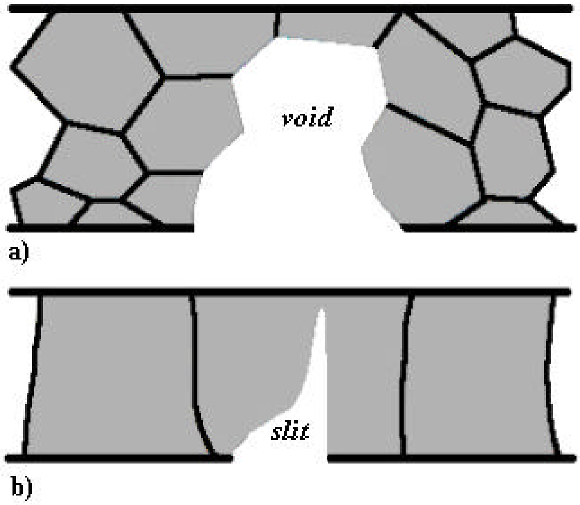

Figure 1.3.3: a) Wide and **b)** narrow (bamboo-like) interconnects.

Void migration may be understood in terms of surface diffusion. Atoms diffuse on the void surface from one portion of the void to the another, so that void appears to translate in the grain. It has been suggested that a rounded void is unstable: the electric current may amplify a small asymmetry in the void shape and cause the void to collapse to a slit (Wang *et al*., 1996). There are two forces that compete to determine the void shape. Surface tension or *"capillary forces"* favours a rounded void, and electric current *"electron wind force"* favours the slit. That is under the electric current a void collapse to a slit.

Figure 1.3.4 illustrates a void, as atoms diffuse along the internal void surface. For simplicity, it is assumed that the void is across the thickness h, and the conductor is isotropic. Both electric field and surface energy drive diffusion:

$$J = \frac{Dd}{\Omega kT}\left(-eZ^{*} + \Omega g\,\frac{dk}{dl}\right) \tag{1.3.7}$$

Here J is the surface flux of atoms (the number of atoms passing per unit length per time), D is the surface diffusivity, d is the thickness of the surface layer taking part in the diffusion process Ω is the atomic volume, g is the surface energy, k is the curvature of the surface (positive for a rounded void), and l is the arc length.

The physical meaning of Eq. (1.3.7) is that atoms will diffuse in the direction of electron flow if the electric wind force dominates, but toward the position with large curvature if the capillary forces dominate.

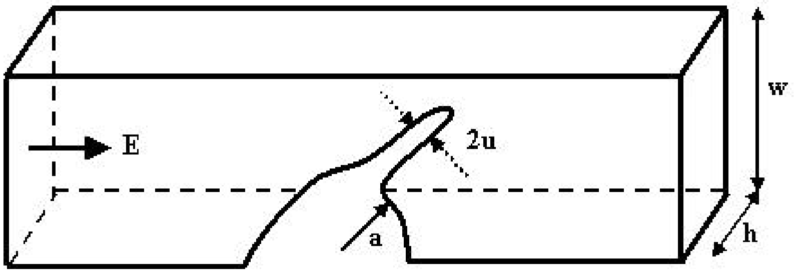

Figure 1.3.4: A narrow slit emanates from a rounded void.

Subjected to an electric field, a circular void can translate in a conductor, without changing its shape, as atoms diffuse from one portion of to void surface to another. The moving circular void is a solution to Eq. (1.3.7); the surface energy does not drive diffusion in this situation, because the curvature is constant on the void surface (Ho, 1970). However, the following consideration indicates that the circular void is unstable when the electric field is large. The field projected on the slit surfaces tends to move atoms away from the slit-tip and extend the slit. The surface energy has to opposite effect: It tends to move atoms toward the slit tip and heal the slit. A dimensionless number emerges from Eq. (1.3.7) and this consideration:

$$c = \frac{eZ^{*} r J a^{2}}{g\Omega} \tag{1.3.8}$$

with a being the size of the void. When c is small, the surface energy dominates, and the void will remain rounded. When c is large, the electric field dominates, and the slit will form (Suo, *et al.*, 1994). It is concluded that slit-like failures will therefore be dominant in wide lines with large voids and/or at high current densities. However, this calculation did not take into account the effects of finite line width and the resulting current crowding with progressive void growth. Also, the competition with void growth is neglected, which results in a reserved current density dependence (Kraft and Arzt, 1997).

1.3.1. Black's Law

If the electrons at zero fields are considered to have an entirely random motion, both before and after being accelerated and colliding with ions with nearly elastic collisions, they pass on all of their momentum to the ions. The rate of mass transport by momentum transfer between thermally activated ions and the electrons is directly proportional to the number of activated ions or targets available per cm^3, the number of electrons per second available for striking the activated ions, and the momentum of these electrons. This may be expressed as:

$$
\begin{aligned}
R = F.&(\text{electron momentum}) \\
&.(\text{number of electrons passing through a unit volum e per second}) \\
&.(\text{effective targed cross-section}) \\
&.(\text{aluminum activated ion density})
\end{aligned}
\qquad (1.3.1.1)
$$

where R is the rate of mass transport and F is a constant.

The additional momentum P picked up by an electron falling through an electric field a distance of its mean free path l, with an average velocity v, is

$$P = eE\frac{l}{v} = erJ\frac{l}{v} = eEt = erjt \qquad (1.3.1.2)$$

The average velocity v is determined mainly by the thermal velocity v_t and is perturbed only slightly by the drift velocity v_{drift}. t is the mean free time between collisions, e is the charge on electron, r is the volume resistivity, and j is the current density.

The number of electrons per second, which are transported through a unit volume of metal, is related to j by

$$N = nv_{drift} = \frac{j}{e} \qquad (1.3.1.3)$$

where n is the electron density.

One may consider the number of activated ions per cubic centimeter in the metal to follow the Arrhenius equation as a function of temperature. Thus,

$$\text{Activated aluminum ion density} = F_1 e^{(-f/kT)} \tag{1.3.1.4}$$

Where, f is the activation energy in electron volts, k is the Boltzmann's constant, T is the film temperature in degrees Kelvin, and F_1 is a constant for a given metal and diffusion process.

The median-time-to-failure in hours (MTTF) of a metal film conductor is related to rate of mass transfer and the conductor cross sectional area by

$$R = \frac{F_2 w t_f}{MTTF} \tag{1.3.1.5}$$

where F_2 is a constant, w is the conductor width, and t_f is the film thickness expressed as centimeters. The film cross sectional area enters directly into this expression since it determines the minimum void size, which must form to cause an open circuit.

Eq. (1.3.1.1) may be rewritten by substituting Eq. (1.3.1.2) – Eq. (1.3.1.5) as

$$\begin{aligned} \frac{wt_f}{MTTF} &= F\left(erj\frac{l}{v}\right)\frac{j}{e}cs_{ionic}F_1 e^{-\left(\frac{f}{kT}\right)} \\ &= F\left(r\frac{l}{v}cs_{ionic}j^2\right)F_1 e^{-\left(\frac{f}{kT}\right)} \end{aligned} \tag{1.3.1.6}$$

where cs_{ionic} is ionic scattering cross section. The first term in parenthesis on the right-hand side of this last equation is the force acting between conducting electrons and the ions, while the second term expresses the density of the activated ions as a function of temperature. This equation neglects the opposing force due to the electric field. By consolidation of the constants the Black's Law may be expressed as (Black, 1969):

$$MTTF = Aj^{-2}\exp\left(\frac{f}{kT}\right) \tag{1.3.1.7}$$

The constant A embodies several physical properties including, the volume resistivity of the metal, the electron free time between collisions or the electron free path and average velocity, the effective ionic scattering cross section for electrons, the frequency factor for self-diffusion of aluminum in aluminum, and a factor relating rate of mass transport with MTTF.

1.4. Experimental Observations

Experimental observations of the failure development during electromigration indicate that electromigration failure is the result of complicated competition between growth, shape change and motion of voids (Arzt *et al.*, 1994). The interaction between these mechanisms is not well understood, although several important attempts have been made to model such events. Void motion has been treated, for example by Ho (1970), with the result that small voids migrate more rapidly. More recently, Nix and Artz (1992) have suggested that a critical void size exists for which void motion is minimum; the consequence could be that larger voids catch up with smaller ones, moving more rapidly as they do so and resulting in a catastrophic mechanism of void growth and failure. As described by Børgesen *et al*, (1991) grain boundaries can trap voids until they reach a critical size.

First, voids are not static but rather show motion, usually in the direction opposing the electron wind. This has been confirmed by several in situ scanning electron microscopy (SEM) on unpassivated Al lines, and field-emission SEM or scanning transmission electron microscopy (STEM), imaging back-scattered electrons, on passivated Al lines. It was also observed that voids can "heal" by breaking up into smaller fragments or grow by coalescing with other voids.

Second, besides "classical" grain boundary diffusion, surface and interface diffusion can contribute to the damage development. This is suggested by in situ transmission electron microscopy (TEM) studies on large grained Al stripes and films revealing voids inside the grains. These voids had grown in the direction of current flow lines, sometimes without apparently interacting with grain boundaries. Thinning of large regions within a single grain in an Al film during electromigration testing was observed. Both observations cannot be explained if the grain boundaries are the only diffusion paths.

Third, voids do not grow in a self-similar manner, but can show significant shape changes. This point has been especially emphasized as a result of electromigration tests that were interrupted several times for damage characterization in an SEM (Kraft, *et al.*, 1993). A typical void shape has been identified which appears to be necessary for the development of a failure site. The resulting fatal void often has a slit-like morphology, which gives the appearance of a crack perpendicular to the line. Following detailed experimental observations states that these slits frequently do not follow grain boundaries, as might be expected, but are transgranular. Again these observations indicate the necessity to consider mass transport mechanisms other than the grain boundary diffusion.

According to damage analysis performed by Kraft and Arzt (1997) there are two important observations;

Failure by slit-like voids, which are frequently (but not always) transgranular, is predominant for conductor lines with a pronounced bamboo structure.

All fatal voids in lines with a bamboo or near-bamboo grain structure exhibit an asymmetry with respect to the electron flow direction.

It has been seen that this asymmetrical void shape and, in particular, the slit-like voids are the result of shape changes during the damage evolution.

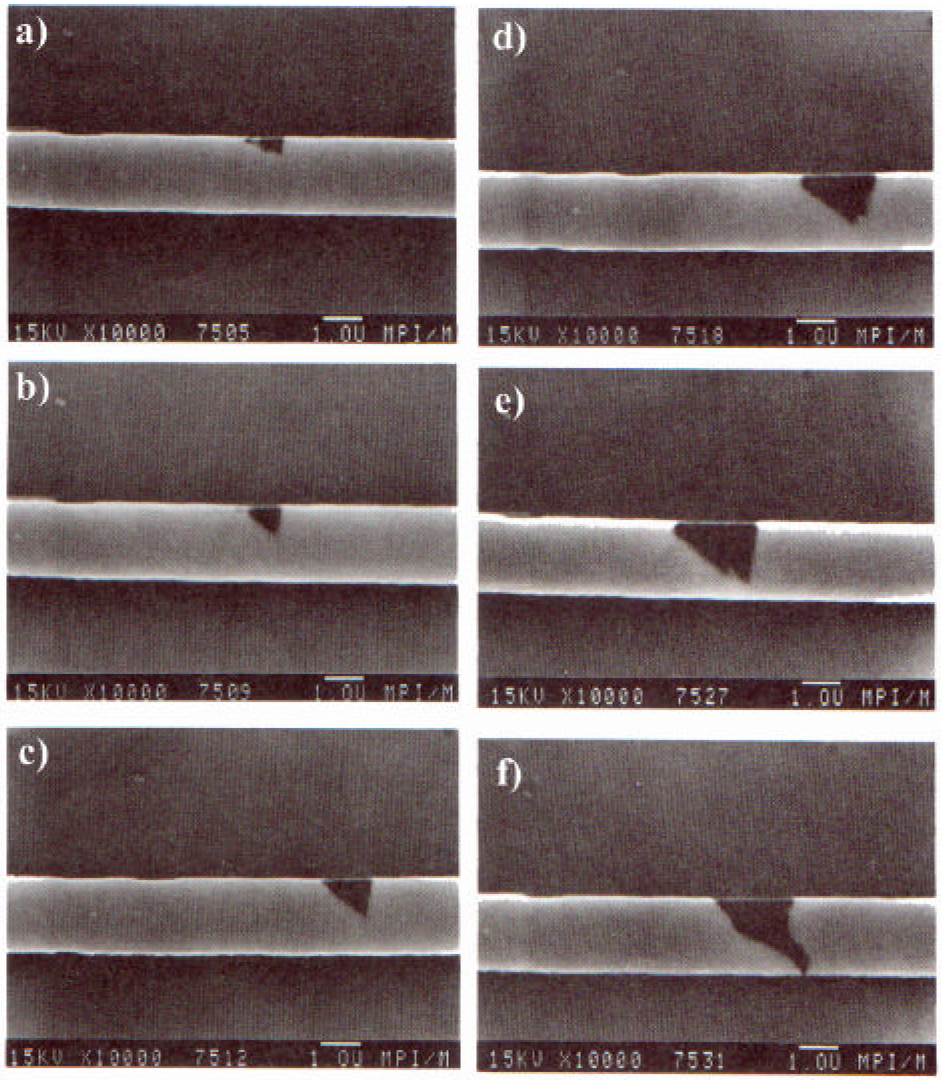

Figure 1.4.1: SEM micrographs showing a time sequence of the same site on a conductor line after **a)** 24.3 h, **b)** 44.5 h, **c)** 65.8 h, **d)** 131.8 h, **e)** 177.2 h, and **f)** 190.1 h (Arzt, *et al.*, 1994).

Figure 1.4.1 shows a typical sequence of void growth in a 1.8 *m*-wide line of the standard metallization stressed with a current density of 1.6 MA/cm^2. These micrographs were taken during interruptions of the test. In all of these and the following micrographs, the direction of the electron flow is from right to left.

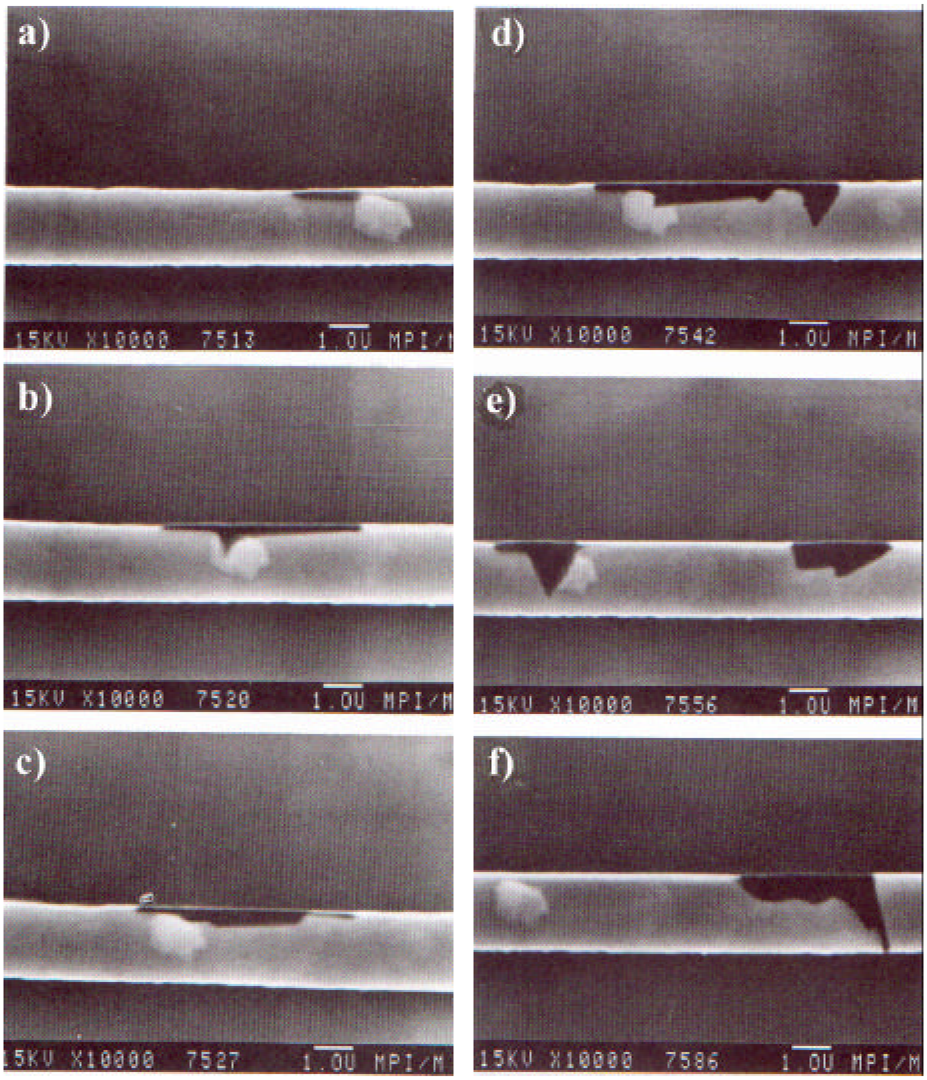

Figure 1.4.2: SEM micrographs showing a time sequence of the same site on a conductor line after **a)** 65.8 h, **b)** 131.8 h, **c)** 177.2 h, **d)** 341.9 h, **e)** 528.6 h, and **f)** 780.6 h (Arzt, *et al.*, 1994).

In figure 1.4.2, the development of another typical damage site in a different line during the same test is presented.

Comparing the two fatal voids in figure 1.4.1-f and figure 1.4.2-g, it is striking that the void contour that turned against the direction of the electron flow is more or less perpendicular to the line (Arzt, *et al.*, 1994).

The main observations of Arzt, *et al.* (1994) significant for the failure mechanism, pertains to the fact that fatal voids have a typical slit or wedge shape with a pronounced asymmetry. Figure 1.4.3 illustrates this observation schematically: Figure 1.4.3-a shows a void with a straight cathode boundary oriented perpendicular to the line. An opposite boundary configuration of a fatal void (Figure 1.4.3-b) was never observed. Certainly in an earlier stage of void growth this shape can occur, but does not seem to be critical; instead the void has to change its shape in order to become fatal. The electron wind is expected to interact with the void shape in a way suggested qualitatively in figure 1.4.3: The driving force for electromigration on a void surface depends, to a first approximation, on the angle of this surface relative to electron flow. Therefore a driving force does not appear on a surface perpendicular to the electron flow. Following this reasoning a void with a shape shown in figure 1.4.3-a becomes critical, because the electromigration-induced mass flux from 2 to 1 is larger than from 3 to 2. Consequently, mass is removed at 2, the void grows across the line, and causes failure. Contrary to this, a void with a shape as in figure 1.4.3-b should be uncritical, because electromigration-induced mass flux from 3 to 2 is larger than from 2 to 1. Thus the void grows along the line, like the void shown in figure 1.4.4-a to c, until it changes the shape to a critical configuration shown in figure 1.4.4-d.

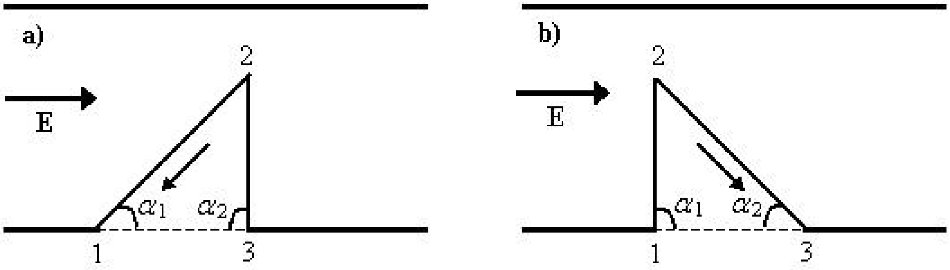

Figure 1.4.3: Schematic illustration of the interaction between the void shape and the electron wind. **a)** Critical void shape, **b)** Uncritical void shape.

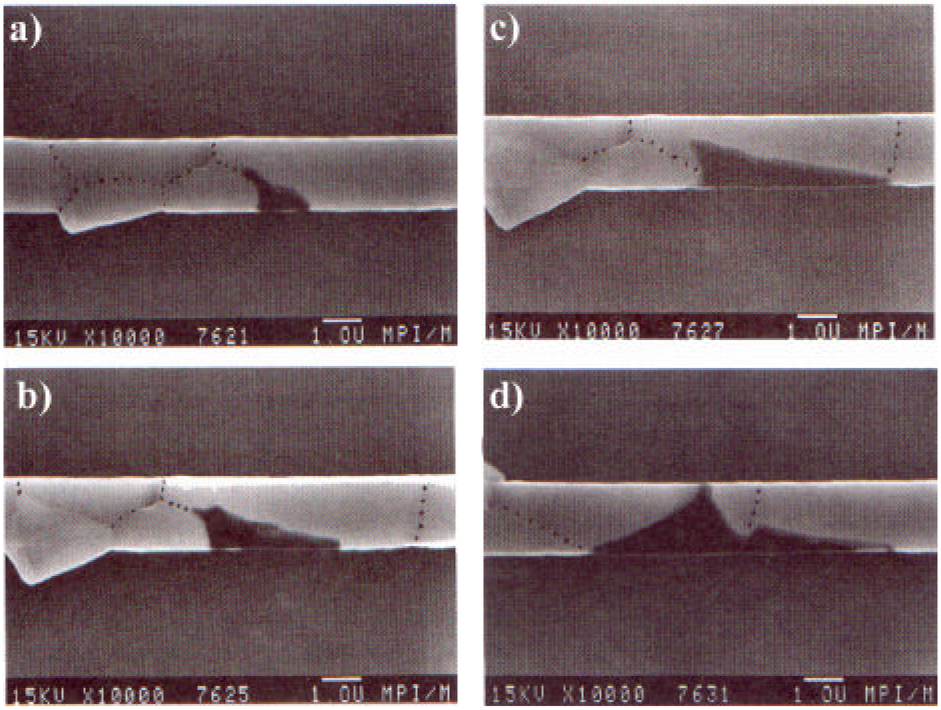

Figure 1.4.4: SEM micrographs showing a time sequence on a conductor line of the “reflowed” film after **a)** 12.2 h, **b)** 16.5 h, **c)** 25.52 h, and **d)** 42.2 h (Arzt, *et al.*, 1994).

This simple model is also consistent with figures 1.4.1 and 1.4.2 (and many other observations). Figure 1.4.1 shows a void with a critical shape, which produced the failure without any significant shape changes. Figure 1.4.2 illustrates a void with an uncritical shape until one part of the void broke away and moved along the line. This second void finally stopped moving and grew with a critical shape at the expense of the other fragment, producing the open circuit. For the failure of the line the growth of the void to a certain size was not sufficient, the void morphological change was also necessary.

In summary, there is a sequence of void behavior as follows:

1. Void nucleation occurs at the line edge, probably where it is intersected by a grain boundary. Nucleation takes up only a small part of the lifetime.
2. Void growth appears to be linear with time, as would be expected from electromigration kinetics at a constant current density. In order to continue growing, a void has to have a critical shape.
3. Void motion is not always observed, but in several cases a void moved over some microns, opposite to the electron wind, until it became fatal.
4. Shape change of a void is often the final step to produce the failure. It may take up a substantial fraction of a lifetime of a line.

At least two fundamental problems pose themselves in the light of these observations. First, why do the voids depart from an energetically favorable circular shape in the first place? And second, what is the driving force behind the characteristic asymmetry in critical voids? The first effect could due to faceting because of anisotropic surface energy. The second, however, must be related to the electron wind.

1.4.1. Lifetime Measurement

The distribution of failure time is a critical factor for the prediction of electromigration reliability. The importance of correctly determining the statistical model governing the electromigration failure process arises from semiconductor manufacturing, in which the extrapolation of circuit performance to low failure percentage (commonly 1% or 0.1 %) is required (Christou, 1994).

The lifetime measurement of conductor lines is the most commonly used method for evaluating electromigration resistance. The results usually follow a log-normal distribution and are given in terms of a median time-to failure (MTF), or t_{50}, which is the time to reach a failure of 50% of a group of identical conductor lines. In order to obtain the result of lifetime measurement in a reasonable time frame, the electromigration lifetime test is carried out under a set of accelerated test conditions at elevated temperatures and with high current densities. The data are then extrapolated to the device operating conditions, which are usually at room temperature and with current density below 5.10^5 A.cm^{-2}, by an Arrhenius-like empirical equation:

$$MTTF = Aj^{-n} \exp\left(\frac{f}{kT}\right) \qquad (1.4.1.1)$$

where n is known as the current density exponent.

In the Black's Law, given by Eq. (1.3.1.7), the exponent of the current density is calculated as -2.

Experimental values of the current density exponent, n, have been found generally in the range of 1 to 3, but large values, such as 10, have also been reported (Ho and Kwok, 1989).

1.5. Failure Mechanisms

The three predominant mechanism in electromigration failure process discussed here include those associated with the metallurgical-statistical properties of the interconnect, the thermal accelerating process, and the healing effects.

The metallurgical-statistical properties of a conductor film refer to the microstructure parameters of the conductor material such as the grain size distribution, the distribution of grain boundary misorientation angles, and the inclinations of grain boundaries with respect to electron flow. These metallurgical parameters can only be dealt with statistically because they usually appear to be random (Christou, 1994).

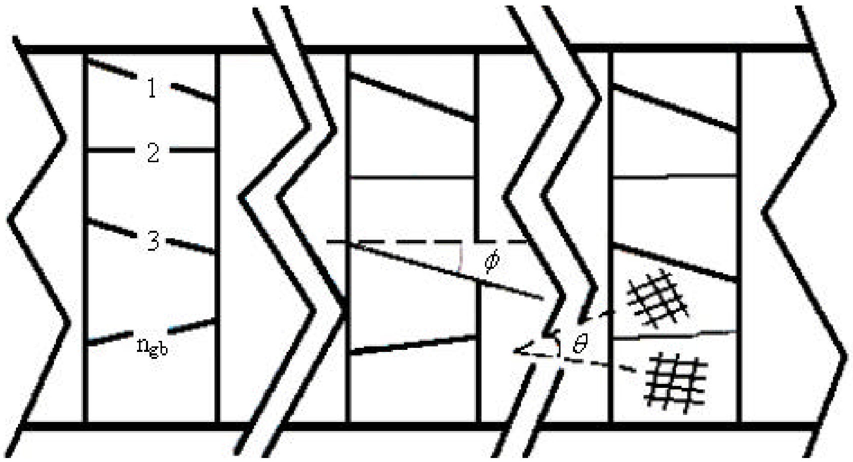

Figure 1.5.1: Schematic illustration of grains, grain boundaries, grain boundary misorientation angles, q 's, and inclination angles, F 's.

As illustrated in figure 1.5.1, the misorientation angle, q , between the two grains defining the grain boundary determines the mobility of the atoms in that boundary; the grain boundary inclination with respect to the electron flow, F , partially determined by grain size variation, determines the effectiveness of the applied electric field in that grain boundary; and the grain size variation determines the change in the number of the atomic paths across a cross section of the interconnect. The variation of all these microstructural parameters over a film causes a non-uniform distribution of atomic flow rate. Therefore non-zero atomic flux divergence exists at the places where the number of atoms flowing into the area is not equal to the number of atoms flowing out of that area per unit time (Lloyd, 1980). With the non-zero atomic flux divergence, there will be either a mass depletion (divergence > 0) or accumulation (divergence <0), leading to formation of voids and hillocks.

Failure results either from voids growing over the entire line width that cause breaking of the line or extrusions that cause short circuits to neighbouring lines. These failure modes can be seen in figure 1.5.2. and figure 1.5.3.

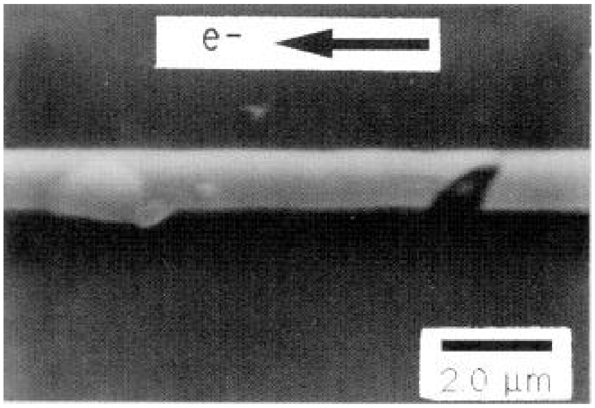

Figure 1.5.2: Open circuit failure (Nix, *et al.*, 1992).

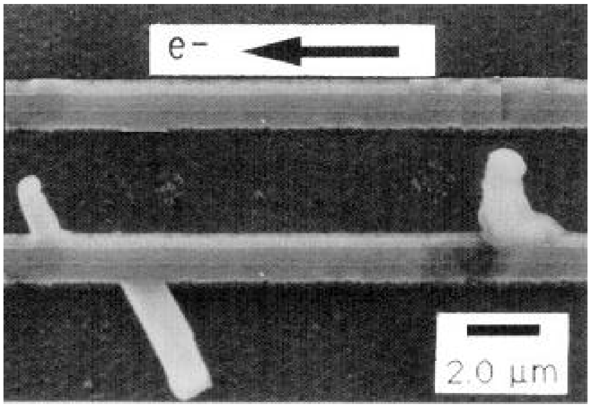

Figure 1.5.3: Hillocking, short circuit failure (Nix, *et al.*, 1992).

The thermal accelerating process refers to the acceleration process of electromigration damage due to the local increase in temperature. A uniform temperature distribution along an interconnect is possible only before any electromigration damage occurs. Once a void is initiated, it causes the current density to increase in the vicinity around itself because it reduces the cross sectional area of the conductor.

The increase of the local current density is referred as the current crowding. Since joule heating is proportional to the square of current density, the current crowding effect leads to a local temperature rise around the void that in turn further accelerates the void growth. The whole process continues till the void is large enough to break the line (Sigsbee, 1973). Such a process can be seen in figure 1.5.4.

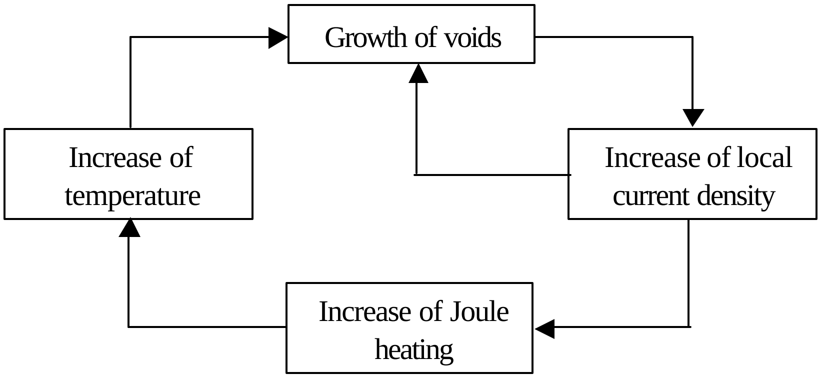

Figure 1.5.4: Thermal acceleration loop during electromigration.

The healing effects refer to those caused by the atomic flow in the direction opposite to the electron wind force, the back-flow, during or after electromigration. This back-flow of mass begins to take place once a redistribution of mass has begun to form. It tends to reduce the failure rate during electromigration and partially heals the damage after current is removed. The cause of this back-flow of mass is the inhomogenities, such as temperature and/or concentration gradients, resulting from electromigration damage.

1.5.1 Slit-like Voiding

At the present stage of miniaturization, “bamboo” or “near-bamboo” lines, which consist mainly single crystals in series, are commonly present in advanced microelectronic devices. According the Arzt *et al.*, (1996) the following mechanisms are identified during Scanning Electron Microscope (SEM) observations.

- Nucleation of a void, after a certain incubation time, at the sidewalls of the line (most likely at a defect),
- Faceting of the void surface,
- Motion of the void in the direction against the electron flow,
- Growth of the void,
- Shape change of the void to a slit like geometry, producing the final failure of the line.

Slit-like transgranular voids have repeatedly been found in bamboo structures and have prompted considerable debate on the mechanism of their formation (Sanches *et al.*, 1992a; Sanches *et al.*, 1992b; Sanches *et al.*, 1992c; Rose, 1992).

Observations of Arzt *et al.*, (1996) show unambiguously that the decisive process is a shape change mechanism (and not a mechanical cracking process, as may be hypothesized). The mechanism of shape change must rely on diffusion along the void surface; it has been found to occur even without further void growth. In many instances slits are found to be transgranular, as has been confirmed by imaging with a focused ion–beam microscope (FIM) (Sanches *et al.*, 1992a), or with the transmission electron microscope (TEM) (Rose, 1992). Hence the damage process is many cases no longer correlated with the grain structure of the line.

Several mechanisms now contribute to the failure event: void growth requires diffusion along the line surfaces (interfaces with surface oxide) or, less likely, along dislocation cores; and void motion can proceeded, like shape change.

1.6. Bamboo Structures

Demands for higher density Si integrated circuits continue to push interconnect dimensions to smaller sizes. When interconnect line widths are smaller than or close to the average grain diameter of the original continuous Al film from which the lines were patterned, their reliability improves, but is limited by fundamentally changed electromigration processes. For example, a line whose width is greater than the average grain diameter of the continuous film has a continuous network of grain boundaries. However, if the line width is similar to or smaller than the average grain diameter of the continuous film, some of the grains span the line width, so that the grain boundary path along the line is interrupted by spanning grains (bamboo grains). This line, a so-called near-bamboo line, consists of a mixture of polygranular clusters and bamboo grains. Electromigration or current-induced atomic diffusion occurs by grain boundary diffusion in non-bamboo lines, but occurs by a mixture of mechanisms in near-bamboo lines, so that lifetimes and failure mechanisms change in narrow lines.

As the level of integration increases, interconnect line widths decrease, and as hotter and cleaner deposition processes are used, average grain size increases. Furthermore, in integrated circuit processing, interconnects are subjected to successive high-temperature steps after patterning, such as passivation and packaging. During these postpatterning high temperature processes, the grain structure of lines evolves to more bamboo like microstructures due to grain growth (Joo and Thompson, 1997). All these trends have led to near-bamboo and bamboo microstructures common in modern interconnect materials.

In near-bamboo lines, electromigration is expected to occur along at least two fundamentally different paths. In the polygranular clusters, atoms diffuse along grain boundaries; in bamboo grains, atoms diffuse through the volume of the grains. Electromigration induced failure mechanisms should be affected by the dominant diffusion mechanism. Long polygranular clusters lead to the “erosion-void” mechanisms observed in wide lines, in which significant atomic diffusion occurs along grain boundaries. Lines with predominantly bamboo grains can fail by other mechanisms, including the formation of the so-called slit like voids, which are very narrow but propagate across the lines to cause failure (Sanches *et al.*, 1990). Slit like voids usually form inside a grain and not along the grain boundary (i.e., they are intra-granular). The formation of intra-granular voids clearly indicates that these voids are associated with diffusion mechanisms other than grain boundary diffusion.

1.7. Triple Junction Problem

The subject of capillary-driven shape and microstructural evolution in solids still represents a challenging theoretical problem in materials science. It combines the exciting possibility to make quantitative prediction about the behavior of real material as diverse as, sapphire and ice, with the elegancy of the fundamental laws of physics. The importance of this subject for materials science is connected with the fundamental role of surfaces and heterophase boundaries in physical and chemical processes in solids, in stability of structure and properties of materials. Wetting, sintering, grain growth, grain boundary grooving, growth of thin films, and stability of multilayer, represents just a few examples.

In the early fifties, this area partially put into a solid quantitative framework by the classical works of Herring (1951), Von Neumann (1952) and Mullins (1957) which strictly rely on the equilibrium thermodynamics and the Gibbs description of interfaces and surfaces (Gibbs, 1948; Defay *et al*. 1966). Mullins (1957) made the very first analytical study that was related to the grooving of a grain boundary without having the grain boundary diffusion by considering the triple junction to have the equilibrium capillarity configuration satisfying the Young (1805) relationship. Chuang and Rice (1973), Pharr and Nix (1979), and also Huang *et al*. (2000) studied very similar problem namely the creep cavity growth on grain boundary. They consider two coupled processes, namely the surface diffusion taking place on the interface separating the bulk phase from the cavity, and the grain boundary diffusion driven by the gradient of the normal stress acting in the boundary. Triple junction is the place where these two processes are coupled. The boundary conditions at the triple junction are assumed to be the continuity of the chemical potential, the conservation of mass, and again the equilibrium capillarity configuration for the geometry. In the later studies by Needleman and Rice (1980), Pan and Cocks (1993 and 1995), Cocks (1994) and Kucherenko *et al.* (2000), exactly similar thermostatic boundary conditions were employed at the triple junction regardless of the nature of the numerical methods adopted by them. Most recently Khenner *et al.* (2001), have performed extensive numerical simulation of grain-boundary grooving by the level set method, but still utilized local thermodynamic equilibrium conditions at the groove roots that were earlier also assumed by Ohring (1971) in his analytical studies on electromigration damage in thin films relying on the Mullins theory of thermal grooving.

These boundary conditions, as admitted by many investigators working in this field, are mutually incompatible at the triple junction even though they are widely used in their formulations relying on the validity of Herring's relationship between the chemical potential and the curvature, which is itself questionable at that geometric singularity.

At the triple junction there is no way of defining single curvature because of the large discontinuity due to finite dihedral angle. Therefore Herring's relationship, which is valid for only smoothly variying surfaces, can not be used at the triple junction.

Continuity of the chemical potential implicitly asumes that there is a local equilibrium which violates the possibility of internal entropy production. However the triple junction motion is completely natural (irreversible) process.

The driving force not only depends on the curvature gradient but also depends on the gradient of the gibbs free energy difference between bulk and surface layers. In reality this additional term becomes responsible for the growth of the void surface layer during the shape evolution.

Takahashi *et al*. (1991) made similar studies on the void shrinkage process utilizing two different numerical but rather ad hoc models. One of them always restricts dihedral angle q to the value of the equilibrium balance. In the other model, the local equilibrium at the triple junction is ignored (free dihedral angle). The second model resulted in a bonding pressure exponent that is in agreement with the experimental observations, namely; the dihedral angle is not always constant and changes as increasing net stress is applied to the bond-interface.

The triple junction steady state kinetics is also investigated recently by Gottstein and Shvindlerman (2002), in their studies related to the grain growth in 2D polycrystals by utilizing a modified version of the Von Neumann-Mullins relationship (2001) as a basis for the theoretical work. As a driving force for the triple junction mobility they assume an ad hoc connection, which may be valid only for the symmetrically disposed dihedral angles having an equilibrium value exactly equal to $p/3$. Very similar problem, namely the grain boundary crack growth in interconnects with electric field is considered by Liu *et al*. (2001). They proposed that one has steady state shape evolution having an equilibrium angle at the crack apex by further arguing that the crack apex does not constitute a point source of entropy production, which is actually the key point in our theory of irreversible processes associated with the evolution dynamics of closed curved interfaces having triple junction singularities.

Recently non-boundary tracking methods have been increasingly applied to simulate complex microstructural evolutions, including the Monte Carlo methods, the cellular automata, and the phase field method (Mahadevan and Bradley, 1999). In the phase field approach the field variables governed by semi-phenomenological equations of motion, e.g. the Cahn-Hillard non-linear diffusion equation for the density field, (Cahn and Hillard, 1958), and the time-dependent Ginzburg-Landau equation for the long-range order parameter field (Lifshitz and Pitaevskii, 1980). Kazaryan *et al.* (1999) generalized phase field approach by incorporating the rigid-body rotation for the computer simulation of sintering by further assuming that the triple junction velocity can be determined from the steady state requirement at the grain boundary.

Triple-junction motion is also investigated by Cahn *et al.* (1996) for an Allen-Cahn / Cahn-Hilliard system utilizing long time asymptotics (Cahn and Hillard, 1958; Novick-Cohen, 2001), which is still incorporated by the requirement of the uniform displacement. They also assumed that one has local physico-chemical equilibrium and continuity of chemical potentials at the junction. However the more serious restriction associated with the method of phase field is the utilization of symmetric free energy form “double well potential” which results not only equal interfacial energies but also hinders the particle growth process as admitted by the author themselves.

1.8. Methods to Improve Electromigration Resistance

One of the goals in studying electromigration in thin-film conductors is to devise methods to improve the electromigration resistance of interconnects. In the past, this practical aspect of electromigration study has been emphasized, particularly among the industrial laboratories. As seen from the electromigration induced damage formation process, it is clear that the basic requirement for reducing damage is to minimize the local divergence of the atomic flux. This can be accomplished, in principle, by reducing the magnitude of the atomic flux and/or the inhomogeneity of the parameters controlling the mass transport (Ho and Kwok, 1989). Since the damage process is complex in nature, methods found to be effective often incorporate several factors for reducing the flux divergence.

The magnitude of the atomic flux is determined by the electromigration driving force and the grain boundary diffusivity. Thus, to reduce the atomic flux, the choice is to reduce the driving force and/or the diffusivity. To reduce the driving force has some basic difficulties since it requires either a chance in the scattering process responsible for the effective charge or a reduction in the current density. The scattering process is intrinsic, thus difficult to change. A reduction in the current density is not practical since the current density is dictated by device requirements and the tendency is to increase its magnitude for smaller devices. This leaves the choice to reduce the grain boundary diffusivity. To achieve this, the most common approach is by solute addition although it should be emphasized that solute addition can contribute to the improvement by other effects, e.g. grain structure modification, and is not confined only to the reduction in diffusivity. The best-known example of solute addition is the improvement of electromigration resistance in Al stripes by the addition of Cu (Ames *et al.*, 1970). Other solute elements such as Mg, Mn and Ti have also been shown to be effective in improving the electromigration lifetime in Al stripes (Gangulee and d'Heurle, 1973). Solute elements or impurities in the thin film can reduce the magnitude of the electromigration flux, which has been attributed to the segregation of these impurities at the grain boundaries and their interaction with the migration ions. Since the solubility of Cu in Al is only about 0.16 at. % at 300 °C (Hansen, 1958), excess Cu atoms are likely to segregate at the Al grain boundaries. It was observed in a marker experiment (Ho *et al.*, 1975) that Cu addition of an amount exceeding the solubility limit could reduce the electromigration flux of Al at the grain boundary. Cu also forms second-phase compound particles with Al, which serve as sources of Cu atoms to Al grain boundaries.

Efforts in reducing the flux inhomogeneity have been focused on the modification of grain size and microstructure. Improvements of electromigration resistance in single-crystal Al stripes (d'Heurle and Ames, 1970) and in conductor composed of a chain of Al single-crystal grains (Herzig and Wiemann, 1974) or fabricated from large-grain Al films (Pierce and Thomas, 1981) have been reported. Microstructure modifications, such as the use of bamboo grain structure in Al (Pierce and Thomas,

1981) and Al-Cu (Vaidya *et al.*, 1980; Kwok, 1987) fine lines, have also been shown to be effective in improving the electromigration resistance.

Another approach for improving the electromigration resistance in thin-film conductors is to provide a cover of a protective layer called overcoat. The mechanism for the improvement is not well understood although it is likely that the overlayer alters the source or the sink condition of the free surface so as to reduce the rate of supplying, or annihilating, defects from the surface to the grain boundary. The increase in electromigration lifetime in Al stripes with a layer of glass was first reported by Black (1969). In general, the electromigration lifetime of most conductors increases by about an order of magnitude when covered with a glass passivation layer (Ho and Kwok, 1989).

A combination of solute addition and structure modification has been used to improve the electromigration resistance of Al and Al-Cu fine lines. The method is to incorporate an al-transition metal intermetallic sandwich layer in the conductor, either in the middle or as top and bottom layers (Howard and Ho, 1977). The improvement in the electromigration lifetime was found to be 50 – 100 times (Howard *et al.*, 1978). The intermetallic layer was formed by reacting Al with a thin layer of a transition metal, e.g. Cr, Hf or Ti. These transition elements have been found to serve several purposes. First, they reduce the electromigration rate of Al. second, the intermetallic layer was found to serve as a barrier to prevent the linkage of voids formed in the top and the bottom Al - Cu layers. And third, it modifies the microstructure in the top and bottom Al - Cu layer, e.g., to induce a columnar grain structure, thus reducing structural divergent sites for damage formation (Kwok *et* *al*., 1984). A similar approach has been found bay Gardner *et al.* (1985) in a later study to be effective in improving the electromigration resistance of Al lines.

CHAPTER 2

IRREVERSIBLE THERMOKINETIC THEORY OF SURFACES & INTERFACES

2.1. Introduction

As entirely discussed in Chapter 1.7, up to now all the theoretical studies related to the interfaces and surfaces, which are reported and cited in the literature, are strictly relying on the classical thermodynamics as a general tool for the macroscopic description of physico-chemical processes with some obscure modifications in the concept and usage of chemical potentials, and the free energies especially in the presence of externally imposed force fields (electrical, magnetic, etc.) without considering their original strictly mathematical definitions by Gibbs (1948). The more serious limitation of these approaches lies in the fact that the methods are based on reversible processes and true equilibrium states.

This chapter focuses on the irreversible or nonequilibrium thermodynamic treatment of the shape evolution dynamics of closed surfaces and interfaces composed of ordinary points and the interfacial triple junction singularities (Ogurtani and Oren, 2001-a). By relying only on the fundamental postulates of linear irreversible thermodynamics as advocated by Prigogine (1961) for the bulk phases, Ogurtani (2000) has obtained a compact and rigorous analytical theory of a network of interfaces that are interconnected by triple junctions and embedded in bulk phases by utilizing the more realistic monolayer model of Verschaffelt (1936) and Guggenheim (1959) for the description of interfaces and surfaces. A brief summary of Ogurtani theory on the triple junction is reported recently by Oren and Ogurtani (2002) in connection with their computer simulation studies on the effect of various combinations of grain textures on the life time and the failure mechanisms of thin film interconnects with bamboo structure.

In this chapter, first of all, the linear thermodynamics of irreversible processes are introduced in section 2.2 for surfaces as well as for bulk phases using the conventional macro-formulation for homogeneous and isotropic close systems as a starting point for the local micro discrete formulation adopted in this work. In section 2.3 the entropy production associated with the virtual displacement of ordinary points and the singular point such as a triple junction are treated rather rigorously by using micro-discrete (straight) interfacial elements as a starting convenient mathematical tools and then passing to the continuum representation by applying legitimate limit procedures frequently employed in calculus. The generalized forces and conjugate fluxes associated with the triple junction are obtained in terms of the asymmetric dihedral angles and the specific Gibbs free energies related to the void surface layer and the grain boundary interface, respectively. The longitudinal and transverse displacement velocities of the triple junction are also deduced as a by-product of this treatment. In section 2.4 a universal mathematical model for the void shape evolution dynamics in the presence of the void – grain boundary interaction is developed by introducing a novel normalization and scaling procedures which completely eliminate the any necessity for the knowledge of the specific material properties. This unique formulation based upon the monolayer model of autonomous interfaces is resulted mathematically sound and physically plausible boundary conditions that are necessary and sufficient for the unique solution of the nonlinear partial differential equation, which dictates the kinetic behavior of voids during intragranular and intergranular motion.

2.2. Irreversible Thermokinetics of Micro-Discrete Open Composite Systems with Interfaces

The term microscopic region refers to any small two or three-dimensional region containing a number of molecules sufficiently large not only for microscopic fluctuations to be negligible but also all of the intensive properties are homogeneous in space. The composite system, considered here, has at least two physico-chemically distinct domains (or phases in most general sense) separated by thin layers of interfaces, that are not only mutually interacting by the exchange of matter and energy but they are also completely open to the surroundings through the moving or immobile boundaries.

In this theory, the general view points of Guggenheim (1957), van der Waals and Bakker (1928) are adopted as far as the interface between any two phases or domains is concerned. Namely, the interface is autonomous, finite but a thin layer across which the physical properties and/or the structures vary continuously from those of the interior of one phase to those of the interior of the other. Figure 2.2.1 shows such a system. Since the interfacial layer is a material system with well-defined volume and material content, its thermodynamic properties do not require any special definition. One may speak of its temperature, entropy, free energy, and composition and so on just as for a homogeneous bulk phase. The only functions that call for special comment are the pressure and the interfacial (surface) tension.

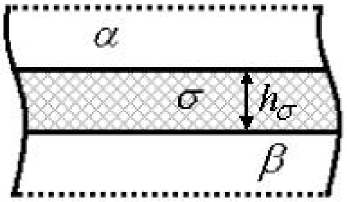

Figure 2.2.1: Structure of the interface s , which separates the phases a and b .

The total reversible work, $d\Delta w$, done on a flat surface phase with micro-extent, indicated in terms of Δ space-scaling operator, by variations of its volume $d\Delta V_s$, and area $d\Delta A_s$ (keeping its material content unaltered, but stretching) is given by the following well known expression, assuming that the component of the stress tensor along the surface normal P is quasi-homogeneous in the layer and other transverse two components denoted by [P-Q] are equal (rotational symmetry) but heterogeneous (in the absence of electrostatic and other non-mechanical force fields),

$$d\Delta w = -\overline{P} d\Delta V_s + g\, d\Delta A_s \tag{2.2.1}$$

where, $\overline{P}$ is the mean isotropic pressure in the layer, and g is called the surface tension, whose value and the location of the surface in which it acts can be uniquely determined by the knowledge of the transverse component of the stress tensor as demonstrated by Buff (1955). Its value may be given roughly by

$$g = \int_0^{h_s} Q dz\,, \tag{2.2.2}$$

where, Q is the deviatoric part of the stress tensor and h_s is the thickness of the surface layer and the integration is performed along the surface normal. The above given expression for the reversible work becomes $-\overline{P} d\Delta V_a$ for a homogeneous bulk phase in the formulation of the first law of thermodynamics. In the conventional theory of irreversible processes (Prigogine, 1961 and Glansdorff and Prigogine, 1971), it has been postulated that the Gibbs formula, which is derived for the reversible changes, is also valid for irreversible processes. However in the present formulation, it is tacitly postulated that the differential form of the Helmholtz free energy in equilibrium thermodynamics has the same validity for irreversible changes. Mathematically this assumption is exactly equivalent to the Gibbs formula used extensively in standard treatment.

The local anisotropic properties of the medium are now automatically embedded in the intensive variables, which are characterized by second order tensors or dyadics.

Hence the Helmholtz free energy for an open surface phase of a micro-extent may be written as,

$$d\Delta F_s = -\Delta S_s \, dT_s - P_s \, d\Delta V_s + g d\Delta A_s + \sum_i m_s^i \, d\Delta n_s^i - \sum_j \Delta A_s^j \, dx_s^j \qquad (2.2.3)$$

where, ΔS_s denotes the entropy, m_s^i denotes the chemical potential, Δn_s^i is the number of i^{th} chemical species in the micro-element, dx_s^j is the extent of the homogeneous j^{th} chemical reaction taking place in the phase under consideration, and ΔA_s^j is the affinity of the homogeneous j^{th} chemical reaction and is related to the chemical potentials and the stoichiometric numbers as defined by Th. De Donder *et al.* (1936).

In above relationship, it is assumed that, in a single phase only the homogeneous chemical reactions take place and the phase transitions occurring at the mobile boundaries are not considered in the last term. The Helmholtz free energy change due to the passage of the substance i from the phase to the surroundings is accounted by the fourth term in above expression (frozen chemical reactions). Therefore, in the case of a close system, one should subtract only the term given by $\sum_i m_s^i \, d\Delta n_s^i$, which is closely related to the direct exchange of matter with the surroundings.

For the bulk phase, b, $(a$ or $b)$, one may rewrite very similar expression namely,

$$d\Delta F_b = -\Delta S_b dT_b - P_b d\Delta V_b + \sum_i m_b^i d\Delta n_b^i - \sum_j \Delta A_b^j dx_b^j \qquad (2.2.4)$$

In the case of a composite system as defined previously, the total Helmholtz free energy differential can be immediately written down from Eqs. (2.2.3 and 2.2.4) by using the fact that the extensive thermodynamic quantities are additive. If there would be thermal, hydrostatic and physico-chemical equilibrium in the multi-phase system with plane interfaces there is no need to add subscripts to T, P and m^i; there must have values uniform throughout the various phases (bulk and surface) present in the system. For the present non-equilibrium case, first it will be assumed that no such restrictions on the system, but later a system at thermal equilibrium will be treated. For the present problem the system is an open composite system, and it is composed of two bulk phases (interconnect and the embedded void) and two surface phases (the interface between void and interconnect, and the grain boundary separating two different regions of the interconnect).

The second principle of thermodynamics postulates the existence of a state function called entropy (from the Greek *eutrwph*, meaning *evolution*, (Prigogine, 1961)) that possesses the following properties,

The entropy of the system is an extensive property; therefore if the system consists of several parts, the total entropy of the system is equal to the sum of the entropies of each part.

The entropy of any system whether it is close or open can change in two distinct ways, namely by the flow of entropy due to the external interactions, $d\Delta S_{ex}$, and by the internal entropy production due to the changes inside the system, $d\Delta S_{in}$. Symbolically, one may write this as,

$$d\Delta S = d\Delta S_{in} + d\Delta S_{ex} \tag{2.2.5}$$

The entropy increase $d\Delta S_{in}$ due to changes taking place inside the system is positive for all natural or irreversible changes, is zero for all reversible changes and is never negative.

For a close system external entropy contribution has a very simple definition, and it is given by $d\Delta S_{ex} = dq/T$ where dq is the heat received by the system from its surroundings. Now, let us generalize the first law of thermodynamics for any infinitesimal change associated with an open system. For an open system, in which not only the energy but also the matter exchange takes place between the system and its surroundings, the conservation of energy becomes,

$$d\Delta\Phi = d\Delta U - d\Delta w = d\left[\Delta F + T\Delta S\right] - d\Delta w \tag{2.2.6}$$

where, $d\Delta\Phi$ is the energy received by the system, in terms of heat and matter transfer processes from the surroundings, $d\Delta U$ is the internal energy change, and $d\Delta w$ is the reversible work done on the system by the external agents, and this work is equal to $-Pd\Delta V$ or $-[Pd\Delta V - gd\Delta A]$ depending upon whether one deals with the bulk phase or the surface phase, respectively.

Eq. (2.2.6) and Eq. (2.2.3 or 2.2.4) results the following formula in regards to the total differential of the total entropy for the phase, k (surface or bulk phases);

$$d\Delta S = \frac{d\Delta\Phi}{T_k} - \sum_i \frac{m_k^i}{T_k} d\Delta n_k^i + \sum_j \frac{\Delta A_k^j}{T_k} dx_k^j \qquad \text{(Total Entropy Change)} \qquad (2.2.7)$$

where the summations with respect to i and j indicate summation over different chemical species and over different reactions taking place simultaneously in the same phase, respectively.

The Eq. (2.2.7) can be divided into two parts, similar to the Prigogine (1961), who applied such a splitting procedure to the systems consist of two open phases but the system is closed as a whole:

The first two terms of Eq. (2.2.7), correspond to the rate of external entropy flow term (REF): namely,

$$\frac{d\Delta S_{ex}}{dt} = \frac{1}{T_k}\frac{d\Delta\Phi}{dt} - \sum_i \frac{m_k^i}{T_k}\frac{d\Delta n_k^i}{dt} \qquad \text{(Rate of Entropy Flow (REF))} \qquad (2.2.8)$$

And the last term of Eq. (2.2.7), on the other hand constitutes to the internal entropy production term (IEP): namely,

$$\frac{d\Delta S_{in}}{dt} = \sum_j \frac{\Delta A_k^j}{T_k}\frac{dx_k^j}{dt} \geq 0 \qquad \text{(Internal Entropy Production (IEP))} \qquad (2.2.9)$$

As one might expect that, the IEP in a single phase directly related to the chemical reactions taking place in the region whether it is closed or open. Only the REF is affected from the matter flow through the open boundary (Ogurtani, 2000).

One may also write down the power dissipation, $\Delta \mathrm{P}$, for natural changes, which is a very useful function, which is also known as Helmholtz dissipation function (Haase, 1969), for the treatment of the isothermal processes taking place in multi-phase systems with uniform and continuous temperature distribution, and it is given by the following expression.

$$\Delta \mathrm{P} = T \frac{d\Delta S_{in}}{dt} = \sum_{i} \Delta A^{i} \frac{dx^{i}}{dt} \geq 0 \qquad (2.2.10)$$

Inequalities given by Eqs. (2.2.9 and 2.2.10) are valid for any natural change, taking place in any phase whether it is bulk or surface. Only difference between these two expressions is that the first one is valid for any type of natural changes taking place in the system but the second one is restricted only for the isothermal natural processes.

For a global composite system having discontinuous (heterogeneous) phases, there are two additional IEP terms, one is due to the internal entropy flow associated with the transfer of chemical species from one subdomain to another subdomain; and the other one is due to the energy transfer between the subdomains of the composite system.

This second IEP term for a composite system immediately drops out if the subdomains have identical temperatures. The total differential of the entropy for such a system is;

$$d\Delta S = \left\{ \begin{array}{l} -\sum_{i,k} \frac{m_k^i}{T_k} d\Delta n_{k\leftrightarrow s}^i + \sum_k \frac{d\Delta\Omega_{k\leftrightarrow s}}{T_k} \\ -\sum_{i,k} \frac{m_k^i}{T_k} d\Delta n_k^i + \sum_k \frac{d\Delta\Omega_k}{T_k} + \sum_{j,k} \frac{\Delta A_k^j}{T_k} dx_k^j \end{array} \right\} \quad \text{(Total Entropy Change)} \quad (2.2.11)$$

where the double summations with respect to k and i or j indicate summation over various phases (bulk or surface) and over different chemical species or reactions taking place simultaneously in the same phase, respectively. $d\Delta\Omega_k$ is the amount of energy transported to the individual phase from the other phases present in the global system due to heat or matter exchange. In Eq (2.2.11), the subscript $k\leftrightarrow s$ indicates that the matter and energy exchange takes place between the phases of the system, k, and the surrounding, s.

By performing the splitting procedure to the Eq. (2.2.11) similar to the single-phase systems: The REF from the surrounding to an open composite system may be written as,

$$\frac{d\Delta S_{ex}}{dt} = -\sum_{i,k} \frac{m_k^i}{T_k} \frac{d\Delta n_{k\leftrightarrow s}^i}{dt} + \sum_k \frac{1}{T_k} \frac{d\Delta\Omega_{k\leftrightarrow s}}{dt} \qquad \text{(REF)} \qquad (2.2.12)$$

and the IEP due to the irreversible processes:

$$\frac{d\Delta S_{in}}{dt} = -\sum_{i,k} \frac{m_k^i}{T_k}\frac{d\Delta n_k^i}{dt} + \sum_k \frac{1}{T_k}\frac{d\Delta\Omega_k}{dt} + \sum_{j,k}\frac{\Delta A_k^j}{T_k}\frac{dx_k^j}{dt} \qquad \text{(IEP)} \qquad (2.2.13)$$

On the other hand the first term contributes to IEP of a composite system as long as one has chemical potential differences between respective sub-domains regardless the transfer process isothermal or not.

A comparison of the IEP expressions, for the single-phase system, Eq. (2.2.9), and the composite system, Eq. (2.2.13), immediately shows us that the internal entropy production IEP is not an additive property of a thermodynamic system composed of interacting open sub-systems unless the whole system is in complete physico-chemical equilibrium state (uniform temperature and chemical potential distributions).

At the onset, it should be clearly stated that in the case of an open composite system having only homogeneous chemical reactions with inactive external boundaries (no chemical reaction or phase transition occurring there) any ordinary exchange of matter and/or energy with its surroundings only contributes to the total entropy flow term, and it is noting to do with the IEP.

2.3. Irreversible Thermokinetic Theory of Voids with the Triple Junction Singularities

Before using the concepts developed in the previous section let us define the system under consideration. Figure 2.3.1 shows the void – grain boundary – interconnect system, namely the void nucleated on the grain boundary that separates interconnect into two different subdomains.

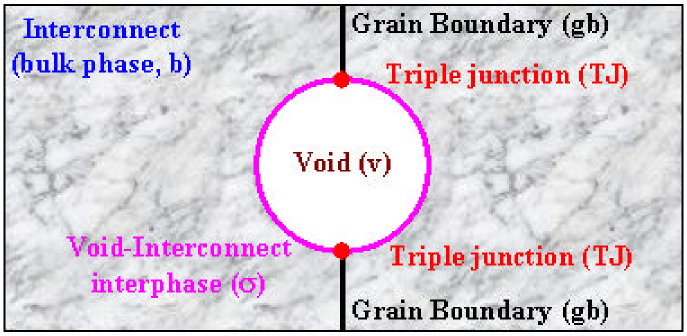

Figure 2.3.1: The void-grain boundary-interconnect system.

In the formulation of the problem through the evaluation of the internal entropy production, IEP, and the external entropy flow, REF, terms associated with the boundary displacement, no assumption is made in regards to the kinetics of the growth process other than the conservation laws and the fundamental postulates of linear irreversible thermodynamics. Considering the closed curved interfaces in two-dimensional space, or the general cylindrical surfaces in three-dimensional space, let us obtain the formulas necessary to describe the void motion.

2.3.1. Ordinary Point Motion Along the Surface Normal

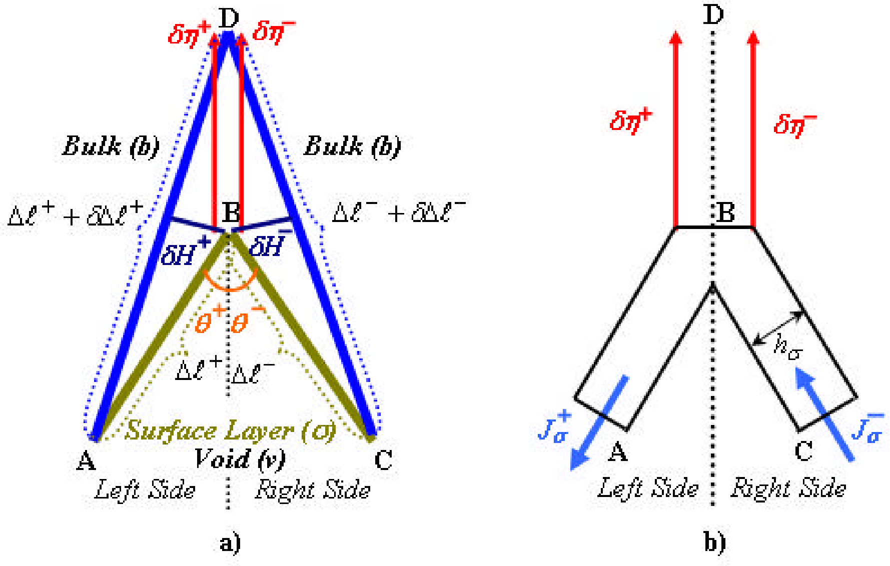

Figure 2.3.1.1: Ordinary point motion along the void surface normal. **a)** Macro-structure, **b)** Micro-structure. ABC: void interfacial layer and dh: virtual displacement of the ordinary point along the void surface normal.

During the derivation of the formula for the global IEP associated with the arbitrary virtual displacement, dh, of the interfacial loop of a finite thickness, which separates the void, denoted by v, from the interconnect, denoted by b, having multi-components, one has to integrate the rate of local entropy density change along the curved interface in order to obtain desired connection between generalized forces and conjugate fluxes. The rate of local entropy density change is the only quantity, which has the additive property that allows to be integrated. Therefore, not only the local internal entropy production (source term), but also the external entropy flow term should be evaluated for the virtual displacement.

i. Internal Entropy Production

The IEP of an open composite system is given by the Eq. (2.2.13). As far as the void – interconnect surface layer is concerned, it is assumed that the whole system is in thermal equilibrium, T, and there is no insitu chemical reactions is taking place. These assumptions drop out the second and the third terms of Eq. (2.2.13), as discussed before. Then the only non-vanishing term of IEP, which represents an additional contribution in the composite system due to internal entropy flow associated with the transfer of chemical species from one sub-domain to another sub-domain, is given by,

$$\frac{d\Delta S_{in}}{dt} = -\frac{1}{T}\sum_{i,j} m_j^i \frac{d\Delta n_j^i}{dt} \tag{2.3.1.1}$$

Double summations with respect to i and j indicate summations over different chemical species and over various phases (b, v and s), respectively.

Now, let us calculate the internal entropy variation for the left hand side sub-system when the ordinary point moves along the surface normal with a distance dh^+. From figure 2.3.1.1, one immediately finds the following variational relationships among various quantities by assuming that: $\Delta\ell^+ >> dh^+$ and $\Delta\ell^- >> dh^-$;

$$d\Delta\ell^{+} = dh^{+}\cos q^{+} \qquad \text{and} \qquad dH^{+} = dh^{+}\sin q^{+} \tag{2.3 1.2}$$

$$d\Delta n_b^{+} = -\frac{1}{2\Omega_b}\Delta\ell^{+}\sin q^{+} dh^{+} \tag{2.3.1.3}$$

$$d\Delta n_v^{+} = \frac{1}{2\Omega_v}\Delta\ell^{+}\sin q^{+} dh^{+} \tag{2.3.1.4}$$

$$d\Delta n_s^{+} = \frac{h_s}{\Omega_s}\cos q^{+} dh^{+} \tag{2.3.1.5}$$

where Ω_s , Ω_b *and* Ω_v are the mean atomic specific volumes, associated with the void surface layer, bulk and void phases, respectively. $\Delta\ell^{+}$ and $\Delta\ell^{-}$ denote segment lengths of the void surface layer just next to the ordinary point right and left hand sides, respectively. h_s is the thickness of the surface layer and assumed to be invariant. $d\Delta n_v^{+}$ and $d\Delta n_b^{+}$ are the number of atoms gain in the reaction zones associated with the void – interfacial layer and the bulk – interfacial layer respectively, while the transformation processes are taking place there during the virtual displacement of the interfacial layer. $d\Delta n_s^{+}$ is equal to the net atomic gain by the interfacial layer denoted by s due to enlargement (extension without stretching) of that layer during the displacement operation. d and Δ are variational and micro-discretization operators, respectively.

One can obtain exactly similar expressions for the other side of the ordinary point, which will be identified by a negative sign as superscript in the following formulas:

$$d\Delta\ell^{-} = dh^{-}\cos q^{-} \qquad \text{and} \qquad dH^{-} = dh^{-}\sin q^{-} \tag{2.3.1.6}$$

$$d\Delta n_b^{-} = -\frac{1}{2\Omega_b}\Delta\ell^{-}\sin q^{-}dh^{-} \tag{2.3.1.7}$$

$$d\Delta n_v^{-} = \frac{1}{2\Omega_v}\Delta\ell^{-}\sin q^{-}dh^{-} \tag{2.3.1.8}$$

$$d\Delta n_s^{-} = \frac{h_s}{\Omega_s}\cos q^{-}dh^{-} \tag{2.3.1.9}$$

Also, one should recall that in the case of multi-component system, the variations in the number of atomic species could be easily obtained by simply multiplying the total atomic number variations by the respective atomic fractions denoted by x_j^i. As an example, the number of chemical species involved in the left and right hand side bulk phases due to the virtual displacement may be given by

$$d\Delta n_j^{i+} = x_j^i d\Delta n_j^{+} \tag{2.3.1.10}$$

and

$$d\Delta n_j^{i-} = x_j^i d\Delta n_j^{-} \tag{2.3.1.11}$$

Then, one can write down the rate of entropy production due to ordinary point virtual displacement along the void surface normal for the left as well as for the right hand side domains;

$$\frac{d\Delta S_{in}^{+}}{dt} = \frac{1}{T}\left\{\begin{array}{l} \left[\sum_i \left(\frac{x_b^{i+}}{\Omega_b} m_b^{i+} - \frac{x_v^{i+}}{\Omega_v} m_v^{i+}\right)\right]\frac{1}{2}\Delta\ell^{+}\sin q^{+} \\ -\Gamma_s \cos q^{+}\sum_i x_s^{i+} m_s^{i+} \end{array}\right\}\frac{dh^{+}}{dt} \tag{2.3.1.12}$$

and

$$\frac{d\Delta S_{in}^{-}}{dt} = \frac{1}{T}\left\{\begin{array}{l} \left[\sum_i \left(\frac{x_b^{i-}}{\Omega_b} m_b^{i-} - \frac{x_v^{i-}}{\Omega_v} m_v^{i-}\right)\right]\frac{1}{2}\Delta\ell^{-}\sin q^{-} \\ -\Gamma_s \cos q^{-}\sum_i x_s^{i-} m_s^{i-} \end{array}\right\}\frac{dh^{-}}{dt} \tag{2.3.1.13}$$

where, $\Gamma_s = h_s / \Omega_s$ corresponds to the specific mean atomic density associated with the void surface layer.

In above relationship, the special superscript $^{+}$ or $^{-}$ has been employed above the atomic fractions as well as the chemical potentials in order to indicate explicitly that those quantities may depend upon the orientation of the local surface normal. One should also recall that for the multi-component surface phases, $\sum \Gamma_s^i m_s^i$ is exactly equal to the specific Gibbs free energy density associated with the interfacial layer. This may be denoted by g_s. Here, $\Gamma_s^i = \Gamma_s x_s^i$, is by definition known as the specific surface concentration of chemical species in surface layer.

The terms appearing in the first group on the right side of Eq. (2.3.1.12) and (2.3.1.13) such as, $\sum_i c_b^i m_b^i / \Omega_b$ and $\sum_i c_v^i m_v^i / \Omega_v$ are the volumetric Gibbs free energy densities. These quantities are denoted by $\breve{g}_b$ and $\breve{g}_v$, and associated with the bulk phase and void region having their own instantaneous compositions just next to the hypothetical geometric boundaries of the interfacial layer (reaction fronts or zones). Furthermore, these quantities are related to the specific Gibbs free energy densities by the relationship: $g_s = h_s \breve{g}_s$. By using these definitions the following equations are obtained,

$$\frac{d\Delta S_{in}^{+}}{dt} = \frac{1}{T}\left\{\left(\breve{g}_b^{+} - \breve{g}_v^{+}\right)\frac{1}{2}\Delta\ell^{+} \sin q^{+} - g_s^{+} \cos q^{+}\right\}\frac{dh^{+}}{dt} \tag{2.3.1.14}$$

and

$$\frac{d\Delta S_{in}^{-}}{dt} = \frac{1}{T}\left\{\left(\breve{g}_b^{-} - \breve{g}_v^{-}\right)\frac{1}{2}\Delta\ell^{-} \sin q^{-} - g_s^{-} \cos q^{-}\right\}\frac{dh^{-}}{dt} \tag{2.3.1.15}$$

The total internal entropy production is:

$$\begin{aligned}\frac{d\Delta S_{in}}{dt} &= \frac{d\Delta S_{in}^{+}}{dt} + \frac{d\Delta S_{in}^{-}}{dt} \\ &= \frac{1}{T}\left\{\begin{matrix} -\dfrac{\Delta\ell}{2}\left(\breve{g}_{vb}^{+} \sin q^{+} + \breve{g}_{vb}^{-} \sin q^{-}\right) \\ -\left(g_s^{+} \cos q^{+} + g_s^{-} \cos q^{-}\right) \end{matrix}\right\}\frac{dh}{dt}\end{aligned} \tag{2.3.1.16}$$

where $\breve{g}_{vb} = (\breve{g}_v - \breve{g}_b)$, and it corresponds by definition to the volumetric density of Gibbs Free Energy of Transformation (GFET) (negative of the affinity of an interfacial reaction such as condensation or adsorption, $g_{vb} > 0)$ associated with the transformation of the bulk phase into the realistic void phase, which contains chemical species even though they are present in a trace amount. In the case of thermostatic equilibrium between a void phase and an adjacent bulk phase, GFET becomes identically equal to zero, if the reaction front would be a flat interface.

There is a very simple connection between this quantity GFET and the Specific Gibbs Free Energy of transformation between the parent phase and the void phase that may be given by $g_{vb} = \breve{g}_{vb} h_s$. By dividing both sides of the Eq. (2.3.1.16) by $\Delta\ell$, it is obtained that,

$$\frac{d\Delta S_{in} / \Delta\ell}{dt} = -\frac{1}{2T} \begin{Bmatrix} \left(\breve{g}_{vb}^{+} \sin q^{+} + \breve{g}_{vb}^{-} \sin q^{-} \right) \\ + \left(g_s^{+} \dfrac{\cos q^{+}}{\Delta\ell / 2} + g_s^{-} \dfrac{\cos q^{-}}{\Delta\ell / 2} \right) \end{Bmatrix} \frac{dh}{dt} \qquad (2.3.1.17)$$

Now if one applies the limiting procedures such as; first with respect to $dt \to 0$, and then $\Delta\ell \to 0$, and recalls the definition of the local radius of curvature, k , which is given by;

$$k = \lim_{\Delta\ell \to 0} \left(\frac{\cos q}{\Delta\ell / 2} \right) \qquad (2.3.1.18)$$

and also keeps in mind that $\lim_{\Delta\ell \to 0} q^{\pm} = \frac{p}{2}$, $\breve{g}_{vb}^{+} = \breve{g}_{vb}^{-} = \breve{g}_{vb}$ and $g_s^{+} = g_s^{-} = g_s$, one immediately obtains the following continuum relationship for the IEP,

$$\frac{d\Delta \hat{S}_{in}}{dt} = -\frac{1}{T} \left(\breve{g}_{vb} + g_s k \right) \frac{dh}{dt} \qquad \text{(erg/}^{o}\text{K/cm/sec)} \qquad (2.3.1.19)$$

where $d\Delta \hat{S}_{in} / dt$ is the surface density of IEP associated with ordinary points.

ii. Rate of Entropy Flow

Similarly, the external entropy accumulation in the surface phase due to flow of chemical species, i, along the surface layer, J_s^i, and the perpendicular incoming flux intensities from the bulk, $\hat{J}_b^i$, and the void, $\hat{J}_v^i$, phases, can be calculated by using the law of conservation of entropy without the source term or IEP.

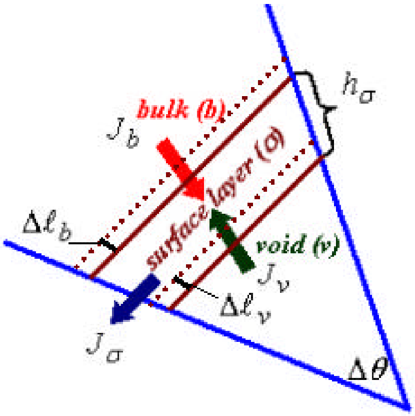

Figure 2.3.1.2: Structure of micro-composite system.

From figure 2.3.1.2 it can be written as,

$$\begin{aligned}
\frac{d\Delta\hat{S}_{ex}}{dt} &= -\frac{\partial}{\partial\ell}J_s + \hat{J}_b + \hat{J}_v \\
&= -\sum_i \frac{\partial}{\partial\ell}\left(\frac{m_s^i}{T_s}J_s^i\right) + \sum_i \frac{m_b^i}{T_b}\hat{J}_b^i + \sum_i \frac{m_v^i}{T_v}\hat{J}_v^i \qquad (2.3.1.20) \\
&= -\sum_i \frac{\partial}{\partial\ell}\left(\frac{m_s^i}{T_s}x_s^i J_s\right) + \sum_i \frac{m_b^i}{T_b}x_b^i \hat{J}_b + \sum_i \frac{m_v^i}{T_v}x_v^i \hat{J}_v
\end{aligned}$$

where, $\hat{J}_v$ and $\hat{J}_b$ are the total atomic flux intensities is such directions that they are perpendicular and oriented towards the interfacial layer, just at the reaction fronts between the void and the interfacial layer and the bulk phase and the interfacial layer, respectively.

By remembering the definitions of the volumetric Gibbs free energy densities, $\breve{g}_k$, given by $\sum_i x_k^i m_k^i / \Omega_k$, where k represents the different phases, and keeping in mind that the global system is in thermal equilibrium, Eq. (2.3.1.20) can be rewritten as:

$$\frac{d\Delta\hat{S}_{ex}}{dt} = -\frac{\Omega_s}{T}\left[\frac{\partial}{\partial\ell}\left(\breve{g}_s J_s\right) + \breve{g}_s\left(\hat{J}_b + \hat{J}_v\right)\right] \qquad (2.3.1.21)$$

where $d\Delta\hat{S}_{ex}/dt$ is the surface density of REF associated with ordinary points.

In this formula it is also assumed that the mean atomic specific volumes of the bulk and the void phases are nearly equal to that of the interfacial layer.

iii. The Local Rate of Change in the Entropy Density

The total entropy production has to be calculated since only this term has the additive property that will be used to calculate the total entropy production of the whole void surface layer under isothermal condition by a path integration procedure. By using Eqs. (2.3.1.19 and 2.3.1.21);

$$\begin{aligned}\frac{d\Delta\hat{S}}{dt} &= \frac{d\Delta\hat{S}_{in}}{dt} + \frac{d\Delta\hat{S}_{ex}}{dt} \\ &= -\frac{1}{T}\left\{(\breve{g}_{vb} + g_s\,k)\frac{dh}{dt} + \Omega_s\left[\frac{\partial}{\partial\ell}(\breve{g}_s\,J_s) + \breve{g}_s\left(\hat{J}_b + \hat{J}_v\right)\right]\right\}\end{aligned} \tag{2.3.1.22}$$

In order to calculate the global rate of entropy change of the whole curved interfacial layer, which is between the void region and the bulk phase, let first take the line integral of Eq. (2.3.1.22) all along the closed curved interface, represented by C, excluding possible singularities such as a triple junction, which may be situated at a point denoted by the open interval $(-e,+e)$, where $e \to 0$. This interface is represented by C^o and equal to $C-(-e,+e)$.

$$\begin{aligned}\oint_{C^o} d\ell\frac{d\Delta\hat{S}}{dt} &= \underset{e\to 0}{\ell im}\int_{+e}^{-e} d\ell\frac{d\Delta\hat{S}}{dt} \\ &= -\frac{1}{T}\underset{e\to 0}{\ell im}\int_{+e}^{-e} d\ell\left\{\begin{array}{l}(\breve{g}_{vb} + g_s\,k)\dfrac{dh}{dt} \\ +\Omega_s\left[\dfrac{\partial}{\partial\ell}(\breve{g}_s\,J_s) + \breve{g}_s\left(\hat{J}_b + \hat{J}_v\right)\right]\end{array}\right\}\end{aligned} \tag{2.3.1.23}$$

In the absence of the particle source and sink terms, the atomic flux divergence is proportional with the amount of mass accumulated or depleted on an interfacial layer, which causes the interface to move in a local normal direction. However in this formulation a more general situation, namely, the additional entropy source terms associated with the normal components of the atomic flows coming from the bulk phase, and the void region due to condensation or evaporation processes that may be summarized by, $\hat{J}_{bv} = \hat{J}_b + \hat{J}_v$, is considered. Hence, the following expression can be written for the conservation of atomic species during the virtual displacement of curved interface having no stretching and thickness variations:

$$[(c_b - c_v) - h_s \bar{\kappa} c_s]\frac{dh}{dt} = \sum_i \frac{\partial J_s^i}{\partial \ell} - \sum_i \left(\hat{J}_b^i + \hat{J}_v^i\right) = \frac{\partial J_s}{\partial \ell} - \hat{J}_{bv} \qquad (2.3.1.24)$$

where, c_b, c_v and c_s are the atomic volumetric concentrations associated with the bulk, void and surface phases, respectively. Now if one considers the following plausible and highly accurate approximations for a realistic void, which may be treated as polyatomic dilute gas, such as: $c_v = 0$ and $h_s \bar{\kappa} = 0$. One would get the following results using the fact that $\Omega_b = c_b{}^{-1}$, which is mostly adapted in the literature (Guggenheim, 1959 and Ogurtani and Oren, 2001-a):

$$\frac{dh}{dt} = \vec{n} \cdot \frac{d\vec{r}}{dt} = \Omega_b \left(\frac{\partial J_s}{\partial \ell} - \hat{J}_{bv} \right) \qquad (2.3.1.25)$$

where, $\vec{n}$ and $\vec{r}$ are the surface normal and the position vectors, respectively.

Now, let us substitute above identity into Eq. (2.3.1.23), and also remember that it is assumed that the mean atomic specific volume of the bulk phase is nearly equal to that of the interfacial layer.

$$\oint_{C^0} d\ell \frac{d\Delta\hat{S}}{dt} = -\frac{\Omega_s}{T} \underset{e\to 0}{\ell im} \int_{+e}^{-e} d\ell \left\{ \begin{array}{l} \left[(\breve{g}_{vb} + g_s\, k)\left(\dfrac{\partial J_s}{\partial \ell} - \hat{J}_{bv}\right) \right] \\ + \left[\dfrac{\partial}{\partial \ell}(\breve{g}_s\, J_s) + \breve{g}_s\, \hat{J}_{bv} \right] \end{array} \right\} \qquad (2.3.1.26)$$

In order to apply the integration by parts let us write Eq. (2.3.1.26) in the following form,

$$\oint_{C^0} d\ell \frac{d\Delta\hat{S}}{dt} = -\frac{\Omega_s}{T} \underset{e\to 0}{\ell im} \left\{ \begin{array}{l} \displaystyle\int_{+e}^{-e} d\ell \left[(\breve{g}_{vb} + g_s\, k) \frac{\partial J_s}{\partial \ell} \right] \\ \displaystyle - \int_{+e}^{-e} d\ell \left[(\breve{g}_{vb} + g_s\, k)\, \hat{J}_{bv} \right] \\ \displaystyle + \int_{+e}^{-e} d\ell \frac{\partial}{\partial \ell}(\breve{g}_s\, J_s) + \int_{+e}^{-e} d\ell \left(\breve{g}_s\, \hat{J}_{bv}\right) \end{array} \right\} \qquad (2.3.1.27)$$

The first group of terms on the right side of the Eq. (2.3.1.27) can be integrated by parts, as shown below; In order to save the space the left side of the equation are not shown in the following two equations.

$$= -\frac{\Omega_s}{T} \underset{e\to 0}{\ell im} \left\{ \begin{array}{l} \displaystyle\int_{+e}^{-e} d\ell \frac{\partial}{\partial \ell}\left[(\breve{g}_{vb} + g_s\, k)\, J_s \right] - \int_{+e}^{-e} d\ell \left[J_s \frac{\partial}{\partial \ell}(\breve{g}_{vb} + g_s\, k) \right] \\ \displaystyle - \int_{+e}^{-e} d\ell \left[(\breve{g}_{vb} + g_s\, k)\, \hat{J}_{bv} \right] \\ \displaystyle + \int_{+e}^{-e} d\ell \frac{\partial}{\partial \ell}(\breve{g}_s\, J_s) + \int_{+e}^{-e} d\ell \left(\breve{g}_s\, \hat{J}_{bv}\right) \end{array} \right\} \qquad (2.3.1.28)$$

After some manipulations and rearrangements,

$$= \frac{\Omega_s}{T} \underset{e \to 0}{\ell im} \left\{ \begin{array}{l} \int\limits_{+e}^{-e} d\ell \left[J_s \frac{\partial}{\partial \ell} \left(\breve{g}_{vb} + g_s k \right) \right] - \left[\left(\breve{g}_{vb} + g_s k \right) J_s \right]_{+e}^{-e} \\ + \int\limits_{+e}^{-e} d\ell \left[\left(\breve{g}_{vb} + g_s k \right) \hat{J}_{bv} \right] - \left[\breve{g}_s J_s \right]_{+e}^{-e} - \int\limits_{+e}^{-e} d\ell \left(\breve{g}_s \hat{J}_{bv} \right) \end{array} \right\} \tag{2.3.1.29}$$

At the final step after the integration by parts procedure, one should carefully split the global rate of entropy change into two parts, namely the REF term and the IEP term by carefully inspecting the individual contributions in Eq. (2.3.1.29).

$$\frac{d}{dt} S_{REF} = \frac{\Omega_s}{T} \underset{e \to 0}{\ell im} \left\{ - \int\limits_{+e}^{-e} d\ell \left(\breve{g}_s \hat{J}_{bv} \right) - \left[\breve{g}_s J_s \right]_{-e} + \left[\breve{g}_s J_s \right]_{+e} \right\} \tag{2.3.1.30}$$

where, the first term is the integrated entropy flow to the void interfacial layer from the embedding parent phases through the incoming matter flux, $\hat{J}_{bv}$. In the same way the last two terms represents the rate of entropy injection, entering and leaving to the interfacial layer at the triple junction singularity respectively.

The remaining terms of Eq. (2.3.1.29) are related to the IEP and given by,

$$\frac{d}{dt} S_{IEP} = \frac{\Omega_s}{T} \underset{e \to 0}{\ell im} \left\{ \begin{array}{l} \int\limits_{+e}^{-e} d\ell \left[J_s \frac{\partial}{\partial \ell} \left(\breve{g}_{vb} + g_s k \right) \right] + \int\limits_{+e}^{-e} d\ell \left[\left(\breve{g}_{vb} + g_s k \right) \hat{J}_{bv} \right] \\ - \left[\left(\breve{g}_{vb} + g_s k \right) J_s \right]_{-e} + \left[\left(\breve{g}_{vb} + g_s k \right) J_s \right]_{+e} \end{array} \right\} \tag{2.3.1.31}$$

This original results clearly confirms that the bulk flow of particles or substances for nonviscous systems appears to be a reversible phenomenon as first discovered by Prigogine (1961), in another content using the velocity of the centre of gravity as a reference system in the calculation of the possible singularity. In the absence of this singularity, the last two terms of Eqs. (2.3.1.30 and 2.3.1.31), become identically zero and drop out completely.

Here it should be clearly stated that the singularities have to be treated individually as a special case, where the discrete formulation of irreversible thermodynamics as suggested and developed by Ogurtani (2000), may be a very powerful tool to handle this problem successfully, as it will be shown in the next section.

After these mentioned drop outs, the following formula obtained for the IEP

$$\frac{d}{dt} S_{IEP} = \frac{\Omega_s}{T} \underset{e\to 0}{\ell im} \left\{ \int_{+e}^{-e} d\ell \left[J_s \, \frac{\partial}{\partial \ell} \left(\breve{g}_{vb} + g_s \, k \right) \right] + \int_{+e}^{-e} d\ell \left[\left(\breve{g}_{vb} + g_s \, k \right) \hat{J}_{bv} \right] \right\} \qquad (2.3.1.32)$$

Before proceeding further, let us turn back to postulates of irreversible thermodynamics: As shown by Prigogine (1961), the internal entropy production of the irreversible processes can be written as a sum of the products of generalized forces or affinities and the corresponding rates or generalized fluxes,

$$\frac{d}{dt} S_{IEP} = \sum_k J_k F_k \geq 0 \qquad (2.3.1.33)$$

By utilizing this postulate, which means by comparing the Eqs. (2.3.1.32 and 2.3.1.33), one obtains the following forces from the integrated IEP expression (2.3.1.32), which is valid for any arbitrary closed loop.

$$F_s = \frac{\Omega_s}{T} \frac{\partial}{\partial \ell} \left(\breve{g}_{vb} + g_s k \right) \tag{2.3.1.34}$$

and

$$F_{vb} = \frac{\Omega_s}{T} \left(\breve{g}_{vb} + g_s k \right) \tag{2.3.1.35}$$

where, F_s and F_{vb} denote longitudinal and transverse generalized forces that are acting on the interfacial layer respectively.

If one considers the additional contributions due to external forces, denoted by $\vec{F}_{ext}$,

$$F_s = \Omega_s \left[\frac{1}{T} \frac{\partial}{\partial \ell} \left(\breve{g}_{vb} + g_s k \right) + \vec{t} \cdot \vec{F}_{ext} \right] \tag{2.3.1.36}$$

and

$$F_{vb} = \Omega_s \left[\frac{1}{T} \left(\breve{g}_{vb} + g_s k \right) + \vec{n} \cdot \vec{F}_{ext} \right] \tag{2.3.1.37}$$

Here $\vec{t}$ and $\vec{n}$ denote unit tangent and normal vectors at the void surface. The external forces were discussed by Ogurtani and Oren (2001-a) in Appendix B of that reference for various kind of external forces, such as electrostatic, elastostatic and magnetic in nature.

Here only the electrostatic external forces will be discussed. The external generalized forces per particle, i, associated with electromigration is given by,

$$\vec{F}_{em}^{i} = -\frac{eZ^{i}}{T}\nabla J \qquad (2.3.1.38)$$

where, J is the electrostatic potential and eZ^{i} is the effective charge of the particle i. The external generalized total force density (per unit volume) associated with electromigration and acting on particles may have the following form for a multi-component system whether it is a bulk phase or an interfacial layer,

$$\vec{F}_{ext} = \vec{F}_{em} = -\frac{1}{T\Omega_s}\left(\sum_i x^i eZ^i\right)\nabla J = -\frac{1}{T\Omega_s}eZ^{*}\nabla J \qquad (2.3.1.39)$$

where, eZ^{*} is the effective charge in multi-component systems.

The last contribution in Eq. (2.3.1.37), $\vec{n}\cdot\vec{F}_{ext}$, becomes identically zero since the normal component of the electric field intensity vanish at the void surface.

Then, according to the Onsager theory (de Groot, 1951 and Prigogine 1961), which connects generalized forces and conjugate fluxes through generalized mobilities, the conjugate fluxes associated with the above forces can immediately be written down, by neglecting the cross-coupling terms between generalized forces and fluxes, as:

$$J_s = \frac{\mathrm{M}_s}{kT}\Omega_s \frac{\partial}{\partial \ell}\left[\left(\breve{g}_{vb} + g_s k\right) - \left\langle eZ^* \right\rangle \frac{J}{\Omega_s}\right] \qquad \text{(Surface Flux)} \qquad (2.3.1.40)$$

and

$$\hat{J}_{vb} = \frac{\mathrm{M}_{vb}}{kT}\Omega_s \left(\breve{g}_{vb} + g_s k\right) \qquad \text{(Incoming net lateral flux density)} \qquad (2.3.1.41)$$

where, M_s / k and M_{vb} / k are the generalized phenomenological mobilities associated with the respective conjugated forces and fluxes, $\left\langle eZ^* \right\rangle$ is the mean value of the effective electromigration charge associated with the interacting species and k is the Boltzmann's constant.

For multi-component systems, where one is interested only in the net atomic (mass) transport regardless to the contributions of individual chemical species, the first generalized-mobility, M_s , may not be easily connected to any combination of the intrinsic surface diffusivities of individual chemical species in the interfacial layer or in the bulk phase. However, for one component system having minor amount of doping elements or impurities, the situation is rather simple where one can easily identify the existence of the following relationship between generalized mobility and the surface self-diffusivity of host matter denoted by $\tilde{D}_s$,

$$\hat{\mathrm{M}}_s = \frac{\mathrm{M}_s}{kT} = \frac{\tilde{D}_s}{kT}\frac{h_s}{\Omega_s} = \frac{\tilde{D}_s}{kT}\Gamma_s , \qquad (2.3.1.42)$$

Hence, for the future discussions, the following compact form will be used, which is more suitable to take other driving forces such as the electromigration drift motion of surface atoms into considerations:

$$J_s = \hat{\mathrm{M}}_s \frac{\partial}{\partial \ell}\left[\Omega_s \left(\breve{g}_{vb} + g_s k\right) - \left\langle eZ^* \right\rangle J\right] \qquad \text{(Surface Flux)} \qquad (2.3.1.43)$$

where $\hat{\mathrm{M}}_s$ may be called surface atomic mobility, and it has the dimension given by $(erg.\sec)^{-1}$.

The generalized mobility, $\mathrm{M}_{vb}\left(cm^2/\sec\right)$, associated with the incoming bulk diffusion flux is related to the transformation rate of chemical species from bulk phase to the interfacial layer or vice versa over the activation energy barrier denoted by ΔG^*_{vb}. Hence, it can be defined according to the transition rate theory of chemical kinetics advocated by Eyring (Yeremin, 1979), as:

$$\mathrm{M}_{vb} = \frac{kT}{h}\exp\left(-\frac{\Delta G^*_{vb}}{kT}\right) \qquad (2.3.1.44)$$

In the future formula one will use rather normalized mobility, which may be defined by $\hat{\mathrm{M}}_{vb} = \mathrm{M}_{vb}/kT$, which has the following dimension $cm^2\left(erg.\sec\right)^{-1}$.

Before giving the mathematical model for the evolution dynamics of void intergranular motion, the formulas that govern the dynamical behavior of triple junction singularity have to be discussed, as will be done in the next section.

2.3.2. Triple Junction Motion

In this section, it is shown that the dynamical behavior of triple junction may be derived as a special case of triple junction singularity by lifting certain geometric constraints on the system and the existence of grain boundary.

As far as the kinetic behavior of a triple junction is concerned it is assumed that, the whole system is in thermal equilibrium and no insitu chemical reaction is taking place other than the phase transformation occurring between void interfacial layer and the grain boundary region. This last point, which is closely connected with the entropy point source term, up to now, is completely omitted in the literature (Rice and Chuang, 1951) in the formulation of conservation of species in terms of flux balance at the triple junction.

In the present theory the sampling domain is a very small composite discrete open micro-system, which is eventually localized into a point of singularity, and situated just in the immediate neighborhood of the junction as illustrated in figure 2.3.2.1. This selected composite micro-system is also connected to the neighboring micro-discrete elements by nodes where the exchange or the flow of matter only contributes to the rate of entropy flow but nothing to do with the internal entropy production.

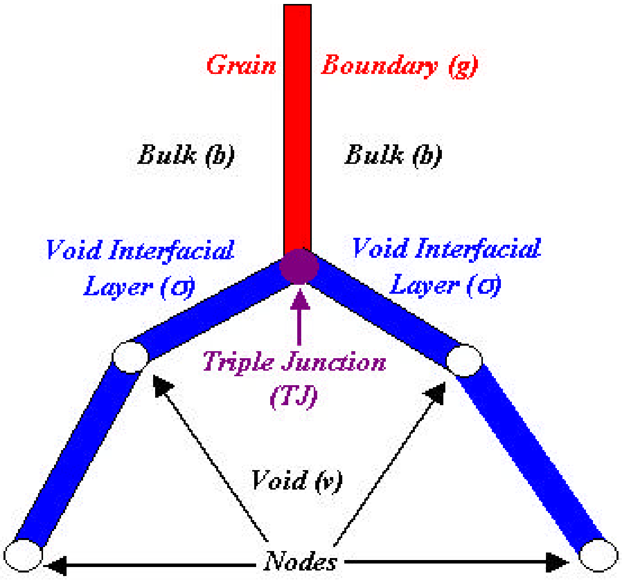

Figure 2.3.2.1: Triple junction micro-system.

In this section, first the individual IEP due to small but finite virtual displacement of a triple junction along the grain boundary is calculated. The sampling region at the triple junction is divided into two sub domains by passing a line, which separates the grain boundary region into two symmetrical parts. This dividing operation means that the IEP resulting from such a displacement of triple junction along the grain boundary can be separately and independently treated for the left and the right hand side domains, because of the lateral constraint on the grain boundary motion. However at the later stage, the IEP associated with the virtual displacement of the triple junction for the whole system will be also calculated. Namely, along the parallel and perpendicular directions with respect to grain boundary orientation, by lifting the constraint on the triple junction motion.

i. Triple Junction Longitudinal Motion

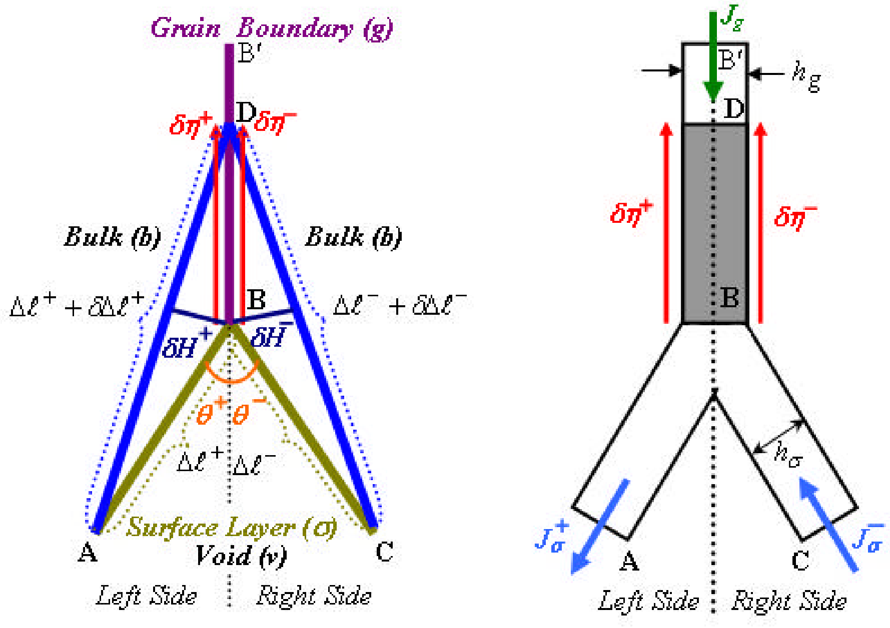

a) b)

Figure 2.3.2.2: Triple Junction Longitudinal Motion. **a)** Macro-structure **b)** Micro-structure. BB′: grain boundary, ABC: void interfacial layer and dh: longitudinal virtual displacement of the triple point along the grain boundary.

Now, similar to the IEP calculation for the ordinary points, let us calculate the internal entropy variation for the left hand side sub-system when the triple junction moves along the grain boundary with a distance dh^{+}. From figure 2.3.2.2, one immediately finds the following variational relationships among various quantities by assuming that: $\Delta\ell^{+} >> dh^{+}$ and $\Delta\ell^{-} >> dh^{-}$;

$$d\Delta\ell^{+} = dh^{+}\cos q^{+} \qquad \text{and} \qquad dH^{+} = dh^{+}\sin q^{+} \tag{2.3.2.1}$$

$$d\Delta n_b^{+} = -\frac{1}{2\Omega_b}\Delta\ell^{+}\sin q^{+} dh^{+} \tag{2.3.2.2}$$

$$d\Delta n_v^+ = \frac{1}{2\Omega_v}\Delta\ell^+ \sin q^+ dh^+ \qquad (2.3.2.3)$$

$$d\Delta n_s^+ = \frac{h_s}{\Omega_s}\cos q^+ dh^+ \qquad (2.3.2.4)$$

$$d\Delta n_g^+ = -\frac{h_g}{2\Omega_g} dh^+ \qquad (2.3.2.5)$$

where, Ω_g is the mean atomic specific volume of the grain boundary phase and h_g is the thickness of the grain boundary region and assumed to be invariant. Even though some of the variables have already been described during the IEP evaluation for the ordinary points, let us discuss all the variables as follows: $d\Delta n_v^+$ and $d\Delta n_b^+$ are the number of atoms gain in the reaction zones associated with the void – interfacial layer and the bulk – interfacial layer respectively, while the transformation processes are taking place there during the virtual displacement of the interfacial layer. $d\Delta n_g^+$ is the total number of atoms gained by the half of the grain boundary during triple junction motion. Similarly, $d\Delta n_s^+$ is identically equal to the net atomic gain by the interfacial layer denoted by s due to enlargement (extension without stretching) of that layer during the displacement operation. d and Δ are variational and micro-discretization operators, respectively. Eventually, by using a set of novel limiting procedures of calculus, they will be replaced by exact differential, and zero that corresponds to the infinitesimal volume or better to say to the singularity associated with the triple junction. One can obtain exactly similar expressions for the other side of the triple junction, which will be identified by a negative sign as superscript in the following formulas:

$$d\Delta\ell^{-} = dh^{-}\cos q^{-} \qquad \text{and} \qquad dH^{-} = dh^{-}\sin q^{-} \tag{2.3.2.6}$$

$$d\Delta n_b^{-} = -\frac{1}{2\Omega_b}\Delta\ell^{-}\sin q^{-} dh^{-} \tag{2.3.2.7}$$

$$d\Delta n_v^{-} = \frac{1}{2\Omega_v}\Delta\ell^{-}\sin q^{-} dh^{-} \tag{2.3.2.8}$$

$$d\Delta n_s^{-} = \frac{h_s}{\Omega_s}\cos q^{-} dh^{-} \tag{2.3.2.9}$$

$$d\Delta n_g^{-} = -\frac{h_g}{2\Omega_g} dh^{-} \tag{2.3.2.10}$$

The Internal Entropy Production (IEP) generation can be calculated for any arbitrary virtual displacement of the triple junction along the grain boundary by applying the only non-vanishing term of Eq. (2.2.13), as discussed before.

One can then write down the rate of entropy production due to triple junction virtual displacement for the left as well as for the right hand side domains using Eqs. (2.3.2.1-5 and 2.3.1.1) and Eqs. (2.3.2.6-10 and 2.3.1.1), respectively. In the case of left hand side the following equation can be obtained:

$$\frac{d\Delta S_{in}^{+}}{dt} = \frac{1}{T}\left\{ \begin{aligned} &\left[\sum_i \left(\frac{x_b^{i+}}{\Omega_b} m_b^{i+} - \frac{x_v^{i+}}{\Omega_v} m_v^{i+} \right)\right] \frac{1}{2}\Delta\ell^{+}\sin q^{+} \\ &+ \left(\frac{\Gamma_g}{2}\sum_i x_g^{i} m_g^{i} - \Gamma_s \cos q^{+} \sum_i x_s^{i+} m_s^{i+} \right) \end{aligned} \right\} \frac{dh^{+}}{dt} \tag{2.3.2.11}$$

and in the case of right hand side the following equation can be obtained:

$$\frac{d\Delta S_{in}^{-}}{dt}=\frac{1}{T}\left\{\begin{array}{l}\left[\sum_{i}\left(\frac{x_b^{i-}}{\Omega_b}m_b^{i-}-\frac{x_v^{i-}}{\Omega_v}m_v^{i-}\right)\right]\frac{1}{2}\Delta\ell^{-}\sin q^{-}\\+\left(\frac{\Gamma_g}{2}\sum_{i}x_g^{i}m_g^{i}-\Gamma_s\cos q^{-}\sum_{i}x_s^{i-}m_s^{i-}\right)\end{array}\right\}\frac{dh^{-}}{dt} \qquad (2.3.2.12)$$

By using the definitions, which were discussed in the previous section, the following equations are obtained from the Eqs. (2.3.2.11 and 2.3.2.12).

$$\frac{d\Delta S_{in}^{+}}{dt}=\frac{1}{T}\left\{\left(\breve{g}_b^{+}-\breve{g}_v^{+}\right)\frac{1}{2}\Delta\ell^{+}\sin q^{+}+\frac{1}{2}g_g-g_s^{+}\cos q^{+}\right\}\frac{dh^{+}}{dt} \qquad (2.3.2.13)$$

and

$$\frac{d\Delta S_{in}^{-}}{dt}=\frac{1}{T}\left\{\left(\breve{g}_b^{-}-\breve{g}_v^{-}\right)\frac{1}{2}\Delta\ell^{-}\sin q^{-}+\frac{1}{2}g_g-g_s^{-}\cos q^{-}\right\}\frac{dh^{-}}{dt} \qquad (2.3.2.14)$$

By taking consecutive limiting procedures such as; first with respect to $dt \to 0$, and then $\Delta\ell \to 0$, one immediately obtains the following differential equations representing IEP associated with the virtual displacement of the left and right sides of the triple junction singularity,

$$\underset{\substack{dt\to 0\\ \Delta\ell\to 0}}{Lim}\frac{d\Delta S_{in}^{+}}{dt}=\frac{d\Delta\hat{S}_{in}^{+}}{dt}=\frac{1}{T}\left(\frac{1}{2}g_g-g_s^{+}\cos q^{+}\right)\frac{dh^{+}}{dt} \qquad (\text{erg}/^{o}\text{K/cm/sec}) \qquad (2.3.2.15)$$

and

$$\underset{\substack{dt\to 0\\ \Delta\ell\to 0}}{Lim}\frac{d\Delta S_{in}^{-}}{dt}=\frac{d\Delta\hat{S}_{in}^{-}}{dt}=\frac{1}{T}\left(\frac{1}{2}g_g-g_s^{-}\cos q^{-}\right)\frac{dh^{-}}{dt} \qquad (\text{erg}/^{o}\text{K/cm/sec}) \qquad (2.3.2.16)$$

On the left sides of above expressions, the ^ symbol has been tacitly employed to emphasize that these entropy production terms are line source in three-dimensional space, due to the fact that cylindrical voids are treated in this formulation. The superscripts have been also employed over the specific Gibbs free energies to indicate that those quantities may depend upon the orientation of the local surface normal vector.

Finally, a local set of discrete microelements in the vicinity of the triple junction, which includes both domains mentioned previously, can be chosen. The entropy production for the combined system can be easily calculated using Eqs. (2.3.2.13) and (2.3.2.14) for the virtual displacement of the triple junction along the grain boundary. The result is as follows:

$$\begin{aligned} \frac{d\Delta S_{in}^{gs}}{dt} &= \frac{d\Delta S_{in}^{+}}{dt} + \frac{d\Delta S_{in}^{-}}{dt} \\ &= \frac{1}{T}\left\{ \begin{array}{l} -\frac{1}{2}\left(\breve{g}_{vb}^{+}\Delta\ell^{+}\sin q^{+} + \breve{g}_{vb}^{-}\Delta\ell^{-}\sin q^{-}\right) \\ + \left[g_{g} - \left(g_{s}^{+}\cos q^{+} + g_{s}^{-}\cos q^{-}\right)\right] \end{array} \right\} \frac{dh_{g}}{dt} \geq 0 \end{aligned} \tag{2.3.2.17}$$

which yields IEP due to longitudinal displacement of the triple junction along the grain boundary, after applying the consecutive limiting procedures as described previously,

$$\frac{d\hat{S}_{in}^{gs}}{dt} = \frac{1}{T}\left[g_{g} - \left(g_{s}^{+}\cos q^{+} + g_{s}^{-}\cos q^{-}\right)\right]\frac{dh_{g}}{dt} \geq 0 \tag{2.3.2.18}$$

where $\breve{g}_{vb} = (\breve{g}_{v} - \breve{g}_{b})$, and it corresponds by definition to the volumetric density of Gibbs Free Energy of Transformation (GFET) (negative of the affinity of an interfacial reaction such as condensation or adsorption, $g_{vb}>0$) associated with the transformation of the bulk phase into the *realistic void* phase which contains chemical species even though they are present in a trace amount. In the case of thermostatic equilibrium between a void phase and an adjacent bulk phase, GFET becomes identically equal to zero, if the reaction front would be a flat interface. There is a very simple connection between this quantity GFET and the Specific Gibbs Free Energy of transformation g_{vb} (evaporation or desorption, $g_{vb}<0$) between the parent phase and void phase that may be given by $g_{vb} = \breve{g}_{vb} h_s$.

Since the entropy production can be split in several ways into fluxes and forces as clearly demonstrated by De Groot (1951); there is a certain freedom exists in the choice of fluxes and forces. The first set of forces and fluxes that is employed by Ogurtani and Oren (2001-a) in connection with ordinary points along the void surface layer and also as demonstrated in the previous section, is more or less thermodynamical in nature. However, the interpretation of these forces is rather abstract and they may be also called as the affinities in the field of irreversible thermodynamics. On the other hand, the second set can be easily understood in terms of *ordinary drag force* versus *velocity* concept, and their physical interpretation is rather straight forward, but its validity is rather restricted to the systems that are in complete thermal equilibrium and the processes are isothermal. Since it has been assumed on the onset that there is a thermal equilibrium in the system, it may be rather used a direct and more plausible approach for the triple junction singularity, namely the concept of power dissipation in the close sense of classical mechanics, and sometimes it is called Helmholtz dissipation function (Haase, 1969). This concept is also advocated and extensively used by Ogurtani and Seeger (1983), in the general formulation of internal friction and dislocation damping phenomenon associated with atomic hopping motions in discrete body centered cubic lattice, that is exposed to the interaction fields which are inhomogeneous in space and fluctuating in time. The power dissipation function is simply given by the internal entropy production multiply by the temperature for an isothermal system, and for the present case obviously it is identically equal to driving force velocity product, namely:

$$T\,\frac{d\hat{S}^{\pm}_{in}}{dt} = \hat{F}^{\pm}\,\frac{dh^{\pm}}{dt} \geq 0 \qquad \text{(erg/cm/sec)} \qquad (2.3.2.19)$$

Hence by comparing this expression with Eq. (2.3.1.15), one can immediately deduce the generalized force for the left side,

$$\hat{F}^{+} = \left(\frac{g_g}{2} - g_s^{+}\cos q^{+}\right) \qquad \text{(dyne/cm)} \qquad (2.3.2.20)$$

and similarly by comparing the Eq. (2.3.2.19) with Eq. (2.3.2.16) and giving attention to sign convention in figure 2.3.2.2 one can write down an equivalent expression, for the right side;

$$\hat{F}^{-} = -\left(\frac{g_g}{2} - g_s^{-} \cos q^{-} \right) \qquad \text{(dyne/cm)} \qquad (2.3.2.21)$$

These generalized forces are associated with the net material flow during the triple junction longitudinal displacement along the grain boundary without making any distinction between intrinsic fluxes related to the individual chemical species. They are also given in terms of per unit length, because in the formulation of the IEP, a sample of unit length in thickness is chosen, and in addition the void surface is assumed to be an arbitrary cylindrical in shape. In the phenomenological relationship between velocity and force, one may prefer to use the force acting on a single atomic particle. Therefore above expressions for generalized forces should be multiplied by an atomic length, d_a, which may be taken as equal to the inter-atomic distance along the sample thickness. Hence, the connection between the triple junction velocity and the atomic generalized force can be now written by introducing the phenomenological longitudinal mobility coefficient $\Re^{long}/kT$,

$$\frac{dh^{+}}{dt} = v_g^{+} = \frac{\Re^{long} d_a}{kT} \left(\frac{g_g}{2} - g_s^{+} \cos q^{+} \right) \qquad (2.3.2.22)$$

and

$$\frac{dh^{-}}{dt} = v_g^{-} = -\frac{\Re^{long} d_a}{kT} \left(\frac{g_g}{2} - g_s^{-} \cos q^{-} \right) \qquad (2.3.2.23)$$

where, the same mobilities for both sides are employed. One can now immediately formulate the atomic fluxes coming from the triple junction towards the both sides of the void surface layer. These are simply given by the number of atoms present in a volume swept by the triple junction motion along the grain boundary per unit time, and plus the incoming grain boundary atomic flux $\hat{J}_g$ (# /cm.sec) associated with the long-range drift-diffusion. The velocity of the triple junction is proportional with the net flux accumulated or depleted at the junction. Hence, one writes the following expressions;

$$\frac{dh_g^+}{dt} = \frac{2}{\Gamma_g}\left(\hat{J}_s^+ - \hat{J}_g/2\right) \qquad \text{and} \qquad \frac{dh_g^-}{dt} = \frac{2}{\Gamma_g}\left(\hat{J}_s^- + \hat{J}_g/2\right) \qquad (2.3.2.24)$$

Using these expressions in with Eqs. (2.3.2.22) and (2.3.2.23) for the triple junction velocities, one gets immediately the following generalized conjugate fluxes:

$$\begin{aligned} \hat{J}_s^+ &= \Gamma_g \frac{\Re^{long} d_a}{2kT}\left(\frac{g_g}{2} - g_s^+ \cos q^+\right) + \hat{J}_g/2 \\ &= \Gamma_g \frac{\Re^{long} d_a}{2kT} g_s^+\left(l^+ - \cos q^+\right) + \hat{J}_g/2 \end{aligned} \qquad (2.3.2.25)$$

and

$$\begin{aligned} \hat{J}_s^- &= -\Gamma_g \frac{\Re^{long} d_a}{2kT}\left(\frac{g_g}{2} - g_s^- \cos q^-\right) - \hat{J}_g/2 \\ &= -\Gamma_g \frac{\Re^{long} d_a}{2kT} g_s^-\left(l^- - \cos q^-\right) - \hat{J}_g/2 \end{aligned} \qquad (2.3.2.26)$$

where one takes the sample thickness as one unit length, and also considers the right and left sub-domains separately by splitting the grain boundary diffusion flux equally. At this stage one can immediately write down the expression for the velocity of the triple junction either directly from Eq. (2.3.2.18), or applying the law of conservation of species to the displacement motion of triple junction, and utilizing Eqs. (2.3.2.25) and (2.3.2.26) for the out-going fluxes from the transformation front:

$$\begin{aligned} v_g^{long} &= \frac{dh_g}{dt} = \left(\hat{J}^+ - \hat{J}^- - \hat{J}_g\right)\frac{1}{\Gamma_g} \\ &= \frac{1}{\Gamma_g}\left\{ \begin{array}{l} \left[\Gamma_g \dfrac{\Re^{long} d_a}{2kT} g_s^+ \left(l^+ - \cos q^+\right) + \hat{J}_g / 2\right] \\ -\left[-\Gamma_g \dfrac{\Re^{long} d_a}{2kT} g_s^- \left(l^- - \cos q^-\right) - \hat{J}_g / 2\right] - \hat{J}_g \end{array} \right\} \\ &= \frac{\Re^{long} d_a}{2kT}\left[g_s^+ \left(l^+ - \cos q^+\right) + g_s^- \left(l^- - \cos q^-\right)\right] \end{aligned} \qquad (2.3.2.27)$$

In above flux relations, l^- and l^+ are very important parameters which may be assumed to be constant and equal especially in the case of isotropic behavior of surface phases. They may be called as the wetting parameters and are given by the following expressions:

$$l^- = \frac{g_g}{2g_s^-} \qquad \text{and} \qquad l^+ = \frac{g_g}{2g_s^+} \qquad (2.3.2.28)$$

The specific Gibbs free energy of the void surface layer may depend on the orientation of the local surface normal due to the anisotropic behavior of the surface tension γ and/or the specific Helmholtz free energy itself in crystalline solids (Defay *et. al.*, 1966).

In above expressions, a phenomenological mobility coefficient have been introduced and denoted by $\Re^{long}$, which may be called as the reaction rate constant associated with the phase transformation denoted symbolically by $s \Leftrightarrow gb$. For the present case, it refers a transformation, which takes place continuously and reciprocally between two surface phases, namely, between the interfacial layer and the grain boundary region just at the triple junction. This phenomenological mobility does not make any distinction between individual chemical species and their rate of transfer over the activation energy barrier. It is strongly dependent on the temperature, and that may be formulated according to the activated complex rate theory of chemical reactions (Yeremin, 1979) as follows:

$$\Re^{long} = \left(\frac{kT}{h}\right)\exp\left(-\frac{\Delta G^{*}_{s,g}}{kT}\right) \qquad (2.3.2.29)$$

In above expression $\Delta G^{*}_{s,g}$ is the Gibbs free energy of activation for the transformation of surface phase, s, into the grain boundary phase, g, or vice versa. Eqs. (2.3.2.22 and 2.3.2.23) clearly show that in the case of thermostatic equilibrium at the triple junction, the displacement velocity becomes identically equal to zero regardless of the magnitude of the grain boundary flux. Thermostatic equilibrium establishes when the dihedral angles have reached those values, which make generalized forces given in Eqs. (2.3.2.20) and (2.3.2.21) identically equal to zero, under the assumed constrain on the triple junction, namely no lateral motion is possible. Similarly in above equation, the fluxes associated with the void surface diffusion, they may go through certain modifications in the case of anisotropic behavior of the void surface layer as demonstrated by Ogurtani and Oren (2001-a) and Oren and Ogurtani (2002). In the case of isotropic specific Gibbs free energies above equation may be written in the following form by utilizing Eq. (2.3.2.27) and the dimensionless parameter l, which is given by $l = g_g/(2g_s)$.

$$v_g^{long} = \frac{\Re^{long} d_a g_s}{2kT}\left[2l - \left(\cos q^+ + \cos q^-\right)\right] \quad \text{(cm/sec)} \qquad (2.3.2.30)$$

After obtaining the triple junction longitudinal velocity, let us first calculate the triple junction transverse velocity and then reapplying the constraint on the grain boundary, that is the grain boundaries are immobile, calculate the fluxes necessary to establish the thermostatic equilibrium at the triple junction.

ii. Triple Junction Transverse Motion

Using the technique, developed in the previous sections, the internal entropy production associated with the transverse virtual displacement of the triple junction, namely the motion perpendicular to the grain boundary, can be calculated.

The internal entropy variation for the left hand side sub-system when the triple junction moves perpendicular to the grain boundary with a distance dh^+ can be calculated from figure 2.3.2.3,

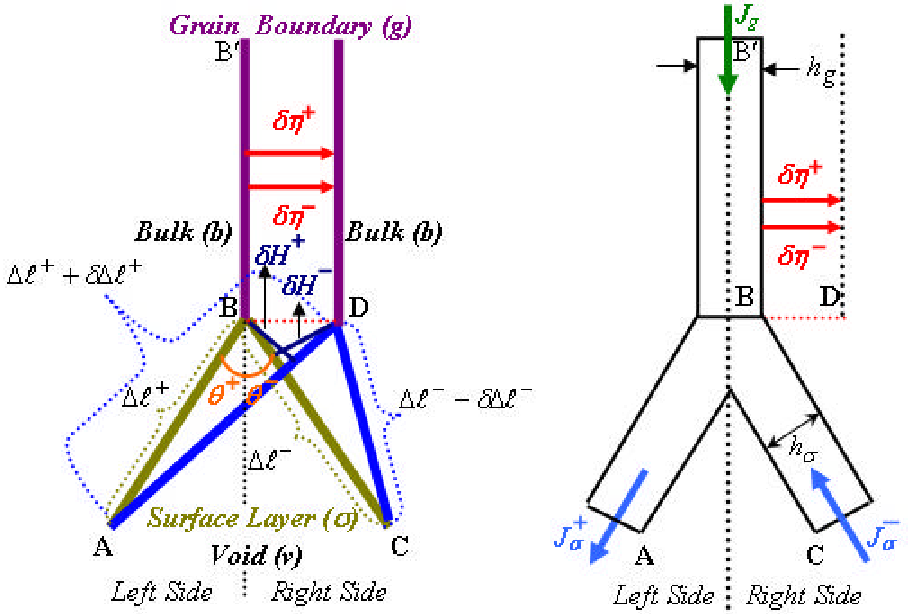

a) b)

Figure 2.3.2.3: Triple Junction Transverse Motion. **a)** Macro-structure **b)** Micro-structure. BB′: grain boundary, ABC: void interfacial layer and dh : transverse virtual displacement of the triple point along the grain boundary.

$$d\Delta\ell^+ = dh^+ \sin\theta^+ \quad \text{and} \quad dH^+ = dh^+ \cos\theta^+ \tag{2.3.2.31}$$

$$d\Delta n_b^+ = \frac{1}{2\Omega_b}\Delta\ell^+ \cos\theta^+ dh^+ \tag{2.3.2.32}$$

$$d\Delta n_v^+ = -\frac{1}{2\Omega_v}\Delta\ell^+ \cos\theta^+ dh^+ \tag{2.3.2.33}$$

$$d\Delta n_s^+ = \frac{h_s}{\Omega_s}\sin\theta^+ dh^+ \tag{2.3.2.34}$$

$$d\Delta n_g^+ = 0 \tag{2.3.2.35}$$

One can obtain exactly similar expressions for the other side of the triple junction, which will be identified by a negative sign as superscript in the following formulas:

$$d\Delta\ell^{-} = dh^{-} \sin q^{-} \qquad \text{and} \qquad dH^{-} = dh^{-} \cos q^{-} \tag{2.3.2.36}$$

$$d\Delta n_b^{-} = -\frac{1}{2\Omega_b} \Delta\ell^{-} \cos q^{-} dh^{-} \tag{2.3.2.37}$$

$$d\Delta n_v^{-} = \frac{1}{2\Omega_v} \Delta\ell^{-} \cos q^{-} dh^{-} \tag{2.3.2.38}$$

$$d\Delta n_s^{-} = -\frac{h_s}{\Omega_s} \sin q^{-} dh^{-} \tag{2.3.2.39}$$

$$d\Delta n_g^{-} = 0 \tag{2.3.2.40}$$

One can than rigorously write down the rate of entropy production due to triple junction virtual transverse displacement for the left as well as the right hand side domains;

$$\frac{d\Delta S_{in}^{+}}{dt} = -\frac{1}{T} \left\{ \begin{array}{l} \left[\sum_i \left(\frac{x_b^{i+}}{\Omega_b} m_b^{i+} - \frac{x_v^{i+}}{\Omega_v} m_v^{i+} \right) \right] \frac{1}{2} \Delta\ell^{+} \cos q^{+} \\ + \Gamma_s \sin q^{+} \sum_i x_s^{i+} m_s^{i+} \end{array} \right\} \frac{dh^{+}}{dt} \tag{2.3.2.41}$$

and

$$\frac{d\Delta S_{in}^{-}}{dt} = \frac{1}{T} \left\{ \begin{array}{l} \left[\sum_i \left(\frac{x_b^{i-}}{\Omega_b} m_b^{i-} - \frac{x_v^{i-}}{\Omega_v} m_v^{i-} \right) \right] \frac{1}{2} \Delta\ell^{-} \cos q^{-} \\ + \Gamma_s \sin q^{-} \sum_i x_s^{i-} m_s^{i-} \end{array} \right\} \frac{dh^{-}}{dt} \tag{2.3.2.42}$$

By using the same definitions, which described in the previous section, the following equations are obtained,

$$\frac{d\Delta S_{in}^{+}}{dt} = -\frac{1}{T}\left\{\left(\breve{g}_{b}^{+} - \breve{g}_{v}^{+}\right)\frac{1}{2}\Delta\ell^{+}\cos q^{+} + g_{s}^{+}\sin q^{+}\right\}\frac{dh^{+}}{dt} \qquad (2.3.2.43)$$

and

$$\frac{d\Delta S_{in}^{-}}{dt} = +\frac{1}{T}\left\{\left(\breve{g}_{b}^{-} - \breve{g}_{v}^{-}\right)\frac{1}{2}\Delta\ell^{-}\cos q^{-} + g_{s}^{-}\sin q^{-}\right\}\frac{dh^{-}}{dt} \qquad (2.3.2.44)$$

By taking consecutive limiting procedures such as; first with respect to $dt \to 0$, and then $\Delta\ell \to 0$, one immediately obtains the following differential equations representing IEP associated with the virtual transverse displacement of the left and right sides of a triple junction singularity,

$$\underset{\substack{dt\to 0\\ \Delta\ell\to 0}}{Lim}\frac{d\Delta S_{in}^{+}}{dt} = \frac{d\Delta\hat{S}_{in}^{+}}{dt} = -\frac{1}{T}g_{s}^{+}\sin q^{+}\frac{dh^{+}}{dt} \qquad (\text{erg}/{}^{o}\text{K/cm/sec}) \qquad (2.3.2.45)$$

and

$$\underset{\substack{dt\to 0\\ \Delta\ell\to 0}}{Lim}\frac{d\Delta S_{in}^{-}}{dt} = \frac{d\Delta\hat{S}_{in}^{-}}{dt} = \frac{1}{T}g_{s}^{-}\sin q^{-}\frac{dh^{-}}{dt} \qquad (\text{erg}/{}^{o}\text{K/cm/sec}) \qquad (2.3.2.46)$$

Finally, the IEP due to transverse displacement of the triple junction along the grain boundary can be calculated, after applying the consecutive limiting procedures as described previously. The result as follows along the designated positive directions:

$$\frac{d\hat{S}_{in}^{trans}}{dt} = -\frac{1}{T}\left(g_s^{+} \sin q^{+} - g_s^{-} \sin q^{-}\right)\frac{dh_g}{dt} \geq 0 \qquad (2.3.2.47)$$

Since it has been assumed on the on set that there is a thermal equilibrium in the system, the Helmholtz dissipation function, as described by Eq. (2.3.2.19), can be used. Then, according to Eq. (2.3.2.47), the projection of the dissipative force acting along the direction perpendicular to the grain boundary may be given by;

$$\hat{F}^{trans} = -\left(g_s^{+} \sin q^{+} - g_s^{-} \sin q^{-}\right) \qquad \text{(dyne/cm)} \qquad (2.3.2.48)$$

This relationship together with Eq. (2.3.2.30) clearly shows that triple junction without having any constrain (completely free junction) can be in complete physico-chemical equilibrium configuration if and only if the specific interphasial Gibbs free energies associated with the grain boundary and the both sides of the void surface layer satisfy a *Nil Vectorial Summation Rule,* which may represented by the following equation; $\vec{g}_g + \vec{g}_s^{+} + \vec{g}_s^{-} = 0$. It should be mentioned here that the similar vectorial connection exist among the surface tensions γ associated with the intersecting interfaces in order to have a mechanical equilibrium at the triple junction, which is also known as Young formula in the literature (Young, 1805).

Above findings related to the transverse virtual motion of the triple junction is very important if one considers a more general problem where the grain boundary migration occurs as a result of some thermally activated processes. In that situation, the transverse component of the triple junction velocity according to Eq. (2.3.2.48) may be given by the following expression;

$$v_g^{trans} = \frac{\Re_g^{trans}}{kT} d_a \left(g_s^- \sin q^- - g_s^+ \sin q^+ \right) \qquad \text{(cm/sec.)} \qquad (2.3.2.49)$$

where d_a is the atomic distance and $\Re_g^{trans}/kT$ is the triple junction transverse migration mobility, and this mobility is a phenomenological coefficient depending upon the temperature of the system through an activation energy barrier.

In the case of lateral constraint on the grain boundary motion, the generalized lateral force now generates a particle flow at and through the triple junction along the void interfacial layer to establish thermostatic equilibrium configuration there by adjusting orientations of the neighboring left and right micro-elements. The conjugate particle flux (transverse flow) associated with this force can be immediately written as;

$$\hat{J}_s^{trans} = -Sign(y)\Gamma_g \frac{\Re_g^{trans}}{kT} d_a \left(g_s^- \sin q^- - g_s^+ \sin q^+ \right) \qquad \text{(\#/cm.sec.)} \qquad (2.3.2.50)$$

In above expression the angle y denotes the amount of rotation of the microelements adjoint to the triple junction in the anti-clockwise direction, and $Sign$ is the usual $sign$ function. A close inspection of above flux expression reveals that the direction of which as such that it tries to eliminate any deviation from the thermostatic equilibrium at the triple junction through the dihedral angles readjustment by transferring mass from one side to another. Where, the direction of mass flow is always towards the establishment of the thermostatic equilibrium configuration, as one expects a priory from the meaning of the postulate of positive internal entropy production in the irreversible thermodynamics.

2.4. Mathematical Model For the Evolution Dynamics of the Void Intergranular and Intragranular Motion

The present model developed in this chapter considers not only the drift-diffusion of chemical species on the realistic void surface but also the direct transfer of chemical species between bulk phase and the void region through the interfacial layer (growth) as a dominant transport mechanisms. In two dimensional space the transgranular and intergranular motion of the void, surface of which is a general cylindrical in shape, can be represented by the normal displacement velocity even for multi-component systems such as aluminum and copper alloys, in terms of normalized and scaled parameters and variables, assuming that there is no charged particle in the void region (perfect insulator).

First of all the time and the scale variables t and ℓ are normalized in the following manner, first of all an atomic mobility associated with the mass flow at the surface layer is defined as it has been already done in section 2.3.1. by the Eq. (2.3.1.42). And then a new time scale is introduced by;

$$t_o = \frac{r_o^4}{\Omega_s^2 \hat{M}_s \, g_s} \tag{2.4.1}$$

where r_o is the mean initial void radius which can be obtained directly from $r_o = \sqrt{A_o / p}$, using the fact that the initial void cross sectional area, A_o, is also an invariant of the motion in the absence of the growth process. Similarly r_o is used as a length scale. In the following formulas the bars over the symbols indicates the normalized and scaled quantities.

The curvilinear coordinate along the void surface (arc length), ℓ, the interconnect with w, and the local curvature, k, that represents the capillary effect are normalized with respect to length scale and the system time, t, is normalized with respect to time scale as shown below:

$$\bar{\ell} = \ell / r_o , \qquad \bar{w} = w / r_o , \qquad \bar{k} = k \, r_o \qquad \text{and} \qquad \bar{t} = t / t_o , \tag{2.4.2}$$

The volumetric Gibbs free energy difference between the realistic void and the bulk phase can be normalized by using the specific Gibbs free energy of the interfacial layer, denoted by g_s ,

$$\bar{g}_{vb} = \frac{\breve{g}_{vb} r_o}{g_s} \tag{2.4.3}$$

The electrostatic potential generated at the void surface may be normalized with respect to the remote applied electric field denoted by E_0 and it is given by

$$\overline{J} = \frac{J}{E_o r_o} \tag{2.4.4}$$

The relative importance of electromigration with respect to capillary forces can be easily represented by a single variable, c , and that may be called as the *electron wind intensity*, as it will be shown later this is a very important experimental parameter in the simulations.

$$c = \frac{e\left|\widehat{Z}\right| E_o r_o^2}{\Omega_s \, g_s} \tag{2.4.5}$$

and similarly one may normalize the generalized mobility $\hat{\mathrm{M}}_{vb}$ associated with the interfacial displacement reaction taking place during the void growth process, $\hat{\mathrm{M}}^{long}$ and $\hat{\mathrm{M}}^{trans}$, which correspond to the longitudinal and transverse triple junction mobilities , with respect to the mobility of the surface diffusion denoted by $\hat{\mathrm{M}}_s$,

$$\overline{\mathrm{M}}_{vb} = \frac{\hat{\mathrm{M}}_{vb} r_o^2}{\hat{\mathrm{M}}_s}, \qquad \overline{\mathrm{M}}^{long} = \frac{\hat{\mathrm{M}}^{long}}{\hat{\mathrm{M}}_s} \qquad \text{and} \qquad \overline{\mathrm{M}}^{trans} = \frac{\hat{\mathrm{M}}^{trans}}{\hat{\mathrm{M}}_s} \tag{2.4.6}$$

where,

$$\hat{\mathrm{M}}^{long} = \frac{\Re^{long}}{kT}\frac{h_g}{\Omega_g} \qquad \text{and} \qquad \hat{\mathrm{M}}^{trans} = \frac{\Re^{trans}}{kT}\frac{h_s}{\Omega_s} \tag{2.4.7}$$

After these normalizations, the normal displacement velocity for the ordinary points can be obtained by using the surface flux, given by Eq. (2.3.1.40), and the incoming net lateral flux density, given by Eq. (2.3.1.41):

$$\bar{v}_{ord} = \frac{\partial}{\partial\bar{\ell}}\left[D''(J,q)\frac{\partial}{\partial\bar{\ell}}\left(\bar{g}_{vb} + c\bar{J} + \bar{k}\right)\right] - \bar{\mathrm{M}}_{vb}\left(\bar{g}_{vb} + \bar{k}\right) \tag{2.4.8}$$

where, the angular dependent post factor $D''(J,q)$ denotes that the surface drift-diffusion is anisotropic.

and the triple junction velocity in the direction along the grain boundary,

$$\bar{v}_g^{long} = \bar{\mathrm{M}}^{long}\,\frac{\bar{\Omega}_g\bar{d}_a}{2\bar{\Omega}_s^2\bar{h}_g}\left[2\,l - \left(\cos q^+ + \cos q^-\right)\right] \tag{2.4.9}$$

with the following boundary conditions at the triple junction in terms of the right and the left side fluxes;

$$\bar{J}_o^+ = \bar{\mathrm{M}}^{long}\,\frac{\bar{d}_a}{2\bar{\Omega}_s^2}\left(l - \cos q^+\right) + \frac{\bar{J}_g}{2} + \bar{J}_J + \bar{\mathrm{M}}^{trans}\,\frac{\bar{d}_a}{2\bar{\Omega}_s^2}\left(\sin q^- - \sin q^+\right) \tag{2.4.10}$$

and

$$\bar{J}_o^- = -\bar{\mathrm{M}}^{long}\frac{\bar{d}_a}{2\bar{\Omega}_s^2}\left(l - \cos q^-\right) - \frac{\bar{J}_g}{2} + \bar{J}_J + \bar{\mathrm{M}}^{trans}\frac{\bar{d}_a}{2\bar{\Omega}_s^2}\left(\sin q^- - \sin q^+\right) \qquad (2.4.11)$$

where $\bar{J}_g$ and $\bar{J}_J$ denote the normalized atomic fluxes associated with the grain boundary flow, and the drift-diffusion due to electromigration, respectively.

The drift-diffusion normalized atomic flux may be given by

$$\bar{J}_J = -\frac{\overline{\mathrm{M}}_{gb}}{\bar{\Omega}_s}\left(\hat{n}_{gb}\cdot\vec{E}\right)c\,\frac{\partial}{\partial\bar{\ell}}\left(\bar{J}\right) \qquad (2.4.12)$$

where $\overline{\mathrm{M}}_{gb}$ is the grain boundary drift diffusion mobility $\hat{n}_{gb}$ is the normal vector along the grain boundary direction and $\vec{E}_o$ is the remote applied electric field vector.

The first group of terms in above partial differential equation (2.4.8) represents a rather conventional approach, which is very popular in the literature, and closely related to the mass accumulation due to surface diffusion along the void interfacial layer. The second group of terms, which appears first time in the literature, is due to the mass flow associated with the chemical species (vacancy flow in opposite direction) transfer between bulk phase and the void region having curved advancing boundary as a reaction front. This additional contribution to the void displacement process is a natural and rigorous out come of the novel application of the irreversible thermodynamics by Ogurtani (2000) to the curved interfaces using a rather realistic concept of surface phases with finite extent as originally proposed by Guggenheim (1959) and Van Der Waals and Baker (1928), rather that the hypothetical Gibbs (1948) description.

In the next chapter the numerical procedures and methods necessary to solve this boundary value problem will be discussed.

CHAPTER 3

MATHEMATICAL MODEL
&
NUMERICAL PROCEDURES

3.1. Introduction

The physical models discussed in this section are two-dimensional. In most applications, such an assumption is physically valid since the thickness of metallisation lines are usually small (≈ 2000 – 5000 Å) compared with the line width and the size of the voids that have become significant in degrading the line structure (< 1 *m*). The only reason to make such an approximation is to simplify the mathematical analysis and also to reduce the computation time.

In Chapter II, after the normalization procedures, the normal displacement velocity for the ordinary points was obtained as

$$\bar{v}_{ord} = \underbrace{\frac{\partial}{\partial\bar{\ell}}\left[D''(J,q)\frac{\partial}{\partial\bar{\ell}}\left(\bar{g}_{vb}+c\bar{J}+\bar{\kappa}\right)\right]}_{\text{Mass accumulation due to the surface diffusion along the void interfacial layer}}\underbrace{-\bar{\mathrm{M}}_{vb}\left(\bar{g}_{vb}+\bar{\kappa}\right)}_{\text{Mass flow associated with the chemical species transfer between the bulk and the void region, having a curved advancing boundary as a reaction front}} \qquad (3.1.1)$$

It should be emphasized that the normalized Gibbs free energy (affinity) of the interfacial reaction with respect to the surface Gibbs free energy denoted as $\overline{g}_{vb}$ is in general not constant, but rather a function of space and time due to any possible compositional variations at the reaction front during the void evolution phenomenon. Therefore, the exact solution of the growth problem, which may be the future objective, still involves the complete numerical solution of the time dependent diffusion equation with drift (convective) term, and coupled to pseudo-static electric field by utilizing proper boundary and initial conditions.

However, for the present situation, namely a void in a thin film interconnect, in which the athermal vacancy concentration is extremely high (super saturation) because of the constant rate of vacancy creation due to the existence of severe internal stresses associated with the bended dislocation network and the thermal mismatch between the interconnect and the substrate material, one may assume that $\overline{g}_{vb}$ is constant of space and time. According to the extensive experimental studies performed by Blech (1976) and his coworkers (Kinsbron *et al.* 1977), at the end of the incubation period the steady state concentration profile established in the sample and over-all drift-diffusion phenomenon is controlled by the interface transfer reactions at the cathode and the anode ends. These observations give very strong indication that the vacancy concentration stays invariant at the advancing void surface layer. Therefore, under any circumstances for gross computer simulations, it is a reasonable approximation to assume that the normalized Gibbs free energy of interfacial reaction stays constant of time and space (isotropic), namely $\nabla\overline{g}_{vb} = 0$. Then Eq. (3.1.1) becomes,

$$\bar{v}_{ord} = \vec{n}\cdot\frac{\partial\bar{r}}{\partial\bar{t}} = \frac{\partial}{\partial\bar{\ell}}\left[D''(J,q)\frac{\partial}{\partial\bar{\ell}}\left(c\bar{J}+\bar{k}\right)\right] - \bar{\mathrm{M}}_{vb}\left(\bar{g}_{vb}+\bar{k}\right) \tag{3.1.2}$$

As they were discussed in chapter 2, the triple junction velocity in the direction along the grain boundary is given by,

$$\bar{v}_g^{long} = \bar{\mathrm{M}}^{long}\frac{\bar{\Omega}_g\bar{d}_a}{2\bar{\Omega}_s^2\bar{h}_g}\left[2l-\left(\cos q^{+}+\cos q^{-}\right)\right] \tag{3.1.3}$$

with the following boundary conditions at the triple junction in terms of the right and the left side fluxes;

$$\bar{J}_o^{+} = \bar{\mathrm{M}}^{long}\frac{\bar{d}_a}{2\bar{\Omega}_s^2}\left(l-\cos q^{+}\right)+\frac{\bar{J}_g}{2}+\bar{J}_J+\bar{\mathrm{M}}^{trans}\frac{\bar{d}_a}{2\bar{\Omega}_s^2}\left(\sin q^{-}-\sin q^{+}\right) \tag{3.1.4}$$

and

$$\bar{J}_o^{-} = -\bar{\mathrm{M}}^{long}\frac{\bar{d}_a}{2\bar{\Omega}_s^2}\left(l-\cos q^{-}\right)-\frac{\bar{J}_g}{2}+\bar{J}_J+\bar{\mathrm{M}}^{trans}\frac{\bar{d}_a}{2\bar{\Omega}_s^2}\left(\sin q^{-}-\sin q^{+}\right) \tag{3.1.5}$$

In the present model, a constant electric field E_o is imposed far away from the void surface, which generates an electrical field denoted by E, having zero normal components at the void – interconnect interfacial layer as well as the upper and lower interconnect boundaries. In this model it is also assumed that at the upper and lower interconnect boundaries the vacancy concentration is kept constant. Figure 3.1.1 shows the schematic representation of the model, which is under discussion.

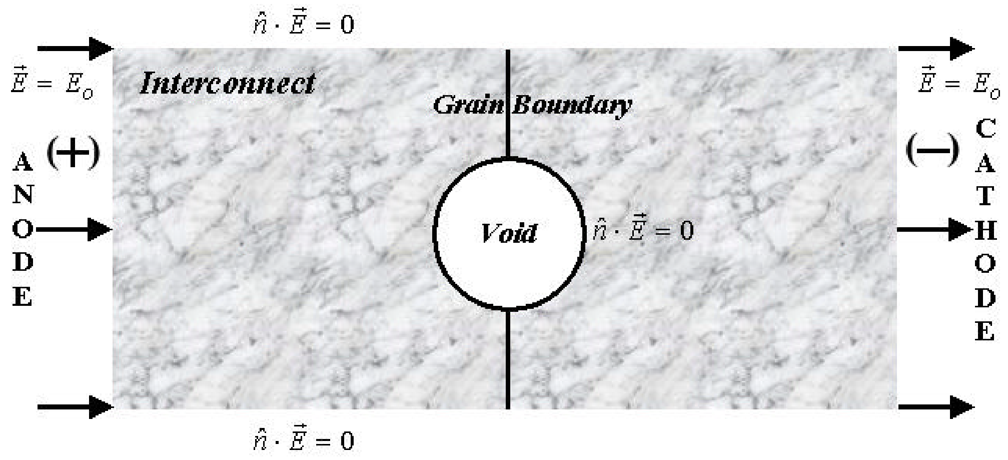

Figure 3.1.1: The schematic representation of the problem.

3.2. Program *“Electromigration”*

In the following subsections the numerical methods are discussed as in the order as the computer program ***“Electromigration”***, which is a *C code*.

i. Preparation of the Initial System

First of all the initial system that is composed of the void surface and the interconnect edges, is simulated by employing hypocycloid algebra in connection with the discretization procedure having a finite number of nodes using predetermined segment lengths. Even thought the used model is two-dimensional, in order to take the advantage of using vector algebra, the system nodes is represented by the three-dimensional vectors described as, $\vec{r}^{\langle i \rangle} = \begin{vmatrix} x \\ y \\ 0 \end{vmatrix}$.

After knowing the node position vectors, it is straight forward to calculate the segment lengths, s, and the centroid position vectors, $\vec{r}_c$, such as:

$$s_i = \left|\Delta\vec{r}^{\langle i\rangle}\right| \quad \text{where} \quad \Delta\vec{r}^{\langle i\rangle} = \vec{r}^{\langle i+1\rangle} - \vec{r}^{\langle i\rangle} \tag{3.2.1}$$

and

$$\vec{r}_c^{\langle i\rangle} = \frac{\vec{r}^{\langle i+1\rangle} + \vec{r}^{\langle i\rangle}}{2} \tag{3.2.2}$$

Figure 3.2.1 shows an example of such an initial system.

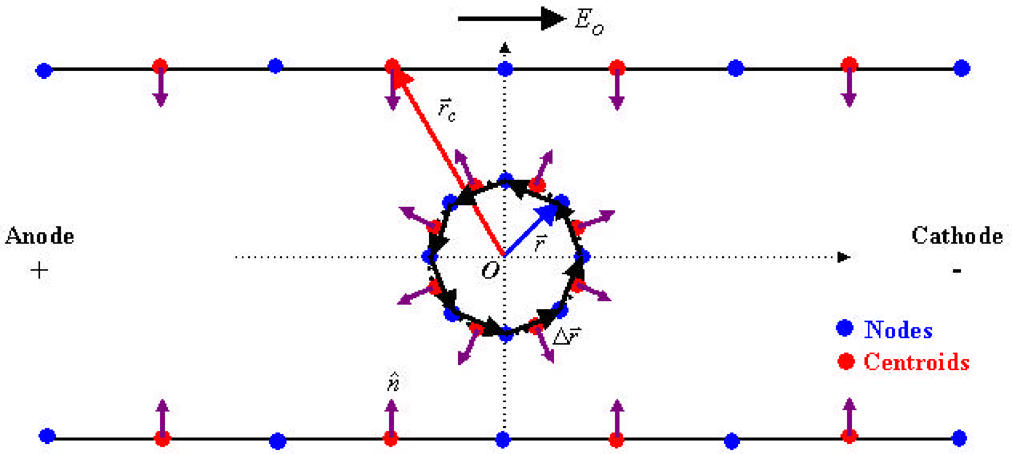

Figure 3.2.1: Example initial system; $\vec{r}^{\langle i\rangle}$ is the node position vector, $\vec{r}_c^{\langle i\rangle}$ is the centroid position vector, $\hat{n}^{\langle i\rangle}$ is the normal vector at the centroids, $\Delta\vec{r}^{\langle i\rangle}$ is the vector that connects the successive nodes and s_i represents the segment lengths.

ii. Calculation of the Turning Angles at the Nodes

The turning angles at the nodes are calculated by using the definitions of the vector and the dot products of the two vectors and the figure 3.2.2.

$$q_i = \begin{cases} \arcsin\left(\dfrac{\Delta\vec{r}^{\langle i\rangle} \times \Delta\vec{r}^{\langle i+1\rangle}}{\left|\Delta\vec{r}^{\langle i\rangle}\right|\left|\Delta\vec{r}^{\langle i+1\rangle}\right|}\right) & \text{if } \Delta\vec{r}^{\langle i\rangle} \cdot \Delta\vec{r}^{\langle i+1\rangle} \geq 0 \\ p - \arcsin\left(\dfrac{\Delta\vec{r}^{\langle i\rangle} \times \Delta\vec{r}^{\langle i+1\rangle}}{\left|\Delta\vec{r}^{\langle i\rangle}\right|\left|\Delta\vec{r}^{\langle i+1\rangle}\right|}\right) & \text{otherwise} \end{cases} \tag{3.2.3}$$

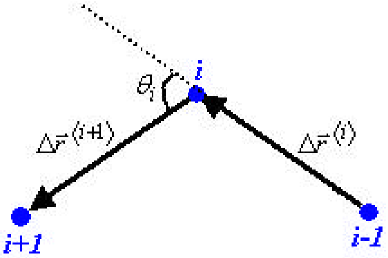

Figure 3.2.2: The segment turning angle, q_i, at the node i.

iii. Calculation of Node Curvatures

The curvatures at the nodes can be evaluated at each node by using a discrete geometric relationship in connection with the fundamental definition of radius of curvature and the normal vector.

Let us define some geometric relationships; first of all the curvature of a circle with radius r_i (radius of curvature) is $1/r_i$ and furthermore three point in the plane define a unique circle whose circumference pass from all of these three points. Figure 3.2.3 shows such a circle that passes from the three successive void nodes $i-1$, i, at which the local curvature is wanted to calculate, and $i+1$ by using the known values of the segment lengths, s_i, and the segment turning angle q_i.

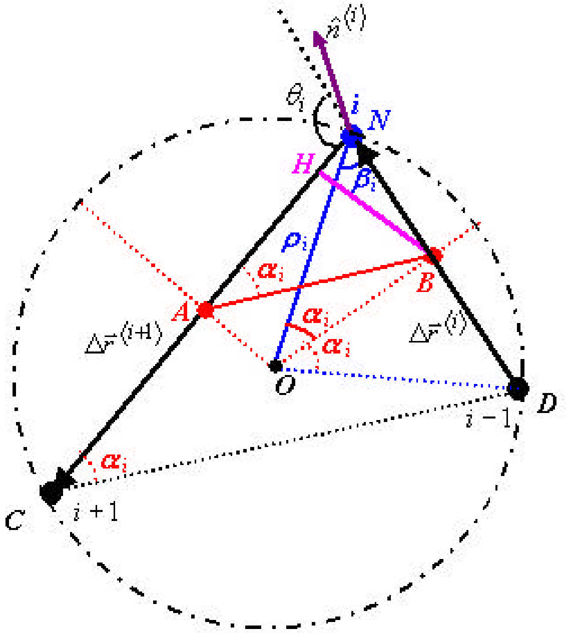

Figure 3.2.3: The unique circle that pass from the three successive void nodes, O is the center of the circle, $s_i = |DN|$, $s_{i+1} = |CN|$, $|OB| \perp |DN|$, $|OA| \perp |CN|$ and $|AB| // |CD| \perp \hat{n}^{\langle i \rangle}$.

From figure 3.2.3 one can immediately write down the following identities.

$$r_i = \frac{s_i}{2\sin(a_i)} \qquad (3.2.4)$$

where a_i is the angle $B\hat{O}N$ and it is very easy to see that this angle also equals to $B\hat{A}N$. Then, the curvature at the node i is given by:

$$k_i = \frac{1}{r_i} = \frac{2\sin(a_i)}{s_i} \tag{3.2.5}$$

In order to calculate the value of the angle a_i, first of all let us calculate the value of the tangent of the angle a_i.

$$\begin{aligned}
\tan(a_i) &= \frac{|BH|}{|AH|} = \frac{|BH|}{|AN| - |HN|} = \frac{|BN|\sin(p - q_i)}{|AN| - |BN|\cos(p - q_i)} \\
&= \frac{|BN|\sin(q_i)}{|AN| + |BN|\cos(q_i)} \\
&= \frac{\frac{1}{2} s_i \sin(q_i)}{\frac{1}{2} s_{i+1} + \frac{1}{2} s_i \cos(q_i)} = \frac{\sin(q_i)}{\frac{s_{i+1}}{s_i} + \cos(q_i)}
\end{aligned} \tag{3.2.6}$$

Using the Eq. (3.2.5) and (3.2.6), the local curvature is given by

$$k_i = \frac{2\sin\left(\operatorname{atan}\left(\frac{\sin(q_i)}{\frac{s_{i+1}}{s_i} + \cos(q_i)}\right)\right)}{s_i} \tag{3.2.7}$$

iv. Calculation of the Local Line Normal Vectors

In order to calculate the normal vectors at the void nodes, let us calculate the value of the angle $O\hat{N}D$; from figure 3.2.3 one can easily write that $b_i = (p\ /2) - a_i$.

Then first multiply $\Delta\vec{r}^{\langle i \rangle}$, which is the vector that connects the successive nodes by the anticlockwise rotation matrix in order to obtain a vector along the local line normal vector as shown below,

$$\vec{n}^{\langle i \rangle} = \begin{vmatrix} \cos(b_i) & \sin(b_i) & 0 \\ \sin(b_i) & \cos(b_i) & 0 \\ 0 & 0 & 1 \end{vmatrix} \cdot \Delta\vec{r}^{\langle i \rangle} \qquad (3.2.8)$$

After that it is straightforward to calculate the local line normal vector namely, $\hat{n}^{\langle i \rangle} = \vec{n}^{\langle i \rangle} / \left|\vec{n}^{\langle i \rangle}\right|$.

v. Calculation of the Electrostatic Potentials by using the Indirect Boundary Element Method solution of the Laplace's Equation

At this point before proceeding further, a brief description of the indirect boundary element method (IBEM) is given, and then by using this method the electrostatic potentials at the void surface and the interconnect edges are calculated.

The boundary element method (BEM) is now a well-established numerical technique for the solution of a wide range of engineering problems. The main advantage of the BEM is its unique ability to provide a complete problem solution in terms of boundary values only (Brebbia and Dominguez, 1992).

An initial restriction of the BEM was that the fundamental solution (FS) to the original partial differential equation was required in order to obtain an equivalent boundary integral equation (Partridge *et al.*, 1992).

There exist two basic types of boundary element method, the indirect and the direct methods (Beer and Watson, 1992). The precursor of the BEM's was the Trefftz method (Brebbia and Dominguez, 1992) in which an approximate solution of the boundary value problem is obtained by the superposition of FS's where the source points are located outside the domain, and it only remains to adjust the intensities of the sources to obtain the best possible agreement between the boundary conditions satisfied by the approximate solution and the actual boundary conditions.

In IBEM the solution is again obtained by the superposition of FS's but instead of the sources being located at a finite number of points outside the domain they are distributed continuously over its boundary. The intensity of the distribution is usually known as the density function (DF). The partial differential equation is automatically satisfied at every interior point of the domain, and the only thing that is required is to satisfy the boundary conditions by the suitable choice of the DF. Once the DF has been solved, physically meaningful results at boundary and interior points of the domain are computed by integration over the boundary.

In this problem one is seeking the solution of a Laplace equation in a two dimensional domain that is given by the following equation

$$\nabla^2 J(r) = 0 \tag{3.2.9}$$

with the following boundary conditions, namely Neumann boundary conditions,

$$\hat{n} \cdot \nabla J(r) = \hat{n} \cdot \frac{\partial J(r)}{\partial r} \hat{r} = 0 \tag{3.2.10}$$

where the scalar function $J(r)$ is the electrostatic potential at the boundaries.

For a two dimensional problem, the source is assumed to be distributed along a line of infinite length from $z = -\infty$ to $z = \infty$ and the fundamental solution $U(P,Q)$, which satisfies the Laplace equation and represents the field generated by a concentrated unit charge at *P (source point)* acting at a point *Q (field* or *observation point)*, is given by (Paris and Canas, 1997):

$$U(P,Q) = \frac{1}{2p} \ln \frac{1}{r} \tag{3.2.11}$$

where r is the distance from source point to field point. Figure 3.2.4 shows the variation of the FS for the two-dimensional potential problems, at which the source is at the origin.

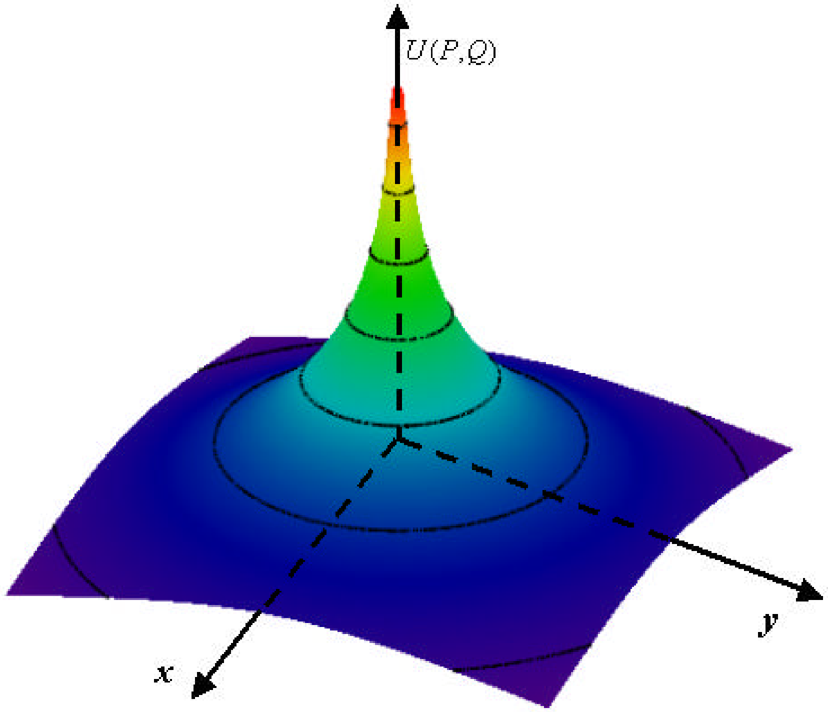

Figure 3.2.4: Graph of the FS of Laplace equation for two-dimensional problems.

By using the FS, given in Eq. (3.2.11), the directional derivative of the FS, which satisfy Laplace equation, can be obtained as,

$$\begin{aligned} T(P,Q) &= \hat{n}\cdot\nabla U(P,Q) = \hat{n}\cdot\frac{\partial U(P,Q)}{\partial r}\hat{r} = \hat{n}\cdot\frac{\partial U(P,Q)}{\partial r}\frac{\vec{r}}{|\vec{r}|} \\ &= -\frac{1}{2p|\vec{r}|}\hat{n}\cdot\frac{\vec{r}}{|\vec{r}|} = -\frac{1}{2p}\frac{|\hat{n}||\vec{r}|\cos(q)}{|\vec{r}|^{2}} \\ &= -\frac{1}{2p}\frac{\cos(q)}{|\vec{r}|} \end{aligned} \tag{3.2.12}$$

where q is the angle between the line QP and the outward normal $\hat{n}$ as shown in figure 3.2.5. Figure 3.2.6 shows the variation of the directional derivative of FS where the flow is in the x direction.

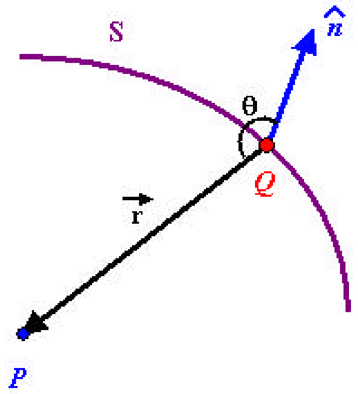

Figure 3.2.5: Notation for the FS of Laplace Equation.

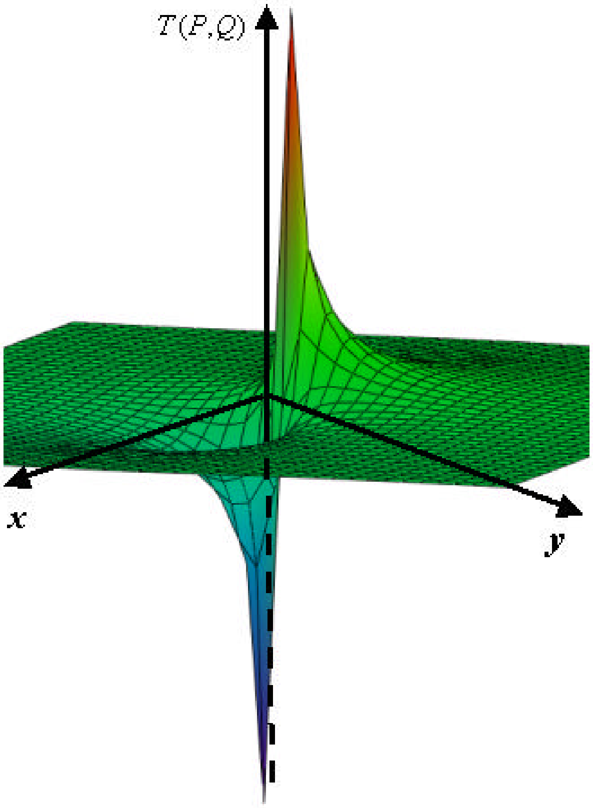

Figure 3.2.6: Graph of the directional derivative of FS for two-dimensional problems.

In the IBEM, one seeks a solution in the form of

$$u(Q) = \int_S U(P,Q)m(P)dS_P \qquad (3.2.13)$$

where the density function $m(P)$ is the intensity of sources, which are continuously distributed over the boundary S of the domain. In two-dimensional problems, dS means with respect to arc length. The subscript $_P$ means that in the integration the point moves over the boundary whilst the point Q stays still. Since $U(P,Q)$ satisfies the governing partial differential equation everywhere except at P, $u(Q)$ as defined by Eq. (3.2.13) satisfies the differential equation at all interior points of the domain, but not on its surface S. Eq. (3.2.13) is referred to as the integral representation.

At this point the only thing that must be satisfied is the boundary conditions. When considering how to do this, it should be borne in mind that the solution must satisfy the governing partial differential equation at all points inside the domain and also on the surface S. The integral representation does not do this, and it follows that for the Neumann boundary conditions it is necessary to equate the limiting values as Q on S is approached from inside the domain of $u(Q)$ and $\hat{n} \cdot \nabla u(Q)$ as defined by Eq. (3.2.13) to the given boundary data.

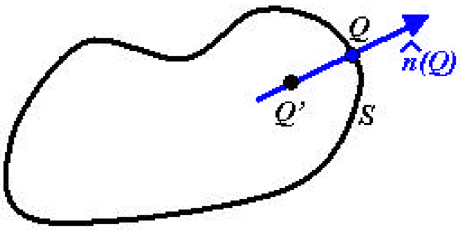

Figure 3.2.7: Satisfaction of boundary condition in the IBEM

For the Neumann condition, one must set the limiting value as *Q'* approaches *Q* (figure 3.2.7) of the derivative in the direction $n(Q)$ of $u(Q')$ as defined by Eq. (3.2.13) to its given value $\bar{t}(Q)$. The function $U(P,Q')$ is bounded and so it is permissible to differentiate under the integral sign:

$$\begin{aligned}\hat{n}\cdot\nabla u(Q) &= \int_S \hat{n}\cdot U(P,Q)m(P)dS_P \\ &= \int_S T(P,Q)m(P)dS_P\end{aligned} \qquad (3.2.14)$$

Where $T(P,Q')$ is given by Eq. (3.2.12)

One may now write

$$\lim_{Q'\to Q}\frac{\partial u}{\partial n}(Q') = \bar{t}(Q) \qquad (3.2.15)$$

To illustrate the behavior of the function $\partial u/\partial n(Q')$ as *Q'* approaches and passes through *S* at *Q'* let us take *Q* to be on a straight part of the boundary of a two-dimensional domain, and let us suppose that over this straight part of the boundary $m(P)$ is constant and therefore equal to $m(Q)$. $S(Q,n)$ denotes the straight part AB of the boundary as shown in figure 3.2.8, where e denotes the distance QQ'.

$$\frac{\partial u}{\partial n}(Q') = I_1(Q') + I_2(Q') \qquad (3.2.16)$$

where

$$I_1(Q') = \int_{S(Q,n)} T(P,Q')m(P)dS_P \tag{3.2.17}$$

and

$$I_2(Q') = \int_{S-S(Q,n)} T(P,Q')m(P)dS_P \tag{3.2.18}$$

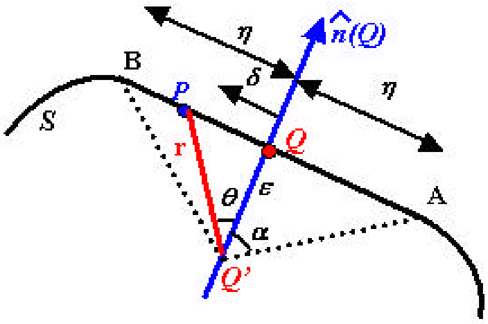

Figure 3.2.8: Limit of integral over *AB* as *Q'* approaches *Q*

The function $I_2(Q')$ varies continuously as *Q'* approaches and passes through S. When *Q'* is inside the domain as shown in figure 3.2.8,

$$I_1(Q') = \int_{-n}^{n} \frac{\cos q}{2pr} m(P)ds = m(Q)\int_{-a}^{a} \frac{1}{2pr} dq \tag{3.2.19}$$

where $a = \tan^{-1}\frac{n}{e}$. By integrating and substituting limits one finds that

$$I_1(Q') = m(Q)\frac{a}{p} \tag{3.2.20}$$

and so since a tents to $p/2$ as Q' approaches Q,

$$\lim_{Q'\to Q} I_1(Q') = \frac{1}{2}m(Q) \tag{3.2.21}$$

When Q' is at Q, $T(P,Q') = 0$ for all P in $S(Q,n)$, and so $I_1(Q) = 0$. Therefore,

$$\lim_{Q'\to Q} \frac{\partial u}{\partial n}(Q') = \int_S T(P,Q)m(P)dS_P + \frac{1}{2}m(Q) \tag{3.2.22}$$

Substituting this result into Eq.3.2.15 gives

$$\frac{1}{2}m(Q) + \int_S T(P,Q)m(P)dS_P = \bar{t}(Q) \tag{3.2.23}$$

which is the integral equation for the Neumann boundary condition.

For the purpose of numerical analysis there is a significant restriction that is the point Q can not be located at an edge or corner, or at any point at which $\bar{t}(Q)$ is discontinuous. Edges and discontinuous $\bar{t}(Q)$ occur frequently in engineering analysis. As the point P on S approaches Q, for two-dimensional case it remains bounded. It should be borne in mind however that in the analysis is leading to this conclusion it is supposed that $m(Q)$ is bounded and indeed continuous, whereas analogy with the distribution of electrical charge over a conducting surface suggest that edges, corners and discontinuities of $\bar{t}(Q)$. The generality of the method may therefore be greater than that suggested by existing mathematical analysis.

In the simplest implementation of the IBEM of solution of Laplace's equation, the boundary S is represented by straight-line elements in two dimensions, and it is supposed that over each of these elements $m(Q)$ is constant. Simultaneous equations for the value of $m(Q)$ are obtained by taking point Q in Eq. (3.2.13) to be located at the centroid of each of these elements in turn. Let there be N elements $S_1, S_2, \ldots, \mathrm{S_N}$, then for the present problem, the simultaneous equations are

$$\frac{1}{2}m(Q_i)+\sum_{j=1}^{N}\Delta T_{ij}\, m(Q_j)=\bar{t}m(Q_i), \qquad i=1, 2, \ldots, N \tag{3.2.24}$$

where

$$\Delta T_{ij} = \int_{S_j} T(P_j, Q_i)\, dS_{p_j} \tag{3.2.25}$$

Since in Eq. (3.2.24) the point Q_i is at the centroid of an element, the surface smoothness condition for validity of that equation is always satisfied.

For a finite domain, the matrix of equation coefficients is singular in the limit as the number of elements tends to infinity and it is necessary for example to take $u(Q)$ to be zero at one of the elemental centroids; Eq. (3.2.24) is then written at that centroid and at all the others. For an infinite domain, the integral representation can model at infinity $u(Q) = \ln \frac{1}{r_o} \int_S m(P) dS_p$ where r_o is distance from an arbitrary chosen reference point in two dimensions, but not a non-zero constant value. Therefore, the solution of the Neumann boundary value problem, and the matrix of equation coefficients are not singular in the limit as the number of elements tends to infinity.

It is possible to evaluate analytically the integral ΔT_{ij}: note that since the elements are straight, $T(P_i, Q_i) = 0$ everywhere on the element S_i and so in Eq. (3.2.14), $\Delta T_{ii} = 0$ and leading diagonal coefficients all equal ½. The matrix coefficients of Eq. (3.2.24) are dimensionless in the sense that they have the same numerical values regardless of the choice of the unit of distance.

Here let us turn back to the problem at which the direction of the applied electric field is in the positive x direction.

Now let us seek a solution as the sum of two parts, these being the electrostatic potential due to applied electric field that would exist if the void were not there, and a perturbation of that solution chosen so that the sum of the two parts satisfies the boundary conditions.

$$J(r) = J^{\mathrm{I}}(r) + J^{\mathrm{II}}(r) \tag{3.2.26}$$

The boundary condition given by Eq. (3.2.10) indicates that the electric field at the boundary along the boundary normal direction is zero.

$$\begin{aligned} \mathrm{E}(Q) &= -grad(J(Q)) \\ &= -grad(J^{\mathrm{I}}(Q)) - grad(J^{\mathrm{II}}(Q)) = \mathrm{E}^{\mathrm{I}}(Q) + \mathrm{E}^{\mathrm{II}}(Q) = 0 \end{aligned} \tag{3.2.27}$$

For the present problem; if there is no void inside the interconnect the electrostatic potential that corresponds the electrostatic applied voltage along the negative x direction according to the coordinate system shown in figure 3.2.9, is given by

$$J^{\mathrm{I}}(Q) = -E_o x = -E_o \vec{r} \cdot \left|\begin{matrix}1\\0\\0\end{matrix}\right| = -E_o r \cos(f) \tag{3.2.28}$$

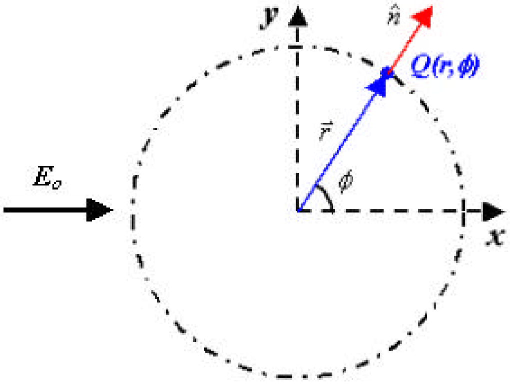

Figure 3.2.9: Coordinate system

From the solution in Eq. (3.2.27), the normal component of the electric field on the boundaries may be calculated as

$$\mathrm{E}^{\mathrm{I}}(Q) = -grad(J^{\mathrm{I}}(Q)) = -\hat{n}\cdot\nabla J^{\mathrm{I}}(Q) = -E_0 \cos(f) \tag{3.2.29}$$

By comparing the Neumann boundary conditions given in Eq. (3.2.27) and the Eq. (3.2.29) it is found that the normal component of the electric field due to the fictitious charges distributed along the boundaries have to be given by

$$\mathrm{E}^{\mathrm{II}}(Q) = -\mathrm{E}^{\mathrm{I}}(Q) = E_0 \cos(f) \tag{3.2.30}$$

Now the problem is to adjust the magnitude of the fictitious charges, denoted by m_i, such that to satisfy the Eq. (3.230) in order to satisfy the boundary conditions. Noting that the normal derivative of the FS is $T(P,Q)$, the boundary condition at the point Q_i can be satisfied by using the Eq. (3.2.24).

$$\frac{1}{2}m(Q_i) + \sum_{j=1}^{N} \Delta T_{ij}\, m(Q_j) = \mathrm{E}^{\mathrm{I}}(Q_i), \tag{3.231}$$

where N is the number of charges and $\Delta T_{ij} = \Delta T(P_i, Q_j)$ and it may be calculated by using the integral given by the Eq. (3.2.25). After finding the charge distribution that satisfy the boundary conditions the $J^{\mathrm{II}}(Q)$ can be calculated as

$$J^{\mathrm{II}}(Q_i) = \sum_{j=1}^{N} \Delta U_{ij}\, m(Q_j), \tag{3.2.32}$$

where $\Delta U_{ij} = \Delta U(P_i, Q_j)$ and it may be calculated by using the following integral

$$\Delta U_{ij} = \int_{S_j} U(P_j, Q_i)\, dS_{p_j} \tag{3.2.33}$$

These integrals can be calculated numerically by using the trapezoidal rule. By using the notation in figure 3.2.10 and assuming that the charge density function at a given segment distributed uniformly, the formulas for $\Delta T_{i,j}$ and $\Delta U_{i,j}$ may be found as,

$$\begin{aligned}
\Delta T_{i,j} &= \int_{s_j} \frac{\cos(q)}{2pr} ds_j = \frac{1}{2p} \sum_{k=0}^{m-1} \frac{1}{2} \left(\frac{\cos(q_{k+1})}{r_{k+1}} + \frac{\cos(q_k)}{r_k} \right) \Delta s_k \\
&= \frac{\Delta s}{2p} \left[\frac{1}{2} \left(\frac{\cos(q_0)}{r_0} + \frac{\cos(q_m)}{r_m} \right) + \sum_{k=1}^{m-1} \frac{\cos(q_k)}{r_k} \right] \\
&= \frac{s_j}{2pm} \left[\frac{1}{2} \left(\frac{\hat{n}_j \cdot \vec{r}_0}{|\vec{r}_0|^2} + \frac{\hat{n}_j \cdot \vec{r}_m}{|\vec{r}_m|^2} \right) + \sum_{k=1}^{m-1} \frac{\hat{n}_j \cdot \vec{r}_k}{|\vec{r}_k|^2} \right]
\end{aligned} \tag{3.2.34}$$

and

$$\begin{aligned}
\Delta U_{i,j} &= \int_{s_j} \frac{1}{2p} \ln \frac{1}{r} ds_j = \frac{1}{2p} \sum_{k=0}^{m-1} \frac{1}{2} \left(\ln \frac{1}{r_{k+1}} + \ln \frac{1}{r_k} \right) \Delta s_k \\
&= \frac{\Delta s}{2p} \left[\frac{1}{2} \left(\ln \frac{1}{r_0} + \ln \frac{1}{r_m} \right) + \sum_{k=1}^{m-1} \ln \frac{1}{r_k} \right] \\
&= -\frac{s_j}{2pm} \left[\frac{1}{2} \left(\ln|\vec{r}_0| + \ln|\vec{r}_m| \right) + \sum_{k=1}^{m-1} \ln|\vec{r}_k| \right]
\end{aligned} \tag{3.2.35}$$

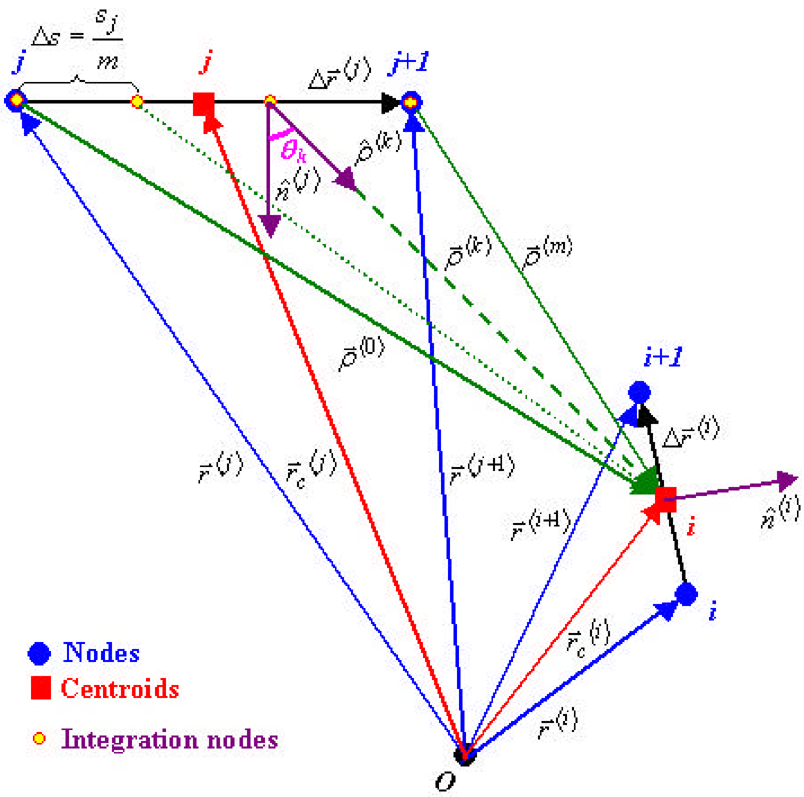

Figure 3.2.10: Segment division for the numerical integration, m_d is the number of division.

The vector $\mathrm{E}^{\mathrm{I}}{}_i = \mathrm{E}^{\mathrm{I}}(Q_i)$ can be calculated by using the Eq. (3.2.29) and then one obtains the following system of simultaneous equations, which can be solved for the unknown fictitious charges m_i.

$$\Delta T_{i,j} \cdot m_i = \mathrm{E}_i^{\mathrm{I}} \tag{3.2.34}$$

The nodes described in this problem contains three different set at each of which the centroids are continuous. These are the upper interconnect edge (UIE), the lower interconnect edge (LIE) and the void circumference (VC), whose number of centroids are denoted by n_u, n_l and n_v respectively. Then the connectivity matrix is given in the figure 3.2.11, where $n_{ul} = n_u + n_l$ and $n_{ulv} = n_u + n_l + n_v$.

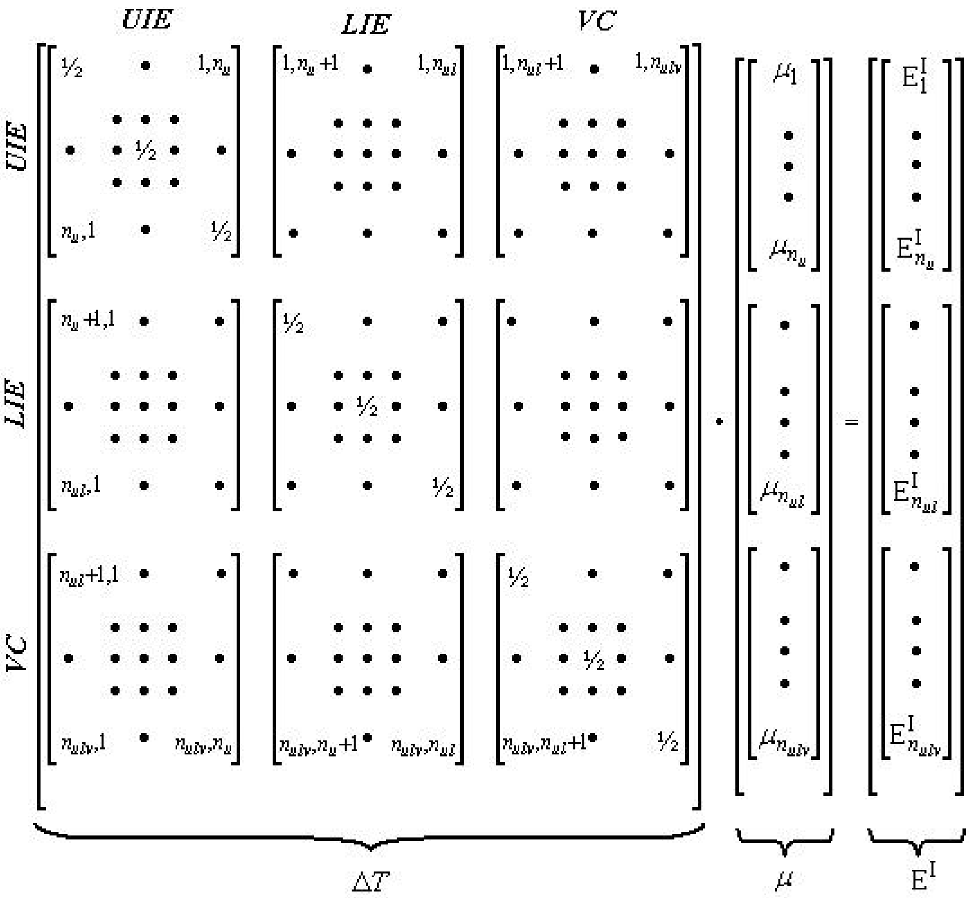

Figure 3.2.11: The connectivity matrix

For the solution of above linear system, Gaussian elimination with back substitution method is performed. Also in this method a pivoting strategy is applied for the error reduction (Mathews, 1992).

In order to test the validity of the IBEM solution, it was assumed that there is a circular void, inside interconnect with an infinite width, and the charge distribution around the void circumference, whose analytical solution is known and given by the Eq. (3.2.35), was calculated.

$$m(f) = -2\cos(f) \tag{3.2.35}$$

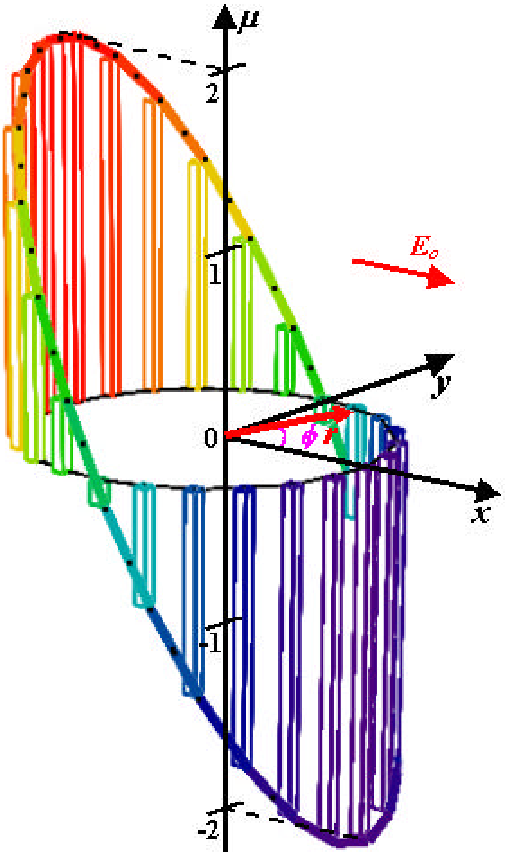

Figure 3.2.12: Charge distribution around a circular void. Bar plot indicates the IBEM solution and the solid line is the analytic al solution.

When one compares the numerical and analytical solutions, which may be seen in figure (3.2.12), there is a perfect match between these two solutions.

After checking the IBEM solution let us continue to go over the program ***"Electromigration"***.

vi. Calculation of Anisotropic Surface Diffusivity

The anisotropic diffusivity of surface atoms is incorporated into the numerical procedure by adapting the following relationship,

$$\tilde{D}_s\,(q\,,f\,) = D_s^o\left\{1 + \mathrm{A}\cos^2\left[m(q - f\,)\right]\right\} \tag{3.2.36}$$

where D_s^0 is the minimum surface diffusivity corresponding to a specific surface orientation, q is the angle formed by the local tangent to the surface and the direction of the applied electric field. A , *m*, and f are dimensionless parameters that determine the strength of the anisotropy, the grain symmetry through the number of crystallographic directions that corresponds to fast diffusion paths, and the misorientation of the symmetry direction with respect to the direction of the applied electric field E_o, respectively. For brevity this angular dependent part of the diffusivity in above equations is denoted by $D''(q\,,f\,)$. Where $N = 2m$ corresponds to the rotational degree of symmetry or fold-number.

The following figures are obtained by using Eq. (3.2.36), in which the minimum surface diffusivity is taken as unity namely $D_s^o = 0$.

Figures 3.2.13 and 3.2.14 shows the diffusion anisotropy of a crystal with a two-fold symmetry where the anisotropy strength is $\mathrm{A} = 5$ and the misorientation angles are $f = 0$ and $f = p\,/\,6$ respectively.

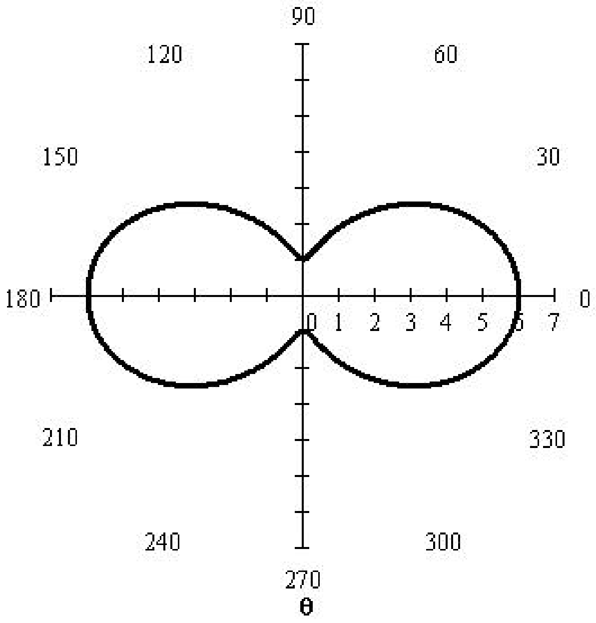

Figure 3.2.13: Diffusion Anisotropy, $D_s^0 = 1$, A = 5, $m = 1$ and $f = 0$

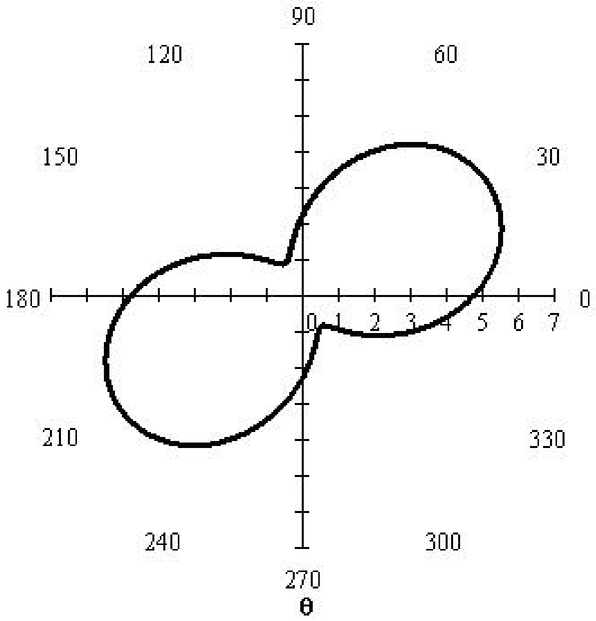

Figure 3.2.14: Diffusion Anisotropy, $D_s^0 = 1$, A = 5, $m = 1$ and $f = p / 6$

Figures 3.2.15 and 3.2.16 show that the diffusion anisotropy of a crystal with a four-fold symmetry where the misorientation angle is $f = 0$ and the anisotropy strengths are $\mathrm{A} = 5$ and $\mathrm{A} = 3$, respectively.

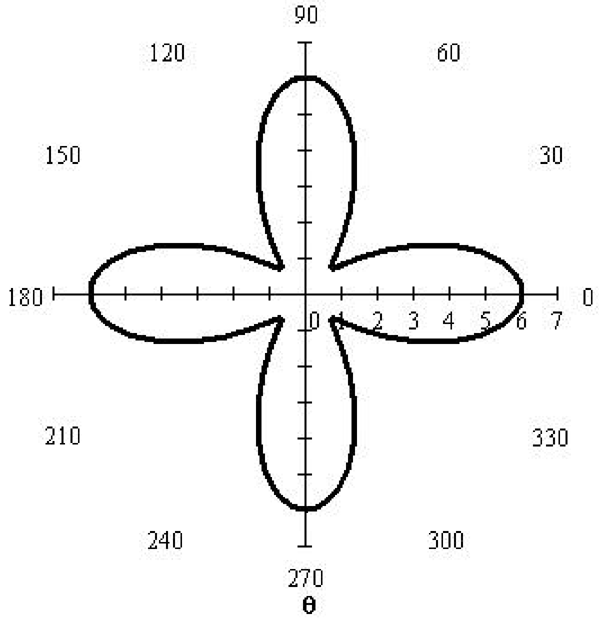

Figure 3.2.15: Diffusion Anisotropy, $D_s^0 = 1$, $\mathrm{A} = 5$, $m = 2$ and $f = 0$

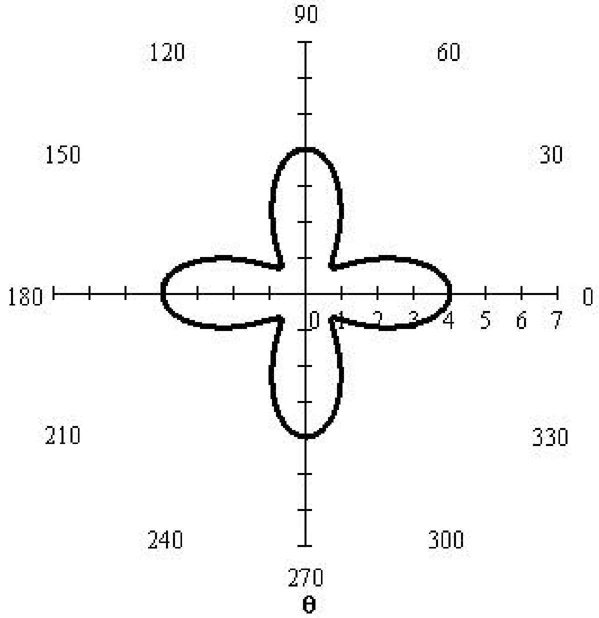

Figure 3.2.16: Diffusion Anisotropy, $D_s^0 = 1$, $\mathrm{A} = 3$, $m = 2$ and $f = 0$

Figure 3.6.17 shows that the diffusion anisotropy of a crystal with a six-fold symmetry where the misorientation angle is $f = 0$ and the anisotropy strength is $\mathrm{A} = 5$.

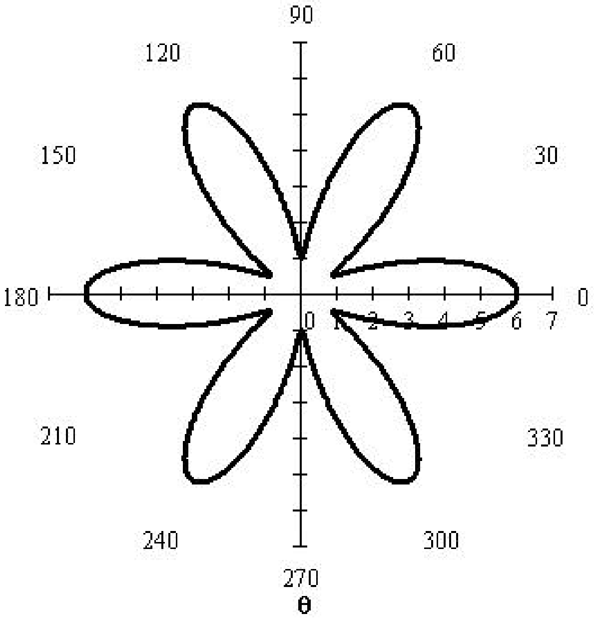

Figure 3.2.17: Diffusion Anisotropy, $D_s^0 = 1$, $\mathrm{A} = 5$, $m = 3$ and $f = 0$

vii. Explicit Euler's Method

Explicit Euler's method (Mathews, 1992) is used to perform the time integration of Eq. (3.1.2) for the void profile evolution. The time step is determined from the maximum surface velocity such that the displacement increment is kept constant for all time step increments. This so-called adapted time step auto-control mechanism combined with the self-recovery effect associated with the capillary term guarantees the long time numerical stability and the accuracy of the explicit algorithm even after performing several hundred to several millions steps.

viii. Remeshing

As it can be seen from the figure 3.2.18 that the void profile experiences a large-scale evolution during the numerical simulations.

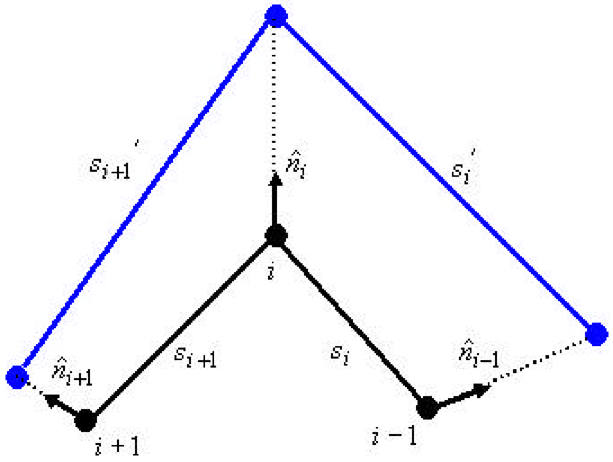

Figure 3.2.18: Void profile evolution, i represents the node number, $\hat{n}_i$ is the local line normal, s_i denotes the segment length between the nodes $i-1$ and i and the primes over the segment lengths indicates the future.

In the present study the numerical methods require that the segment lengths must not be exceeded a critical value in order to keep the accuracy in an acceptable level. And also as the number of nodes increase the computation time is also increases. These two statements require that the segment lengths must be keep in a range between the minimum and the maximum segment lengths, $[s_{\min}, s_{\max}]$, in terms of a prescribed percentage of the mean distance.

If the distance between any two neighboring nodes becomes longer than $s_{\max}$, then the mid-point is converted into a node as illustrated in figure 3.2.19.a.

Similarly, if the distance between any two neighboring nodes becomes shorter than $s_{\min}$, then the further node is removed from the mesh and the new segment is formed as illustrated in figure 3.2.19.b. After such a node removal process the new segment length has t o be controlled whether it is longer than $s_{\max}$ or not.

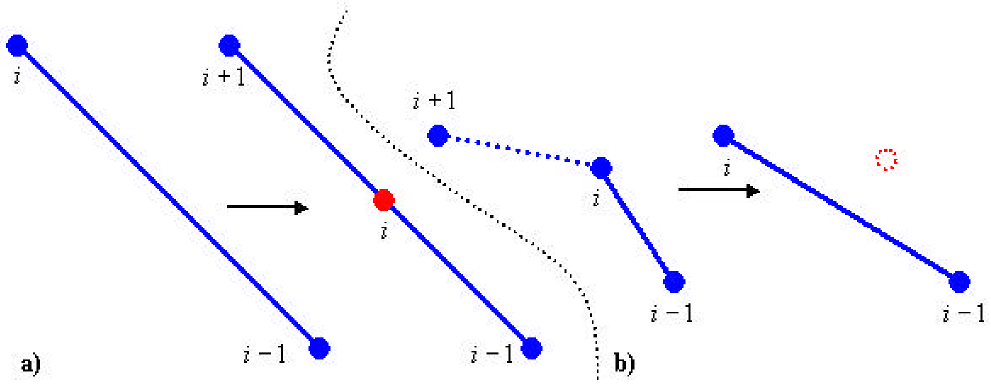

Figure 3.2.19: Remeshing, **a)** The segment length is bigger than the maximum allowable segment length **b)** The segment length is smaller than the minimum allowable segment length

ix. The flowchart of the Program "*Electromigration*"

After explaining the numerical methods used in the program ***"Electromigration"***, let us define the all program as a flowchart, which can be seen in Figure 3.3.1.

The definitions of the input parameters used in the program can be found in the Appendix A.

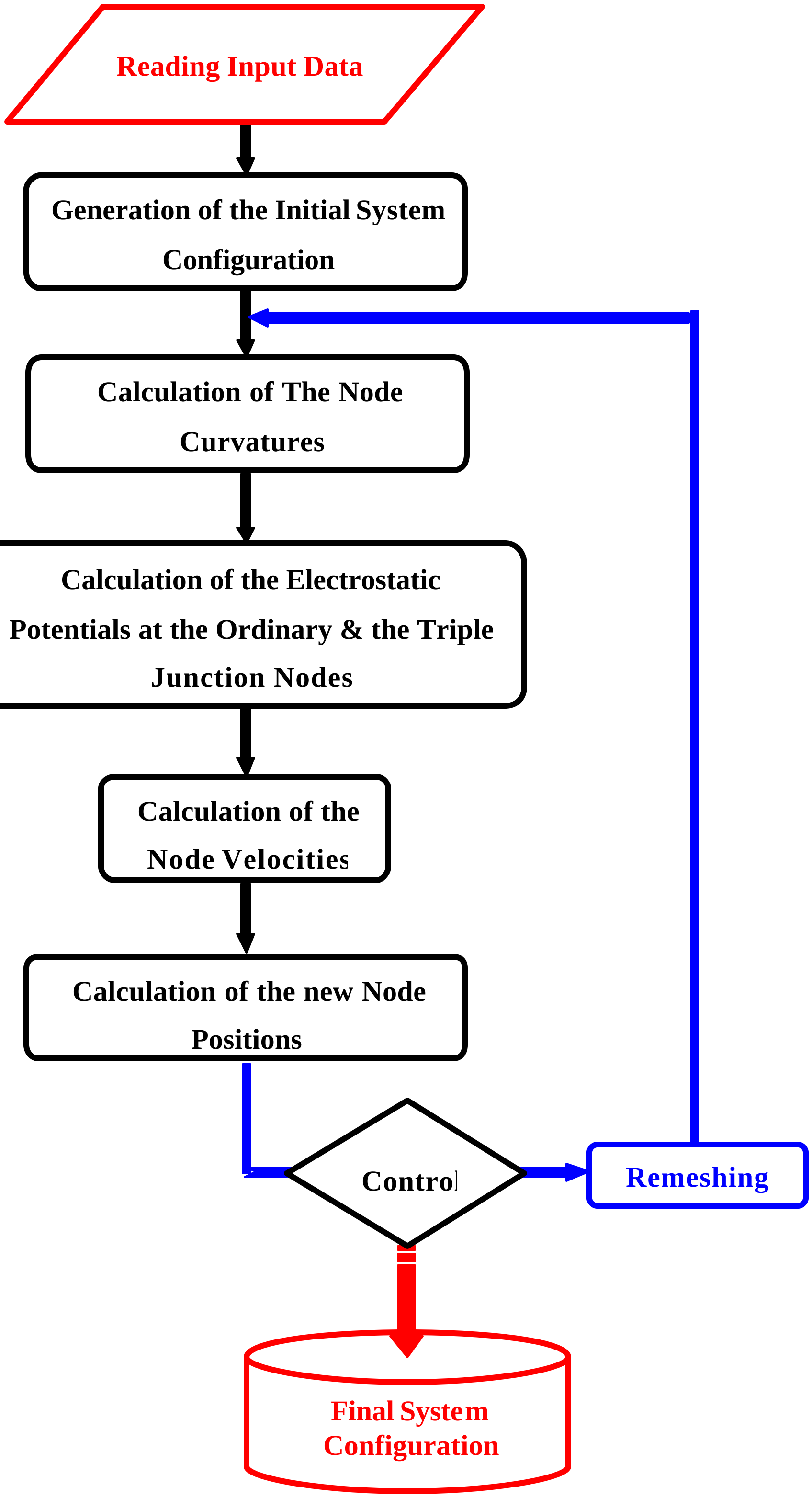

Figure 3.2.20: Program flow chart.

CHAPTER 4

RESULTS AND DISCUSSION

In this chapter, a detailed classification of electromigration induced void morphological evolution of intra- and inter-granular voids in metallic thin films are presented by using the outputs of the program “*Electromigration*”.

The effect of normalized interconnect with and the electron wind intensity on the electrostatic field distribution along the void circumference, which is shown in figure 4.1, is investigated by using the IBEM calculations.

Figure 4.2 shows the electrostatic field distribution along the void circumference for different normalized interconnect widths, when the normalized electron wind intensity is kept constant at $c = 1$. In figure 4.2, the letters A, B, C and D correspond to the points on the void circumference represented by the same letters as shown in figure 4.1.

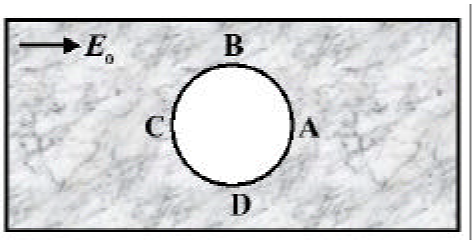

Figure 4.1: Schematic representation of the system.

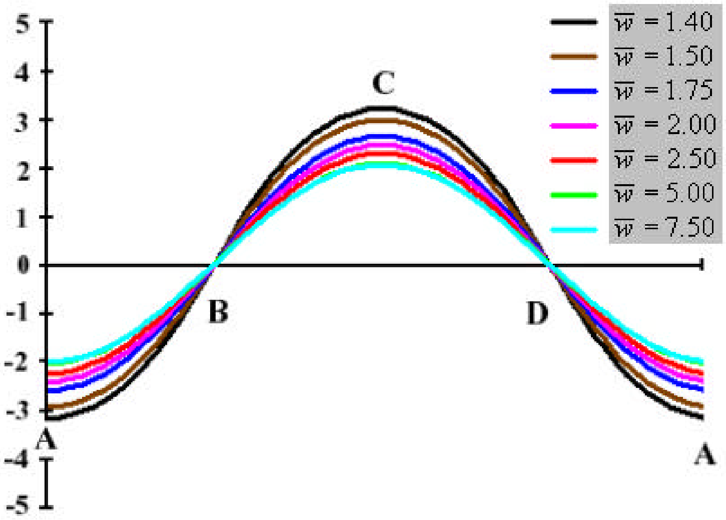

Figure 4.2: Electrostatic field distributions along the void circumference for different normalized interconnect widths. The electron wind intensity: $c = 1$.

From figure 4.2 it may be said that, when the normalized interconnect width is $\overline{w} \geq 5$, the effect of current crowding on the shape evolution may be partially avoided.

Figure 4.3 shows the electrostatic field distribution along the void circumference for different normalized electron widths when the normalized interconnect width is kept constant at $\overline{w} = 1.4$. Similarly in this figure the letters A, B, C and D correspond to the points on the void circumference represented by the same letters as shown in figure 4.1.

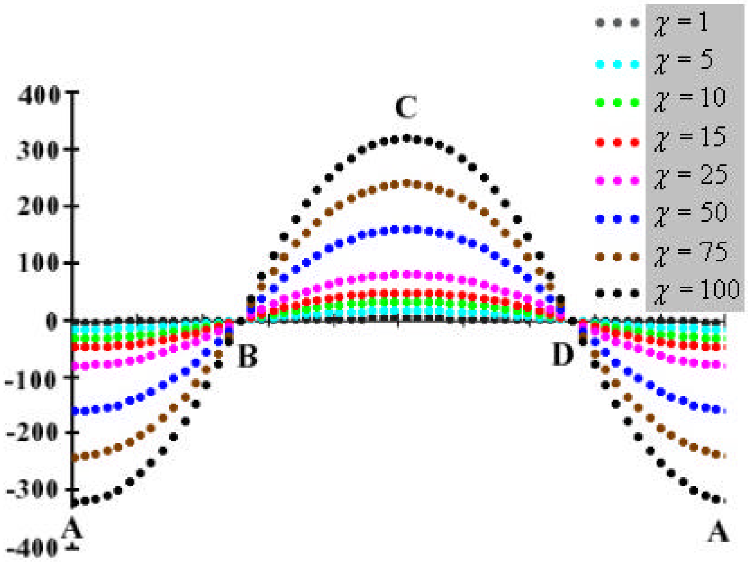

Figure 4.3: Electrostatic field distribution along the void circumference for different electron wind intensities. The normalized interconnect width: $\overline{w} = 1.4$.

4.1. Void Intra-granular Motion

4.1.1. Isotropic Surface Diffusivity

i. Without Void Growth Mechanism

In order to see how the void dynamic proceeds, and what types of final configurations can be generated at the absence of the diffusion anisotropy and the interface controlled growth process, two distinct experiments have been performed utilizing critical and uncritical-asymmetric void shapes.

In figure 4.1.1.1, the initial shape of the void is uncritical, and there is a formation of a new or daughter void in front of the advancing parent. In the case of a critical void the crescent-like slit formation occurs as shown in figure 4.1.1.2, rather than the transverse wedge or slit shape generation, which could produce failure. These experiments do not give any indication of open circuit failure other than some deterioration at the interconnect edges in the absence of void growth and anisotropy in the surface diffusion. The effects of various initial void forms under the large range of electron wind intensities have been investigated recently by Oren (2000-a and 2000-b) and Oren and Ogurtani (2001), who prove that the electromigration phenomena is highly non-linear that is strongly dependent upon the initial state of the system.

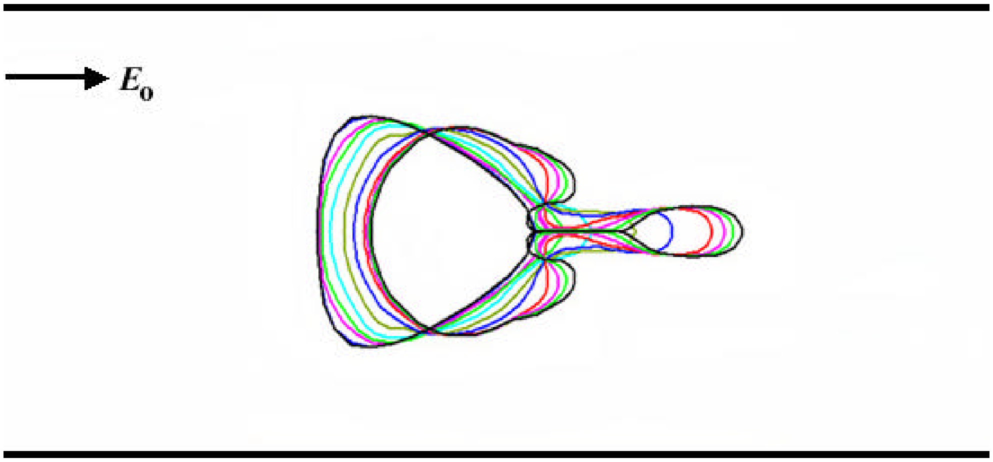

Figure 4.1.1.1: Void morphology evolution for an *Un-critical* initial void configuration under the *Isotropic* surface diffusion conditions without growth process. $c = 100$. Scaled strip width $\overline{w} = 2$.

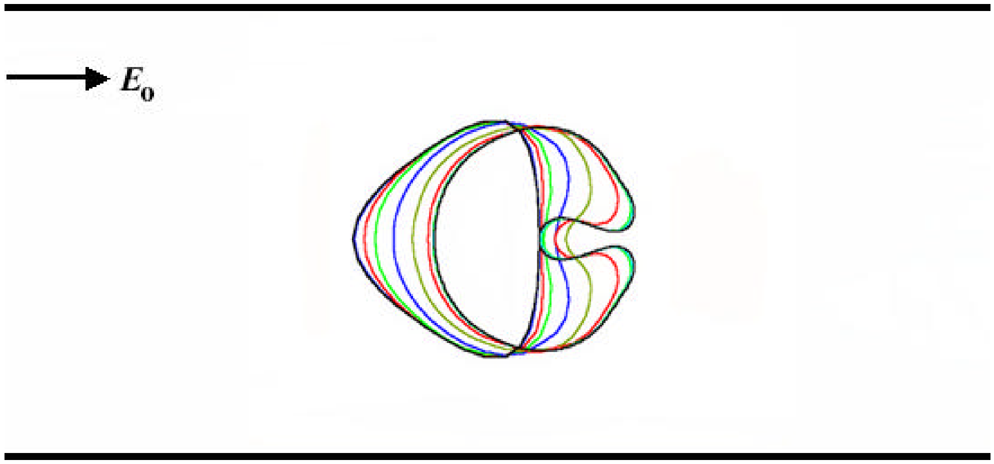

Figure 4.1.1.2: Void morphology evolution for a *Critical* initial void configuration under the *Isotropic* surface diffusion conditions without growth process. Electron wind intensity $c = 100$. Scaled strip width $\overline{w} = 2$.

ii. With Void Growth Mechanism

The effect of the interface controlled growth process, which involves not only the Gibbs free energy of reaction but also the local curvature in connection with the specific surface Gibbs free energy, has been investigated and the representative result obtained is presented in figure 4.1.1.3.

It should be mentioned that, Kraft and Arzt (1997) has also considered the growth process in their extensive simulation studies, by adapting self-similar enlargement of the void with a constant rate of growth. Unfortunately, this ad hoc procedure, which does not take into account the capillary effect through the curvature term, has not been successful in generating any unusual morphological outbreak such as the actual laboratory observations on the real samples.

In this experiment, one has still employed uncritical shape in connection with the isotropic surface diffusion. This figure shows formation of a rather interesting morphology, especially when void is situated at the center of an interconnect, namely first an appearance of a single slit-like void shape at intermediate observation time, and then the evolution towards the dendritic structure (multi-slit) after having a prolong exposure times, rather than giving a fragmentation phenomenon as in the case of figure 4.1.1.1. In this experiment a high normalized electron wind intensity such as $c = 100$ is employed in order to scale down the normalized observation time.

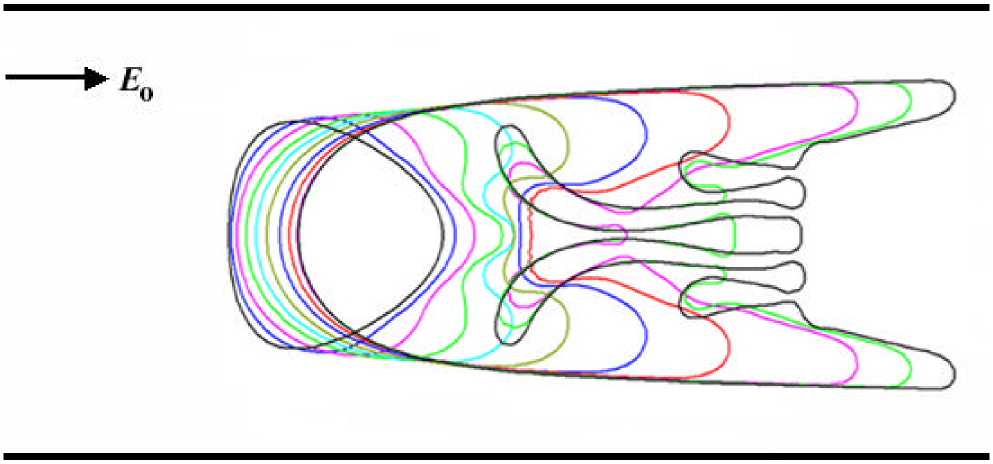

Figure 4.1.1.3: Void morphology evolution (Dendritic Structure) for an *Un-critical* initial void configuration under the *Isotropic* surface diffusion and *Void Growth* conditions ($\Delta\bar{g}_{vb} = -10$, $\bar{M}_{vb} = 10$). Electron wind intensity $c = 100$. Scaled strip width $\bar{w} = 2$.

4.1.2. Anisotropic Surface Diffusivity

Surface diffusion anisotropy is determined by the variation of surface diffusivity with surface orientation and also depends on the grain orientation for each grain of the polycrystalline metallic thin film. In Eq. (3.2.36), the anisotropy of surface diffusion is quantified through the dimensionless parameters, which are fully discussed in section 3.2.vi.

Grain orientation is expressed by the crystallographic direction normal to the surface of the film and the misorientation of the crystallographic symmetry axes in the grain with respect to the applied electrostatic field. The parameter m in Eq. (3.2.36) is an integer number that characterizes the film surface plane; this plane is perpendicular to the cylindrical void surface. In *fcc* metals, such as aluminum, these symmetry axes correspond to $< 110 >$ crystallographic directions. Each of the $\{110\}$ planes contain only one $< 110 >$ axis, therefore these planes have $m = 1$. In the same way, for $\{100\}$ planes $m = 2$ and for $\{111\}$ planes $m = 3$.

The term "*N*-fold" symmetry is used to denote the number of the fast diffusion paths on a crystallographic plane. Since each crystallographic axis corresponds to two opposite directions, $N = 2m$.

Therefore, $[110]$-, $[100]$- and $[111]$- oriented grains are characterized by twofold, fourfold and six fold symmetry respectively.

i. Critical Initial Void Configuration

In figures 4.1.2.1, 4.1.2.2 and 4.1.2.3 the initial void shape is chosen to be critical-asymmetric with respect to the direction of the electron flow which is in the opposite direction of the applied electrostatic field. In these simulation experiments, the constant interface controlled growth process has also been taken into account.

a. Sixfold Crystal Symmetry: *m* = 3

The sixfold crystal symmetry ($m=3$, and $[111]-$oriented grains in Al) in the surface diffusion coefficient becomes a factor in the development of the faceted void as shown in figure 4.1.2.1. It can be seen that at the very beginning the semi hexagonal shaped void develops as would be expected from the sixfold symmetry. In agreement with the Kraft and Arzt (1997) and Gungor and Maroudas (1999) it is found that the facets do not develop exactly along the directions with the highest or lowest diffusivity in general. In the figure, the fast diffusion directions are coinciding with the peak positions in the polar diffusivity graphs.

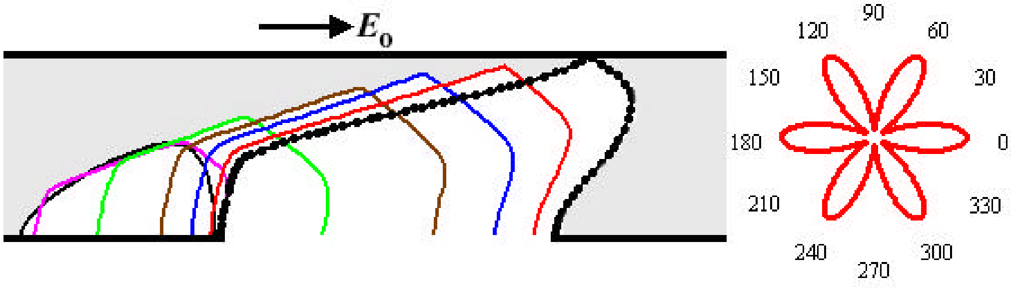

Figure 4.1.2.1: Void morphology evolution for a *critical* initial void configuration ($m=3$, $A=5$, $q=0$, $\Delta\overline{g}_{vb}=-5$, $\overline{M}_{vb}=5$). Electron wind intensity: $c=10$. Scaled interconnect width: $\overline{w}=2$. Normalized failure time: $\overline{t}_f=0.03929$.

In the study of Kraft and Arzt (1997), the authors state that the semi hexagonal void shape is very stable and also even when the void reaches more than 95% of the line width no shape changes are seen. However in our case, especially in the later stages of the evolution, the significant current crowding on the void surface due to the large void size drives a morphological instability that leads to a very blunt slit-like formation. The slit is also faceted and these facets nearly have the same orientations with the facets of the void that formed in the former stages. This observed advancing front causes an open circuit failure by hitting the upper edge of interconnect. The main reason for this difference is that, as mentioned before, Kraft and Arzt (1997) use a self-similar enlargement of the void as a growth process, which is contradictory to the experimental observations.

b. Fourfold Crystal Symmetry: *m* = 2

Figure 4.1.2.2 shows the void morphological evolution in grains having fourfold symmetry ($m = 2$, and $[100]-$ oriented grains in Al) in the anisotropic diffusion coefficient.

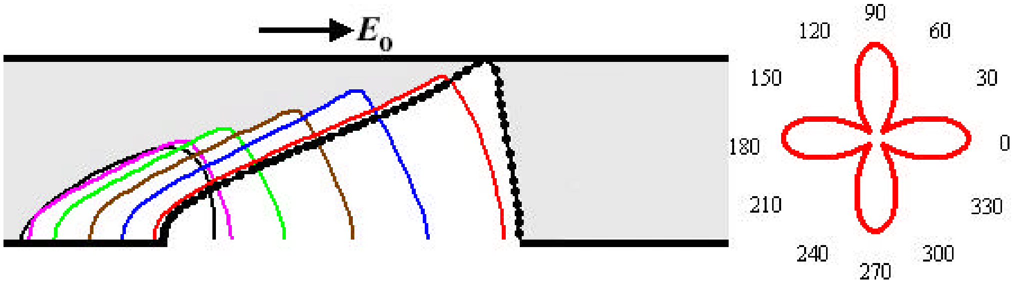

Figure 4.1.2.2: Void morphology evolution for a *critical* initial void configuration ($m = 2$, $A = 5$, $q = 0$, $\Delta\bar{g}_{vb} = -5$, $\overline{M}_{vb} = 5$). Electron wind intensity: $c = 10$. Scaled interconnect width: $\bar{w} = 2$. Normalized failure time: $\bar{t}_f = 0.02909$.

The initially formed faceted morphology evolves into a wedge-like shape, which accelerates the early open circuit failure by hitting the upper edge of interconnects.

c. Twofold Crystal Symmetry: *m* = 1

In figure 4.1.2.3, the twofold symmetry ($m = 1$, and $[110]-$oriented grains in Al) in the surface diffusion becomes a main factor in the development of the straight advancing slit, which accelerates the very early open circuit failure due to a sharp slit hitting the upper edge of the interconnect.

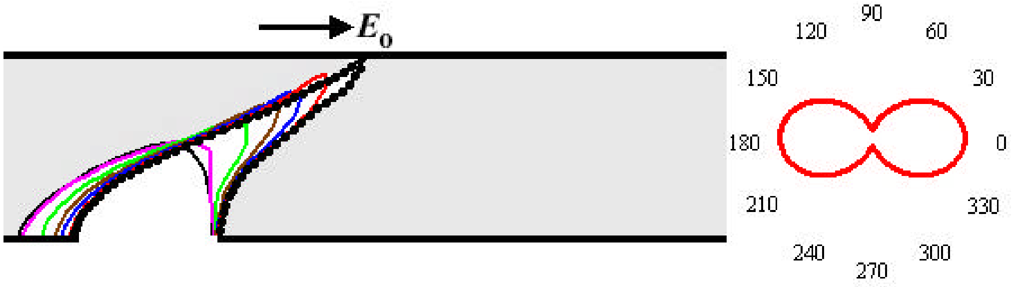

Figure 4.1.2.3: Void morphology evolution for a *critical* initial void configuration ($m = 1$, $A = 5$, $q = 0$, $\Delta\bar{g}_{vb} = -5$, $\bar{M}_{vb} = 5$). Electron wind intensity: $c = 10$. Scaled interconnect width: $\bar{w} = 2$. Normalized failure time: $\bar{t}_f = 0.00329$.

Again, the orientation of the slit does not follow one of the planes with highest or lowest diffusivity. Instead, the slit seems to follows one of the (111) planes.

ii. Uncritical Initial Void Configuration

In figures 4.1.2.4, 4.1.2.5 and 4.1.2.6 the initial void shape is chosen to be uncritical-asymmetric with respect to the direction of the electron flow which is in the opposite direction of the applied electrostatic field.

Similarly in these simulation experiments, the constant interface controlled growth process has also been taken into account.

a. Sixfold Crystal Symmetry: *m* = 3

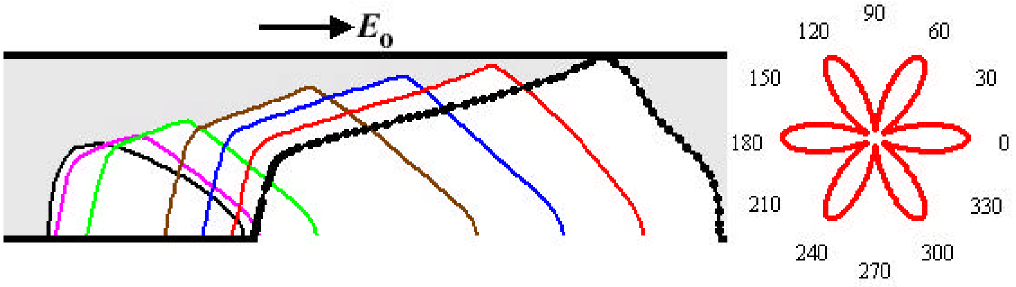

Figure 4.1.2.4: Void morphology evolution for an *uncritical* initial void configuration ($m = 3$, $A = 5$, $q = 0$, $\Delta\bar{g}_{vb} = -5$, $\bar{M}_{vb} = 5$). Electron wind intensity: $c = 10$. Scaled interconnect width: $\bar{w} = 2$. Normalized failure time: $\bar{t}_f = 0.04651$.

b. Fourfold Crystal Symmetry: *m* = 2

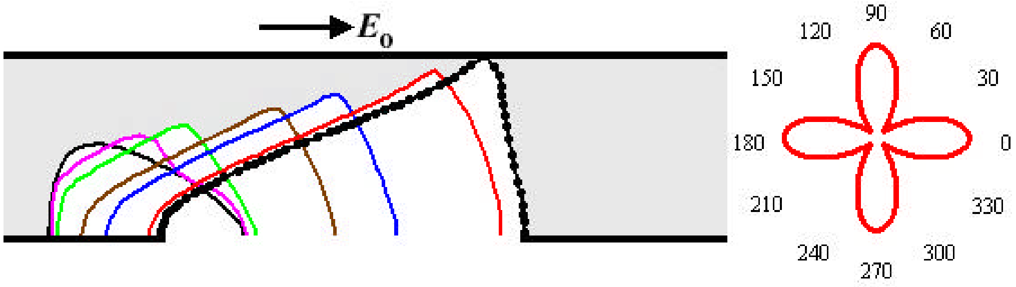

Figure 4.1.2.5: Void morphology evolution for an *uncritical* initial void configuration ($m = 2$, $A = 5$, $q = 0$, $\Delta\bar{g}_{vb} = -5$, $\overline{M}_{vb} = 5$). Electron wind intensity: $c = 10$. Scaled interconnect width: $\bar{w} = 2$. Normalized failure time: $\bar{t}_f = 0.02979$.

c. Twofold Crystal Symmetry: *m* = 1

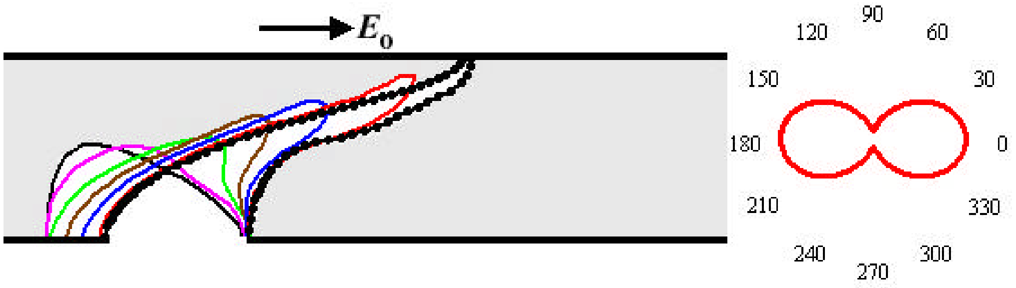

Figure 4.1.2.6: Void morphology evolution for an *uncritical* initial void configuration ($m = 1$, $A = 5$, $q = 0$, $\Delta\bar{g}_{vb} = -5$, $\overline{M}_{vb} = 5$). Electron wind intensity: $c = 10$. Scaled interconnect width: $\bar{w} = 2$. Normalized failure time: $\bar{t}_f = 0.00541$.

These last three figures show that as an intermediate step; the uncritical initial void shape is converted into the critical form as suggested by the experimental studies performed by Arzt *et al.* (1994), and Kraft and Arzt (1997).

From these simulation experiments, which are presented by figures 4.1.2.1-6, the effect of the degree of surface diffusion anisotropy in connection with the normalized time to failure, $\bar{t}_f$, is observed and the relevant data are tabulated in table 4.1.2.1.

Table 4.1.2.1: Influence of the degree of surface diffusion anisotropy on the normalized failure time $\bar{t}_f$.

Fold Number	**Texture for FCC Metals (Al)**	**Critical**	**Uncritical**	
		$\bar{t}_f$	$\bar{t}_f$	t_{50}
2	$(\bar{1}10)$ - [110]	0.00329	0.00541	8170
4	(001) - [100]	0.02909	0.02979	-
6	(111) - $[\bar{1}10]$	0.03929	0.04651	59000

The data indicate that the normalized failure time increases drastically as the degree of symmetry in the surface diffusion anisotropy increases. According to table 4.1.2.1, the normalized effective time to failure $\bar{t}_f$ shows about one order of magnitude enhancement changing from twofold symmetry to sixfold symmetry for both critical and uncritical initially nucleated voids. The lifetime improvements are 11.9 times and 8.6 times for the critical and uncritical cases respectively.

These results are in excellent agreement with the experimental findings of Joo and Thompson (1997), which are given as t_{50} in the last column of the Table 4.1.2.1, concerning Al (110) and Al (111) on SiO_2 substrates. Their experimental observations indicate that when they change the orientation of Al lines from twofold symmetry to sixfold symmetry the lifetime improvement is 7.2.

A comparison of the results presented in table 4.1.2.1, indicates that the uncritical initial void configuration yields about a factor of one and an half longer life time for the interconnect then the critical initial void configuration regardless of the fold number. This tendency is also suggested by the experimental studies performed by Arzt *et al.* (1994). They found that the lifetime improvement is 4.1. However on the long run, both shapes are detrimental for aluminum interconnects especially in the case of twofold symmetry that means $(001)\times[100]$ texture in *fcc* metals.

These computer experiments clearly indicate the importance of the surface diffusion anisotropy for the premature formation of a fatal open circuit configuration, and the further enhancement of this deterioration due to void growth process caused by supersaturated vacancies in the bulk matrix.

Therefore, one should choose the highest symmetry plane and the most close packed direction, such as $\{111\}\left\langle 1\bar{1}0\right\rangle$ in *fcc* metals and alloys as a texture for the metallic interconnect thin films.

4.1.3. Comparison of Simulations with the Experimentally Observed Void Configurations

In figures 4.1.3.1 to 4.1.3.5, the qualitative comparisons, which are carried out between the simulation predictions for electromigration induced void evolution and the observations of such void configurations that have been published in the literature.

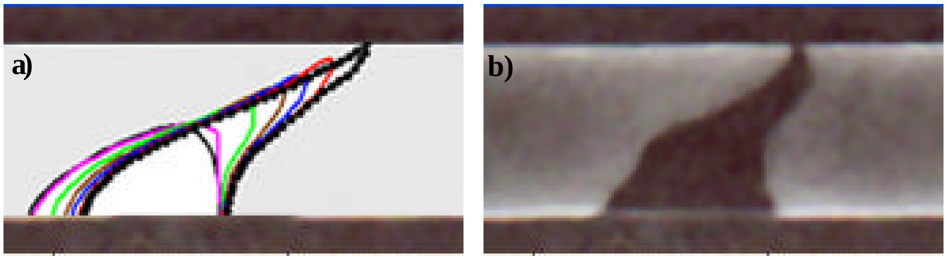

Figure 4.1.3.1: Formation of a narrow slit **a)** Simulation result: ($m=1$, $A=5$, $q=0$, $\Delta\bar{g}_{vb}=-5$, $\overline{M}_{vb}=5$, $c=10$) **b)** SEM micrograph from the work of Arzt *et al.* (1994).

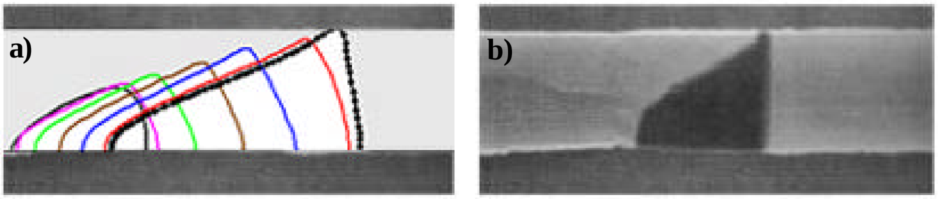

Figure 4.1.3.2: Formation of a faceted void **a)** Simulation result: ($m=2$, $A=5$, $q=0$, $\Delta\bar{g}_{vb}=-5$, $\overline{M}_{vb}=5$, $c=10$) **b)** SEM micrograph from the work of Kraft and Arzt (1997).

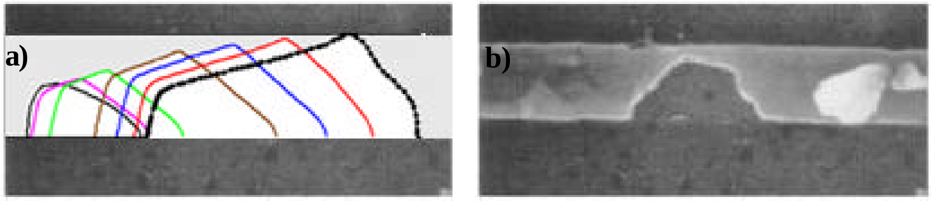

Figure 4.1.3.3: Formation of a semi-hexagonal faceted void **a)** Simulation result: ($m=3$, $A=5$, $q=0$, $\Delta\overline{g}_{vb}=-5$, $\overline{M}_{vb}=5$, $c=10$) **b)** SEM micrograph from the work of Sanchez *et al.* (1990).

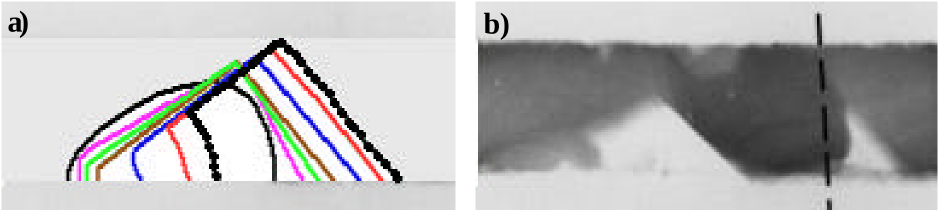

Figure 4.1.3.4: Formation of a faceted void **a)** Simulation result: ($m=2$, $A=5$, $q=0$, $\Delta\overline{g}_{vb}=-10$, $\overline{M}_{vb}=10$, $c=100$) **b)** TEM micrograph from the work of Greer (1998).

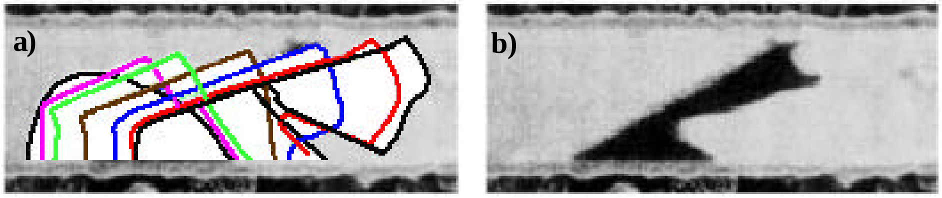

Figure 4.1.3.5: Formation of a faceted slit like element **a)** Simulation result: ($m=2$, $A=5$, $q=0$, $\Delta\overline{g}_{vb}=-10$, $\overline{M}_{vb}=10$, $c=100$) **b)** SEM micrograph from the work of Joo and Thompson (1997).

Even though these comparisons are only qualitative, they validate the model, used for the simulation of void morphological evolution, in terms of its capabilities to capture a wide range of complex non-linear dynamical phenomena.

4.2. Void Intergranular Motion: Void - Grain Boundary Interactions

In this section a comprehensive characterization of the void - grain boundary interactions is presented. In the following computer simulations one uses the boundary conditions that were obtained by the irreversible thermodynamic treatment of the triple junction, in which there are no assumptions such that, a constant dihedral angle or void tip morphology in the vicinity of the triple junction and a constant triple junction velocity as generally used in the literature.

In the void - grain boundary interactions, the wetting parameter, l , which is related to the dihedral angle, is a very important experimental parameter and may be described by assuming the identical left and right wetting parameters, described by the Eq. (2.3.2.28) as follows:

$$l = l^{-} = l^{+} = \frac{g_g}{2g_s} \tag{4.2.1}$$

Commonly in the literature, the dihedral angle is described by the angle that the void phase makes between the two bulk grains (Verhoeven, 1975) as shown in figure 4.2.1.

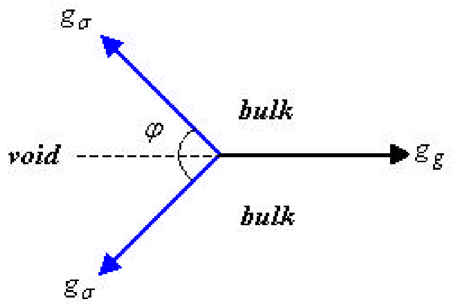

Figure 4.2.1: A surface tension force balance defining the dihedral angle j .

From the Eq. (4.2.1) and the definition of the dihedral angle, the following relationship between these two factors can be found:

$$j = 2\cos(l)^{-1} \tag{4.2.1}$$

4.2.1. The Effect of Wetting Parameter on the Void - Grain Boundary Equilibrium Configuration: Isotropic Surface Diffusivity without Electromigration Forces and Void Growth Mechanism

In order to test the validity of the irreversible thermodynamic treatment of the triple junction presented in Chapter 2, the various experiments were performed utilizing different values of the wetting parameters, l, at the absence of any external forces such as electron wind.

i. Voids Nucleated on the Grain Boundaries

In the following experiments, the morphological evolution of a circular void that is nucleated on a grain boundary is presented in snapshots taken from different time steps. The angle between the lines $|AB|$ and $|AC|$ is exactly equal to the half of the dihedral angle.

In figure 4.2.1.1 the wetting parameter $l = 1$, and this corresponds to the 180° dihedral angle or no wetting condition. As it may be seen from the snapshots figure the circular void is stable for the above parameters. Figure 4.2.1.2 shows the evolution of angle $B\hat{A}C$, which is initially 87° because of the used discretization procedure. As soon as the simulation start the angle $B\hat{A}C$ evolves to the half of the dihedral angle, as dictated by the thermostatic theory.

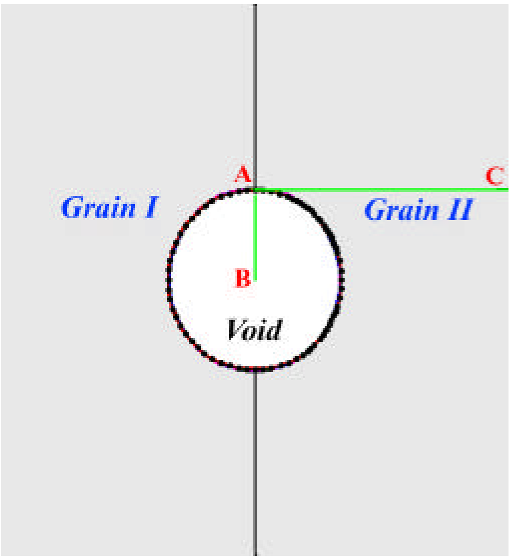

Figure 4.2.1.1: Void morphological evolution to the equilibrium configuration. The wetting parameter: $l = 0$ and the corresponding dihedral angle : $j = 180^\circ$

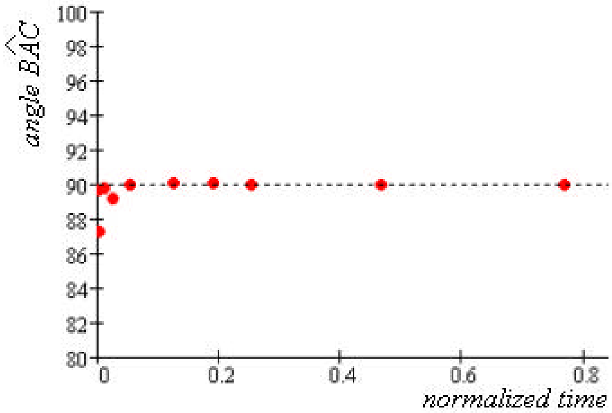

Figure 4.2.1.2: Evolution of angle $B\hat{A}C$. The doted line: $j / 2 = 90^\circ$

In the following figures the effect of the wetting parameter on the void equilibrium morphology can be seen.

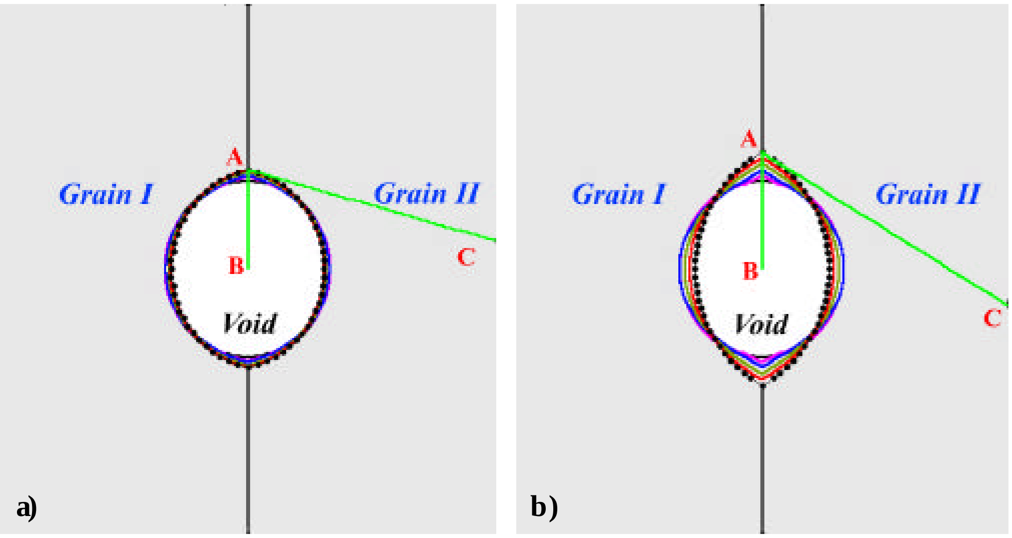

Figure 4.2.1.3: Void morphological evolution to the equilibrium configuration.

a) The wetting parameter: $l = 0.259$; the corresponding dihedral angle: $j = 150^{\circ}$

b) The wetting parameter: $l = 0.5$; the corresponding dihedral angle: $j = 120^{\circ}$

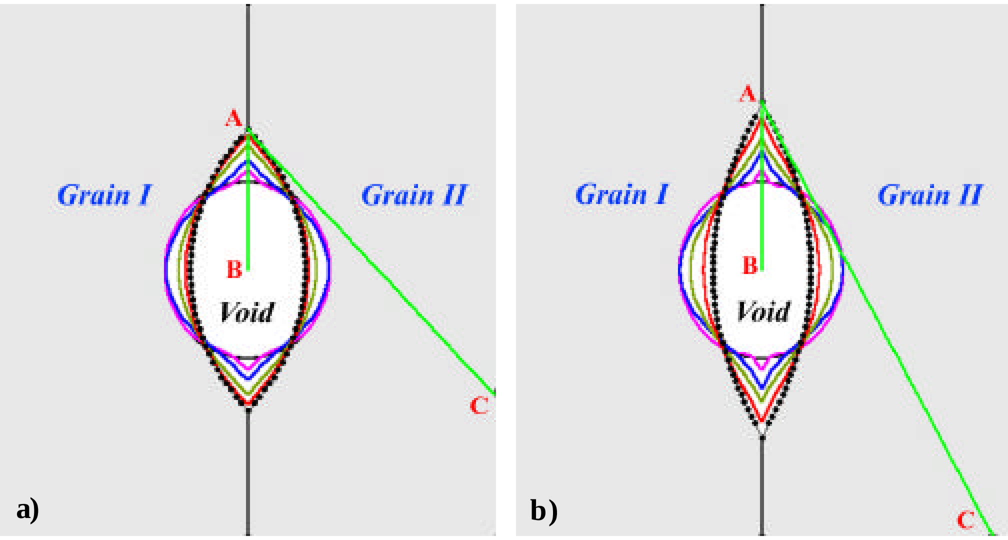

Figure 4.2.1.4: Void morphological evolution to the equilibrium configuration.

a) The wetting parameter: $l = 0.707$; the corresponding dihedral angle: $j = 90^{\circ}$

b) The wetting parameter: $l = 0.866$; the corresponding dihedral angle: $j = 60^{\circ}$

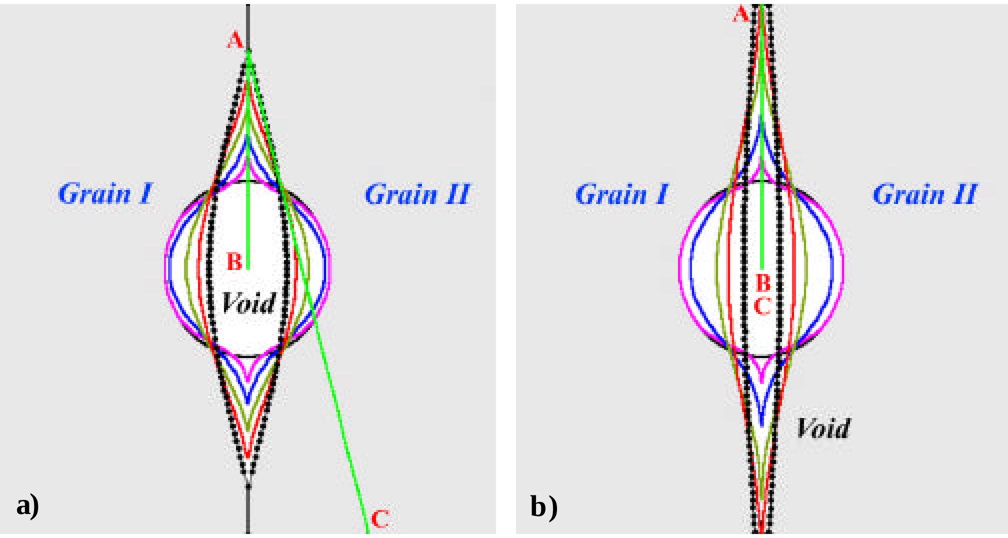

Figure 4.2.1.5: Void morphological evolution to the equilibrium configuration.

a) The wetting parameter: $l = 0.966$; the corresponding dihedral angle: $j = 30^\circ$

b) The wetting parameter: $l = 1$; the corresponding dihedral angle: $j = 0^\circ$

In figure 4.2.1.5-b the dihedral angle is equal to the zero, which correspond to the perfect wetting condition. In this last simulation on the contrary to the previous equilibrium simulations, the system cannot reach to the equilibrium. The only reason is the very long computation time necessary to complete the experiment. As the void wets the grain boundary, which means it is pulled along the grain boundary by capillary forces, the number of nodes necessary to describe the void circumference reaches to the very big numbers. Anyway in this experiment the tendency in the case of perfect wetting is simulated succesfully.

Figure 4.2.1.6 shows the evolution of angle $B\hat{A}C$, from initially 87° to the half of the dihedral angle 0°.

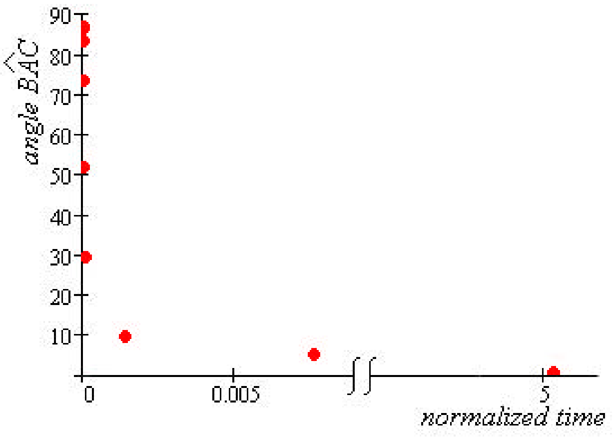

Figure 4.2.1.6: Evolution of angle $B\hat{A}C$. The dihedral angle: $j = 0^\circ$

ii. Voids Nucleated inside the Grains and just Touched to the Grain Boundaries

In this section, the void grain boundary interaction in the case of circular void, which is nucleated inside the grains and just touched to the grain boundaries were simulated.

In figures from 4.2.1.7 to 4.2.1.10, the snapshots from the void grain boundary interaction are presented by utilizing different wetting parameters, from no wetting to complete wetting conditions. In these experiments only the capillary forces are taken into account.

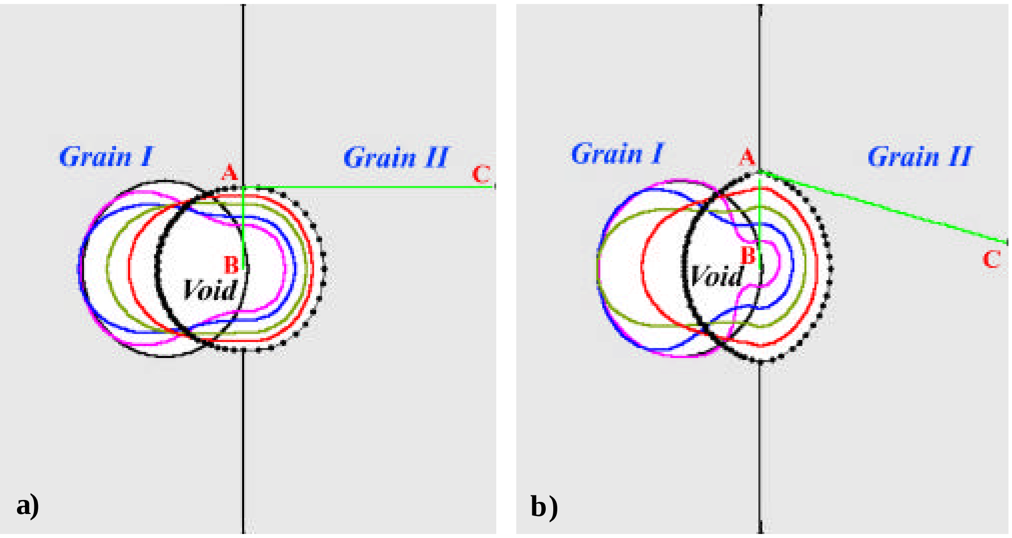

Figure 4.2.1.7: Void morphological evolution to the equilibrium configuration.

a) The wetting parameter: $l = 0$; the corresponding dihedral angle: $j = 180^\circ$

b) The wetting parameter: $l = 0.259$; the corresponding dihedral angle: $j = 150^\circ$

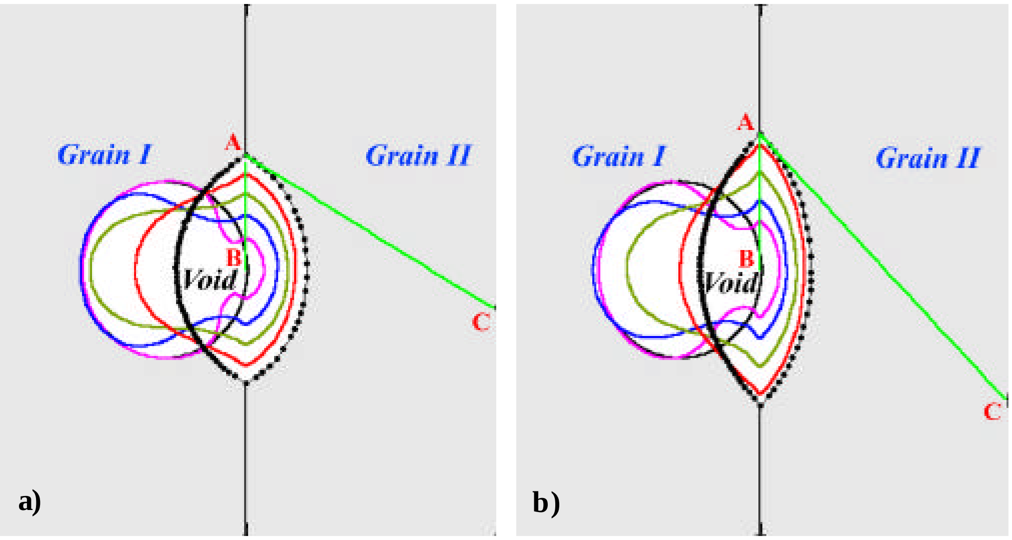

Figure 4.2.1.8: Void morphological evolution to the equilibrium configuration.

a) The wetting parameter: $l = 0.5$; the corresponding dihedral angle: $j = 120^\circ$

b) The wetting parameter: $l = 0.707$; the corresponding dihedral angle: $j = 90^\circ$

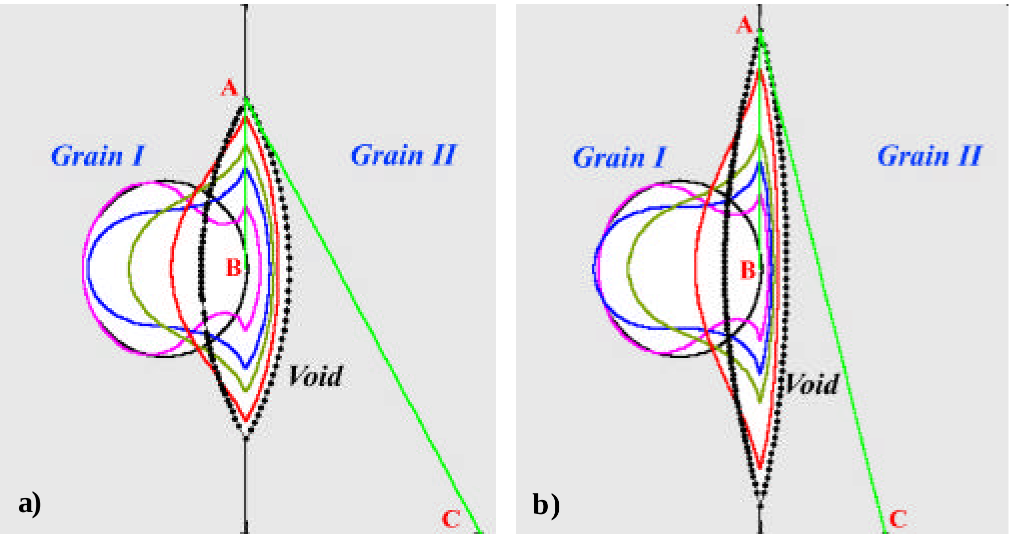

Figure 4.2.1.9: Void morphological evolution to the equilibrium configuration.

a) The wetting parameter: $l = 0.866$; the corresponding dihedral angle: $j = 60^\circ$

b) The wetting parameter: $l = 0.966$; the corresponding dihedral angle: $j = 30^\circ$

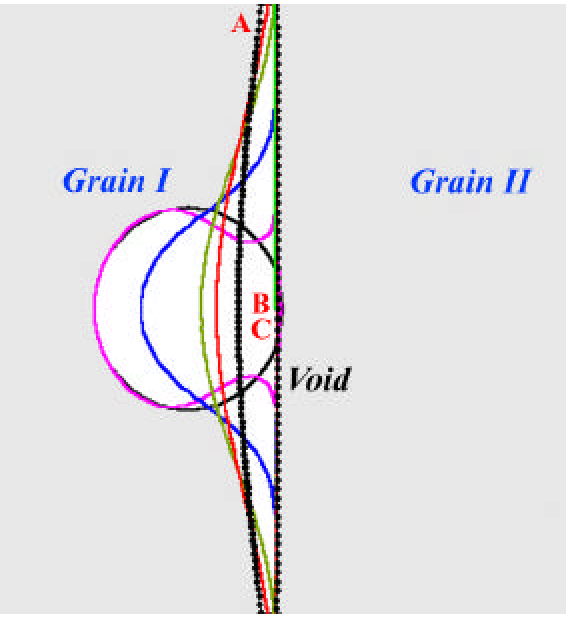

Figure 4.2.1.10: Void morphological evolution to the equilibrium configuration. The wetting parameter: $l = 1$ and the corresponding dihedral angle : $j = 0^\circ$

These figures show that the void - grain boundary system starts to evolve towards the equilibrium configuration having proper dihedral angles dictated by thermostatic theory, as soon as they have in close contact with each other's. The rate of this shape evolution process seems to be controlled by three independent unit processes, namely the mobility of surface drift-diffusion, and the generalized mobilities associated with longitudinal movement of triple junction and the transverse flow of matter through the junction, respectively. The first one corresponds to the long-range material transport, and the other two are closely related to in situ chemical species transfer reactions (highly localized fashion) taking place at the triple junction.

Since our computer simulation experiments operate in the normalized and scaled time and space domains, in the absence of growth phenomenon and grain boundary drift-diffusion, one only deal with two normalized mobilities which are designated as longitudinal and transverse triple junction generalized mobilities.

iii. Voids Nucleated at the Intersection of Three Grains

In this section, the shape evolution behaviour of a void, which is nucleated at the triple junction of intersecting three grains, is demonstrated at the absence of the electron wind.

In figures from 4.2.1.11 to 4.2.1.14, the snapshots from the void grain boundary interaction are presented by utilizing different wetting parameters, again from no wetting to complete wetting conditions.

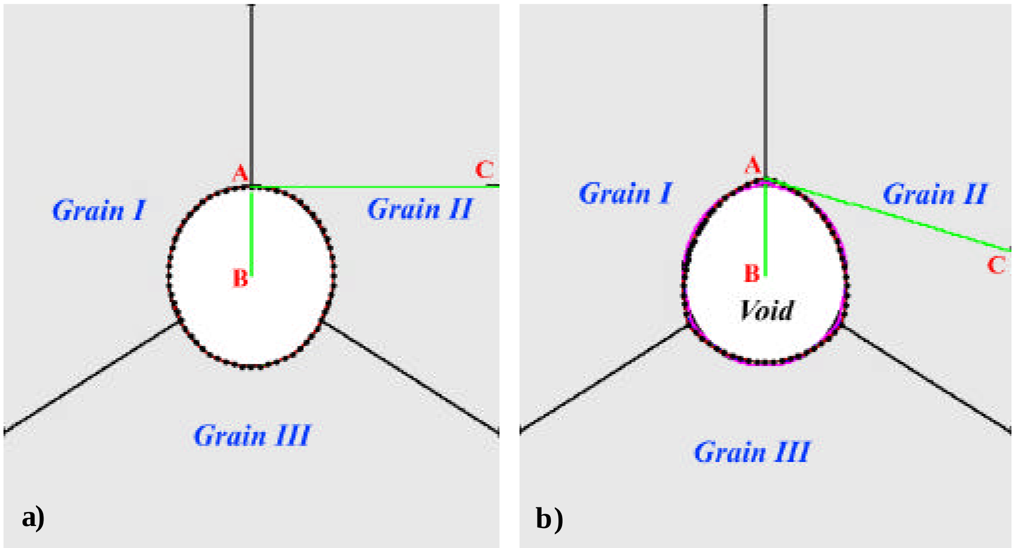

Figure 4.2.1.11: Void morphological evolution to the equilibrium configuration.

a) The wetting parameter: $l = 0$; the corresponding dihedral angle: $j = 180^\circ$

b) The wetting parameter: $l = 0.259$; the corresponding dihedral angle: $j = 150^\circ$

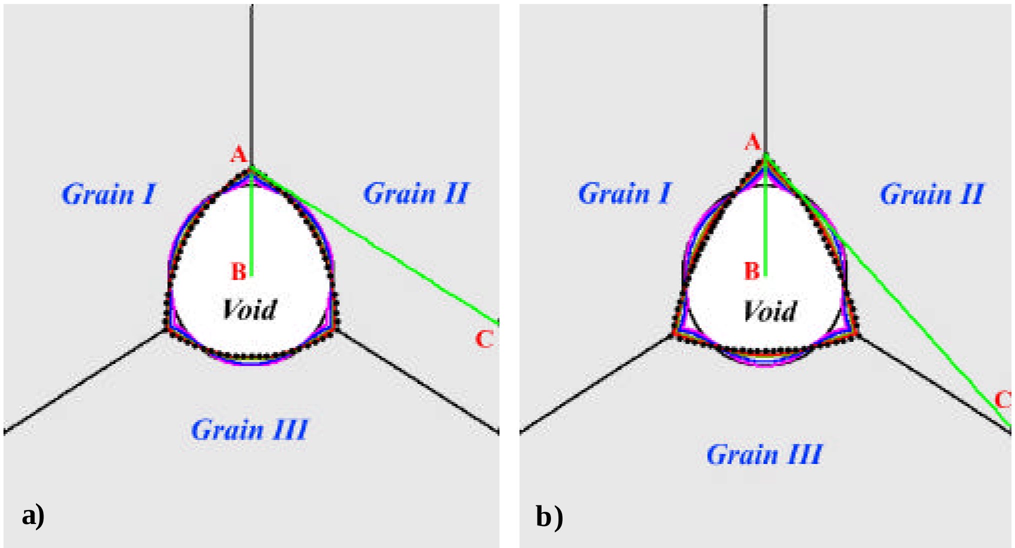

Figure 4.2.1.12: Void morphological evolution to the equilibrium configuration.
a) The wetting parameter: $l = 0.5$; the corresponding dihedral angle: $j = 120^\circ$

b) The wetting parameter: $l = 0.707$; the corresponding dihedral angle: $j = 90^\circ$

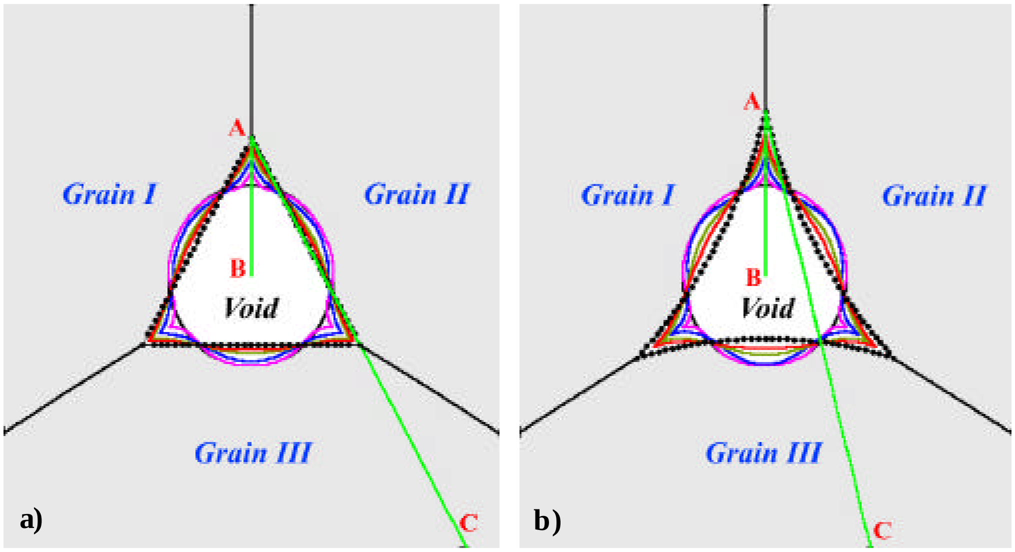

Figure 4.2.1.13: Void morphological evolution to the equilibrium configuration.

a) The wetting parameter: $l = 0.866$; the corresponding dihedral angle: $j = 60^{\circ}$

b) The wetting parameter: $l = 0.966$; the corresponding dihedral angle: $j = 30^{\circ}$

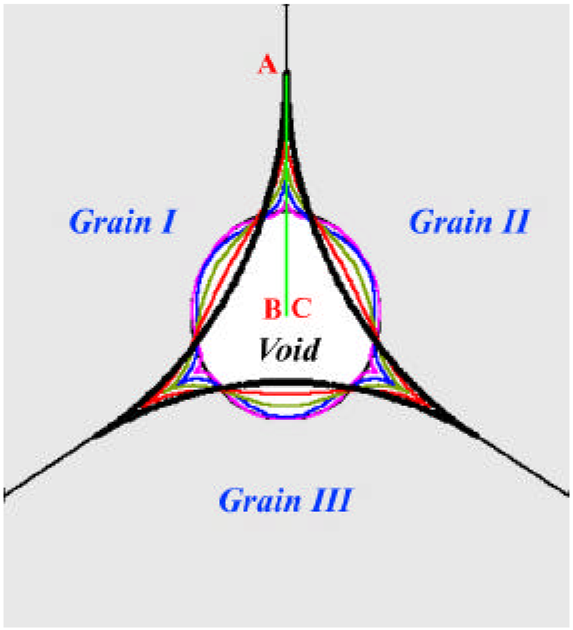

Figure 4.2.1.14: Void morphological evolution to the equilibrium configuration. The wetting parameter: $l = 1$ and the corresponding dihedral angle : $j = 0^{\circ}$

In figure 4.2.1.13-a the dihedral angle is $j = 60^\circ$, and the corresponding equilibrium configuration is a triangle, where the node curvatures is exactly equal to zero.

Especially in figures 4.2.1.13-b and 4.2.1.14, there is a substantial change in the final shape of the void, namely, a steady state transformation from convex void counters towards the concave morphology in order to yield maximum penetration while still keeping the void volume invariant.

This behavior shows that the concave morphology is the real equilibrium configuration for the voids, for which the dihedral angle is less than the 60°.

This fact namely the negative curvature at the singularity is mentioned first time in the literature in this work (Ogurtani and Oren, 2002), as an outcome of a rigorous theory of surfaces and interfaces.

These figures indicate that the final void or cavity configurations are excellent agreement with those morphologies obtained in usual laboratory experiments as well as with the predictions of the thermostatic theories, which of course can only be applicable to the equilibrium shapes.

4.2.2. Isotropic Surface Diffusivity with Electromigration Forces and without Void Growth Mechanism - Prediction of Cathode Failure Times in Bamboo Structures

In order to evaluate the effect of the current crowding on the morphology as well as on the mean time to failure (MTTF) of the interconnects with bamboo structure a series of simulation experiments is done on the void grain boundary interactions.

In the following figures from 4.2.2.1 to 4.2.2.7, the results of extensive computer simulation experiments on the void detachment process from the grain boundaries in aluminum bamboo interconnects are demonstrated.

In these experiment the detachment kinetics of voids, which are initially situated or nucleated at the grain boundaries is investigated.

Since the specific Gibbs free energy density of aluminum for the free surface and for the grain boundary is equal to $0.980\,Jm^{-2}$ and $0.324\,Jm^{-2}$ respectively (Liu *et al.*, 2001), in all of the following series of experiments the wetting parameter is taken as $l = 0.165$.

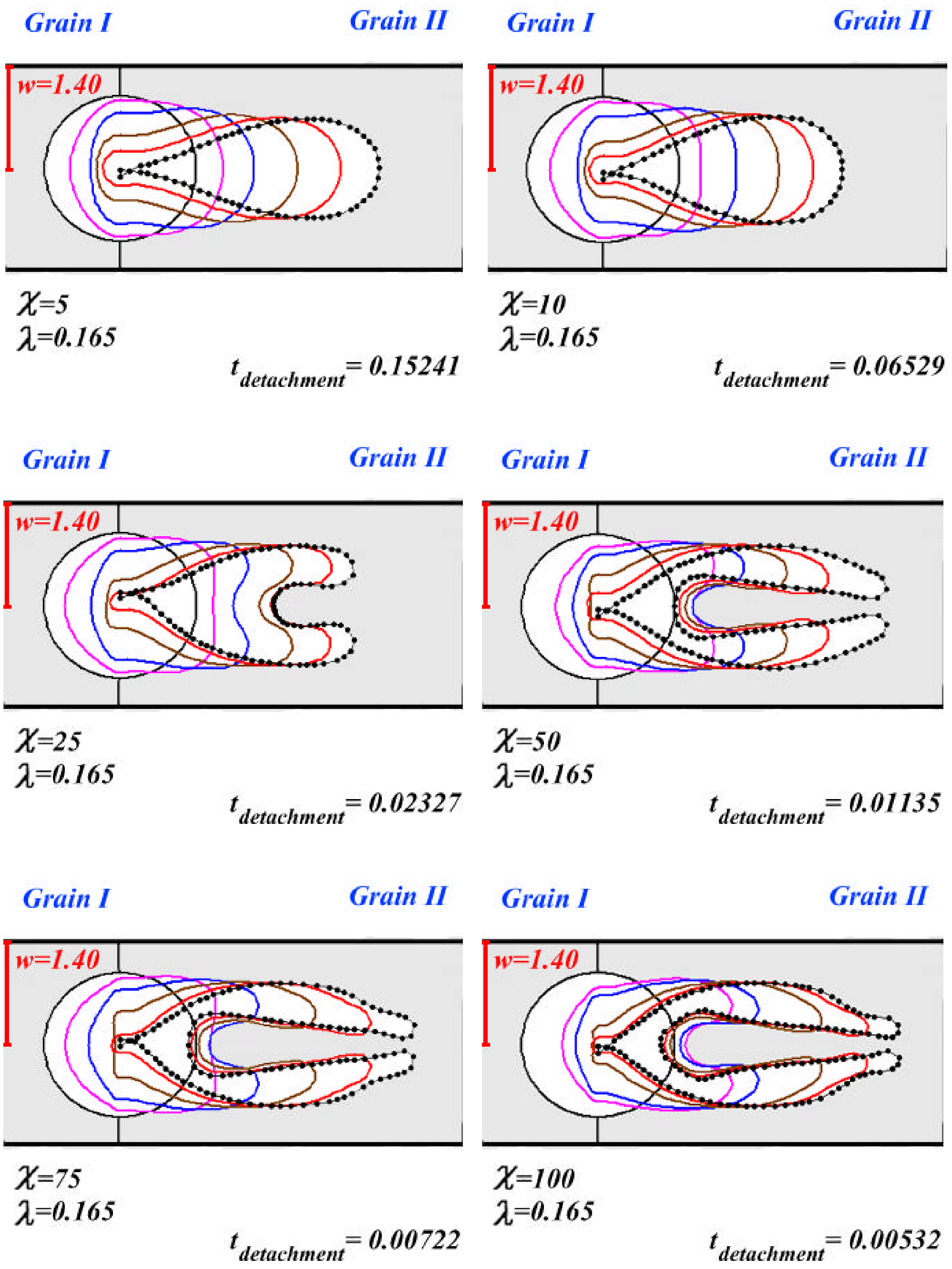

Figure 4.2.2.1: Void detachment process for different normalized electron wind intensities; the normalized interconnect with: $\overline{w} = 1.4$

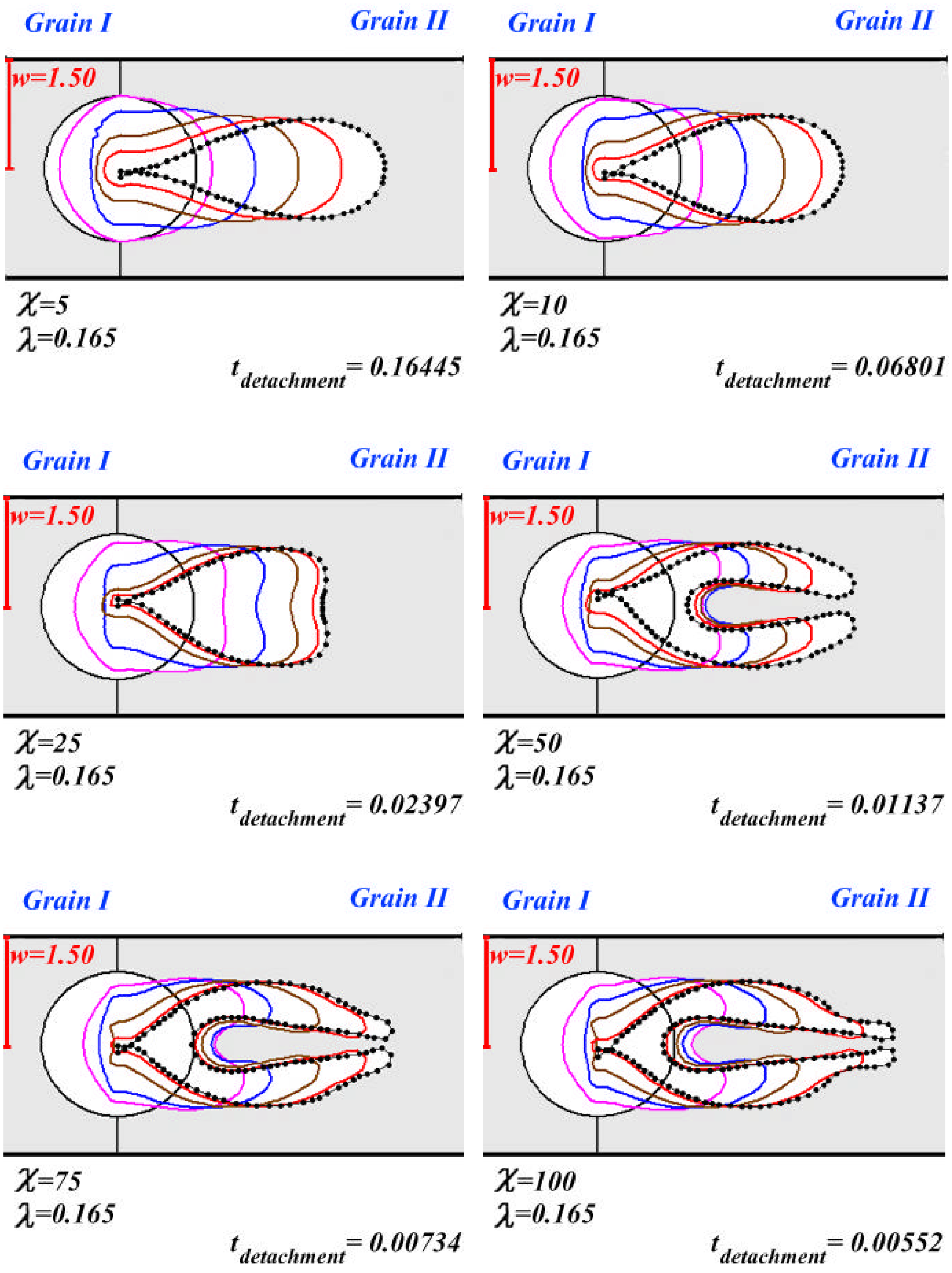

Figure 4.2.2.2: Void detachment process for different normalized electron wind intensities; the normalized interconnect with: $\overline{w} = 1.5$

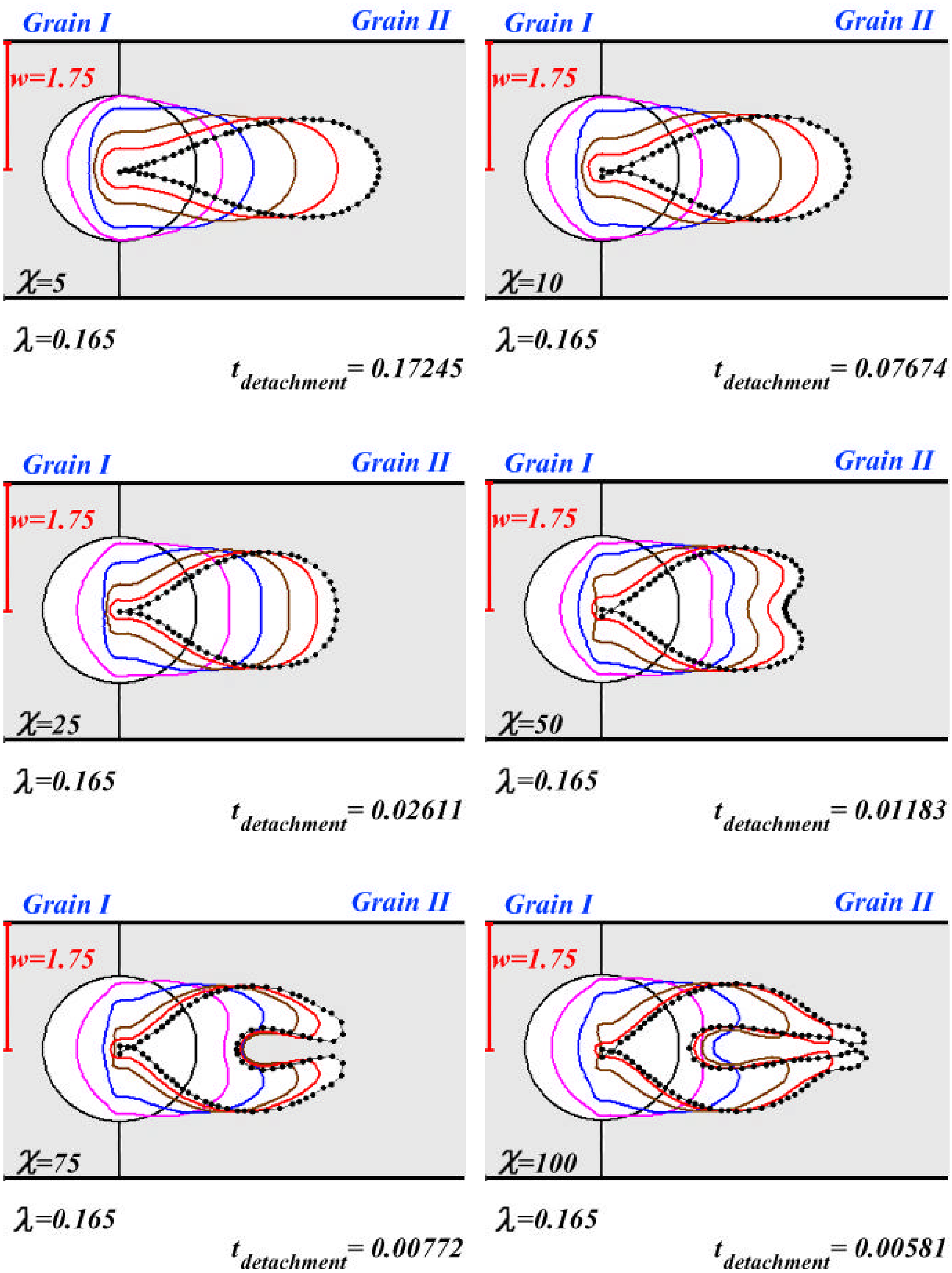

Figure 4.2.2.3: Void detachment process for different normalized electron wind intensities; the normalized interconnect with: $\overline{w} = 1.75$

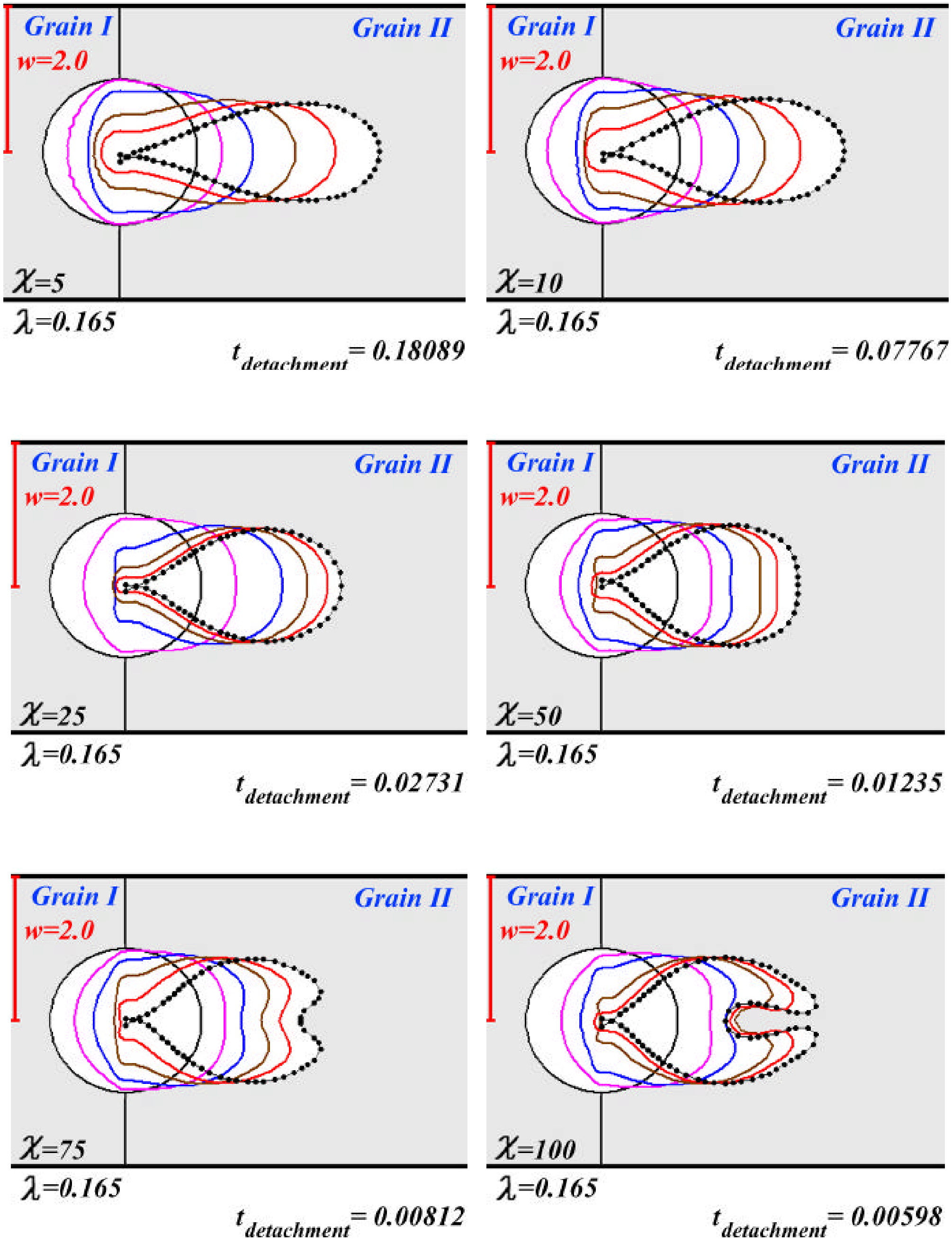

Figure 4.2.2.4: Void detachment process for different normalized electron wind intensities; the normalized interconnect with: $\overline{w} = 2.0$

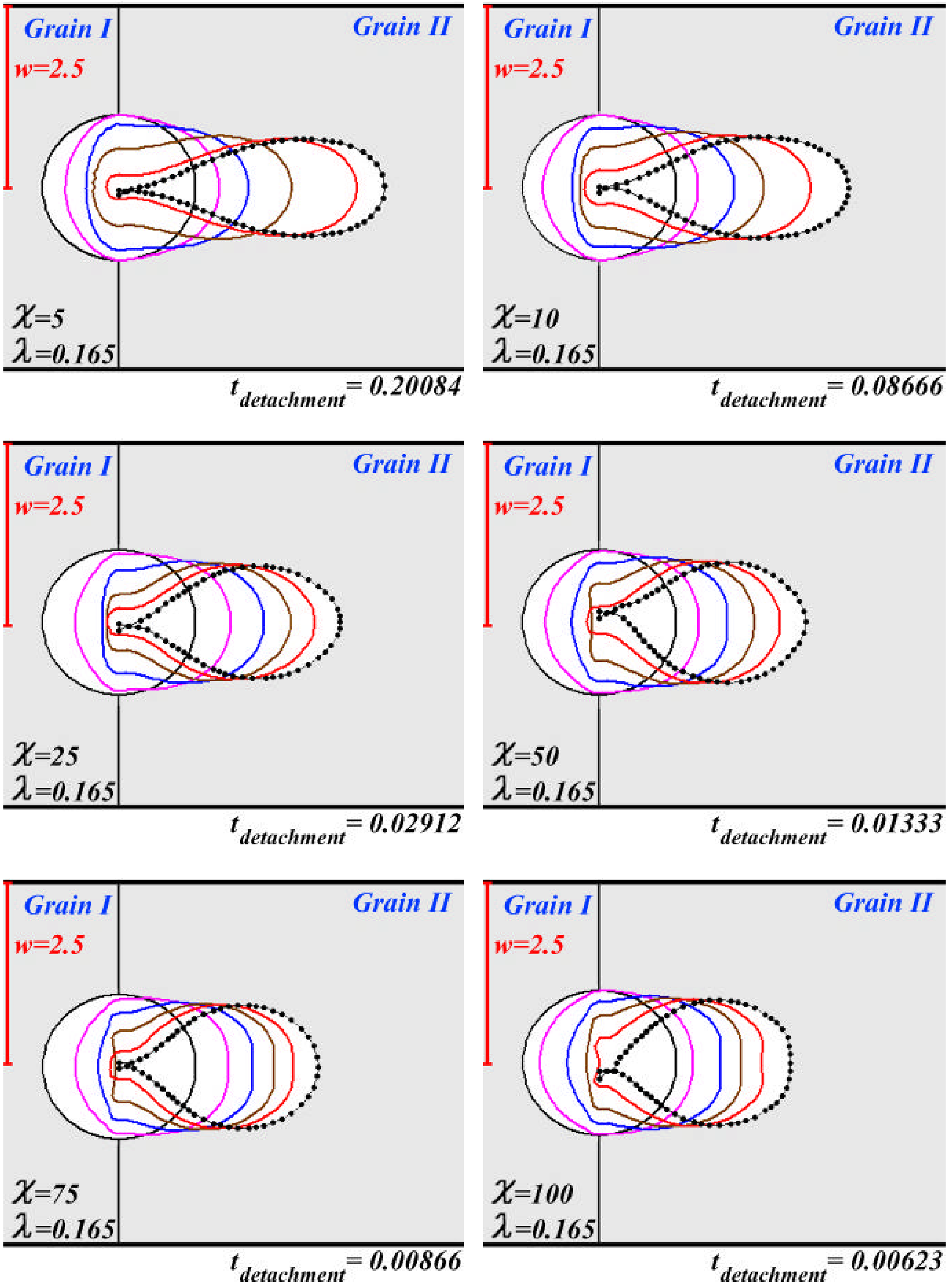

Figure 4.2.2.5: Void detachment process for different normalized electron wind intensities; the normalized interconnect with: $\overline{w} = 2.5$

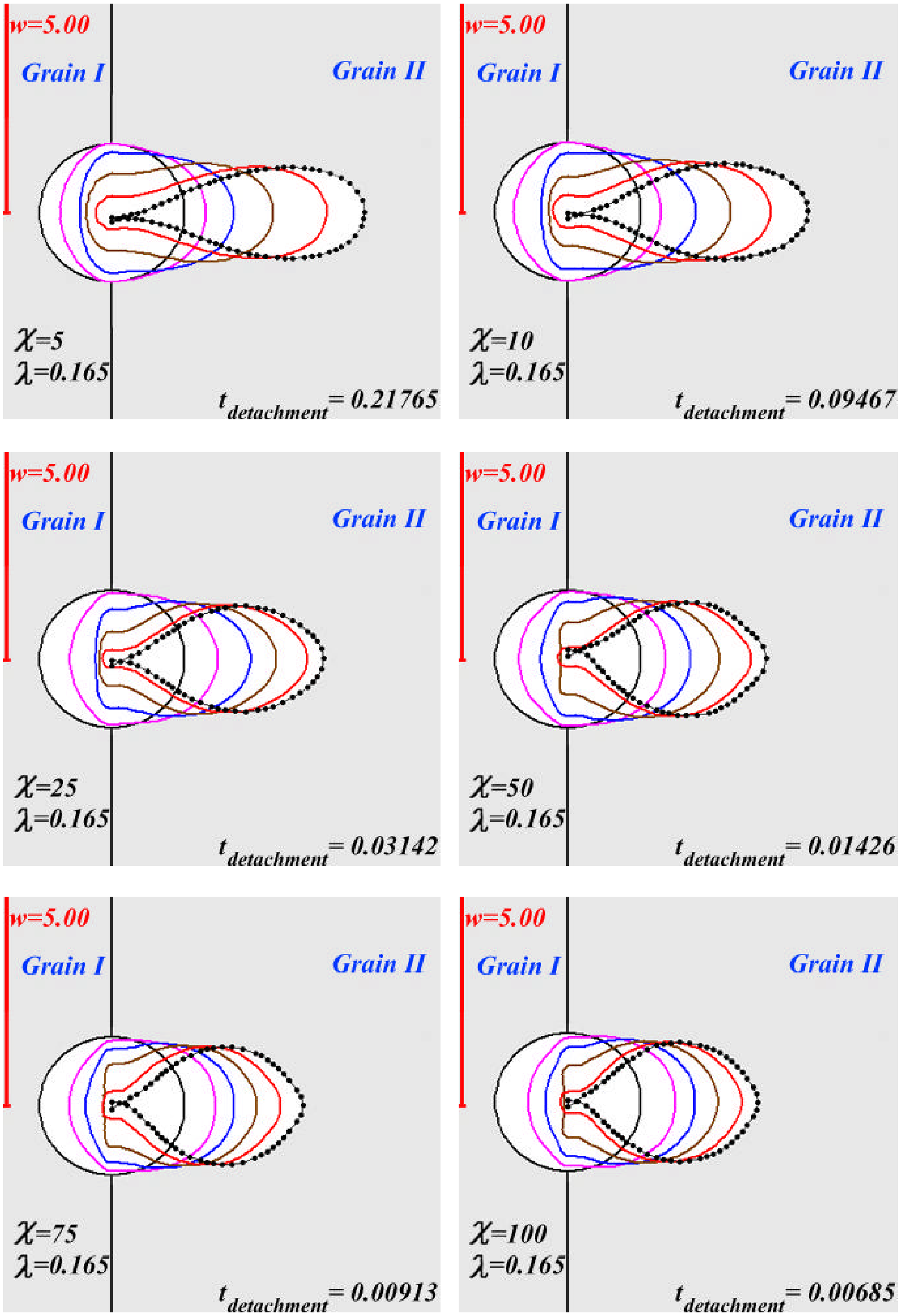

Figure 4.2.2.6: Void detachment process for different normalized electron wind intensities; the normalized interconnect with: $\overline{w} = 5.0$

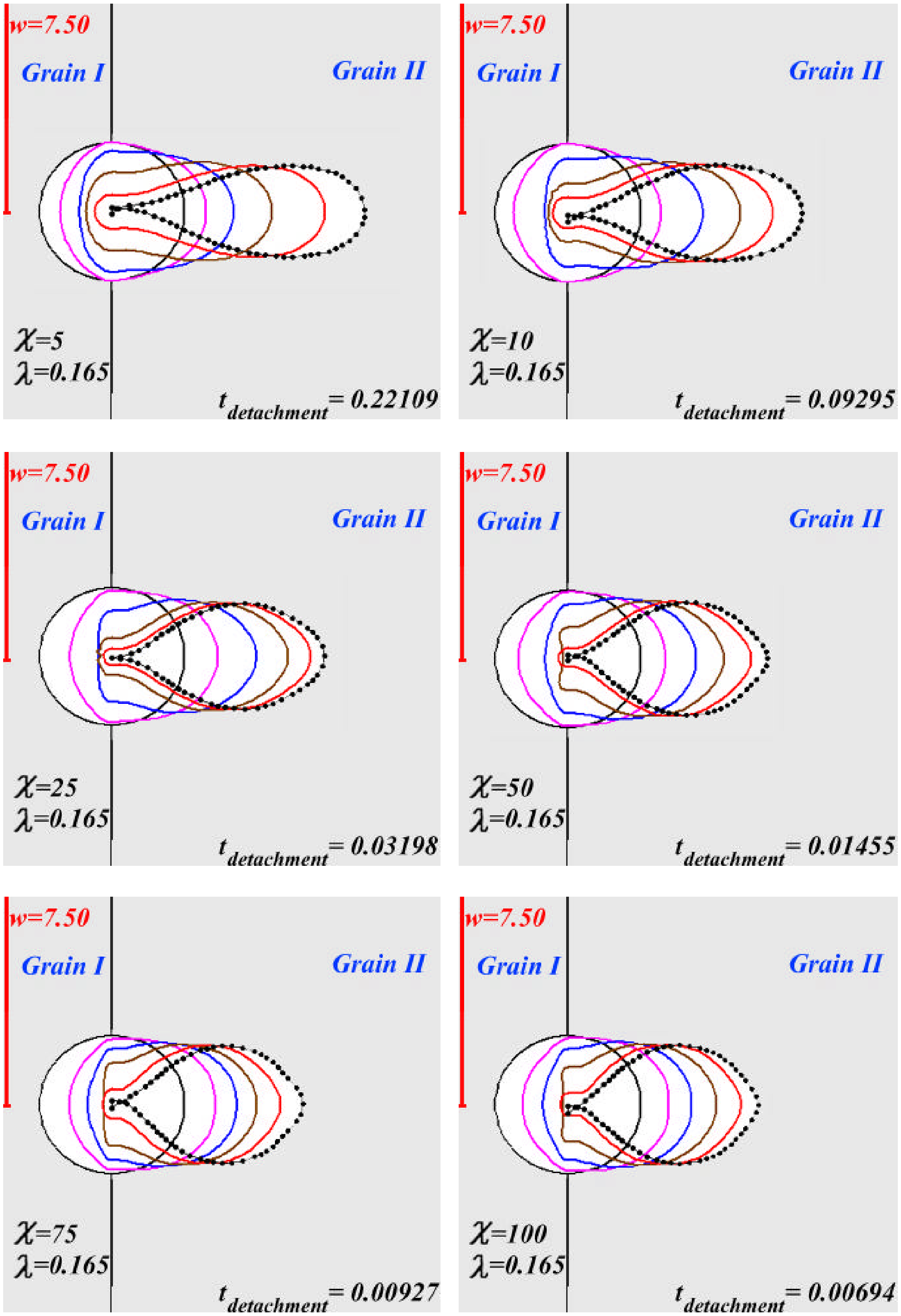

Figure 4.2.2.7: Void detachment process for different normalized electron wind intensities; the normalized interconnect with: $\overline{w} = 7.5$

The profound effect of the electron wind intensities χ on the shape evolution dynamics is observed in thin film aluminum interconnects. The relationship between the void detachment normalized time and the electron wind intensity is presented very systematic fashion in figure 4.2.2.8 for different normalized interconnect widths, in the range of 1.4 to 7.5.

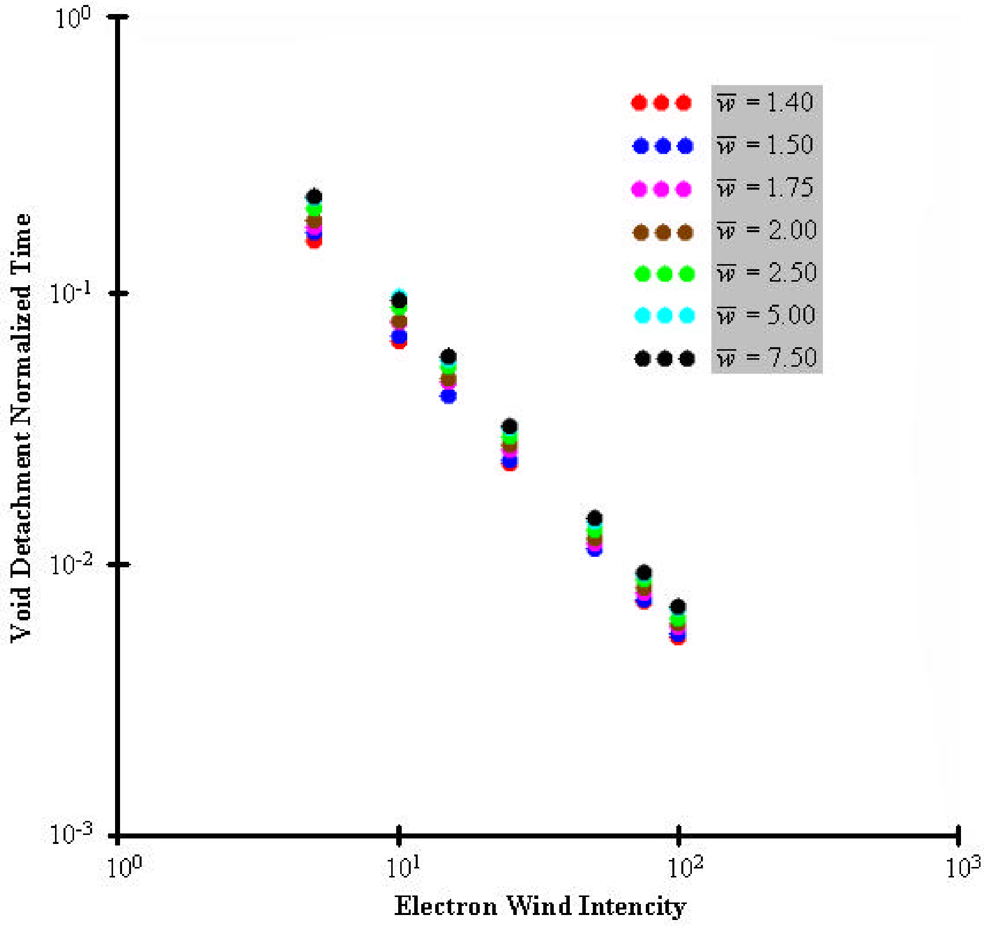

Figure 4.2.2.8: Void detachment normalized time vs. electron wind intensity graph for different normalized interconnect widths.

As can be seen immediately from the double logarithmic graphs in figure 4.2.2.8 that all those experimental points for a given normalized line width lie down on a straight line; and the following general relationship between the void detachment normalized time and the electron wind intensity may be written directly:

$$\bar{t}_d(\overline{w}, c) = i(\overline{w})\, c^{\,s(\overline{w})} \qquad (4.2.2.1)$$

in order to find the normalized interconnect width, $\overline{w}$, dependence of the intercept $i(\overline{w})$ and the slope $s(\overline{w})$ in Eq. (4.2.2.1), for each $\overline{w}$, $i(\overline{w})$ and $s(\overline{w})$ were found by using a least square data fitting method. And the relevant data can be seen in figure 4.2.2.9 and 4.2.2.10 for the intercept and the slope respectively.

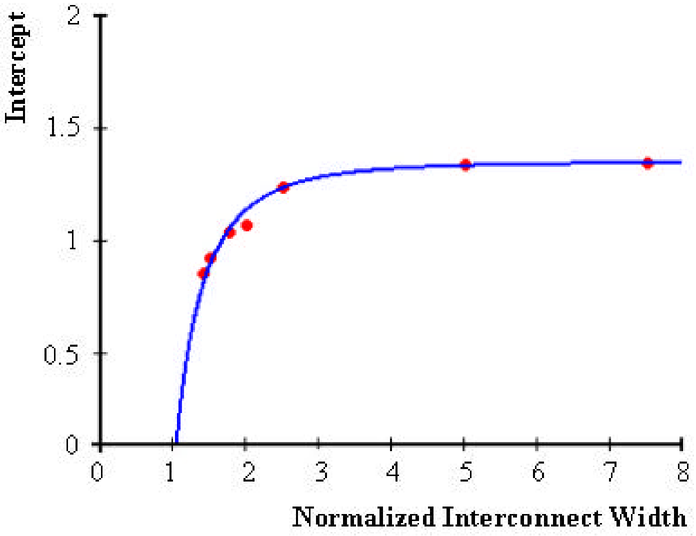

Figure 4.2.2.9: Intercept vs. normalized interconnect width.

From the data points, given in figure 4.2.2.9, the following relationship, whose graph can also be seen in the figure as the solid line, is found for the $\overline{w}$ dependence of the intercept;

$$i(\overline{w}) = 1.35\left(1 - \frac{1}{\overline{w}^{2.7}}\right) \tag{4.2.2.2}$$

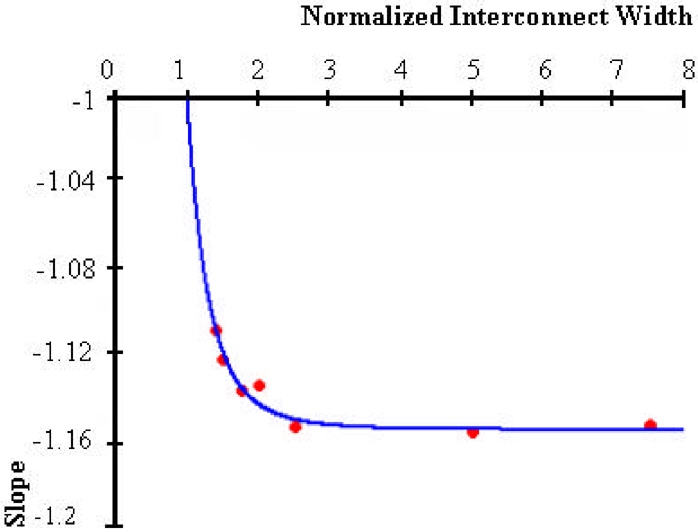

Figure 4.2.2.10: Slope vs. normalized interconnect width.

Similarly, from the data points, given in figure 4.2.2.10, the following relationship, whose graph can also be seen in the figure as the solid line, is found for the $\overline{w}$ dependence of the slope;

$$s(\overline{w}) = -1.155\left(1 - \frac{1}{(\overline{w} + 0.5)^5}\right) \tag{4.2.2.3}$$

By applying the inverse scaling procedures utilizing the normalized parameters that are given in Chapter 2.4 to our analytical findings deduced from Fig. 4.2.2.11, one can easily find the following equation for the void-grain boundary detachment time:

$$t_d = i(w, r_o)\frac{kTr_o^{\,4+2s(w,r_o)}}{D_s h_s \left(g_s \Omega_s\right)^{1+s(w,r_o)}}(eZrj)^{s(w,r_o)}(\mathrm{sec.}) \qquad (4.2.2.4)$$

In this model it is assumed that the interconnect failure takes place at the cathode end of the line by the accumulation of the voids, which are initially trapped or nucleated at the grain boundaries, under the action of the applied electromigration forces. Figure 4.2.2.11 shows the representation of such a failure mechanism.

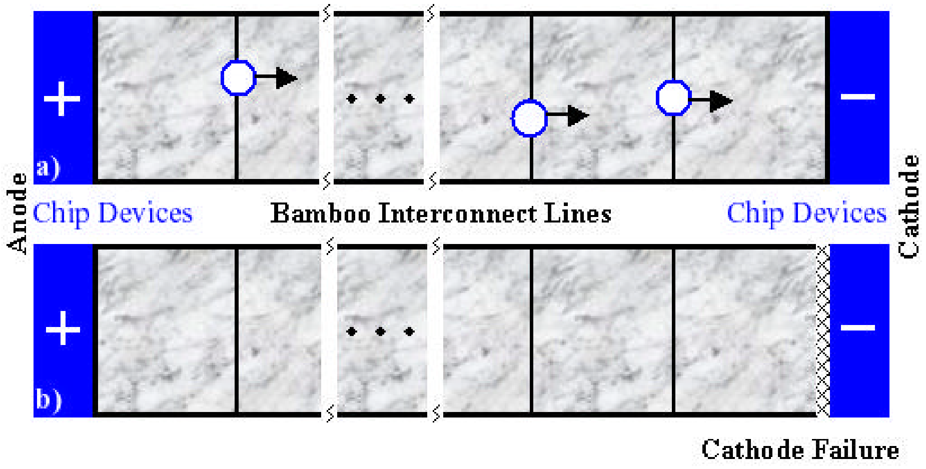

Figure 4.2.2.11: Cathode pad failure mechanism by loosing the electrical contact at the cathode. **a)** Interconnect with initially nucleated voids **b)** Failed interconnect.

In Eq. (4.2.2.4), $i(w, r_o)$ and $s(w, r_o)$ are given by the present choice of wetting parameter, which is equal to $l = 0.165$, and it is found that this parameter is sensitive to the wetting parameter, therefore the given formulas is in progress for only aluminum interconnects.

These simulation findings may be utilized even more effectively if one collaborates them, as a first order approximation with the analytical theory of Ho (1970) for a circular void in an infinite conductor, which gives the steady-state velocity by the relationship;

$$v = \frac{2\Omega_s \hat{\mathrm{M}}_s \, eZ\, r\, j}{r_o} \tag{4.2.2.5}$$

Therefore, the mean flight time for a void between two successive bamboo grain boundaries may be estimated as

$$t_{flight} = \frac{\ell_g}{v} = \frac{\ell_g r_o kT}{2D_s\, h_s} (eZrj)^{-1} (\text{sec.}) \tag{4.2.2.6}$$

where ℓ_g is the mean distance between bamboo grain boundaries or the grain size.

Since the detachment and the flight constitute two series or consecutive unit operations before the failure to occur, the effective cathode-pad failure time (CPFT) associated with a void initially nucleated at the $n_b{}^{th}$ bamboo grain is given by;

$$\begin{aligned} t_f &= n_b \left\lfloor t_d + t_{flight} \right\rfloor \\ &= n_b \left[\begin{matrix} i(w,r_o) \dfrac{kTr_o{}^{4+2s(w,r_o)}}{D_s\, h_s\, (g_s\, \Omega_s)^{1+s(w,r_o)}} (eZrj)^{s(w,r_o)} \\ + \dfrac{\ell_g r_o kT}{2D_s\, h_s} (eZrj)^{-1} \end{matrix} \right] (\text{sec.}) \end{aligned} \tag{4.2.2.7}$$

Since generally in the literature the unit of MTTF is given by hours it is convenient to write the Eq. (4.2.2.7) in terms of hours:

$$t_f = \frac{n_b}{3600}\left[\begin{array}{l} i(w,r_o)\dfrac{kT{r_o}^{4+2s(w,r_o)}}{D_s\,h_s\,(g_s\,\Omega_s)^{1+s(w,r_o)}}(eZrj)^{s(w,r_o)} \\ +\dfrac{\ell_g r_o kT}{2D_s\,h_s}(eZrj)^{-1} \end{array}\right](hrs.) \qquad (4.2.2.8)$$

where n_b is the mean number of bamboo grain boundaries that void is crossing before it contributes to the fatal breakdown at the cathode pad.

By using CPFT expression given by Eq. (4.2.2.8), it is possible to find the upper and lower boundaries of lifetime for such a failure process. In order to calculate these mentioned boundaries for the possible failure times for interconnects with bamboo or even near-bamboo structures it is needed to know that the value of threshold or critical void size for detrapping. For a given system parameters there is a threshold value for the void size only above which the voids detraps from the grain boundary and below which the voids are stationary at the grain boundaries.

In order to find this mentioned threshold value the necessary simulation experiments were carried out and the relevant data is presented in figure 4.2.2.12, in which the solid line is obtained by applying a best-fit procedure to the simulation data.

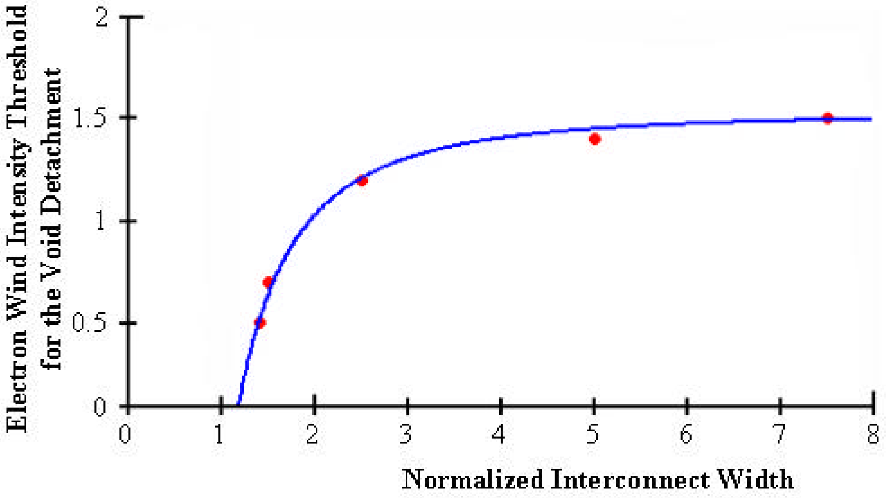

Figure 4.2.2.12: Electron wind intensity threshold value for the void detachment process vs. normalized interconnects width.

The obtained formula for the electron wind intensity threshold for the void detachment from the experimental points is given by:

$$c(\overline{w}) = 1.53\left(1 - \frac{1.3}{\overline{w}^2}\right) \qquad (4.2.2.9)$$

Similarly, by applying the inverse normalization procedure to Eq. (4.2.2.9), the critical radius for void detachment is found as a function of interconnect width and the applied current density and it is given by:

$$r_{crt}(w, j) = \left(\frac{1.3}{w^2} + \frac{eZrj}{1.53 g_s \Omega_s}\right)^{-1/2} \qquad (4.2.2.10)$$

In figure 4.2.2.13, the graph of critical void size for the detachment vs. applied current density for different interconnect widths can be seen.

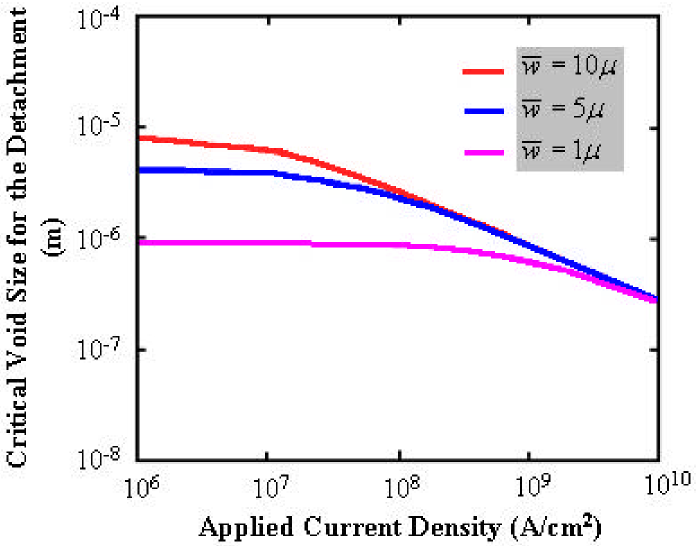

Figure 4.2.2.13: Critical void size for the detachment vs. applied current density for different interconnect widths.

The upper bond cathode failure time (UBCFT) can be estimated by assuming that the grain boundary in the neighborhood of the anode may also contribute to the CPFT phenomenon by dismissing only one void, which is the largest in size to move or detach from the grain boundary to break down the electrical contact at the cathode pad. From Eq. (4.2.2.10) this void size, which may be called as $r_{\max}$, can be calculated and given by the following expression:

$$r_{\max}(w) = \underset{j \rightarrow 0}{\ell im}\left[r_{crt}(w,\, j)\right] = \frac{w}{\sqrt{1.3}} \qquad (4.2.2.11)$$

The upper value of n_b, which now may be used in Eq. (4.2.2.8) can be estimated by knowing the location of the grain boundary situated just next to the anode pad, namely, $n_b = \frac{L}{\ell_g} - 1$ where L is the interconnect length. The substitution of these values of n_b and $r_{\max}$ in Eq. (4.2.2.8) immediately reveals the expression for UBCFT as:

$$UBCFT = \frac{\frac{L}{\ell_g} - 1}{3600} \left[\begin{array}{l} i(w, r_{\max}) \dfrac{kT r_o^{4+2s(w,r_{\max})}}{D_s\, h_s\, (g_s\, \Omega_s)^{1+s(w,r_{\max})}} (eZrj)^{s(w,r_{\max})} \\ + \dfrac{\mathrm{lg}\, r_o kT}{2 D_s\, h_s} (eZrj)^{-1} \end{array} \right] (hrs.) \quad (4.2.2.12)$$

Similarly the lower bond cathode failure time (LBCFT) can be formulated by the following argument. The connection presented by Eq. (4.2.2.8) immediately indicates that an interior void that is nucleated or trapped at the grain boundary having a radius just at the onset of the threshold level for the detrapping to occur is more detrimental for the catastrophic failure of interconnects at the cathode pads compared to any other larger interior voids. Consequently the lower bond for the cathode failure time (LBCFT) for interconnects with bamboo or even near-bamboo structures may be calculated by considering only those voids having threshold or critical size for detrapping. The substitution of r_{crt}, which is given by the Eq. (4.2.2.10), into Eq. (4.2.2.8) for the value of r_o and by taking $n_b = 1$, one obtains the following expression for LBCFT after some trivial manipulations:

$$LBCFT = \frac{1}{3600}\left\{ \begin{array}{l} i(w, r_{crt}(w, j)) \dfrac{kT(r_{crt}(w, j))^{4+2s(w, r_{crt}(w, j))}}{D_s\, h_s\, (g_s\, \Omega_s)^{1+s(w, r_{crt}(w, j))}} \\ \cdot (eZrj)^{s(w, r_{crt}(w, j))} \\ + \dfrac{\ell_g r_{crt}(w, j) kT}{2 D_s\, h_s} (eZrj)^{-1} \end{array} \right\} (hrs.) \qquad (4.2.2.13)$$

Since in the literature only the median time to failure (MTTF) or the time for the 50% failure are reported, one may add some raw statistics into Eq. (4.2.2.8) by taking into account the fact that each grain boundary is a potential site for the nucleation and growth of a void having critical size. Then only those grain boundaries, which are situated at the mid positions of the sampling interconnects and ejecting voids with critical size will be mainly responsible in contributing to the measured values of MTTF assuming that the test specimens are equally partitioned by the bamboo grains. Hence, one may have the following trivial expression for MTTF, which can be deduced from Eq. (4.2.2.8) by taking the $n_b = \frac{L}{2\ell_g}$,

$$MTTF = \frac{L}{7200\, \lg}\left\{ \begin{array}{l} i(w, r_{crt}(w, j)) \dfrac{kT(r_{crt}(w, j))^{4+2s(w, r_{crt}(w, j))}}{D_s\, h_s\, (g_s\, \Omega_s)^{1+s(w, r_{crt}(w, j))}} \\ \cdot (eZrj)^{s(w, r_{crt}(w, j))} \\ + \dfrac{\lg\, r_{crt}(w, j) kT}{2 D_s\, h_s} (eZrj)^{-1} \end{array} \right\} (hrs.) \qquad (4.2.2.14)$$

In order to test the prediction power of these formulas, they are tested with the experimental findings in the literature in terms of MTTF and temperature or current density. Initially, the temperature effect on the MTTF were investigated where the aluminum interconnect test materials chosen for this representation have the structural parameters tabulated in table 4.2.2.1, as deduced from the experimental studies performed by Black (1969) in near-bamboo, Schreiber and Grabe (1981) in polycrystalline and Lytle and Oates (1992) in bamboo aluminum lines.

Table 4.2.2.1: Aluminum structural parameters used in the experimental literature.

Structural Parameters	*Black (1969)*	*Schreiber and Grabe (1981)*	*Lytle and Oates (1992)*
$2w\ (m)$	15	10	1.25
$L\ (m)$	1372	800	6100
$\ell_g\ (m)$	8	1.5	1.2
$j\ (MAcm^{-2})$	0.75	1	3
$T\ (^oK)$	400-550	425-525	460-550
Line Type	Near-Bamboo	Polycrystalline	Bamboo

Table 4.2.2.2: Aluminum parameters, used in the experimental literature and the necessary universal constants.

Aluminum Parameters		*Universal Constants*	
Z_{Al}	8	e	$1.6 \cdot 10^{-19}\ C$
r_{Al}	$2.74 \cdot 10^{-8}\ ohm \cdot m$	k	$1.38 \cdot 10^{-23}\ J/atom{-}^oK$
$\Omega_{s\ Al}$	$1.66 \cdot 10^{-29}\ m^{-3}$		
$h_{s\ Al}$	$2.86 \cdot 10^{-10}\ m$		
$g_{s\ Al}$	$0.98\ J \cdot m^{-2}$		

The value of effective charge, Z_{Al}, given in Table 4.2.2.2, gives the most consistent analysis of the data concerning the current and temperature dependence of experimentally observed MTTF values reported in the literature.

In figure 4.2.214 the experimental median time to failure versus inverse temperature data on the aluminum interconnect with bamboo or near-bamboo microstructures, which are reported by three different authors are presented as a semi-logarithmic plot in connection with the best matching MTTF and/or LBCFT curves.

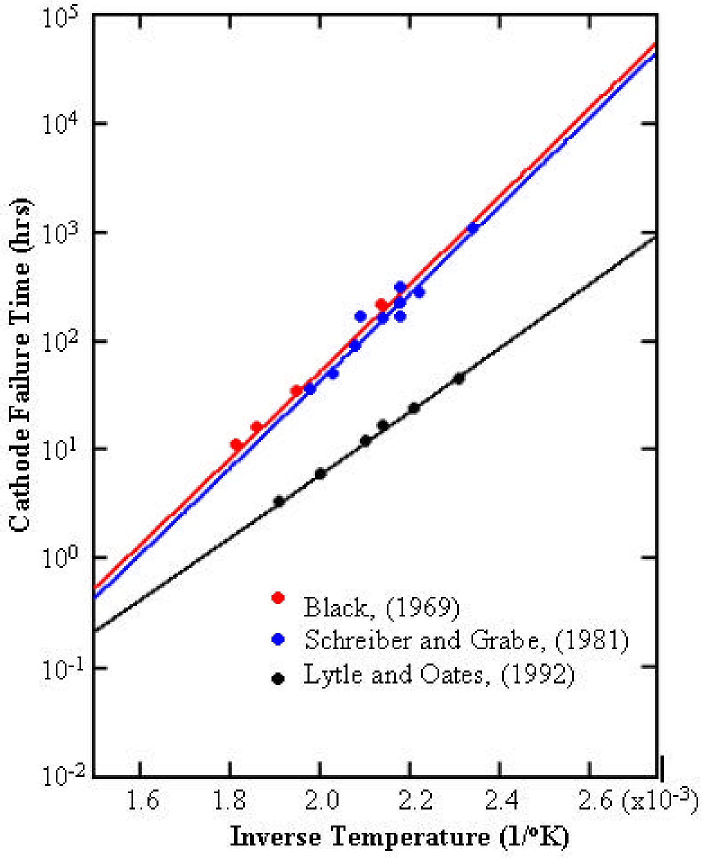

Figure 4.2.2.14: Cathode failure time vs. inverse temperature.

The experimental findings by Black (1969) for large crystallites and Lytle and Oates (1981) for the no-voids specimens are analyzed by MTTF curve fittings, which resulted a new set of diffusion coefficients for the void and/or the technical surface atomic migration such as $D = 2.0 \cdot 10^{-2} e^{-0.84eV/kT} (m^2 \sec^{-1})$ and $D = 1.0 \cdot 10^{-2} e^{-0.84eV/kT} (m^2 \sec^{-1})$, respectively. Test specimens used by these authors have the median line width versus grain size ratios of about $2w/l_g = 1.9$ and 1.0, respectively, which are also tested at different current densities. The SEM micrographs shows that void responsible for the line failure is nucleated at the Al/SiO$_2$ interface, and most probably at the triple junction between the intersecting grain boundary and the technical surface. This also explains why one has obtained high activation enthalpies for these specimens. Because of the contamination of the void surface by oxygen and silicon atomic species during the nucleation stage, a new set of trap centers for the vacancies are created there, which inhibits their motion by contributing an extra binding energies to the activation enthalpy of motion, and in addition it may cause substantial decrease in their concentration as well.

The most interesting situation in figure 4.2.2.14 arises in the analysis of the data presented by Schreiber and Grabe (1981) in terms of LBCFT formula utilizing the microstructure information given by these authors, which indicates that the line width versus grain size ratio is about equal to 4. In this case, namely for the polycrystalline materials LBCFT formula developed above results a best fit by employing a diffusion coefficient for the void surface mass transfer as $D_s = 1.5 \cdot 10^{-6} e^{-0.62eV/kT} (m^2 \sec^{-1})$, which is in agreement with the mono-vacancy diffusion coefficient in aluminum reported by Seeger and Mehrer (1969), namely $D_v(Al) = 3.7 \cdot 10^{-6} e^{-0.62eV/kT} (m^2 \sec^{-1})$. This finding strongly supports the fact that the specimens tested by Schreiber and Grabe (1981) are super saturated by mono-vacancies, which are created by the dislocation climb during the relaxation of the (tensile) hydrostatic thermal stresses caused by rigid encapsulation and /or due the stiff substrate attachment procedure.

After temperature test, the effect of current density on the MTTF are tested with the experimental findings in the literature, where the aluminum interconnect test materials chosen for this representation have the structural parameters tabulated in table 4.2.2.3, as deduced from the experimental studies performed by Black (1969) and Schreiber and Grabe (1981) in bamboo aluminum lines and Lytle and Oates (1992) in bi-crystal aluminum lines.

Table 4.2.2.3: Aluminum structural parameters used in the experimental literature.

Structural Parameters	*Kinsborn (1980)*	*Cho and Thompson (1989)*	*Longworth and Thompson (1992)*
$2w\ (m)$	1	2.2	2
$L\,(m)$	250	100	1000
$\ell_g\,(m)$	10	3	500
$j\,(MAcm^{-2})$	2.0	1.2	2.5
$T\ (^oK)$	473	548	523
Line Type	Bamboo	Bamboo	Bi-crystal

In figure 4.2.2.15, the data, obtained from the works of these mentioned authors, are plotted by utilizing Eqs. (4.2.2.12,13 and 14) on a double logarithmic scale as a function of applied current density. In this plot in order to obtain a better view the value of cathode failure times are multiplied with 10 and 100 for the data of Kinsborn (1980) and of Longworth and Thompson (1992) respectively.

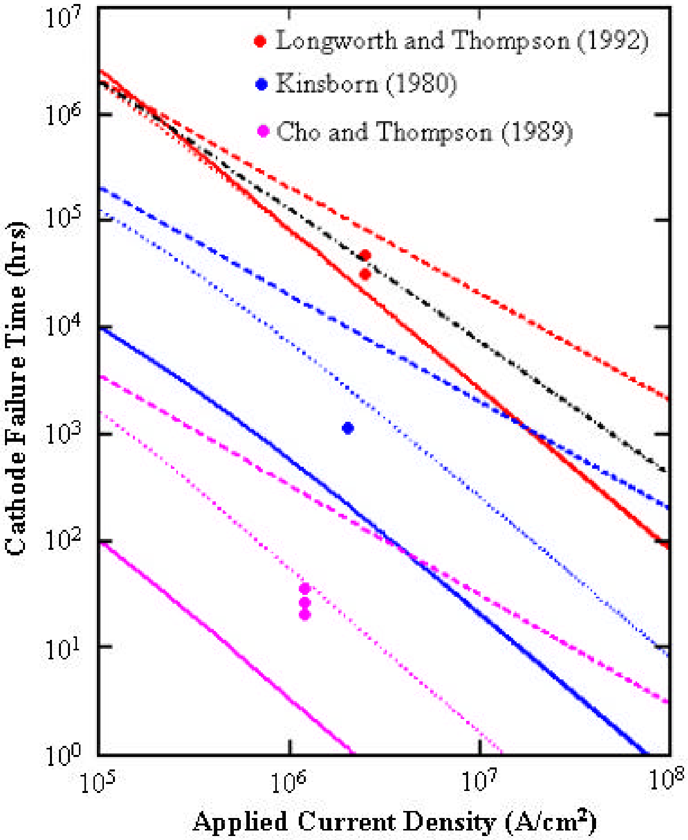

Figure 4.2.2.15: Cathode failure time vs. applied current density (Solid lines: UBCFT, dotted lines: MTTF, dashed lines: LBCFT, dad-dashed line: LGMCFT).

In the computer simulation plots reproduced in this figure, the void surface diffusion coefficient D_s and the effective value of Z are chosen according to that findings by reevaluating the experimental MTTF versus temperature data presented in figure 4.2.2.14 as $D_s = 1.5 \cdot 10^{-6} e^{-0.62eV/kT} (m^2 \sec^{-1})$ and $Z = 8$ respectively.

As can be seen immediately from the plots presented in figure 4.2.2.15 that one has with an exception of bi-crystal excellent agreements between the theory and the experimental results, which are selected from three different laboratories that are utilizing completely different microstructures, current densities and temperatures. For bamboo and near-bamboo structures the correlation between theoretical and experimental MTTF values are almost perfect. In the case of bi-crystals experimental points lie at the mid of the upper bond and lover bond curves in the logarithmic scale. By the way for bi-crystals MTTF formula given by Eq. (4.2.2.14) is exactly equivalent to the expression for LBCFT formula given by Eq. (4.2.2.13). Therefore a priory one may use the logarithmic mean value of LBCFT and UBCFT expressions, which is denoted as LGMCFT, as plotted in figure 4.2.2.15 this line yields better prediction than MTTF expression. Unfortunately, the published experimental observations in the literature have performed on those test specimens, which are not characterized sufficiently as far as the microstructures are concerned.

As can be seen from figure 4.2.2.15 that both median times to failure reported by above cited authors (Longworth and Thompson, 1992) for $\Sigma 13[100]$ and $(115)/(100)$ bi-crystals are in agreement with our prediction utilizing LGMCFT formulation. However, it seems that this agreement is fictitious because the appearance and location of failure sites observed by Longworth and Thompson

(1992) indicate that the failure mechanism is likely to involve an accelerated grain boundary grooving induced by electromigration.

Experimental current density exponent reported for polycrystalline aluminum in the literature (Chang and Thompson, 1997; Arzt *et al.*, 1996) shows rather a wide range of values $|n| = 1 \text{ to } 6$ depending upon the alloying elements, the microstructure, the processing and service conditions, and the method of data analysis. According to Chang and Thompson (1997) and Arzt *et al.* (1996) the current-density dependence of the MTTF of a single-crystal Al conductor line reveals that the exponent n is closer to -2 rather than -1 and the activation enthalpy of the process is about $1.0\,\text{eV}$. The value of the current exponent urged them to speculate that the nucleation of void is the rate controlling step rather than the void motion and growth in their experimental studies. In order to explain the activation enthalpy in this magnitude, which does not coincide with any known drift-diffusion paths, these authors made further conjecture that the drift-diffusion path goes through the interfacial layer between Al and Al_2O_3. However, Schreiber (1981) clearly states that up to now no one has even measured the electromigration kinetics at the technical surfaces such as (Al - Al_2O_3) interface. Because of the fact that the existence of the strong covalent bond between chemical species such as aluminum and oxygen at that interface reduces drastically not only the electrical conduction but also the atomic hopping motion through the vacancy exchange mechanism which relies on the bound breaking and bending during the vacancy formation and displacement, respectively.

The careful measurements by Schafft *et al.* (1985) on Al lines covered with SiO_2 passivation layers revealed the effect of heating on n and by knowing the temperature increase of the line they were able to subtract its contribution from the measured MTTF are obtained $n = -1.5$. Liu *et al.* (2001) obtained exactly same current exponent n for the void growth rate, which is propagating along the grain boundary, in interconnects with an electrical current. Similarly Suo *et al.* (1994) and Klinger *et al.* (1966) found that the slit propagation speed is proportional to $E_0^{3/2}$, which yields an equivalent current exponent since MTTF is inversely connected to the propagation velocity.

For the complete interconnect failure process, a value of $n = -2$ as a current exponent was introduced by Black (1969) based on the assumption that the momentum transfer from electrons to Al atoms is proportional to the Al flux and the drift velocity of electrons. This is in contradiction to the common atomistic description of electron transport (Wever, 1973). A more rigorous derivation of $n = -2$ by Shatzkes and Lloyd (1986) and Kirchheim and Kaeber (1991) relies on the assumption that the time necessary for the attainment of a supersaturation of vacancies in semi-infinite Al line is equal to the median time to failure, MTTF. Kirchheim and Kaeber (1991) also observed that if the MTTF values are plotted with respect to the current density, j, instead of the reduced current density $\left(j - j_{crit}\right)$ one would get the slope about $n = -1.5$ in double logarithmic scale. All these model calculations inherently assume that the interconnect failure takes place at the cathode pad (or stud) by the accumulation or creation of voids in that region. Therefore, the failure mechanisms associated with the slit or wedge shape defects formation by growing inter or edge voids while they are proceeding along the interconnect are completely ignored by these authors (Black, 1969; Shatzkes and Lloyd, 1986; Kirchheim and Kaeber, 1991).

The MTTF concept developed in this study was also used for the determination of current exponent. In order to do that the structural parameters tabulated in table 4.2.2.3 were used. In figure 4.2.2.16 the MTTF vs. applied current density graph can be seen for a wider range of applied current density and without any multiplication as done in figure 4.2.2.15.

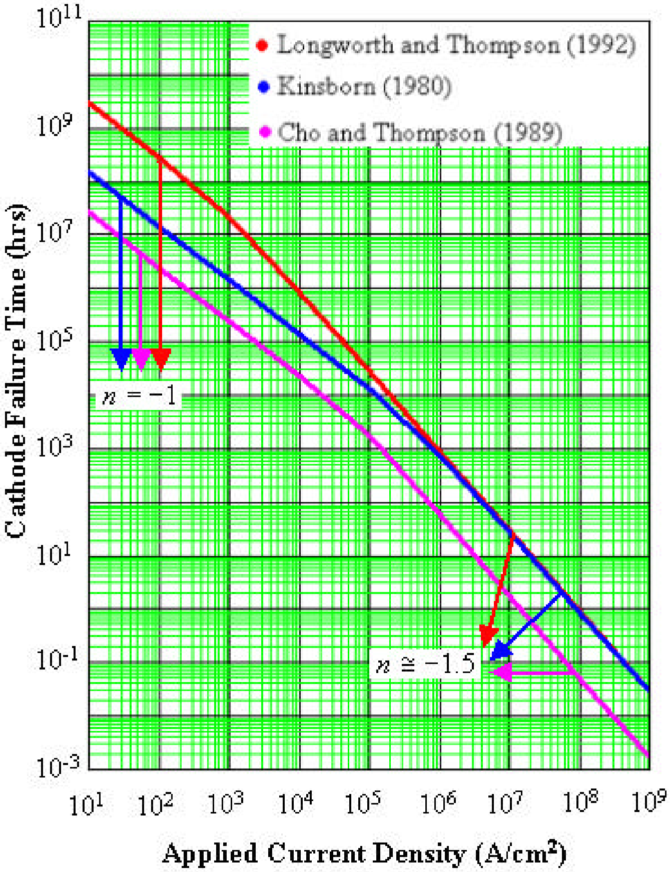

Figure 4.2.2.16: MTTF vs. applied current density.

Figure 4.2.2.16 shows clearly that the apparent current exponent is given by $n \cong -3/2$ and $n = -1$ for low and high current density domains, respectively, having a smooth transition point, which is strictly depending upon the grain size. The large grain size prefers to have a lower current density transition point than the small grain size materials.

As far as the current density dependence is concerned the MTTF relationship, which can be directly applicable to the pre-existing (the stress induced voids) over-critical size voids indicates that there may be two different regimes exist namely low current density region and high current density region. The first regime is governed by the first term of Eq. (4.2.2.14), namely detachment term, and the second regime is controlled by the second term of Eq. (4.2.2.14), which is noting but the mean flight time of a void before it reaches the cathode pad or stud.

Similarly, according to figure 4.2.2.15, the curves, which represent the UBCFT for the selected, interconnect system parameters clearly indicate that the difference between LBCFT and UBCFT increases with the current density. The current exponent is found to exactly $n = -1$, and UBCFT lines are in agreement with the experimentally observed upper bond for the lognormal distribution of failure times with wide variety of microstructures.

According to the relationship UBCFT, which is the only expression presented above that involves a linear line width $2w_0$ dependence is not in accord with the suggestion made by Arzt *et al.* (1996) for the bamboo structures. They found that, as w_0 is decreased, median time to failure MTTF decreases to a minimum and then increases continuously having a turning point at about $2w_0 / \ell_g \cong 2$. Actually Arzt *et al.* (1996) clearly stated that when grain size and line width are comparable, a 'near bamboo' structure results with strong flux divergences at the ends of the polycrystalline segments. Therefore, one may speculate that the region studied by Cho and Thompson (1989) where the grain size is less than the line width should be considered as polycrystalline material rather than the simple bamboo structure as suggested by Arzt *et al.* (1996). Eq. (4.2.2.14) is also clearly reveals that the mean lifetime is directly proportional with the interconnect line length or the stud-to-stud distance.

CONCLUSIONS

A completely normalized and scaled partial differential equation obtained by using irreversible thermodynamic treatment of morphological evolution of curved void surface layer, interacting with the grain boundaries, at the presence of electromigration-induced forces. This phenomenological treatment is very useful for the computer simulation studies of electromigration phenomena in metallic thin film interconnects.

The computer experiments clearly indicate the importance of the surface diffusion anisotropy for the open circuit failures in interconnects by leading the premature formation of a slit or wedge shaped void circuit configuration, and the further enhancement of this deterioration due to void growth process caused by supersaturated vacancies in the bulk matrix.

In order to increase the lifetime of the metallic interconnect thin films having bamboo structure one should choose the highest symmetry plane and the most close-packed direction, such as $\{111\}\left\langle 1\bar{1}0\right\rangle$ in fcc metals and alloys as a texture. The normalized failure time $\bar{t}_f$ indicates that for a given electromigration force intensity; the surface diffusivity should be kept as small as possible. In the case of anisotropic surface diffusivity, this requirement can be achieved by proper texture selection as described above. Another possibility may be to use certain doping elements that preferentially segregate at void interface and having high affinity to trap mobile vacancies in so doing hinder their hopping motion.

The normalized growth rate parameter ($\hat{\mathrm{M}}_{vb}\Delta\bar{g}_{vb}$) should also be kept as small as possible. In order to give an idea for the importance of this parameter, aluminum interconnect material properties are utilized, and it is found that $\hat{\mathrm{M}}_{vb}\Delta\bar{g}_{vb} = -1$ corresponds to $10^{-1} m^2 / hour$ in the rate of void area increase at room temperature, which is factor of three smaller than the value being employed in the work of Kraft and Arzt (1997) in their computer simulation studies, where electron intensity parameter is about $c = 1$. The achievement of this second condition is more complicated because it may depend on many factors through generalized mobility as well as the Gibbs free energy of transformation. Since $\Delta\bar{g}_{vb}$ is a normalized quantity, this second requirement can be partially achieved by increasing the surface specific Gibbs free energy by doping with certain alloying elements that prefers segregation at free surfaces (Ogurtani, 1975; 1979). In addition, $\Delta\bar{g}_{vb} \leq 0$ relies on the vacancy supersaturation at the bulk region. Any trapping sites for vacancies such as alloying elements having large hydrostatic strain field, $Tr\,\overline{\overline{l}} >> 0$, (compression) may be very effective to hinder the growth process. Similarly, nano-size finely dispersed second phase particles and/or inclusions, which are generating large hydrostatic stress fields $Tr\,\overline{\overline{s}} >> 0$ will be very powerful agents to inhibit growth phenomenon, because they do not only trap the vacancies ($\Delta\bar{g}_{vb} = 0$), but also create barriers ($\hat{\mathrm{M}}_{vb} = 0$) for the motion of the interface between void and bulk phase.

It may be also stated that the most important stage in the development of the void, which cause damage is the heterogeneous nucleation of vacancy clusters to form void embryos just at the interface between substrate (and/or passivation layer) and the interconnect matrix. The rate of occurrence of this event could definitely be controlled by selecting those substrate materials having very high surface specific Gibbs free energies compared to the specific Gibbs free energy associated with the interface between substrate and the interconnect.

The present computer simulation studies have resulted certain fundamental and analytical connections concerning the void-grain boundary detachment time and the threshold level of the normalized electron wind intensity at the on set of the detrapping process. These expressions are combined together to produce three important and technologically useful relationships in the evaluation of the mean time to failure or the upper and lower bonds for the life time of an interconnect in terms of the applied current density, surface diffusivity, and the structural parameters such as grain size, line width and the interconnect stud to stud length. Even though these expressions obtained for an isotropic bamboo structure they still give excellent prediction of MTTF not only for the near-bamboo structures but also for the polycrystalline or bi-crystalline interconnects as can be easily anticipated from figure 4.2.2.15.

Unfortunately in general, experimental evidence (Chang and Thompson, 1997); Arzt et al., 1996; Seeger and Mehrer, 1969) indicates that the heterogeneous nucleation of voids at the specimen edges decorated by triple junctions is predominant mechanisms in polycrystalline materials (bamboo or near bamboo structures), the rate of which is few orders of magnitude higher than the homogenous nucleation of interior voids. Therefore one should try to inhibit heterogeneous nucleation at the technical specimen surfaces by introducing compression stresses utilizing special coating material and thermo mechanical treatments.

This model, however still does not take into account explicitly the incubation time for the homogeneous nucleation of interior voids by assuming a priory that the rate controlling unit processes are the void detachment from the grain boundaries and its migration kinetics between two successive boundaries. Therefore, if one could suppress the heterogeneous nucleation of the edge voids at the triple junction that is the intersection point between bamboo grain boundary and the technical surface of the interconnect, then substantial improvement in the interconnect life time may be realized. One way of achieving this objective is to produce some kind of hot sputtered coating layer on the cold interconnect substrate that should generate residual compressive stresses at the technical surfaces at the device operating temperature. By this way it is possible to inhibit vacancy clustering and eventually void nucleation at the specimen edges and triple junctions. One order of magnitude enhancement obtained by Arzt *et al.* (1996) in Al-Si-Cu interconnects by utilizing hot sputtering conditions rather then the cold sputtering justifies this speculation that the compressive stresses at the technical surface are very important agent to inhibit the heterogeneous nucleation and thereby to improve the service life of the interconnects.

The present theory may be very useful to obtain the full knowledge of the surface diffusivities by furnishing not only the activation enthalpies but also the diffusion constant denoted by D_o in the literature. Analysis of the numerous experimental data cited in this thesis (Black, 1969; Cho and Thompson, 1989; Longworth and Thompson, 1992; Lytle and Oates, 1992; Schreiber and Grabe, 1981; Kisbron, 1980) gives very consistent and highly accurate values for diffusion constant and the enthalpy namely: $D_o = 1.5 \cdot 10^{-6} m^2 / \sec$ and $Q = 0.62 eV$. These values are very close to those reported by Seeger and Mehrer (1969) for mono-vacancies in aluminum. Therefore the present simulation studies strongly reveal the fact that the inner void dictated failure mechanisms is solely controlled by the athermal mono-vacancy diffusion along the void interface, which means that there is a substantial vacancy saturation in those test specimens reported above cited references. Similarly, in those interconnect specimen where the failure occurs by voids nucleated at the technical surfaces or edges the failure kinetics has completely different drift-diffusion parameters, and in the case of aluminum can be given as $D_s = 2.0 \cdot 10^{-2} e^{(-0.84 eV)} m^2 / \sec$.

As a final point, the followings are the future recommendations:

As discussed in this thesis, Gibbs free energy enters into the formulation, which is in general not constant, but rather a function of space and time due to any possible compositional variations at the reaction front during the void evolution phenomenon. Therefore, the exact solution of the growth problem still involves the complete numerical solution of the time dependent diffusion equation with drift (convective) term, and coupled to pseudo-static electric field by utilizing proper boundary and initial conditions.

The real challenging problem in the repertoire is the simulation of Blech Effect concurrently occurring with void evolution dynamics in those interconnects, which are supported or encapsulated by the stiff insulating materials causing extremely high stresses (tension and/or compression) during the unavoidable process and operation oriented thermal cycling treatment.

BIBLIOGRAPHY

AMES I., d'HEURLE F. M., and HORSTMAN R., IBM J. Res. Develop., **4**, 461 (1970).

ARZT E., and NIX W. D., J. Mater. Res. **6**, 731-736 (1991).

ARZT E., KRAFT O., NIX W. D. and SANCHEZ J. E., J. Appl. Phys., **76** (3), 1563 (1994).

ARZT E., O. KRAFT, SPOLENAK R. and YOUNG-CHANG Joo, Z. Metallk., **87**, 934 (1996).

BARDEEN J. and HERRING C., *Atom Movements* (American Society for Metals, Ed: J. H. Hollomon, Cleveland, Ohio, USA), p. 87 and 93 (1951).

BARSOUM M.W., *Fundamentals of Ceramics* (The McGraw-Hill Companies, Inc., New York, USA) (1997).

BEER G. and WATSON J. O., *Introduction to Finite and Boundary Element Methods for Engineers* (John Wiley & Sons, New York, USA), p. 141 (1992).

BLACK J. R., IEEE ED, **16**, 338 (1969).

BLECH I. A., J. Appl. Phys., **47**, 1203-1208 (1976).

BOWER A.F., and FREUND L. B., Mat. Res. Soc. Symp. Proc. (Eds: A. S. Oates, W. F. Filter, R. Rosenberg, A. L. Greer, K. Gadepally), V **391**, p. 177 (1995).

BREBBIA C. A. and DOMINGUEZ J., *Boundary Elements An Introductory Course* (McGraw Hill, New York, USA), p. 160 (1992).

BUFF F. P., J. Chem. Phys., **23**, 419 (1955).

CAHN J., ELLIOTT C., and NOVICK-COHEN A., Eur. J. Appl. Math., **7**, 287 (1996).

CHAN J. W. and HILLARD J. E., J. Chem. Phys., **28**, 258 (1958).

CHANG J. Y. and THOMPSON C. V., J. Appl. Phys., **81** (9), 6062 (1997).

CHO J., and THOMPSON C. V., Appl. Phys. Lett., **54**, 2577 (1989).

CHRISTOU A., *Electromigration & Electronic Devise Degradation*, (John Wiley & Sons, Inc., New York, USA) (1994).

CHUANG T. and RICE J. R., Acta Metall., **21**, 1625 (1973).

COCKS A. C. F., Acta Metall. Mater., **42** (7), 2197 (1994).

De DONDER Th. and Van RYSSELBERGHE P., *Affinity* (Stanford University Press, Menlo Park, California, USA) (1936).

De GROOT S. R., *Thermodynamics of Irreversible Processes* (North-Holland Pub. Co., Amsterdam, Holland), p. 98 (1951).

DEFAY R., PRIGOGINE I., and BELLEMANS A., *Surface Tension and Adsorption* (John Wiley & Sons, New York, USA) (1966).

d'HEURLE F. M., and AMES I, Appl. Phys. Lett., **16**, 80 (1970).

GANGULEE A., and d'HEURLE F. M., Thin Solid Films, **16**, 227 (1973).

GAO Y. X, FAN H., XIAO Z., Mechanics of Materials, **32**, 315 (2000).

GARDNER D. S., MICHALKA T. L., FLINN P. A., BARBEE Jr T. W., SARASWAT K. S., and MEINDL J. D., IEEE Trans. Electron. Devices, **ED-32** (1985).

GERARDIN M., C. R. Acad. Sci., **53**, 727 (1861).

GIBBS W., *The Collected Works of J. Willard Gibbs, Vol. I Thermodynamics* (Yale University Press, USA), p. 226 (1948).

GLANSDORFF P., and PRIGOGINE I., *Thermodynamics of Structure, Stability and Fluctuations* (Wiley-Interscience, New York, USA), p. 126 (1971).

GOTTSTEIN G. and SHVINDLERMAN L. S., Acta Mater., **50**, 703 (2002).

GREER A. L., http://www.msm.cam.ac.uk/mkg/e_mig.html (1998).

GUGGENHEIM E. A., *Thermodynamics*, 3rd Edition (North-Holland, Amsterdam, Holland), p. 46 and 375 (1959).

GUNGOR M. R. and MAROUDAS D., J. Appl. Phys., **85** (4), 2233 (1999).

HAASE R., *Thermodynamics of Irreversible Processes* (Addison-Wesley, Massachusetts, USA), p. 245 (1969).

HANSEN M., *Constitution of Binary Alloys* (McGraw-Hill, New York, USA) (1958).

HERRING C., *The Physics of Powder Metallurgy*, (Ed: W. E. Kinston, McGraw Hill, New York, USA), p. 143 (1951).

HERZIG C. H., and WIEMANN W., Phys. Status. Solidi A, **26**, 459 (1974).

HO P. S., J. Appl. Phys., **41**, 64 (1970).

HO P. S., LEWIS J. E., and HOWARD J. K., Thin Solid Films, **25**, 302 (1975).

HO P. S., and KWOK T., Rep. Prog. Phys., **52**, 301 (1989).

HOWARD J. K., and HO P. S., US patent, 4017890 (1977).

HOWARD J. K., WHITE J. F.,and HO P. S., J. Appl. Phys., **49**, 4083 (1978).

HUANG P., LI Z. and SUN J., Model. Simul. Mater. Sci. Eng., **8**, 843 (2000).

HUNTINGTON, H.B., and GRONE, A.R., J. Phys. Chem. Solids, **20**, 76 (1961).

JOO Y. C. and THOMPSON C. V., J. Appl. Phys., **81** (9), 6062 (1997).

KAZARYAN A., WANG Y. and PATTON B. R., Scripta Mater., **41** (5), 487 (1999).

KHENNER M., AVERBUCH A., ISRAELI M. and NATHAN M., J. Comput. Phys., **170**, 764 (2001).

KINSBRON E., BLECH I. A., and KOMEM Y., Thin Solid Films, **46**, 139 (1977).

KINSBRON E., Appl. Phys. Lett., **36**, 968 (1980).

KIRCHHEIM R., Acta Metall. Mater. **40**, 309 (1992).

KIRCHHEIM R. and KAEBER U., J. Appl. Phys., **70**, 172 (1991).

KLINGER L. M., CHU X., MULLINS W. W. and BAUER C. L., J. Appl. Phys., **80**, 6670 (1966).

KORHONEN M. A., PASZKIET C. A., and LI C. Y., J. Appl. Phys., **69**, 8083 (1991).

KRAFT O., MÖCKL U. E., and ARZT E., Quality and Reliability Eng. Int., **11**, 279 (1995).

KRAFT O. and ARZT E., Acta Metall., **45**, 1599 (1997).

KRÖNER E., *Kontinuumstheorie der Vwersetzungen und Eigenspannungen*, (Springer, Berlin, Germany) (1958).

KUKHERENKO S., PAN J. and YEOMANS J. A., Comput. Mater. Sci., **18**, 76 (2000).

LAPLACE P. S., *Mechanique Ceileste* (suppl. au X Livre, Impr. Imeriale), V **10**, p. 147 (1806).

LIFSHITZ E. M. and PITAEVSKII L. P., *Statistical Physics* (Pergamon Press, Oxford, England), Part II, p. 178 (1980).

LIU C. Y., LEE S. and CHUANG T. J., Mat. Sci. Eng. B-Solid, **86**, 101 (2001).

LLOYD J. R., and NAKAHARA S., Thin Solid Films, **72**, 451 (1980).

LLOYD J. R., Semicond. Sci. Technol., **12**, 1177 (1997).

LONGWORTH H. P. and THOMPSON C. V., Appl. Phys. Lett., **60**, 2219 (1992).

LYTLE S. A. and OATES A. S., J. Appl.Phys., **71**, 174 (1992).

MADDEN M. C., ABRATOWSKI E. V., MARIEB T. and FLINN P. A., Mat. Res. Soc. Symp. Proc. (Eds: C. V. Thompson, J. R. Lloyd), V**265**, 33 (1992).

MAHADEVAN M., and BRADLEY R. M., J. Appl. Phys., **79** (9), 6840 (1996).

MAHADEVAN M. and BRADLEY R. M., Physica D, **126**, 201 (1999).

MATHEWS J. H., *Numerical Methods for Mathematics, Science and Engineering* (Prentice-Hall International Edition, New Jersey, USA), p. 148 (1992).

MULLINS W. W., J. Appl. Phys., **28** (3), 333 (1957).

MULLINS W. W., Interface Sci., **9**, 12 (2001).

MURR L. E., *Interfacial Phenomena in Metals and Alloys* (Addison-Wesley Pub. Co.), p. 10 (1975).

NEEDLEMAN A. and RICE J. R., Acta Metall., **28**, 1315 (1980).

NIX W. D., Metall. Trans., **20**A, 2217 (1989).

NIX W. D., and ARZT E., Metall. Trans., **23**A, 2007 (1992).

NOVICK-COHEN A., Physica D, **137**, 1 (2001).

NOWICK A. S. and BERRY B. S., *Anelastic Relaxation in Crystalline Solids*, (Academic Press, New York, USA), p. 180 (1972).

OHRING M., J. Appl. Phys., **42** (7), 2653 (1971).

OGURTANI T. O., Metall. Trans. AIME, **6**A, 493 (1975).

OGURTANI T. O., Metall. Trans. AIME, **10**A, 1505 (1979).

OGURTANI T. O. and SEEGER A. K., J. Chem. Phys., **79** (10), 5041 (1983).

OGURTANI T. O. and SEEGER A. K., J. Appl. Phys., **55**, 2857 (1984).

OGURTANI T. O., *Irreversible Thermokinetics Theory of Surfaces and Interfaces with a Special Reference to Triple Junctions (unpublished)* (2000).

OGURTANI T. O. and OREN E. E., J. Apply. Phys., **90** (3), 1564 (2001-a).

OGURTANI T. O. and OREN E. E., Mat. Res. Soc. Symp. Proc. (Eds: D. Edelstein, G. Dixit, Y. Yasuda, T. Ohba), V **16**, p. 483 (2001-b).

OGURTANI T. O. and OREN E. E., *Irreversible Thermokinetics Theory of Surfaces and Interfaces with a Special Reference to Void Intergranular Motion under the action Electromigration Forces, (unpublished)* (2003).

ONO S. and KONDO S., *Encyclopedia of Physics* (Ed. Flügge, Berlin, Germany), Vol. **X**, p. 159 (1960).

OREN E. E., M. Sc. Thesis, Middle East Technical University (2000-a).

OREN E. E., METU/D-VoidSim (Dynamic Void Simulator) is accessible on the World Wide Web at http://www.csl.mete.metu.edu/ (2000-b)

OREN E. E. and OGURTANI T. O., Mat. Res. Soc. Symp. Proc. (Ed: S. Lahiri), V**714** E, p. L9.2.1 (2001).

OREN E. E. and OGURTANI T. O., Mat. Res. Soc. Symp. Proc. (Eds: C. S. Ozkan, R. C. Cammarata, L. B. Freund, H. Gao), V**695**, p. L.5.5.1 (2002).

PAN J. and COCKS A. C. F., Comput. Mater. Sci., **1**, 95 (1993).

PAN J. and COCKS A. C. F., Acta Metall. Mater., **43** (4), 1395 (1995).

PARIS F. and CANAS J., *Boundary Element Method, Fundamentals and Applications* (Oxford University Press Inc., New York, USA), p. 35 (1997).

PARK Y. J., ANDLEIGHT V. K. and THOMPSON C. V., J. Appl. Phys., **85**, 3546 (1999).

PARTRIDGE P. W., BREBBIA C. A. and WROBEL L. C., *The Dual Reciprocity Boundary Element Method* (Computational Mechanics Publications, Southampton, England), p. 18 (1992).

PHARR G. M. and NIX W. D., Acta Metall., **27**, 1615 (1979).

PRIGOGINE I., *Introduction to Thermodynamics of Irreversible Processes* (Interscience, New York, USA), p. 28, 29 and 34, (1961).

RICE J. and CHUANG T. J., J. Am. Ceram. Soc., **64** (1), 50 (1981).

SANCHES J. E., Mc KNELLY L. T., and MORRIS J. W., J. Electron. Mater., **19**, 1213 (1990).

SANCHES J. E., KRAFT O., ARZT E., J. Appl. Phys., **61**, 3121 (1992-a).

SANCHES J. E., McKNELLY L.T., and MORRIS J.W., J. Appl. Phys., **72**, 3201 (1992-b).

SANCHES J.E., RANDLE V., KRAFT O., ARZT E., *Submicrometer Metallization: The Challenges, Opportunities, and Limitations* (SPIE, Bellingham, Washington, USA) p. 222 (1992-c).

SCHAFFT H. A., GRANT T. C., SAXENA A. N. and KAO C. Y., IEEE Proc. Reliability Phys. Symp., **93** (1985).

SCHIMSCHAK M. and KRUG J., J. Appl. Phys., **87**, 695 (2000).

SCHREIBER H. U., Solid-State Electron., **24**, 583 (1981).

SCHREIBER H. U. and GRABE B., Solid-State Electron., **24,** 1135 (1981).

SEEGER A. and MEHRER H., *Vacancies and Interstitials in Metals* (Eds: A. Seeger, D. Schumacher, W. Shilling, and Diehl, North-Holland Publ., Amsterdam, Holland), pp. 1-58 (1969).

SHATZKES M. and LLOYD J. R., J. Appl. Phys., **59**, 3890 (1986).

SIGSBEE R.A., J. Appl. Phys., **44** (6), 2533 (1973).

SUO Z., WANG W., and YANG M., Appl. Phys. Lett., **64**, 1944 (1994).

SUO Z., WANG W., and HAO T. H., J. Appl. Phys., **79**, 2394 (1996).

SURH M. P., J. Appl. Phys., **85**, 8145 (1999).

TAKAHASHI Y., TAKAHASHI K. and NIGHIGUCHI K., Acta Metall. Mater., **39** (12), 3199 (1991).

VERSCHAFFELT J. E., Bull. Ac. Roy. Belgium (Cl. Sc.), **22**, 373 (1936).

Von-NEUMANN J., *Metal Interfaces* (American Society for Testing Materials, Cleveland, USA), p. 108 (1952).

Van Der WAALS and BAKER J. D., *Handbook Experimental Physik* (Springer-Verlag, Berlin, Germany), Vol.**6** (1928).

VERHOEVEN J. D., *Fundamentals of Physical Metallurgy* (John Wiley & Sons, Inc., New York, USA) (1975).

WANG W., SUO Z., and HAO T. H., J. Appl. Phys., **79**, 2394 (1996).

WEVER H., *Elektro-und-Thermotransport in Metallen* (Johann Ambrosius Barth, Leibzig, Germany) (1973).

YEREMIN E. N., *The Foundation of Chemical Kinetics* (MIR Publishers, Moscow, Russia), p. 215 (1979).

YOUNG T., Philos. Trans. R. Soc. London, **95**, 65 (1805).

APPENDIX-A

DEFINITIONS OF THE INPUT PARAMETERS

ro:	the initial void radius
e:	void exantricity
shape:	void shape parameter
deltat:	initial time interval
t:	initial loop number
nl:	final loop number
epsmin:	minimum segment length used in the remeshing process
epsmax:	maximum segment length used in the remeshing process
ksi:	normalized electron wind intensity
time:	real time
mint:	integration segment number (odd)
sl:	interconnect length
sw:	interconnect width
mdiv:	number of division
vsl:	void segment length coefficient
dm:	mean segment lenght
delta:	grain boundary thickness
omega:	atomic volume
gb1:	node number or the location of the first grain boundary
dihedral1:	equilibrium dihedral angle between the first grain boundary and the void

lamda1:	wetting parameter for the first grain boundary
tat1:	first grain boundary tilt angle
mfold1:	half-fold number for the first grain
adif1:	anisotropy intensity for the first grain
tang1:	texture tilt angle for the first grain
gb2:	node number or the location of the second grain boundary
dihedral2:	equilibrium dihedral angle between the second grain boundary and the void
lamda2:	wetting parameter for the second grain boundary
tat2:	second grain boundary tilt angle
mfold2:	half-fold number for the second grain
adif2:	anisotropy intensity for the second grain
tang2:	texture tilt angle for the second grain
mgb:	grain boundary longitudinal mobility
tmgb:	grain boundary transverse mobility
mdrift:	grain boundary drift mobility
mobility:	normalized bulk mobility coefficient
eta:	normalized bulk gibbs free energy

APPENDIX-B

LIST OF COMPUTER PROGRAM

```
/*Electromigration*/

#include "p2c/p2c.h"
#include <stdlib.h>

typedef double arr1[701];
typedef double arr2[3][701];
typedef double arr3[701][701];


Static arr1   xi, x, y, dx, s, teta, alfa_, kapkap, beta, v, psi,
              diff, dteta, ekap, fieldi, fieldii, fieldt, fieldtn,
              drij, mrij, mu, c, fieldif, fieldiif, ulas, bre, cre,
              fx, fy, delu, rrq, rrq1, rrkq, kz, sk, gbn1, gbn2,
              gbn1t, gbn2t, vect, aefield;

Static arr2   r, delr, anti, ru, rl, rit, no, lln, rj, rij, rm,
              rmrot, rs, nc, rc, rcijo, rcij, rcv, noc, rcw, trac;

Static arr3   tt, ttt, tut;

Static long   k, m, nl, mpow, ms, t, finstep, ka, kki, kkj, mint,
              mdiv, stackno, mm, mv, gb1, gb2;

Static double pi, ds, ro, e, rmax, rmin, control, newdata, gbdata,
              deltat, epstime, ww, sl, sw, time, shape, ao, are,
              brea, crea, xc, yc, epsmin, epsmax, sigma, ksi, dm,
              delta, sav, vsl, mobility, eta, mdrift, eep, es, dxx,
              dot, ddot, omega, dotp, vmax, mgb, tmgb, ta1, ta2,
              tat1, tat2, gbr1, gbr2, gbl1, gbl2, dihedral1,
              dihedral2, lamda1, lamda2, tang1, tang2, adif1,
              adif2, tta1, tta2, mfold1, mfold2, vtrans1, vtrans2,
              fieldup1, fieldup2, fielddown1, fielddown2,
              fieldleft1, fieldleft2, fieldright1, fieldright2,
              fieldgb1, fieldgb2, curve, sign, vmineq;

Static FILE *f, *g;

Static Char sy[256];
```

```
/*auxiliary functions and procedures*/


/*this function determines the record time steps*/

Static long timer(m, e)
long m, e;
{
 long ki, powa;
 powa = 1;
 if (e != 0)
 {
  for (ki = 1; ki <= e; ki++)
    powa *= m;
 }
  return powa;
}

/*this function finds the dot product of two vectors*/

Static double dotpro(a0, a1, a2, b0, b1, b2)
double a0, a1, a2, b0, b1, b2;
{
 return (a0 * b0 + a1 * b1 + a2 * b2);
}

/*this function finds the vector product of two vectors*/

Static Void vectorpro(a0, a1, a2, b0, b1, b2)
double a0, a1, a2, b0, b1, b2;
{
 vect[0] = a1 * b2 - a2 * b1;
 vect[1] = a2 * b0 - a0 * b2;
 vect[2] = a0 * b1 - a1 * b0;
}

/*this function finds the magnitude of the vectors*/

Static double magnitude(a, b, c)
double a, b, c;
{
 return sqrt(a * a + b * b + c * c);
}

/*this function finds the arcsin(teta)"*/

Static double arcsin_(okst)
double okst;
{
 double arcs, sens;
 sens = 0.0000000001;
 if (okst > 1 - sens)
   arcs = pi / 2;
 else if (okst < sens - 1)
   arcs = pi / -2;
 else if (okst < sens)
 {
  if (okst > -sens)
    arcs = 0.0;
  else
```

```
    arcs = atan(1 / sqrt(1 / (okst * okst) - 1));
 }
 else
    arcs = atan(1 / sqrt(1 / (okst * okst) - 1));
 if (okst < 0)
   arcs = -arcs;
 return arcs;
}

/*this function finds the angle between two vectors*/

Static double angle(a0, a1, a2, b0, b1, b2)
double a0, a1, a2, b0, b1, b2;
{
 double angles, dd;
 dotp = dotpro(a0, a1, a2, b0, b1, b2);
 dd = magnitude(a0, a1, a2) * magnitude(b0, b1, b2);
 angles = arcsin_((a0 * b1 - a1 * b0) / dd);
 if (dotp <= 0)
   angles = pi - angles;
 if (angles > pi)
   angles -= 2 * pi;
 if (angles < 0)
   angles = 2 * pi + angles;
 return angles;
}

/*this function finds the void area*/

Static double area(k, r)
long k;
double (*r)[701];
{
 long ki;
 double areas;
 areas = 0.0;
 for (ki = 0; ki <= k - 2; ki++)
   areas += (r[0][ki] * r[1][ki + 1] - r[1][ki] * r[0][ki + 1]) /
             2;
 areas += (r[0][k - 1] * r[1][0] - r[1][k - 1] * r[0][0]) / 2;
 return areas;
}

/*production of a anticlockwise rotation matrix*/

Static Void antirotma(w)
double w;
{
 anti[0][0] = cos(w);
 anti[0][1] = -sin(w);
 anti[0][2] = 0.0;
 anti[1][0] = sin(w);
 anti[1][1] = cos(w);
 anti[1][2] = 0.0;
 anti[2][0] = 0.0;
 anti[2][1] = 0.0;
 anti[2][2] = 1.0;
}
```

```
/*Gauss Jordan elimination method in the solution of simulataneous
  set equations au=b*/

Static Void trian(colon, tek, cift_)
long colon;
double *tek;
double (*cift_)[701];
{
 arr3 cift;
 long ki, kj, kk, de;
 double tot, bol, max;
 arr3 trio;
 arr1 ddd;
 for (ki = 0; ki <= colon; ki++)
   cift[ki][colon + 1] = tek[ki];
 for (ki = 0; ki <= colon; ki++)
 {
  max = fabs(cift[ki][ki]);
  de = ki;
  for (kk = ki; kk <= colon; kk++)
  {
   if (max < fabs(cift[kk][ki]))
   {
    max = cift[kk][ki];
    de = ki;
   }
  }
  if (de != ki)
  {
   for (kk = 0; kk <= colon + 1; kk++)
   {
    ddd[kk] = cift[ki][kk];
    cift[ki][kk] = cift[de][kk];
    cift[de][kk] = ddd[kk];
   }
  }
  bol = cift[ki][ki];
  for (kj = 0; kj <= colon + 1; kj++)
    cift[ki][kj] /= bol;
  for (kk = ki; kk <= colon; kk++)
  {
   if (kk != ki)
   {
    for (kj = 0; kj <= colon + 1; kj++)
      trio[ki][kj] = cift[ki][kj] * cift[kk][ki];
    for (kj = 0; kj <= colon + 1; kj++)
      cift[kk][kj] -= trio[ki][kj];
   }
  }
 }
 ulas[colon] = cift[colon][colon + 1];
 for (ki = 1; ki <= colon; ki++)
 {
  tot = 0.0;
  for (kj = 1; kj <= ki; kj++)
    tot += ulas[colon - kj + 1] * cift[colon - ki][colon - kj + 1];
  ulas[colon - ki] = cift[colon - ki][colon + 1] - tot;
 }
}
```

```
/*main procedures*/

/*this procedure generates the upper and lower part of the strip*/

Static Void ulpart()
{
 long kl;
 for (kl = 0; kl <= mdiv*2; kl++)
 {
  ru[0][kl] = (kl - mdiv) * sl / mdiv;
  ru[1][kl] = sw;
  ru[2][kl] = 0.0;
  rl[0][kl] = (kl - mdiv) * sl / mdiv;
  rl[1][kl] = -sw;
  rl[2][kl] = 0.0;
 }
}

/*in this program ro should be always chosen as equal to unity
  which is simply the mean radius of a equivalent circular void
  having the same area*/

/*this procedure genarates the shape of the void*/

Static Void void_()
{
 long kj, kl;
 double TEMP;
 xi[0] = 0.0;
 kj = 0;
 es = ds;
 eep = ds * exp(-6 * log(10.0));
 while (es > eep)
 {
  while (xi[kj] < pi)
  {
   x[kj] = ro * sqrt(1 + e * e) * cos(xi[kj]) + ro * e * cos(shape
           * xi[kj]);
   y[kj] = ro * sqrt(1 + e * e) * sin(xi[kj]) - ro * e * sin(shape
           * xi[kj]);
   TEMP = -ro * sqrt(1 + e * e) * sin(xi[kj]) - shape * ro * e *
          sin(shape * xi[kj]);
   dx[kj] = TEMP * TEMP;
   TEMP = ro * sqrt(1 + e * e) * cos(xi[kj]) -  shape * ro * e *
          cos(shape * xi[kj]);
   dx[kj] = ds / sqrt(dx[kj] + TEMP * TEMP);
   xi[kj + 1] = xi[kj] + dx[kj];
   kj++;
  }
  m = kj - 1;
  dxx = pi - xi[m];
  TEMP = -ro * sqrt(1 + e * e) * sin(xi[kj]) - shape * ro * e *
         sin(shape * xi[kj]);
  es = TEMP * TEMP;
  TEMP = ro * sqrt(1 + e * e) * cos(xi[kj]) - shape * ro * e *
         cos(shape * xi[kj]);
  es = dxx * sqrt(es + TEMP * TEMP);
  ds += es / (m + 2);
  kj = 0;
 }
```

```
 for (kl = m + 1; kl < m*2; kl++)
 {
  x[kl] = x[m * 2 - kl];
  y[kl] = -y[m * 2 - kl];
 }
 x[m] = ro * sqrt(1 + e * e) * cos(pi) + ro * e * cos(shape * pi);
 y[m] = ro * sqrt(1 + e * e) * sin(pi) - ro * e * sin(shape * pi);
 y[m * 2] = y[0];
 x[m * 2] = x[0];
 k = m * 2;
}

/*this procedure generates 3-d vectors as position vectors and then
  loads them as columns on a node-position matrix denotes by
  r(x,y,t)*/

Static Void rxyt()
{
 long kj;
 for (kj = 0; kj < k; kj++)
 {
  r[0][kj] = x[kj];
  r[1][kj] = y[kj];
  r[2][kj] = 0.0;
 }
}

/*this procedure combines the void and the strip*/

Static Void stack()
{
 long kl;
 for (kl = 0; kl <= mdiv*2; kl++)
 {
  rit[0][kl] = ru[0][kl];
  rit[1][kl] = ru[1][kl];
  rit[2][kl] = ru[2][kl];
 }
 for (kl = mdiv * 2 + 1; kl <= mdiv*4+1; kl++)
 {
  rit[0][kl] = rl[0][kl - mdiv * 2 - 1];
  rit[1][kl] = rl[1][kl - mdiv * 2 - 1];
  rit[2][kl] = rl[2][kl - mdiv * 2 - 1];
 }
 for (kl = mdiv * 4 + 2; kl <= mdiv*4+k+2; kl++)
 {
  rit[0][kl] = r[0][kl - mdiv * 4 - 2];
  rit[1][kl] = r[1][kl - mdiv * 4 - 2];
  rit[2][kl] = r[2][kl - mdiv * 4 - 2];
 }
 stackno = mdiv * 4 + k + 2;
}

/*this procedure calculates difference vectors between successive
  position vectors and their magnitudes*/

Static Void delr1()
{
 long kj, ki;
 for (ki = 0; ki < k; ki++)
```

```
 {
  if (ki == 0)
  {
   for (kj = 0; kj <= 2; kj++)
     delr[kj][ki] = r[kj][0] - r[kj][k - 1];
  }
  else
  {
   for (kj = 0; kj <= 2; kj++)
     delr[kj][ki] = r[kj][ki] - r[kj][ki - 1];
  }
 }
 for (ki = 0; ki < k; ki++)
 {
  s[ki] = sqrt(delr[0][ki] * delr[0][ki] + delr[1][ki] *
               delr[1][ki] + delr[2][ki] * delr[2][ki]);
 }
}

/*this procedure calculates the angle between the two successive 3-
  d vectors and in given set of vectors. the range -p and +p*/

Static Void psir()
{
 long ki;
 teta[k - 1] = angle(delr[0][k - 1], delr[1][k - 1], delr[2][k -
                     1], delr[0][0], delr[1][0], delr[2][0]);
  for (ki = 0; ki <= k-2; ki++)
    teta[ki] = angle(delr[0][ki], delr[1][ki], delr[2][ki],
                     delr[0][ki + 1], delr[1][ki + 1], delr[2][ki +
                     1]);
}

/*This procedure calculates the diffusivities for polycrystal
  interconnect lines*/

Static Void anisotropygb()
{
 long ki;
 double TEMP;
 for (ki = 0; ki < k; ki++)
 {
  dteta[ki] = angle(1.0, 0.0, 0.0, delr[0][ki], delr[1][ki],
                    delr[2][ki]);
  if (ki <= gb1)
  {
   TEMP = cos(mfold1 * (dteta[ki] - tta1));
   diff[ki] = 1 + adif1 * (TEMP * TEMP);
  }
  else if (ki <= gb2)
  {
   TEMP = cos(mfold2 * (dteta[ki] - tta2));
   diff[ki] = 1 + adif2 * (TEMP * TEMP);
  }
  else if (ki > gb2)
  {
  TEMP = cos(mfold1 * (dteta[ki] - tta1));
  diff[ki] = 1 + adif1 * (TEMP * TEMP);
  }
 }
```

```
}

/*This procedure calculates the diffusivities for single crystal
   interconnect lines*/

Static Void anisotropy()
{
 long ki;
 double TEMP;
 for (ki = 0; ki < k; ki++)
 {
  dteta[ki] = angle(1.0, 0.0, 0.0, delr[0][ki], delr[1][ki],
                    delr[2][ki]);
  TEMP = cos(mfold1 * (dteta[ki] - tta1));
  diff[ki] = 1 + adif1 * (TEMP * TEMP);
 }
}

/*this procedure calculates the local curvature and the local line
   normal vector at any given node knowing the successive segment
   vector set*/

Static Void kappa()
{
 long ki, kj;
 for (ki = 0; ki < k; ki++)
 {
  if (ki == k - 1)
    alfa_[ki] = atan(sin(teta[ki]) / (s[0] / s[ki] +
                cos(teta[ki])));
  else
    alfa_[ki] = atan(sin(teta[ki]) / (s[ki + 1] / s[ki] +
                cos(teta[ki])));
  kapkap[ki] = 2 * sin(alfa_[ki]) / s[ki];
  beta[ki] = (pi - 2 * alfa_[ki]) / 2;
  antirotma(-beta[ki]);
  for (kj = 0; kj <= 2; kj++)
    no[kj][ki] = anti[kj][0] * delr[0][ki] + anti[kj][1] *
                 delr[1][ki] + anti[kj][2] * delr[2][ki];
  for (kj = 0; kj <= 2; kj++)
    lln[kj][ki] = no[kj][ki] / magnitude(no[0][ki], no[1][ki],
                  no[2][ki]);
 }
}

/*this procedure calculates the normal unit vectors at the
   centroids for the upper and lower cut interfaces plus the void.
   Directions towards the interconnect material*/

Static Void noc1()
{
 long kj, ki;
 for (kj = 0; kj < k; kj++)
 {
  nc[0][kj] = delr[1][kj] / s[kj];
  nc[1][kj] = -(delr[0][kj] / s[kj]);
  nc[2][kj] = 0.0;
 }
 for (ki = 0; ki < mdiv*2; ki++)
 {
```

```
  noc[0][ki] = 0.0;
  noc[1][ki] = -1.0;
  noc[2][ki] = 0.0;
 }
 for (ki = mdiv * 2; ki < mdiv*4; ki++)
 {
  noc[0][ki] = 0.0;
  noc[1][ki] = 1.0;
  noc[2][ki] = 0.0;
 }
 for (kj = 0; kj <= 2; kj++)
 {
  for (ki = mdiv * 4; ki <= mdiv * 4 + k - 2; ki++)
    noc[kj][ki] = nc[kj][ki - mdiv * 4 + 1];
 }
 for (kj = 0; kj <= 2; kj++)
   noc[kj][mdiv * 4 + k - 1] = nc[kj][0];
}

/*this procedure calculates the centroid position vectors for the
  void only*/

Static Void rcv1()
{
 long ki, kj;
 for (ki = 0; ki < k; ki++)
 {
  for (kj = 0; kj <= 2; kj++)
  {
   if (ki == k - 1)
     rcv[kj][ki] = (r[kj][0] + r[kj][k - 1]) / 2;
   else
     rcv[kj][ki] = (r[kj][ki + 1] + r[kj][ki]) / 2;
  }
 }
}

/*this procedure calculates the centroid position vectors for the
  whole system*/

Static Void rcw1()
{
 long ki, kj;
 for (ki = 0; ki <= stackno - 4; ki++)
 {
  if (ki < mdiv * 2)
  {
   for (kj = 0; kj <= 2; kj++)
     rcw[kj][ki] = (rit[kj][ki + 1] + rit[kj][ki]) / 2;
  }
  else if (ki >= mdiv * 2)
  {
   if (ki < mdiv * 4)
   {
    for (kj = 0; kj <= 2; kj++)
      rcw[kj][ki] = (rit[kj][ki + 2] + rit[kj][ki + 1]) / 2;
   }
  }
  if (ki >= mdiv * 4)
  {
```

```
   for (kj = 0; kj <= 2; kj++)
     rcw[kj][ki] = (rit[kj][ki + 3] + rit[kj][ki + 2]) / 2;
  }
 }
 for (kj = 0; kj <= 2; kj++)
   rcw[kj][stackno - 3] = (rit[kj][mdiv * 4 + 2] + rit[kj][stackno
                           - 1]) / 2;
}

/*indirect boundary element method*/

/*this is an electrostatic connection matrix utilizing the element
  centroids, m is the numder of subsegment used in the integration
  procedure*/

/*this procedure calculates the normal component of the electric
  field at the centroid positions on the boundary due to uniformly
  distrubuted charge, using IBEM*/

Static Void tin()
{
 long ki, kj, kl, km;
 double total, tot, rcos, rcms;
 double TEMP;
 kz[0] = 0.0;
 kz[1] = 0.0;
 kz[2] = 1.0;
 mv = mdiv * 4 + 2;
 mm = mdiv * 4 + k - 1;

 for (ki = 0; ki < mdiv * 2; ki++)
   sk[ki] = sl / mdiv;

 for (ki = mdiv * 2; ki < mdiv * 4; ki++)
   sk[ki] = sl / mdiv;

 for (ki = 1; ki < k; ki++)
   sk[mdiv * 4 + ki - 1] = s[ki];
 sk[mdiv * 4 + k - 1] = s[0];

 for (ki = 0; ki <= mm; ki++)
 {
  for (kj = 0; kj <= mm; kj++)
  {
   if (ki == kj)
     tt[ki][kj] = 0.5;
   else
   {

    if (ki == mm)
    {
     if (kj < mdiv * 2)
     {
      for (kl = 0; kl <= 2; kl++)
        rcijo[kl][ki] = ( rit[kl][ki + 2] + rit[kl][mv] - 2 *
                          rit[kl][kj]) / 2;
      for (km = 0; km <= mint; km++)
      {
       for (kl = 0; kl <= 2; kl++)
       rc[kl][km] = rcijo[kl][ki] - km * (rit[kl][kj + 1] –
```

```
                rit[kl][kj]) / mint;
  }
 }
}

if (kj == mm)
{
 if (ki >= mdiv * 2)
 {
  if (ki < mdiv * 4)
  {
   for (kl = 0; kl <= 2; kl++)
   rcijo[kl][ki] = (rit[kl][ki + 2] + rit[kl][ki + 1] - 2 *
                    rit[kl][kj + 2]) / 2;
   for (km = 0; km <= mint; km++)
   {
    for (kl = 0; kl <= 2; kl++)
      rc[kl][km] = rcijo[kl][ki] - km * (rit[kl][mv] –
                   rit[kl][kj + 2]) / mint;
   }
  }
 }
}

if (kj == mm)
{
 if (ki < mdiv * 2)
 {
  for (kl = 0; kl <= 2; kl++)
    rcijo[kl][ki] = ( rit[kl][ki + 1] + rit[kl][ki] - 2 *
                      rit[kl][kj + 2]) / 2;
  for (km = 0; km <= mint; km++)
  {
   for (kl = 0; kl <= 2; kl++)
   rc[kl][km] = rcijo[kl][ki] - km * (rit[kl][mv] - rit[kl][kj
                + 2]) / mint;
  }
 }
}

if (kj == mm)
{
 if (ki >= mdiv * 4)
 {
  if (ki < mm)
  {
   for (kl = 0; kl <= 2; kl++)
   rcijo[kl][ki] = (rit[kl][ki + 3] + rit[kl][ki + 2] - 2 *
                    rit[kl][kj + 2]) / 2;
   for (km = 0; km <= mint; km++)
   {
    for (kl = 0; kl <= 2; kl++)
      rc[kl][km] = rcijo[kl][ki] - km * (rit[kl][mv] –
                   rit[kl][kj + 2]) / mint;
   }
  }
 }
}

if (ki == mm)
```

```
{
 if (kj >= mdiv * 2)
 {
  if (kj < mdiv * 4)
  {
   for (kl = 0; kl <= 2; kl++)
   rcijo[kl][ki] = (rit[kl][ki + 2] + rit[kl][mv] - 2 *
                    rit[kl][kj + 1]) / 2;
   for (km = 0; km <= mint; km++)
   {
    for (kl = 0; kl <= 2; kl++)
      rc[kl][km] = rcijo[kl][ki] - km * (rit[kl][kj + 2] –
                   rit[kl][kj + 1]) / mint;
   }
  }
 }
}

if (ki == mm)
{
 if (kj >= mdiv * 4)
 {
  if (kj < mm)
  {
   for (kl = 0; kl <= 2; kl++)
   rcijo[kl][ki] = (rit[kl][ki + 2] + rit[kl][mv] - 2 *
                   rit[kl][kj + 2]) / 2;
   for (km = 0; km <= mint; km++)
   {
    for (kl = 0; kl <= 2; kl++)
      rc[kl][km] = rcijo[kl][ki] - km * (rit[kl][kj + 3] –
                   rit[kl][kj + 2]) / mint;
   }
  }
 }
}

if (ki < mdiv * 2)
{
 if (kj < mdiv * 2)
 {
  for (kl = 0; kl <= 2; kl++)
  rcijo[kl][ki] = (rit[kl][ki + 1] + rit[kl][ki] - 2 *
                   rit[kl][kj]) / 2;
  for (km = 0; km <= mint; km++)
  {
   for (kl = 0; kl <= 2; kl++)
     rc[kl][km] = rcijo[kl][ki] - km * (rit[kl][kj + 1] –
                  rit[kl][kj]) / mint;
  }
 }
}

if (ki < mdiv * 2)
{
 if (kj >= mdiv * 2)
 {
  if (kj < mdiv * 4)
  {
   for (kl = 0; kl <= 2; kl++)
```

```
   rcijo[kl][ki] = (rit[kl][ki + 1] + rit[kl][ki] - 2 *
                    rit[kl][kj + 1]) / 2;
   for (km = 0; km <= mint; km++)
   {
    for (kl = 0; kl <= 2; kl++)
      rc[kl][km] = rcijo[kl][ki] - km * (rit[kl][kj + 2] –
                   rit[kl][kj + 1]) / mint;
   }
  }
 }
}

if (ki < mdiv * 2)
{
 if (kj >= mdiv * 4)
 {
  if (kj < mm)
  {
   for (kl = 0; kl <= 2; kl++)
   rcijo[kl][ki] = (rit[kl][ki + 1] + rit[kl][ki] - 2 *
                    rit[kl][kj + 2]) / 2;
   for (km = 0; km <= mint; km++)
   {
    for (kl = 0; kl <= 2; kl++)
      rc[kl][km] = rcijo[kl][ki] - km * (rit[kl][kj + 3] –
                   rit[kl][kj + 2]) / mint;
   }
  }
 }
}

if (ki >= mdiv * 2)
{
 if (ki < mdiv * 4)
 {
  if (kj < mdiv * 2)
  {
   for (kl = 0; kl <= 2; kl++)
   rcijo[kl][ki] = (rit[kl][ki + 2] + rit[kl][ki + 1] - 2 *
                    rit[kl][kj]) / 2;
   for (km = 0; km <= mint; km++)
   {
    for (kl = 0; kl <= 2; kl++)
      rc[kl][km] = rcijo[kl][ki] - km * (rit[kl][kj + 1] –
                   rit[kl][kj]) / mint;
   }
  }
 }
}

if (ki >= mdiv * 2)
{
 if (ki < mdiv * 4)
 {
  if (kj >= mdiv * 2)
  {
   if (kj < mdiv * 4)
   {
    for (kl = 0; kl <= 2; kl++)
      rcijo[kl][ki] = (rit[kl][ki + 2] + rit[kl][ki + 1] - 2 *
```

```
                       rit[kl][kj + 1]) / 2;
    for (km = 0; km <= mint; km++)
    {
     for (kl = 0; kl <= 2; kl++)
       rc[kl][km] = rcijo[kl][ki] - km * (rit[kl][kj + 2]
                    – rit[kl][kj + 1]) / mint;
    }
   }
  }
 }
}

if (ki >= mdiv * 2)
{
 if (ki < mdiv * 4)
 {
  if (kj >= mdiv * 4)
  {
   if (kj < mm)
   {
    for (kl = 0; kl <= 2; kl++)
      rcijo[kl][ki] = (rit[kl][ki + 2] + rit[kl][ki + 1] - 2 *
                       rit[kl][kj + 2]) / 2;
    for (km = 0; km <= mint; km++)
    {
     for (kl = 0; kl <= 2; kl++)
       rc[kl][km] = rcijo[kl][ki] - km * (rit[kl][kj + 3]
                    – rit[kl][kj + 2]) / mint;
    }
   }
  }
 }
}

if (ki >= mdiv * 4)
{
 if (ki < mm)
 {
  if (kj >= mdiv * 4)
  {
   if (kj < mm)
   {
    for (kl = 0; kl <= 2; kl++)
      rcijo[kl][ki] = (rit[kl][ki + 3] + rit[kl][ki + 2] - 2 *
                        rit[kl][kj + 2]) / 2;
    for (km = 0; km <= mint; km++)
    {
     for (kl = 0; kl <= 2; kl++)
       rc[kl][km] = rcijo[kl][ki] - km * (rit[kl][kj + 3]
                    – rit[kl][kj + 2]) / mint;
    }
   }
  }
 }
}

if (ki >= mdiv * 4)
{
 if (ki < mm)
 {
```

```
     if (kj >= mdiv * 2)
     {
      if (kj < mdiv * 4)
      {
       for (kl = 0; kl <= 2; kl++)
         rcijo[kl][ki] = ( rit[kl][ki + 3] + rit[kl][ki + 2] - 2
                           * rit[kl][kj + 1]) / 2;
       for (km = 0; km <= mint; km++)
       {
        for (kl = 0; kl <= 2; kl++)
          rc[kl][km] =  rcijo[kl][ki] - km * (rit[kl][kj + 2] –
                        rit[kl][kj + 1]) / mint;
       }
      }
     }
    }
   }

   if (ki >= mdiv * 4)
   {
    if (ki < mm)
    {
     if (kj < mdiv * 2)
     {
      for (kl = 0; kl <= 2; kl++)
        rcijo[kl][ki] = (rit[kl][ki + 3] + rit[kl][ki + 2] - 2 *
                         rit[kl][kj]) / 2;
      for (km = 0; km <= mint; km++)
      {
       for (kl = 0; kl <= 2; kl++)
         rc[kl][km] = rcijo[kl][ki] - km * (rit[kl][kj + 1] –
                      rit[kl][kj]) / mint;
      }
     }
    }
   }

   for (kl = 0; kl <= 2; kl++)
   {
    total = 0.0;
    for (km = 1; km < mint; km++)
    {
     TEMP = magnitude(rc[0][km], rc[1][km], rc[2][km]);
     tot = TEMP * TEMP;
     total += rc[kl][km] / tot;
    }
    rcij[kl][ki] = total;
    TEMP = magnitude(rc[0][0], rc[1][0], rc[2][0]);
    rcos = TEMP * TEMP;
    TEMP = magnitude(rc[0][mint], rc[1][mint], rc[2][mint]);
    rcms = TEMP * TEMP;
    rcij[kl][ki] += 1.0 / 2 * (rc[kl][0] / rcos + rc[kl][mint] /
                    rcms);
   }
   tt[ki][kj] = sk[kj] / 2 / pi / mint * (noc[0][ki] * rcij[0][ki]
                + noc[1][ki] * rcij[1][ki] + noc[2][ki] *
                rcij[2][ki]);
  }
 }
}
```

```
}

/*c is the normal component of the electric field on the void plus
  strip surfaces due to the applied voltage along the x-axis.*/

Static Void elf()

{
 long ki;
 for (ki = 0; ki <= mm; ki++)
   c[ki] = noc[0][ki];
}

/*calculation of the electrostatic potential due to the boundary
  charge distribution at any point in the interior region or at the
  boundary*/

Static Void field()

{
 long ki, kj, kl, km;
 double eta, tot;

/*below line generates mu that is the charge to be inserted in
  order to satisfy the neumann boundary condition along the void
  surface, by using procedure trian*/

 trian(mm, c, tt);

 for (ki = 0; ki <= mm; ki++)
   mu[ki] = -ulas[ki];

/*mu is a charge density function at a given segment which is
  assumed to be uniformly distributed along each segment.*/

 /*Calculation of grain boundary normal vectors*/

 /*gb1*/

 gbn1[0] = cos(ta1);
 gbn1[1] = sin(ta1);
 gbn1[2] = 0.0;

 /*gb1+pi/2 rotation ACW*/

 gbn1t[0] = cos(ta1 + pi / 2);
 gbn1t[1] = sin(ta1 + pi / 2);
 gbn1t[2] = 0.0;

 /*gb2*/

 gbn2[0] = cos(ta2);
 gbn2[1] = sin(ta2);
 gbn2[2] = 0.0;

 /*gb2+pi/2 rotation ACW*/

 gbn2t[0] = cos(ta2 + pi / 2);
 gbn2t[1] = sin(ta2 + pi / 2);
 gbn2t[2] = 0.0;
```

```
/*Calculation of position vectors for the TJ surrounding nodes*/

for (ki = 0; ki <= 2; ki++)
{
 rcw[ki][stackno - 2] = r[ki][gb1] + gbn1[ki] * ds;   /*up*/
 rcw[ki][stackno - 1] = r[ki][gb1] - gbn1[ki] * ds;   /*down*/
 rcw[ki][stackno] = r[ki][gb1] + gbn1t[ki] * ds;      /*left*/
 rcw[ki][stackno + 1] = r[ki][gb1] - gbn1t[ki] * ds;  /*right*/

 rcw[ki][stackno + 2] = r[ki][gb2] + gbn2[ki] * ds;   /*up*/
 rcw[ki][stackno + 3] = r[ki][gb2] - gbn2[ki] * ds;   /*down*/
 rcw[ki][stackno + 4] = r[ki][gb2] + gbn2t[ki] * ds;  /*left*/
 rcw[ki][stackno + 5] = r[ki][gb2] - gbn2t[ki] * ds;  /*right*/
}
for (ki = 0; ki <= stackno + 5; ki++)
  fieldi[ki] = -1 * rcw[0][ki];
for (ki = 0; ki <= stackno + 5; ki++)
{
 for (kj = 0; kj <= stackno - 3; kj++)
 {
  if (kj == stackno - 3)
  {
   for (kl = 0; kl <= 2; kl++)
   {
    rrq[kl] = rit[kl][stackno - 1] - rcw[kl][ki];
    rrq1[kl] = rit[kl][mv] - rcw[kl][ki];
   }
   eta =  1.0 / 2 * (log(magnitude(rrq[0], rrq[1], rrq[2])) +
          log(magnitude(rrq1[0], rrq1[1], rrq1[2])));
   tot = 0.0;
   for (km = 1; km < mint; km++)
   {
    for (kl = 0; kl <= 2; kl++)
      rrkq[kl] = rit[kl][stackno - 1] + km * (rit[kl][mv] –
                 rit[kl][stackno - 1]) / mint - rcw[kl][ki];
    tot += log(magnitude(rrkq[0], rrkq[1], rrkq[2]));
   }
   delu[kj] = -1.0 / 2 / pi / mint * fabs(sk[stackno - 3]) * (tot
              + eta);
  }
  else if (kj >= mdiv * 4)
  {
   if (kj < stackno - 3)
   {
    for (kl = 0; kl <= 2; kl++)
    {
     rrq[kl] = rit[kl][kj + 3] - rcw[kl][ki];
     rrq1[kl] = rit[kl][kj + 2] - rcw[kl][ki];
    }
    eta = 1.0 / 2 * (log(magnitude(rrq[0], rrq[1], rrq[2])) +
          log(magnitude(rrq1[0], rrq1[1], rrq1[2])));
    tot = 0.0;
    for (km = 1; km < mint; km++)
    {
     for (kl = 0; kl <= 2; kl++)
       rrkq[kl] =  rit[kl][kj + 2] + km * (rit[kl][kj + 3] –
                  rit[kl][kj + 2]) / mint - rcw[kl][ki];
         tot += log(magnitude(rrkq[0], rrkq[1], rrkq[2]));
    }
    delu[kj] = -1.0 / 2 / pi / mint * fabs(sk[kj]) * (tot + eta);
```

```
  }
 }
 else if (kj >= mdiv * 2)
 {
  if (kj < mdiv * 4)
  {
   for (kl = 0; kl <= 2; kl++)
   {
    rrq[kl] = rit[kl][kj + 2] - rcw[kl][ki];
    rrq1[kl] = rit[kl][kj + 1] - rcw[kl][ki];
   }
   eta = 1.0 / 2 * (log(magnitude(rrq[0], rrq[1], rrq[2])) +
         log(magnitude(rrq1[0], rrq1[1], rrq1[2])));
   tot = 0.0;
   for (km = 1; km < mint; km++)
   {
    for (kl = 0; kl <= 2; kl++)
      rrkq[kl] =  rit[kl][kj + 1] + km * (rit[kl][kj + 2] –
                  rit[kl][kj + 1]) / mint - rcw[kl][ki];
    tot += log(magnitude(rrkq[0], rrkq[1], rrkq[2]));
   }
   delu[kj] = -1.0 / 2 / pi / mint * fabs(sk[kj]) * (tot + eta);
   }
  }
  else
  {
   for (kl = 0; kl <= 2; kl++)
   {
    rrq[kl] = rit[kl][kj] - rcw[kl][ki];
    rrq1[kl] = rit[kl][kj + 1] - rcw[kl][ki];
   }
   eta = 1.0 / 2 * (log(magnitude(rrq[0], rrq[1], rrq[2])) +
         log(magnitude(rrq1[0], rrq1[1], rrq1[2])));
   tot = 0.0;
   for (km = 1; km < mint; km++)
   {
    for (kl = 0; kl <= 2; kl++)
    rrkq[kl] = rit[kl][kj] + km * (rit[kl][kj + 1] - rit[kl][kj])
               / mint - rcw[kl][ki];
    tot += log(magnitude(rrkq[0], rrkq[1], rrkq[2]));
   }
   delu[kj] = -1.0 / 2 / pi / mint * fabs(sk[kj]) * (tot + eta);
  }
 }
 fieldii[ki] = 0.0;
 for (kl = 0; kl <= stackno -3; kl++)
    fieldii[ki] += delu[kl] * mu[kl];
}
for (ki = 0; ki < k; ki++)
{
 fieldif[ki] = fieldi[ki + mdiv * 4];
 fieldiif[ki] = fieldii[ki + mdiv * 4];
 fieldt[ki] = fieldif[ki] + fieldiif[ki];
}
for (ki = 0; ki < k; ki++)
{
 if (ki == 0)
   fieldtn[ki] =  (fieldt[0] * s[0] + fieldt[k - 1] * s[1]) /
                  (s[0] + s[1]);
 else
```

```
   {
    if (ki == k - 1)
      fieldtn[ki] = (fieldt[k - 2] * s[0] + fieldt[k - 1] * s[k –
                    1]) / (s[k - 1] + s[0]);
      else
      fieldtn[ki] = (fieldt[ki - 1] * s[ki + 1] + fieldt[ki] *
                    s[ki]) / (s[ki + 1] + s[ki]);
   }
 }
 fieldup1 = fieldi[stackno - 2] + fieldii[stackno - 2];
 fielddown1 = fieldi[stackno - 1] + fieldii[stackno - 1];
 fieldleft1 = fieldi[stackno] + fieldii[stackno];
 fieldright1 = fieldi[stackno + 1] + fieldii[stackno + 1];
 fieldgb1 = (fieldup1 + fielddown1 + fieldleft1 + fieldright1) / 4;
 fieldup2 = fieldi[stackno + 2] + fieldii[stackno + 2];
 fielddown2 = fieldi[stackno + 3] + fieldii[stackno + 3];
 fieldleft2 = fieldi[stackno + 4] + fieldii[stackno + 4];
 fieldright2 = fieldi[stackno + 5] + fieldii[stackno + 5];
 fieldgb2 = (fieldup2 + fielddown2 + fieldleft2 + fieldright2) / 4;
}

/*this procedure performs the remeshing by eliminating those
  segments smaller than rmin and dividing those which are
  greater than rmax into two parts and also keeps the grain
  boundary triple junction as a stable point.*/

/*with grain boundary, (asimetric)*/

Static Void remeshinggb()
{
 long ki, kj, crm, gnew1, gnew2;
 double mag, ai, bi, ci;
 ka = 1;
 delr1();
 rm[0][0] = r[0][0];
 rm[1][0] = r[1][0];
 rm[2][0] = r[2][0];

 /*Zone 1*/

 for (ki = 1; ki < gb1; ki++)
 {
  mag = magnitude(delr[0][ki], delr[1][ki], delr[2][ki]);
  if (mag >= rmax)
  {
   for (kj = 0; kj <= 2; kj++)
   {
    rm[kj][ka] = (r[kj][ki - 1] + r[kj][ki]) / 2;
    rm[kj][ka + 1] = r[kj][ki];
   }
   ka += 2;
  }
  if (mag < rmax)
  {
   if (mag > rmin)
   {
    for (kj = 0; kj <= 2; kj++)
      rm[kj][ka] = r[kj][ki];
    ka++;
   }
```

```
 }
 if (mag <= rmin)
 {
  for (kj = 0; kj <= 2; kj++)
    delr[kj][ki + 1] += delr[kj][ki];
 }
}

/*Node gb1*/

mag = magnitude(delr[0][gb1], delr[1][gb1], delr[2][gb1]);
if (mag >= rmax)
{
 for (kj = 0; kj <= 2; kj++)
 {
  rm[kj][ka] = (rm[kj][ka - 1] + r[kj][gb1]) / 2;
  rm[kj][ka + 1] = r[kj][gb1];
 }
 gnew1 = ka + 1;
 ka += 2;
}
if (mag < rmax)
{
 if (mag > rmin)
 {
  for (kj = 0; kj <= 2; kj++)
    rm[kj][ka] = r[kj][gb1];
  gnew1 = ka;
  ka++;
 }
}
if (mag <= rmin)
{
 ai = delr[0][gb1] + delr[0][gb1 - 1];
 bi = delr[1][gb1] + delr[1][gb1 - 1];
 ci = delr[2][gb1] + delr[2][gb1 - 1];
 mag = magnitude(ai, bi, ci);
 if (mag >= rmax)
 {
  for (kj = 0; kj <= 2; kj++)
  {
   rm[kj][ka - 1] = (r[kj][gb1] + rm[kj][ka - 2]) / 2;
   rm[kj][ka] = r[kj][gb1];
  }
  gnew1 = ka;
  ka++;
 }
 else
 {
  for (kj = 0; kj <= 2; kj++)
    rm[kj][ka - 1] = r[kj][gb1];
  gnew1 = ka - 1;
 }
}

/*Zone 2*/

for (ki = gb1 + 1; ki < gb2; ki++)
{
 mag = magnitude(delr[0][ki], delr[1][ki], delr[2][ki]);
```

```
 if (mag >= rmax)
 {
  for (kj = 0; kj <= 2; kj++)
  {
   rm[kj][ka] = (r[kj][ki - 1] + r[kj][ki]) / 2;
   rm[kj][ka + 1] = r[kj][ki];
  }
  ka += 2;
 }
 if (mag < rmax)
 {
  if (mag > rmin)
  {
   for (kj = 0; kj <= 2; kj++)
     rm[kj][ka] = r[kj][ki];
   ka++;
  }
 }
 if (mag <= rmin)
 {
  for (kj = 0; kj <= 2; kj++)
    delr[kj][ki + 1] += delr[kj][ki];
 }
}

/*Node gb2*/

mag = magnitude(delr[0][gb2], delr[1][gb2], delr[2][gb2]);
if (mag >= rmax)
{
 for (kj = 0; kj <= 2; kj++)
 {
  rm[kj][ka] = (rm[kj][ka - 1] + r[kj][gb2]) / 2;
  rm[kj][ka + 1] = r[kj][gb2];
 }
 gnew2 = ka + 1;
 ka += 2;
}
if (mag < rmax)
{
 if (mag > rmin)
 {
  for (kj = 0; kj <= 2; kj++)
    rm[kj][ka] = r[kj][gb2];
  gnew2 = ka;
  ka++;
 }
}
if (mag <= rmin)
{
 ai = delr[0][gb2] + delr[0][gb2 - 1];
 bi = delr[1][gb2] + delr[1][gb2 - 1];
 ci = delr[2][gb2] + delr[2][gb2 - 1];
 mag = magnitude(ai, bi, ci);
 if (mag >= rmax)
 {
  for (kj = 0; kj <= 2; kj++)
  {
   rm[kj][ka - 1] = (r[kj][gb2] + rm[kj][ka - 2]) / 2;
   rm[kj][ka] = r[kj][gb2];
```

```
  }
  gnew2 = ka;
  ka++;
 }
 else
 {
  for (kj = 0; kj <= 2; kj++)
    rm[kj][ka - 1] = r[kj][gb2];
  gnew2 = ka - 1;
 }
}
```

*/*Zone 3*/*

```
for (ki = gb2 + 1; ki < k; ki++)
{
 mag = magnitude(delr[0][ki], delr[1][ki], delr[2][ki]);
 if (mag >= rmax)
 {
  for (kj = 0; kj <= 2; kj++)
  {
   rm[kj][ka] = (r[kj][ki - 1] + r[kj][ki]) / 2;
   rm[kj][ka + 1] = r[kj][ki];
  }
  ka += 2;
 }
 if (mag < rmax)
 {
  if (mag > rmin)
  {
   for (kj = 0; kj <= 2; kj++)
     rm[kj][ka] = r[kj][ki];
   ka++;
  }
 }
 if (mag <= rmin)
 {
  if (ki == k - 1)
  {
   for (kj = 0; kj <= 2; kj++)
     delr[kj][0] += delr[kj][k - 1];
  }
  else
  {
   for (kj = 0; kj <= 2; kj++)
     delr[kj][ki + 1] += delr[kj][ki];
  }
 }
}
```

*/*Node 0*/*

```
mag = magnitude(delr[0][0], delr[1][0], delr[2][0]);
if (mag >= rmax)
{
 for (kj = 0; kj <= 2; kj++)
 {
  rm[kj][ka] = (rm[kj][ka - 1] + rm[kj][0]) / 2;
  rm[kj][ka + 1] = rm[kj][0];
 }
```

```
  crm = ka + 1;
 }
 if (mag < rmax)
 {
  if (mag > rmin)
  {
   for (kj = 0; kj <= 2; kj++)
     rm[kj][ka] = rm[kj][0];
   crm = ka;
  }
 }
 if (mag <= rmin)
 {
  ai = delr[0][0] + delr[0][k - 1];
  bi = delr[1][0] + delr[1][k - 1];
  ci = delr[2][0] + delr[2][k - 1];
  mag = magnitude(ai, bi, ci);
  if (mag >= rmax)
  {
   for (kj = 0; kj <= 2; kj++)
   {
    rm[kj][ka - 1] = (rm[kj][0] + rm[kj][ka - 2]) / 2;
    rm[kj][ka] = rm[kj][0];
   }
   crm = ka;
  }
  else
  {
   for (kj = 0; kj <= 2; kj++)
     rm[kj][ka - 1] = rm[kj][0];
   crm = ka - 1;
  }
 }
 k = crm;
 gb1 = gnew1;
 gb2 = gnew2;
}

/*this procedure generates the initial system*/

Static Void generate()
{
 void_();   /*procedure*/
 rxyt();   /*procedure*/
 ao = area(k, r);
}

/*this procedure gets the initial parameters from a file called
  electromigration.dat*/

Static Void getparam()
{
 f = fopen("phd-2g.dat", "r");

 /*experiment type parameters*/

 fscanf(f, "%lg%*[^\n]", &newdata);
 getc(f);   /*1: if 0 new experiment if 1 continuous from
                 cont.dat*/
 fscanf(f, "%lg%*[^\n]", &gbdata);
```

```
getc(f);   /*2:  if 0 no gb if 1 gb*/
fscanf(f, "%lg%*[^\n]", &control);
getc(f);   /*3:  if 1 equilibrium, if 2 failure, if 3 detachment
                 experiment, if 4 both case 1 or 3*/

/*interconnect-void system parameters*/

fscanf(f, "%lg%*[^\n]", &ro);
getc(f);   /*4:  the radius of the void*/
fscanf(f, "%lg%*[^\n]", &e);
getc(f);   /*5:  void exantricity*/
fscanf(f, "%lg%*[^\n]", &shape);
getc(f);   /*6:  void shape*/
fscanf(f, "%ld%*[^\n]", &t);
getc(f);   /*7:  initial loop number*/
fscanf(f, "%ld%*[^\n]", &ms);
getc(f);   /*8:  data record number*/
fscanf(f, "%lg%*[^\n]", &deltat);
getc(f);   /*9:  initial time interval*/
fscanf(f, "%lg%*[^\n]", &epstime);
getc(f);   /*10: time step correction*/
fscanf(f, "%lg%*[^\n]", &epsmin);
getc(f);   /*11: minimum segment length*/
fscanf(f, "%lg%*[^\n]", &epsmax);
getc(f);   /*12: maximum segment length*/
fscanf(f, "%lg%*[^\n]", &ksi);
getc(f);   /*13: electron wind intensity*/
fscanf(f, "%ld%*[^\n]", &nl);
getc(f);   /*14: loop number*/
fscanf(f, "%lg%*[^\n]", &time);
getc(f);   /*15: real time*/
fscanf(f, "%ld%*[^\n]", &mint);
getc(f);   /*16: integration segment number (odd)*/
fscanf(f, "%lg%*[^\n]", &sl);
getc(f);   /*17: strip length coefficient*/
fscanf(f, "%lg%*[^\n]", &sw);
getc(f);   /*18: strip width coefficient*/
fscanf(f, "%ld%*[^\n]", &mdiv);
getc(f);   /*19: division*/
fscanf(f, "%lg%*[^\n]", &vsl);
getc(f);   /*20: void segment length coefficient*/
fscanf(f, "%lg%*[^\n]", &dm);
getc(f);   /*21: mean segment lenght*/

/*grain boundary parameters*/

fscanf(f, "%ld%*[^\n]", &gb1);
getc(f);   /*22: location of the first grain boundary*/
fscanf(f, "%lg%*[^\n]", &dihedral1);
getc(f);   /*23: equilibrium dihedral angle between gb1 and void*/
fscanf(f, "%lg%*[^\n]", &tat1);
getc(f);   /*24: gb1 tilt angle*/
fscanf(f, "%lg%*[^\n]", &mfold1);
getc(f);   /*25: half-fold number for the first grain*/
fscanf(f, "%lg%*[^\n]", &adif1);
getc(f);   /*26: anisotropy intensity for the first grain*/
fscanf(f, "%lg%*[^\n]", &tang1);
getc(f);   /*27: texture tilt angle for the first grain*/

fscanf(f, "%ld%*[^\n]", &gb2);
```

```
 getc(f);   /*28: location of the second grain boundary*/
 fscanf(f, "%lg%*[^\n]", &dihedral2);
 getc(f);   /*29: equilibrium dihedral angle between gb2 and void*/
 fscanf(f, "%lg%*[^\n]", &tat2);
 getc(f);   /*30: gb2 tilt angle*/
 fscanf(f, "%lg%*[^\n]", &mfold2);
 getc(f);   /*31: half-fold number for the second grain*/
 fscanf(f, "%lg%*[^\n]", &adif2);
 getc(f);   /*32: anisotropy intensity for the second grain*/
 fscanf(f, "%lg%*[^\n]", &tang2);
 getc(f);   /*33: texture tilt angle for the second grain*/

 fscanf(f, "%lg%*[^\n]", &mgb);
 getc(f);   /*34: grain boundary longitudinal mobility*/
 fscanf(f, "%lg%*[^\n]", &tmgb);
 getc(f);   /*35: grain boundary transverse mobility*/
 fscanf(f, "%lg%*[^\n]", &mdrift);
 getc(f);   /*36: grain boundary drift mobility*/

 /*interconnect kinetic parameters*/

 fscanf(f, "%lg%*[^\n]", &mobility);
 getc(f);   /*37: normalized bulk mobility coefficient*/
 fscanf(f, "%lg%*[^\n]", &eta);
 getc(f);   /*38: normalized bulk gibbs free energy*/

 /*equilibrium parameter*/

 fscanf(f, "%lg%*[^\n]", &vmineq);
 getc(f);   /*39: in the equilibrum experiments minimum node
                  displacement for the equilibrium*/

 pi = 3.14159265358979323846264338327950;

 ds = vsl * ro;                 /** void segment length*/
 sl *= ro;                      /** strip length*/
 sw *= ro;                      /** strip width*/
 delta = 0.1 * ro;              /** grain boundary thickness*/
 omega = delta * delta * delta; /** the atomic volume*/

 lamda1 = cos(dihedral1 * pi / 180); /** wetting parameter for the
                                         first grain*/
 lamda2 = cos(dihedral2 * pi / 180); /** wetting parameter for the
                                         second grain*/

 ta1 = tat1 * pi / 180;         /** gb1 tilt angle in rad*/
 ta2 = tat2 * pi / 180;         /** gb2 tilt angle in rad*/

 tta1 = tang1 * pi / 180;       /** texture tilt angle in rad*/
 tta2 = tang2 * pi / 180;       /** texture tilt angle in rad*/
}

/*this procedure gets the last parameters of the void, calculated
  previously, from a file called cont.txt*/

Static Void getcontparam()
{
 long aii;
 double sil;
 f = fopen("cont.txt", "r");
```

```
fscanf(f,"%lg%lg%lg%lg%lg%lg%lg%lg%lg%ld%ld%ld%lg%ld%lg%lg%lg%ld%ld
       %lg%lg%*[^\n]", r[0], r[1], &sil, &sil, &sil, &sil, &sil,
       &sil, &sil, &k, &t, &ms, &time,&mm, &sil, &sil, &sil, &gb1,
       &gb2, &tat1, &tat2);
 getc(f);
 for (aii = 1; aii <= k; aii++)
 {
  fscanf(f, "%lg%lg%*[^\n]", &r[0][aii], &r[1][aii]);
  getc(f);
 }
 ta1 = tat1 * pi / 180;   /** gb1 tilt angle in rad*/
 ta2 = tat2 * pi / 180;   /** gb2 tilt angle in rad*/
}

/*ogurtani model: void-grain boundary interaction under the effect
  of electron wind and thermal streses using IBEM calculations*/

/*finite strip with "grain boundary"*/

Static Void finalgb()
{
 long   aii, ajj;
 double mide, gb1e, gb2e, widthmax, uacc, lacc, utjmin, ltjmax,
        jgbaf1, jgbaf2;
 double TEMP, TEMP1;
 mide = 0.0;
 gb1e = 0.0;
 gb2e = 0.0;
 ulpart();              /*procedure*/
 if (newdata == 0)
   generate();          /*procedure*/
 if (newdata == 1)
   getcontparam();      /*procedure*/
 while (t <= nl)
 {
  delr1();              /*procedure*/
  stack();              /*procedure*/
  psir();               /*procedure*/
  anisotropygb();       /*procedure*/
  kappa();              /*procedure*/

  if (ksi != 0)
  {
   noc1();              /*procedure*/
   rcv1();              /*procedure*/
   rcw1();              /*procedure*/
   tin();               /*procedure*/
   elf();               /*procedure*/
   field();             /*procedure*/
   if (t == 1)
   {
    f = fopen("noc.txt", "a");
    f = tmpfile();
    for (ajj = 0; ajj <= 2; ajj++)
    {
     for (aii = 0; aii < mdiv * 4 +k; aii++)
     fprintf(f, "%14.15f  ", noc[ajj][aii]);
     putc('\n', f);
    }
    fclose(f);
```

```
  f = fopen("rcw.txt", "a");
  f = tmpfile();
  for (ajj = 0; ajj <= 2; ajj++)
  {
   for (aii = 0; aii <= stackno - 3; aii++)
     fprintf(f, "%14.15f  ", rcw[ajj][aii]);
   putc('\n', f);
  }
  fclose(f);

  f = fopen("mu.txt", "a");
  f = tmpfile();
  for (ajj = 0; ajj <= mm; ajj++)
    fprintf(f, "%14.15f\n", mu[ajj]);
  fclose(f);

  f = fopen("field.txt", "a");
  f = tmpfile();
  for (ajj = 0; ajj < k; ajj++)
    fprintf(f, "%14.15f\n", fieldtn[ajj]);
  fclose(f);
 }
}

if (t == 1)
{
 f = fopen("ru.txt", "a");
 f = tmpfile();
 for (aii = 0; aii <= mdiv * 2; aii++)
   fprintf(f, "%14.15f  %14.15f  \n", ru[0][aii], ru[1][aii]);
 fclose(f);

 f = fopen("rl.txt", "a");
 f = tmpfile();
 for (aii = 0; aii <= mdiv * 2; aii++)
   fprintf(f, "%14.15f  %14.15f  \n", rl[0][aii], rl[1][aii]);
 fclose(f);

 f = fopen("rvector.txt", "a");
 f = tmpfile();
 for (ajj = 0; ajj <= 2; ajj++)
 {
  for (aii = 0; aii < k; aii++)
    fprintf(f, "%14.15f  ", r[ajj][aii]);
  putc('\n', f);
 }
 fprintf(f, "%14.15f  ", ao);
 close(f);

 f = fopen("delrvector.txt", "a");
 f = tmpfile();
 for (ajj = 0; ajj <= 2; ajj++)
 {
  for (aii = 0; aii < k; aii++)
  fprintf(f, "%14.15f  ", delr[ajj][aii]);
 putc('\n', f);
 }
 fclose(f);
```

```
 f = fopen("s.txt", "a");
 f = tmpfile();
 for (ajj = 0; ajj < k; ajj++)
   fprintf(f, "%14.15f\n", s[ajj]);
 fclose(f);

 f = fopen("teta.txt", "a");
 f = tmpfile();
 for (ajj = 0; ajj < k; ajj++)
   fprintf(f, "%14.15f\n", teta[ajj]);
 fclose(f);

 f = fopen("diff.txt", "a");
 f = tmpfile();
 for (ajj = 0; ajj < k; ajj++)
   fprintf(f, "%14.15f\n", diff[ajj]);
 fclose(f);

 f = fopen("kapkap.txt", "a");
 f = tmpfile();
 for (ajj = 0; ajj < k; ajj++)
   fprintf(f, "%14.15f\n", kapkap[ajj]);
 fclose(f);

 f = fopen("lln.txt", "a");
 f = tmpfile();
 for (ajj = 0; ajj <= 2; ajj++)
 {
  for (aii = 0; aii < k; aii++)
    fprintf(f, "%14.15f  ", lln[ajj][aii]);
  putc('\n', f);
 }
 fclose(f);
}

if (ksi == 0)
{
 for (aii = 0; aii < k; aii++)
   fieldtn[aii] = 0.0;
}
for (aii = 0; aii < k; aii++)
{
 psi[aii] = ksi * fieldtn[aii];
 ekap[aii] = kapkap[aii] + psi[aii];
}

/*Applied electric field vector*/

aefield[0] = 1.0;
aefield[1] = 0.0;
aefield[2] = 0.0;

/*Calculation of instantaneous grain-boundary left and right
   dihedral angles*/

/*gb1*/

/*teta1 -*/

gbr1 = angle(-gbn1[0], -gbn1[1], -gbn1[2], -delr[0][gb1], -
```

```
             delr[1][gb1], -delr[2][gb1]);

/*teta1 +*/

gbl1 = angle(delr[0][gb1 + 1], delr[1][gb1 + 1], delr[2][gb1 +
             1], -gbn1[0], -gbn1[1], -gbn1[2]);

/*gb2*/

/*teta2 -*/

gbr2 = angle(-gbn2[0], -gbn2[1], -gbn2[2], -delr[0][gb2], -
             delr[1][gb2], -delr[2][gb2]);

/*teta2 +*/

gbl2 = angle(delr[0][gb2 + 1], delr[1][gb2 + 1], delr[2][gb2 +
             1], -gbn2[0], -gbn2[1], -gbn2[2]);

/*node velocities*/

for (ajj = 0; ajj < k; ajj++)
{

 /*0*/

 if (ajj == 0)
 {
  v[ajj] = diff[1] * (ekap[1] - ekap[0]) / s[1] - diff[0] *
           (ekap[0] - ekap[k - 1]) / s[0];
  v[ajj] = 2 * v[ajj] / (s[1] + s[0]) - mobility * (eta +
           kapkap[0]);
 }

 /*k-1*/

 else if (ajj == k - 1)
 {
  v[ajj] = diff[0] * (ekap[0] - ekap[k - 1]) / s[0] - diff[k - 1]
           * (ekap[k - 1] - ekap[k - 2]) / s[k - 1];
  v[ajj] = 2 * v[ajj] / (s[0] + s[k - 1]) - mobility * (eta +
           kapkap[k - 1]);
 }

 /*gb1-1*/

 else if (ajj == gb1 - 1)
 {
  vectorpro(delr[0][gb1], delr[1][gb1], delr[2][gb1], delr[0][gb1
            + 1], delr[1][gb1 + 1], delr[2][gb1 + 1]);
  curve = dotpro(vect[0], vect[1], vect[2], 0.0, 0.0, 1.0);
  if (curve < 0)
    sign = -1.0;
  else
    sign = 1.0;
  vectorpro(delr[0][gb1] / s[gb1], delr[1][gb1] / s[gb1],
            delr[2][gb1] / s[gb1], gbn1[0], gbn1[1], gbn1[2]);
  vtrans1 = dotpro(vect[0], vect[1], vect[2], 0.0, 0.0, 1.0);
  vectorpro(delr[0][gb1 + 1] / s[gb1 + 1], delr[1][gb1 + 1] /
```

```
           s[gb1 + 1], delr[2][gb1 + 1] / s[gb1 + 1], gbn1[0],
           gbn1[1], gbn1[2]);
 vtrans1 -= dotpro(vect[0], vect[1], vect[2], 0.0, 0.0, 1.0);
 jgbaf1 = mdrift * ksi / omega * (fieldup1 - fieldgb1) / ds;
 v[ajj] = mgb * (delta / -2 / omega) * (lamda1 –
          dotpro(delr[0][gb1] / s[gb1], delr[1][gb1] / s[gb1],
          delr[2][gb1] / s[gb1], gbn1[0], gbn1[1], gbn1[2]));
 v[ajj] += diff[gb1] * (psi[gb1] - psi[gb1 - 1]) / s[gb1];
 v[ajj] += diff[gb1 - 1] * (ekap[gb1 - 2] - ekap[gb1 - 1]) /
           s[gb1 - 1] - jgbaf1 / 2;
 v[ajj] += sign * tmgb * delta / omega * vtrans1;
 v[ajj] = 2 * v[ajj] / (2 * s[gb1] + s[gb1 - 1]) - mobility *
          (eta + kapkap[gb1 - 1]);
}

/*gb1*/

else if (ajj == gb1)
{
 v[ajj] = 2 * lamda1 - dotpro(delr[0][gb1 + 1] / s[gb1 + 1],
          delr[1][gb1 + 1] / s[gb1 + 1], delr[2][gb1 + 1] /
          s[gb1 + 1], -gbn1[0], -gbn1[1], -gbn1[2]);
 v[ajj] = mgb * (v[ajj] - dotpro(delr[0][gb1] / s[gb1],
          delr[1][gb1] / s[gb1], delr[2][gb1] / s[gb1], gbn1[0],
          gbn1[1], gbn1[2])) / 2 / omega;
}

/*gb1+1*/

else if (ajj == gb1 + 1)
{
 v[ajj] = mgb * (delta / -2 / omega) * (lamda1 –
          dotpro(delr[0][gb1 + 1] / s[gb1 + 1], delr[1][gb1 + 1]
          / s[gb1 + 1], delr[2][gb1 + 1] / s[gb1 + 1], -gbn1[0],
          -gbn1[1], -gbn1[2]));
 v[ajj] += diff[gb1 + 2] * (ekap[gb1 + 2] - ekap[gb1 + 1]) /
           s[gb1 + 2];
 v[ajj] += diff[gb1 + 1] * (psi[gb1] - psi[gb1 + 1]) / s[gb1 +
           1] - jgbaf1 / 2;
 v[ajj] -= sign * tmgb * delta / omega * vtrans1;
 v[ajj] = 2 * v[ajj] / (s[gb1 + 2] + 2 * s[gb1 + 1]) - mobility
          * (eta + kapkap[gb1 + 1]);
}

/*gb2-1*/

else if (ajj == gb2 - 1)
{
 vectorpro(delr[0][gb2], delr[1][gb2], delr[2][gb2], delr[0][gb2
           + 1], delr[1][gb2 + 1], delr[2][gb2 + 1]);
 curve = dotpro(vect[0], vect[1], vect[2], 0.0, 0.0, 1.0);
 if (curve < 0)
   sign = -1.0;
 else
   sign = 1.0;
 jgbaf2 = mdrift * ksi / omega * (fieldup2 - fieldgb2) / ds;
 vectorpro(delr[0][gb2] / s[gb2], delr[1][gb2] / s[gb2],
           delr[2][gb2] / s[gb2], gbn2[0], gbn2[1], gbn2[2]);
 vtrans2 = dotpro(vect[0], vect[1], vect[2], 0.0, 0.0, 1.0);
 vectorpro(delr[0][gb2 + 1] / s[gb2 + 1], delr[1][gb2 + 1] /
```

```
              s[gb2 + 1], delr[2][gb2 + 1] / s[gb2 + 1], gbn2[0],
              gbn2[1], gbn2[2]);
    vtrans2 -= dotpro(vect[0], vect[1], vect[2], 0.0, 0.0, 1.0);
    v[ajj] = mgb * (delta / -2 / omega) * (lamda2 –
             dotpro(delr[0][gb2] / s[gb2], delr[1][gb2] / s[gb2],
             delr[2][gb2] / s[gb2], gbn2[0], gbn2[1], gbn2[2]));
    v[ajj] += diff[gb2] * (psi[gb2] - psi[gb2 - 1]) / s[gb2];
    v[ajj] += diff[gb2 - 1] * (ekap[gb2 - 2] - ekap[gb2 - 1]) /
              s[gb2 - 1] - jgbaf2 / 2;
    v[ajj] += sign * tmgb * delta / omega * vtrans2;
    v[ajj] = 2 * v[ajj] / (2 * s[gb2] + s[gb2 - 1]) - mobility *
             (eta + kapkap[gb2 - 1]);
   }

   /*gb2*/

   else if (ajj == gb2)
   {
    v[ajj] = 2 * lamda2 - dotpro(delr[0][gb2 + 1] / s[gb2 + 1],
             delr[1][gb2 + 1] / s[gb2 + 1], delr[2][gb2 + 1] /
             s[gb2 + 1], -gbn2[0], -gbn2[1], -gbn2[2]);
    v[ajj] = mgb * (v[ajj] - dotpro(delr[0][gb2] / s[gb2],
             delr[1][gb2] / s[gb2], delr[2][gb2] / s[gb2], gbn2[0],
             gbn2[1], gbn2[2])) / 2 / omega;
   }

   /*gb2+1*/

   else if (ajj == gb2 + 1)
   {
    v[ajj] = mgb * (delta / -2 / omega) * (lamda2 –
             dotpro(delr[0][gb2 + 1] / s[gb2 + 1], delr[1][gb2 + 1]
             / s[gb2 + 1], delr[2][gb2 + 1] / s[gb2 + 1], -gbn2[0],
             -gbn2[1], -gbn2[2]));
    v[ajj] += diff[gb2 + 2] * (ekap[gb2 + 2] - ekap[gb2 + 1]) /
              s[gb2 + 2];
    v[ajj] += diff[gb2 + 1] * (psi[gb2] - psi[gb2 + 1]) / s[gb2 +
              1] - jgbaf2 / 2;
    v[ajj] -= sign * tmgb * delta / omega * vtrans2;
    v[ajj] = 2 * v[ajj] / (s[gb2 + 2] + 2 * s[gb2 + 1]) - mobility
             * (eta + kapkap[gb2 + 1]);
   }

/*rest of the void*/

   else
   {
    v[ajj] = diff[ajj + 1] * (ekap[ajj + 1] - ekap[ajj]) / s[ajj +
             1] - diff[ajj] * (ekap[ajj] - ekap[ajj - 1]) / s[ajj];
    v[ajj] = 2 * v[ajj] / (s[ajj + 1] + s[ajj]) - mobility * (eta +
             kapkap[ajj]);
   }
  }
  vmax = fabs(v[0]);
  for (aii = 1; aii < k; aii++)
  {
   if (fabs(v[aii]) >= vmax)
     vmax = fabs(v[aii]);
  }
  for (ajj = 0; ajj < k; ajj++)
```

```
{
 if (ajj == gb1)
 {
  r[0][ajj] += deltat * v[ajj] * gbn1[0];
  r[1][ajj] += deltat * v[ajj] * gbn1[1];
  r[2][ajj] += deltat * v[ajj] * gbn1[2];
 }
 else if (ajj == gb2)
 {
  r[0][ajj] += deltat * v[ajj] * gbn2[0];
  r[1][ajj] += deltat * v[ajj] * gbn2[1];
  r[2][ajj] += deltat * v[ajj] * gbn2[2];
 }
 else
 {
  r[0][ajj] += deltat * v[ajj] * lln[0][ajj];
  r[1][ajj] += deltat * v[ajj] * lln[1][ajj];
  r[2][ajj] += deltat * v[ajj] * lln[2][ajj];
 }
}

/*calculation of record time step*/

if (t < 257)
  mpow = timer(2L, ms);
else if (t < 1001)
  mpow = (ms - 9) * 100 + 300;
else if (t < 10001)
  mpow = (ms - 16) * 250 + 1000;
else if (t < 20001)
  mpow = (ms - 52) * 1000 + 10000;
else if (t < 100001L)
  mpow = (ms - 62) * 2500 + 20000;
else if (t < 1000001L)
  mpow = (ms - 94) * 5000 + 100000L;
else
  mpow = (ms - 274) * 50000L + 1000000L;

/*system situation control*/

if (control == 1)                 /*equilibrium*/
{
 uacc = 1 + vmineq * epstime;
  lacc = 1 - vmineq * epstime;
  if (mide < fabs(r[0][0] * uacc))
  {
   if (mide > fabs(r[0][0] * lacc))
   {
    if (gb1e < fabs(r[1][gb1] * uacc))
    {
     if (gb1e > fabs(r[1][gb1] * lacc))
     {
      if (gb2e < fabs(r[1][gb2] * uacc))
      {
       if (gb2e > fabs(r[1][gb2] * lacc))
       {
      finstep = t;
      t = nl + 1;
      mpow = t;
       }
```

```
     }
    }
   }
  }
 }
 mide = fabs(r[0][0]);
 gb1e = fabs(r[1][gb1]);
 gb2e = fabs(r[1][gb2]);
}
else if (control == 2)           /*width*/
{
 widthmax = 0.0;
 for (aii = 0; aii < k; aii++)
 {
  if (fabs(r[1][aii]) > widthmax)
    widthmax = fabs(r[1][aii]);
 }
 if (widthmax > sw)
 {
  finstep = t;
  t = nl + 1;
  mpow = t;
 }
}
else if (control == 3)           /*detachment*/
{
 utjmin = r[1][gb1];
 ltjmax = r[1][gb2];
 for (aii = 1; aii <= 10; aii++)
 {
  if (r[1][gb1 - aii] < utjmin)
    utjmin = r[1][gb1 - aii];
  if (r[1][gb2 + aii] > ltjmax)
    ltjmax = r[1][gb2 + aii];
 }
 if (utjmin <= ltjmax)
 {
  finstep = t;
  t = nl + 1;
  mpow = t;
 }
}
else if (control == 4)           /*equilibrium-detachment*/
{
 uacc = 1 + vmineq * epstime;
 lacc = 1 - vmineq * epstime;
 if (mide < fabs(r[0][0] * uacc))
 {
  if (mide > fabs(r[0][0] * lacc))
  {
   if (gb1e < fabs(r[1][gb1] * uacc))
   {
    if (gb1e > fabs(r[1][gb1] * lacc))
    {
     if (gb2e < fabs(r[1][gb2] * uacc))
     {
      if (gb2e > fabs(r[1][gb2] * lacc))
      {
     finstep = t;
     t = nl + 1;
```

```
        mpow = t;
        control = 3.0;
       }
      }
     }
    }
   }
  }
  mide = fabs(r[0][0]);
  gb1e = fabs(r[1][gb1]);
  gb2e = fabs(r[1][gb2]);

 /*detachment*/

 utjmin = r[1][gb1];
 ltjmax = r[1][gb2];
 for (aii = 1; aii <= 10; aii++)
 {
  if (r[1][gb1 - aii] < utjmin)
    utjmin = r[1][gb1 - aii];
  if (r[1][gb2 + aii] > ltjmax)
    ltjmax = r[1][gb2 + aii];
 }
 if (utjmin <= ltjmax)
 {
  finstep = t;
  t = nl + 1;
  mpow = t;
  control = 1.0;
 }
}

/*recording the instantaneous system situation*/

if (t == mpow)
{
 for (aii = 0; aii < k; aii++)
 {
  fx[aii] = r[0][aii];
  fy[aii] = r[1][aii];
 }
 fx[k] = fx[0];
 fy[k] = fy[0];

 /*Calculation of centre of gravity of the void*/

 brea = 0.0;
 crea = 0.0;
 for (aii = 0; aii < k; aii++)
 {
  if (aii == k - 1)
  {
   bre[aii] = (fy[0] + fy[aii]) / 2 * (fx[0] + fx[aii]) / 2 *
              (fx[0] - fx[aii]);
   TEMP = (fy[0] + fy[aii]) / 2;
   cre[aii] = TEMP * TEMP * (fx[0] - fx[aii]);
  }
  else
  {
   bre[aii] = (fy[aii + 1] + fy[aii]) / 2 * (fx[aii + 1] +
```

```
                 fx[aii]) / 2 * (fx[aii + 1] - fx[aii]);
      TEMP = (fy[aii + 1] + fy[aii]) / 2;
      cre[aii] = TEMP * TEMP * (fx[aii + 1] - fx[aii]);
     }
     are = area(k, r);
     brea -= bre[aii];
     crea -= cre[aii];
    }
    xc = brea / are;
    yc = crea / are;

    f = fopen("name.txt", "w");
    rewind(f);
    fprintf(f, "%ld", ms);
    fprintf(f, "csl.txt");
    fclose(f);

    g = fopen("name.txt", "r");
    fgets(sy, 256, g);
    fclose(g);

    f = fopen(sy, "a");
    rewind(f);
    fprintf(f, "%13.13f  %13.13f  %13.13f  %13.13f  %13.13f  %13.13f
            %13.13f  %13.13f  %13.13f  %12ld  %12ld  %12ld  %13.13f
            %12ld  %13.13f  %13.13f  %13.13f  %12ld  %12ld  %13.13f
            %13.13f  %13.13f  %13.13f  %13.13f  %13.13f\n", fx[0],
            fy[0], mu[0], fieldtn[0], lln[0][0], lln[1][0], v[0],
            diff[0], dteta[0], k, t, ms, time, mm, xc, yc, are, gb1,
            gb2, tat1, tat2, gbr1, gbl1, gbr2, gbl2);

    for (aii = 1; aii <= mm; aii++)
      fprintf(f, "%13.13f  %13.13f  %13.13f  %13.13f  %13.13f
              %13.13f  %13.13f  %13.13f  %13.13f\n", fx[aii],
              fy[aii], mu[aii], fieldtn[aii], lln[0][aii],
              lln[1][aii], v[aii], diff[aii], dteta[aii]);
    fclose(f);
    ms++;
   }
   deltat = epstime * dm / vmax;
   rmin = epsmin * dm;
   rmax = epsmax * dm;
   remeshinggb();                    /*procedure*/
   for (aii = 0; aii <= 2; aii++)
   {
    for (ajj = 0; ajj < k; ajj++)
      r[aii][ajj] = rm[aii][ajj];
   }
   time += deltat;
   t++;
  }
}
```

```
/*main program electromigration*/

main(argc, argv)
int argc;
Char *argv[];
{
 getparam();                          /*procedure*/
 printf("  \n");
 printf("Electromigration\n");
 finalgb();                           /*procedure*/
 if (control == 1)
   printf("System Equilibrium Satisfied\n");
 else if (control == 2)
   printf("Interconnect Line Failed\n");
 else if (control == 3)
   printf("Detachment Compleated\n");
 printf("final record no:%ld\n", ms - 1);
 printf("final step:%ld\n", finstep);
 printf("final time:%13.13f\n", time);
 printf("COMPUTER SIMULATION LABORATORY");
 fclose(f);
 fclose(g);
 exit(EXIT_SUCCESS);
}
/* End. */
```

CURRICULUM VITAE

Name: Ersin Emre ÖREN

Date of Birth / Place: February 13, 1975 / Antalya, TURKEY

Nationality: Turkish

Marital Status: Married, (Çigdem Özbag ÖREN)

Daughter: Ayse Doga ÖREN (December 19, 2002)

EDUCATION

***Ph.D*, Metallurgical & Materials Engineering Department**
Middle East Technical University, Ankara, TURKEY
Graduated January 2003, (*3.79/4.00 CGPA*)

***M. Sc*, Metallurgical & Materials Engineering Department**
Middle East Technical University, Ankara, TURKEY
Graduated September 2000, (*3.63/4.00 CGPA*)

***B. Sc*, Metallurgical & Materials Engineering Department**
Middle East Technical University, Ankara, TURKEY
Graduated June 1997, (*3.16/4.00 CGPA*)

***Minor Program*, Solid State Physics in the Department of Physics**
Middle East Technical University, Ankara, TURKEY
Graduated June 1997, (*3.28/4.00 CGPA*)

WORK EXPERIENCE

Research Assistant (1997-2003)
Metallurgical & Materials Engineering Department,
Middle East Technical University, Ankara, TURKEY

Visiting Scientist (15.06.2001-15.09.2001)
Max-Planck-Institut für Metallforschung,
Seestrasse 92, D-70174, Stuttgart, GERMANY
(TUBITAK-NATO-A2 Research Grant)

Student Assistant (1996-1997)
Metallurgical & Materials Engineering Department,
Middle East Technical University, Ankara, TURKEY

AWARDS

- Prof. Dr. Mustafa N. Parlar Education & Research Foundation, ***Middle East Technical University (METU) The Best Thesis Award 2000.***

PUBLICATIONS

A. Thesis

1. Ersin Emre OREN, Ph. D. Thesis, METU, January 2003.
   Computer simulation of electromigration induced void – grain boundary interactions and the prediction of cathode failure times in bamboo structures

2. Ersin Emre OREN, M. Sc. Thesis, METU, September 2000.
   Electromigration – induced transgranular void motion in interconnects with special reference to computer simulation

B. Journal Articles

1. Ersin Emre OREN,
   Computer Simulation of Sintering Behavior of Powder Compacts by the Irreversible Thermodynamics of Curved Surfaces and Interfaces
   Journal of European Ceramic Society, to be submitted, February 2003.

2. Tarik O. OGURTANI and Ersin Emre OREN,
   Irreversible Thermodynamics of the Interfacial Triple Junction with a Special Reference to Void Intergranular Motion under the Action of Electromigration
   Physical Review B, to be submitted, January 2003.

3. Ali KALKANLI and Ersin Emre OREN,
   Variation of Phase Morphology in Gas Atomized, Spray Deposited and Melt Spun Al-Fe-V-Si Alloy
   Powder Metallurgy and Metal Ceramics, submitted, September 2002.

4. Tarik O. OGURTANI, M. Rauf GUNGOR and Ersin Emre OREN,
   Interactive Computer Simulation of Dislocation Damping Spectra Associated with the Coupled Motion of Geometric Kinks and Point Defects Subjected to the Bulk Segregation Phenomenon
   Journal of Applied Physics, Volume **91**, Issue 4, pp. 1860-1870, February 2002.

5. Tarik O. OGURTANI and Ersin Emre OREN,
   Computer Simulation of Void Growth Dynamics Under the Action of Electromigration and Capillary Forces in Narrow Thin Interconnects
   Journal of Applied Physics, Volume **90**, Issue 3, pp. 1564-1572, August 2001.

6. Ersin Emre OREN and A. C. TAS,
   Hydrothermal Synthesis of Pure and Dy Doped $BaTiO_3$ *Powders at 90 °C*
   Metallurgical and Materials Transactions B, Volume **30**, pp. 1089-1093, December 1999.

7. Ersin Emre OREN, E. TASPINAR and A. C. TAS,
   Preparation of Lead Zirconate ($PbZrO_3$) *by Homogeneous Precipitation and Calcination*
   Journal of American Ceramic Society, Volume **80**, Issue 10, pp. 2714-16, 1997.

C. Conference & Meeting Presentations

1. Ersin Emre OREN[*] and Tarik O. OGURTANI,
   Interactive Computer Simulation of Dislocation Damping Spectra Associated with the Coupled Motion of Geometric Kinks and Point Defects Subjected to the Bulk Segregation Phenomenon
   13th International Conference on Internal Friction and Ultrasonic Attenuation in Solids and 1st Scientific Exhibition on Mechanical Spectroscopy Equipment
   Poster Presentation, Bilbao, Spain, July 8-12, 2002.

2. Ersin Emre OREN[*] and Tarik O. OGURTANI,
   Void Intergranular Motion under the Action of Electromigration Forces in Thin Film Interconnects with Bamboo Structure
   MRS 2001 Fall Meeting, "Symposium L: Thin Films, Stresses and Mechanical Properties IX"
   Oral Presentation, Boston, Massachusetts, USA, November 26-30, 2001.

3. Ersin Emre OREN[*] and Tarik O. OGURTANI,
   The Effect of Initial Void Configuration on the Morphological Evolution under the Action of Normalized Electron Wind Forces
   MRS 2001 Spring Meeting, "Symposium L: Materials, Technology, and Reliability for Advanced Interconnects and Low-k Dielectrics"
   Poster Presentation, San Francisco, California, USA, April 16-20, 2001.

---

[*] Presenting author

4. Ersin Emre OREN* and Tarik O. OGURTANI,
Mathematical Modeling of the Void Evolution Dynamics Under the Action of Electromigration and Cappilary Forces in Thin Interconnects
International Conference on Mathematical Modeling and Scientific Computing
Middle East Technical University and Selçuk University
Oral Presentation, Ankara and Konya, Turkey, April 2-6, 2001.

5. Tarik O. OGURTANI, M. Rauf GUNGOR and Ersin Emre OREN*,
Computer Simulation of Internal Friction Spectrum Utilizing an Interactive Kink Chain Mobile Foreign Interstitials Model
Second International School on Mechanical Spectroscopy MS - 2
Invited Presentation, Kraków-Krynica, Poland, December 3-8, 2000.

6. Tarik O. OGURTANI and Ersin Emre OREN*,
Computer Simulation of Void Growth Dynamics under the Action of Electromigration and Capillary Forces in Narrow Thin Interconnects
Advanced Metallization Conference (AMC) 2000, P.IV: Reliability and Modeling
Poster Presentation, San Diego, California, USA, October 3-5, 2000.

7. Ersin Emre OREN* and A. C. TAS,
Hydrothermal Synthesis of Pure and Dy:BaTiO$_3$ *Powders at 90°C, Their Sintering Behavior, and Microstructures of Dy:BaTiO*$_3$ *Powders on Ti-Strips*
Journal of American Ceramic Society, 100th Annual Meeting & Exposition
"SXII - International Symposium on Dielectric Ceramics."
Oral Presentation, Cincinnati, OH, USA, May 3-6, 1998.

8. Ersin Emre OREN* and A. C. TAS,
Preparation of Piezoelectric Lead Zirconate Titanate ($PbZr_{0.52}Ti_{0.48}O_3$) *Powders by Homogeneous Precipitation and Calcination*
Journal of American Ceramic Society, 100th Annual Meeting & Exposition
"SXII - International Symposium on Dielectric Ceramics."
Oral Presentation, Cincinnati, OH, USA, May 3-6, 1998.

9. Ersin Emre OREN*, E. TASPINAR and A.C. TAS,
Chemical Synthesis of Antiferroelectric Lead Zirconate ($PbZrO_3$) *by Homogeneous Precipitation*
III. International Ceramics Congress, Turkish Ceramic Society,
Oral Presentation, Istanbul, Turkey, October 22-25, 1996.

D. Articles in Conference Proceedings

1. Tarik O. OGURTANI, M. Rauf GUNGOR and Ersin Emre OREN,
Interactive Computer Simulation of Dislocation Damping Spectra Associated with the Coupled Motion of Geometric Kinks and Point Defects Subjected to the Bulk Segregation Phenomenon

Mechanical Spectroscopy II, Published in: Solid State Phenomena, Volume **89-**90, pp141-191. Editor: L. B. Magalas, Trans Tech Publications, Switzerland, 2003. ISBN: 3-908450-74-8.

2. Ersin Emre OREN and Tarik O. OGURTANI,
Void Intergranual Motion Under the Action of Electromigration Forces in Thin Film Interconnects with Bamboo Structure
Thin Films: Stresses and Mechanical Properties IX, Vol. 695, pp L5.5.1-L5.5.7. Editors: C. S. Ozkan, R. C. Cammarata, L. B. Freund, H. Gao, Materials Research Society, USA, 2002. ISBN: 1-55899-631-1.

3. Ersin Emre OREN and Tarik O. OGURTANI,
The Effect of Initial Void Configuration on the Morphological Evolution Under the Action of Normalized Electron Wind Forces
Materials, Technology and Reliability for Advanced Interconnects and Low-k Dielectrics II, Vol 714E, pp L9.2.1-L9.2.6. Editor: S. Lahiri, Materials Research Society Online Proceedings, USA, 2001.

4. Tarik O. OGURTANI and Ersin Emre OREN,
A Computer Simulation of Void Dynamics under the Action of Electromigration and Capillary Forces in Narrow Thin Interconnects
Advanced Metallization Conference 2000 (AMC 2000), Vol 16, pp 483-487.
Editors: D. Edelstein, G. Dixit, Y. Yasuda, T. Ohba, Materials Research Society, USA, 2001. ISBN: 1-55899-574-9.

5. Ersin Emre OREN and A. C. TAS,
Hydrothermal Synthesis of Pure and Dy:$BaTiO_3$ *Powders at 90°C, The Sintering Behavior and Microstructures of Dy:*$BaTiO_3$ *Powders on Ti-Strips*
Ceramic Transactions, Vol. 100, pp. 95-104, Editors: K. M. Nair and A. S. Bhalla, The American Ceramic Society, USA, 1999. ISBN: 1-57498-066-1.

6. Ersin Emre OREN and A. C. TAS,
Preparation of Piezoelectric Lead Zirconate Titanate ($PbZr_{0.52}Ti_{0.48}O_3$) *Powders by Homogeneous Precipitation and Calcination*
Ceramic Transactions, Vol. 100, pp. 105-114, Editors: K. M. Nair and A. S. Bhalla, The American Ceramic Society, USA, 1999. ISBN: 1-57498-066-1.

7. Ersin Emre OREN, E. TASPINAR and A.C. TAS,
Chemical Synthesis of Antiferroelectric Lead Zirconate ($PbZrO_3$) *by Homogeneous Precipitation*
III. International Ceramics Congress, Volume II, Engineering Ceramics, pp. 59 65, Editors: V. Günay, H. Mandal and S. Özgen, Turkish Ceramic Society, Istanbul, Turkey, 1996. ISBN: 975-94814-2-1